Vibration from underground railways

A dissertation submitted to the University of Cambridge
for the degree of Doctor of Philosophy

by

Mohammed Farouk Mohammed Hussein
Girton College

December 2004

To my parents

Preface

The work described in this dissertation was carried out at Cambridge University Engineering Department between October 2001 and December 2004. The project was suggested by Dr Hugh Hunt, who also acted as my research supervisor. I am greatly indebted to him for his endless support, enthusiastic guidance, encouragement and interest in all aspects of the work presented here.

I am very grateful to Dr. Srikantha Phani for the interest he showed in this work and also for proof reading of this dissertation. I also thank Dr Geert Lombaert from the Katholieke Universiteit Leuven for his comments on Chapter 3, Mr. Simon Rutherford for proof reading the entire text of the dissertation and Dr. James Talbot for the useful discussions during his work at the Department in my first two years.

I would like to thank Professor Jim Woodhouse and Professor Robin Langely for their interest in this project and for some helpful discussions.

I am grateful for the generous financial support of the Cambridge Overseas Trust and London Underground Limited. I must also thank Dr. Hugh Hunt for his effort in securing funding for my second and third year of research. I also thank Girton College for their support over the past three years.

Special thanks go to my colleagues in the Dynamics and Vibration Group, particularly my office mate Mr. Andrew Grime, for making the research an enjoyable experience.

Finally, I wish to thank my parents. I must mention that without their encouragement and support I would never have been in a position to produce this dissertation.

I declare that, except for commonly understood and accepted ideas or where specific reference has been made to the work of others, this dissertation is the result of my own work and includes nothing which is the outcome of work done in collaboration. This dissertation is approximately 43,400 words in length and contains 86 figures.

Mohammed Hussein
Cambridge
December 2004

Summary

One of the major sources of ground-borne vibration is the running of trains in underground railway tunnels. Vibration is generated at the wheel–rail interface from where it propagates through the tunnel and surrounding soil into nearby buildings. The resulting vibration and re-radiated noise causes annoyance to occupants particularly in the frequency range 0 to 200Hz. An understanding of the dynamic interfaces between track, tunnel and soil is essential before engineering solutions to the vibration problem can be found.

This dissertation is concerned with the development of a computational model to evaluate the effectiveness of vibration countermeasures in underground railway tunnels, such as railpads and floating-slab tracks. The model is based on a new method for calculating the mean power flow from the tunnel, paying attention to that part of the power which radiates upwards to places where buildings' foundations are located. The mean power is calculated for an infinite train moving through the tunnel with a constant velocity.

To evaluate the effectiveness of vibration countermeasures, a comprehensive three-dimensional analytical model is developed. It consists of Euler-Bernoulli beams to account for the rails and the track slab. The slab is modelled in both bending and torsion and coupled via several lines of bearings to "the pipe-in-pipe model", which consists of a thin shell (the inner pipe) representing the tunnel embedded within an infinite continuum with a cylindrical cavity (the outer pipe) representing the surrounding soil. Coupling is performed in the wavenumber–frequency domain.

Wave propagation in the pipe-in-pipe model and floating-slab tracks on rigid foundation are studied. The study shows the effect of vibration countermeasures on the dispersion curves of the track. This in turn has a great effect on the forces generated at the tunnel wall and hence on the vibration propagated to the surrounding soil.

The dissertation also investigates the dynamic effect of moving trains on floating tracks with continuous and discontinuous slabs. Simpler models are used treating the tunnel wall as a rigid foundation. A track with discontinuous slab provides a parametric excitation to moving trains which can be significant especially for high-speed and heavy-axle trains.

Contents

Chapter 1

INTRODUCTION

In 1863 the first underground railway system in the world was opened in London. This was followed by other systems in Glasgow (1896), Paris (1900) and Berlin (1902). Today there are many other underground railways around the world, for instance in New York, Caracas, Athens, Cairo, Tehran and Sydney.

A serious disadvantage of underground railways is that vibration propagates through the tunnel and surrounding soil into nearby buildings causing annoyance to people. Vibration is either perceived directly or it is sensed indirectly as re-radiated noise. A third and very significant source of disturbance is due to movement of household objects, especially mirrors, or by the rattling of windowpanes and glassware.

Research on vibration from underground railways is carried out in response to an ever-increasing number of complaints. The aim of the research is to identify the generation–propagation mechanisms and to provide economic vibration-countermeasures for old underground tracks as well as a better design for new tunnels.

The research in this dissertation aims to develop a better understanding of vibration from underground railways. This chapter provides an introduction to the work presented in the later chapters. It explains the reasons for undertaking this research and sets out the objectives and the outline of the dissertation.

1.1 Motivation for the research

Inhabitants of buildings near railway tunnels often complain about vibration. The problem is of increasing importance for the following reasons:

- the introduction of new underground lines in urban areas;
- the general trend towards buildings with lighter constructions and longer spans which may lead to more vibration in buildings;
- the increasing public sensitivity to noise and vibration;

- the pressure to build on lands not previously used due to their proximity to subways.

To tackle the problem, the following areas should be addressed:

- identifying the permissible levels of vibration in buildings and quantifying the human perception of vibration;
- studying the vibration generation–propagation mechanisms;
- developing a computational tool capable of predicting vibration from underground railways;
- creating a quick computational tool capable of identifying the effect of vibration countermeasures;
- maintaining the best design practice for underground tunnels.

The human perception of vibration is addressed by carrying out interviews with people living near subways along with conducting measurements in laboratories and people's houses, see Chapter 2 for more details. An accurate prediction tool can be built using the Finite Element method (FEM) or the Boundary Element method (BEM). These methods can account for complex geometry provided that the large number of describing parameters are known. However they cannot easily be used as a design tool on account of the long running time involved. Analytical and semi-analytical models in 3D can be used to reduce computational time (at the expense of prediction accuracy) and they can be very useful in understanding the generation–propagation mechanisms.

1.2 Objectives of the research

There are two main aims of this dissertation. The first is to develop a better understanding of vibration from underground railways. The second is to provide a computational tool which can be used in the design of tunnels and to assess the performance of vibration countermeasures. This is important because vibration measurements are difficult to conduct and also because the performance of vibration countermeasures cannot sensibly be evaluated by trial and error. To fulfil these two main aims there are specific objectives that should be achieved:

1. to model various tracks in particular floating-slab tracks with continuous and discontinuous slabs. The model will be used to understand the effect of train velocity and excitation frequency on the generated forces at wheel-rail interface in both types of slabs and to address parametric excitation associated with discontinuous slabs;

2. to develop a 3D model which maintains computational efficiency while accounting for the essential dynamics of the track, tunnel and surrounding soil. This model will account for the different types of slab connectivity on the tunnel wall;

3. to provide a better understanding of wave propagation in the track, tunnel and surrounding soil. This will be addressed by looking into a wave-guide solution;

4. to model power-flow from underground railway tunnels. This will provide a better performance measure than currently available, as it accounts for both the stress and velocity fields around the tunnel. The current measures account only for velocity fields.

1.3 Outline of the dissertation

This dissertation comprises six chapters. Chapter 2 reviews the literature relevant to the work presented in following chapters. It reviews in particular the impact of vibration, excitation mechanisms, modes of propagation, vibration countermeasures and modelling of vibration from surface and underground trains. The chapter identifies areas which should be addressed by research.

Chapter 3 models tracks with continuous and discontinuous slabs under harmonic moving loads. Continuous slabs are modelled using the Fourier transformation method. Wave propagation is studied and the critical velocity is identified. Also a power calculation is performed to verify the results for this type of track. Three different methods are presented to model tracks with discontinuous slabs. These are the Fourier–Repeating-unit method, the Periodic-Fourier method and the Modified-phase method. A train model is coupled to the track to calculate the dynamic effect of slab discontinuity.

A comprehensive model of a railway track in an underground tunnel is presented in Chapter 4. Different types of slab connectivity are modelled. A study is conducted to understand wave propagation in the free tunnel, free soil, a track on rigid foundation and the coupled track-tunnel-soil system.

A new method is presented for calculating vibration from underground railways in Chapter 5. The method is based on calculating the mean power flow from the tunnel, which radiates upwards to places where buildings' foundations are expected to be found. The model presented in Chapter 4 is used to perform the calculation. The method is used to evaluate the effectiveness of vibration countermeasures such as soft railpads and floating-slab tracks.

Finally, based on the work presented in this dissertation, overall conclusions and suggestions for further research are given in Chapter 6.

Chapter 2

LITERATURE REVIEW

Introduction

Researches on ground-borne vibration have gained a special interest in the last two decades. The general structural trend towards lighter constructions with longer spans, along with the introduction of new surface and underground railway-lines in urban areas have led to more vibration inside buildings. This in turn has led to more complaints from occupants of buildings. Researches aim to gain better understanding of the physics behind the generation and propagation of vibration from different sources to buildings and to help decrease the vibration by providing some countermeasures. Many researches have been conducted to study different aspects of the problem. In Cambridge University for example, Hunt [45] investigates ground-borne vibration induced by traffic. Cryer [18] studies vibration in buildings with application to base isolation. Lo [71] investigates vibration transmission through piled foundations. Ng [84] studies transmission of ground-borne vibration from surface railway trains. Forrest [29] models ground vibration from underground railways. Talbot [107] discusses a generic model to assess the performance of base-isolated buildings.

The reader with more interest on ground-borne vibration can find, beside this chapter, other literature reviews for modelling and measuring of ground-borne vibration. For example, Hung and Yang [44] review the studies on ground-borne vibration with emphasis on those induced by trains. Hunt and Hussein [50] discuss prediction and control of ground-borne vibration transmission from road and rail systems and review some of the relevant literature.

This chapter is divided into five sections discussing the impact of vibration, excitation mechanisms, modes of propagation, vibration countermeasures and modelling of vibration from trains. The work of Forrest [29] is of particular interest and discussed at the end of Section 2.5.3 in some detail, as it forms the basis for the work presented in this dissertation.

2.1 Impact of vibration

People are exposed to vibration in daily life in various ways depending on their life style and the nature of their work. Human reaction to vibration is the subject of extensive research. The perception of vibration varies from person to person. According to the BS 6841:1987 [11], there are many factors which influence human response to vibration. The factors fall into two categories:

1. intrinsic variables, which include population type (age, sex, size, fitness, *etc*.), experience, expectation, arousal, motivation, financial involvement, body posture and activities;
2. extrinsic variables, which include vibration magnitude, vibration frequency, vibration axis, vibration input position, vibration duration, seating and other environmental influences (noise, heat, acceleration and light).

Vibration can degrade health, influence activities, impair comfort and cause motion sickness [11], depending on its magnitude, frequency and exposure duration. It is found [2] that exposure to high frequency vibration with low amplitude for long periods of time affects concentration ability, while exposure to low frequency vibration with high amplitude for short periods may cause muscular or internal organ injury. Vibration also can cause malfunctioning of sensitive equipment [37].

Ground-borne vibration is distinctive in that it is generally not problematic above 200 Hz [56]. At higher frequencies the attenuation along the path through the ground is strong. Vibration is observed in buildings and can be attributed to different kind of sources, for instance, transportation systems (road vehicles, trams and trains) and construction activities (piling, excavating and demolishing). In general, the effect of ground-borne vibration is annoyance to people rather than damage to buildings [90,94]. However, damage may occur to historical buildings. It is reported by Hildebrand [43] that fear of damage to historic structures in Stockholm's medieval quarter 'Gamla Stan' has been one of the obstacles to the building of a new railway track intended to relieve overcapacity on the existing lines.

Beside its impact on buildings' occupants and equipment, ground-borne vibration from railway trains can cause instability of track embankments, damage to wayside building foundations, fatigue cracks in sleepers and asymmetrical settlement in ballast [43].

The effect of vibration on occupants depends on the source itself, its distance from the building and the physical properties of the ground supporting the source and the building. Inhabitants perceive vibration either directly as motion in floors and walls or indirectly as re-radiated noise. A third and very significant source of disturbance is due to movement of household objects, especially mirrors, or by the rattling of windowpanes and glassware.

Many studies and standards address the vibration effect on buildings' occupants and equipment. The British standard BS 6472:1992 [10] provides a general guidance on human exposure to building vibration in the frequency range 1 to 80 Hz. It provides curves for equal annoyance for human plotted as root-mean-square acceleration versus frequency. Some measures are used to determine the probability of having adverse comments from the occupants due to annoyance. The vibration dose value (VDV) is used as a vibration measure which takes into account the time history of the vibration (whether continuous or intermittent) for the day or the nighttime.

Experimental work by Duarte and Filho [24] shows that the sensitivity of people to a sinusoidal vibration decreases with frequency up to around 40-50 Hz. This is because the human-head resonates around 20-40 Hz and hence it makes the person sensitive to even low amplitudes of vibration. Sensitivity increases again in the range between 50-100 Hz where the chest wall and ocular globe resonate. The work shows also that women are more sensitive to vibration than men.

Gordon [37] develops a generic vibration criteria (VC curves) for vibration-sensitive equipment. These curves are plotted in similar way to the ISO 2631-2:2003 [54] guidelines for the effects of vibration on people in buildings. Vibration is expressed in terms of its root-mean-square velocity and plotted as a one-third-octave band. For a site to comply with a particular equipment category, the measured one-third octave band velocity must lie below the appropriate criterion curve, see Figure 2.1.

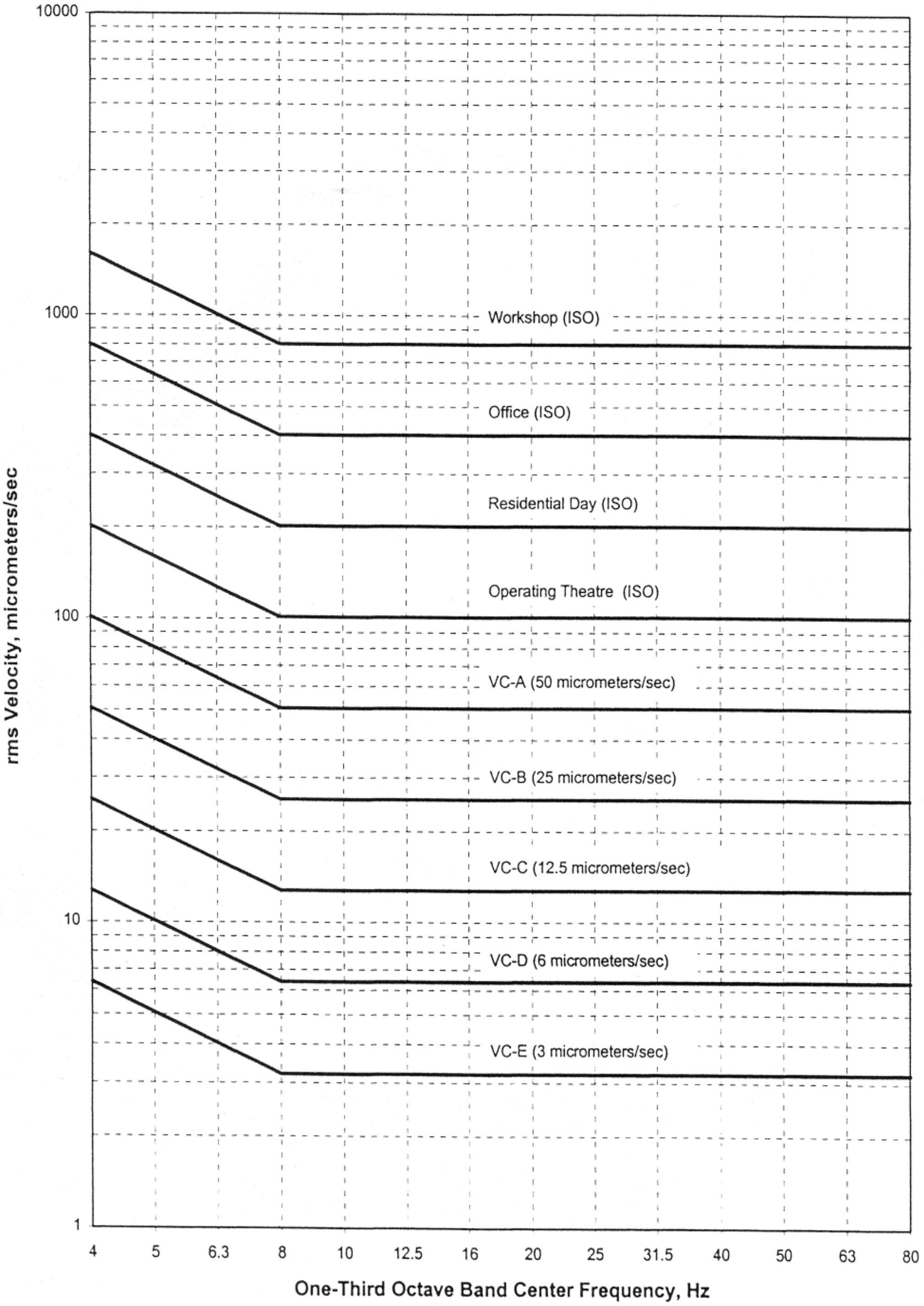

Figure 2.1: Generic Vibration Criterion (VC) curves for vibration-sensitive equipment -showing also the ISO guidelines for people in buildings (reproduced from [37]).

With more complaints about ground-borne vibration, many surveys are conducted to assess the vibration effect on buildings' occupants and to help establishing standards. In Nagoya in Japan for example, the city authority conducts surveys about every five years to investigate the state of noise and vibration environment in the city area [88].

A noise and vibration study by Fields [27], based on interviews with people who live near railway tracks, finds a generally high level of dissatisfaction within 25m of the track. People interviewed in the range 25m to 150m from the track report rapidly-diminishing levels of complaint and for distances beyond 150m there is a uniform and low-level of complaint. The study shows that many factors affect perception such as the duration of vibration, the time of day, background vibration levels and various psychological factors such as whether the railway is visible. Turunen-Rise *et al.* [115] and Klaboe *et al.* [61] present a new Norwegian standard NS8176 for vibration in buildings from road and rail traffic. The standard introduces a single quantity to describe the vibration in buildings. This quantity is the statistical value of maximum velocity or acceleration, $v_{W,95}$ and $a_{W,95}$ respectively. These are calculated by recording the vibration for at least 15 passing trains or vehicles. For each record the 1/3-octave band frequency spectrum is calculated and weighted with weight-values proportional to the human response at each band. Assuming a log-normal distribution of the root-mean-square values, $v_{W,95}$ and $a_{W,95}$ are calculated from the velocity and acceleration with a non-exceeding probability of 95%. In this standard, vibration should be measured in a position and direction in the building which gives the highest vibration. A survey is conducted by questioning people who live in buildings where $v_{W,95}$ and $a_{W,95}$ were calculated using a prediction model. According to the survey, it is found that there is no significant difference in reactions to vibrations from different sources. The prediction model which is validated by some measurements, takes into account the track quality, the ground conditions, distance from vibration sources, vehicle speeds and amplification of the vibration from the ground into the building. According to the study, buildings are classified into four categories (A to D) describing the building state in terms of vibration. In order to provide a common answer format for socio-vibrational studies and a better data exchange from future surveys to assess human perception of vibration in buildings, Klaboe *et al.* [62] present a methodology to standardize carrying out a survey.

Research on ground-borne vibration, especially from underground railways, has recently gained prominence on account of the need to establish new underground tunnels in cities and pressure to put high-speed intercity lines underground near residential areas. A particular feature of underground trains is the widespread notion that once underground the problem of noise goes away. But pure vibration in the absence of noise can be unnerving and more disturbing than vibration from surface trains which are audible. Also of concern is that underground tunnels may pass near building foundations causing significant structural vibration. To address these issues a programme of research entitled CONVURT [16] (CONtrol of Vibration from Underground Rail Traffic) was established under the 5th framework of the EU program for research, technological developments and demonstration. The project has four main objectives: the first is to create validated innovative and quantitative modelling tools to enable accurate prediction of ground-borne vibration transmission into buildings. The second is to develop and evaluate new and cost effective track and tunnel components to reduce ground-borne vibration and especially to develop devices capable of being retrofitted to existing track. The third is to provide scientific input to allow the preparation of international standards. Finally, CONVURT aims to establish guidelines of good practice for underground railway operation in order to maintain minimum vibrations for the lifetime of operation.

2.2 Excitation mechanisms

Significant vibration in buildings near railway tracks and subway tunnels is attributed to moving trains. There are five main mechanisms for the generation of vibration from moving trains. These mechanisms are discussed in the following paragraphs.

The first mechanism arises when successive axles of the train pass by a fixed observation point. The response of the observation point exhibits a peak when the simultaneous position of one of the wheels lies at the nearest track point to the observation point. It shows a trough when the nearest track point to the observation lies between two axles. The mechanism is known as the quasi-static effect and it is modelled by static forces (each force equal to the static force transmitted at the rail-wheel interface) moving along the track with the train velocity. The effect is distinguishable close to the track and it significantly contributes to the low-frequency response in the range 0-20Hz [56,100].

The second is known as the parametric excitation mechanism and it is attributed to varying stiffness under moving wheels. The rail is discretely supported by sleepers at regular distance (typically 0.6m). A moving wheel over the rail experiences high stiffness at a sleeper and low stiffness between two sleepers. When the wheel moves with a constant velocity over the rail, it applies a periodic force with time-periodicity equal to the sleeper spacing divided by the wheel velocity. The force can be decomposed into Fourier series with principle frequency equal to the train velocity divided by the sleeper spacing. A measured acceleration spectra near railway track is presented by Heckl *et al.* [41]. It shows that peaks appear at some distinctive frequencies such as the sleeper-pass frequency and also that the response can be large if the wheel-track resonance coincides with one of the sleeper-pass harmonics, see also [43].

The third mechanism occurs due to height differences at rail joints and crossings. Wheels apply impulsive loading to the rail at these joints because wheel's curvature does not follow sudden jumps or rails' discontinuities. Significant force levels can be produced in the rail and on trains. Also the noise produced by this excitation mechanism is annoying for passengers of the vehicle. This mechanism is becoming less important with the increasingly-widespread use of continuously-welded track.

The fourth source of vibration is that generated by rail and wheel unevenness or roughness. For an ideal case of smooth-wheels train, a mutual force occurs at the wheel-rail interface when a wheel moves over a continuous rail (attached to uniform ground) with a given wavelength-roughness. The mutual force has a frequency equal to the train velocity divided by the wavelength and it is influenced by the inertial force of the train at the same frequency. Typical rail roughness has higher amplitude of unevenness for long wavelengths [30], while wheel roughness seems to have constant unevenness for wavenumbers in the frequency range of interest of ground vibration [22]. A major source of rail roughness is corrugation at wavelengths typically around 25mm to 50mm [85], but they generate vibration at frequencies well above 250Hz. These frequencies are attenuated by the ground and hence they are not transmitted to buildings nearby railways.

The fifth and final mechanism is generated by high-speed trains. In this mechanism very large amplitudes of vibration can be generated when train speeds approach or exceed either the speed of Rayleigh surface waves in the ground or the minimal phase velocity of bending waves in the track, see Figure 2.2. In low-speed urban rail networks no attention should be given to this mechanism because the speed of trains is low compared with all critical wave-propagation speeds. In recent years some attention has been given to this mechanism due to the increasing international trend towards higher speed trains. For the case of very soft soil, critical speed can be easily exceeded by modern trains. If the train velocity exceeds the Rayleigh wave speed, a ground vibration boom occurs. In a location near Ledsgard in Sweden, the Rayleigh wave speed velocity in the ground is around 45m/s. An increase in train speed from about 38m/s to 50 m/s led to an increase of about ten times in the generated ground vibration [67]. If train speed increases further to the point where it reaches the minimal track phase velocity, larger deflections might occur and this might result in train derailment.

There are other special sources of vibration excitation in addition to the five mentioned above. For instance, vibration is generated when a train approaches a bridge due to the change of trackbed stiffness and geometry [47]. However, this can be classified as a parametric excitation.

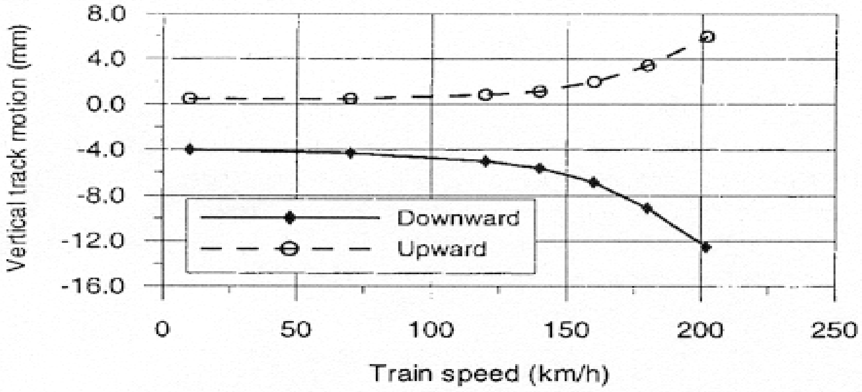

Figure 2.2: Average measured downward and upward vertical displacement of a track with different train velocities (reproduced from [58]).

2.3 Modes of propagation

Vibration propagates from the source to the receiver through motion of particles in the transmission path. One way to understand the motion mechanism is by looking into the wave-guide solution. The simple one-dimensional wave-guide solution results from the differential equation

$$\frac{\partial^2 y(x,t)}{\partial x^2} = \frac{1}{{c_0}^2} \frac{\partial^2 y(x,t)}{\partial t^2} \tag{2.1}$$

where y is the particle displacement, c_0 is constant, x and t are the distance and time respectively. The solution of this equation can be written as

$$y = A_1 Y(x - c_0 t) + A_2 Y(x + c_0 t) \tag{2.2}$$

which describes a non-dispersive (*i.e.* wave speed is independent of the excitation frequency) propagating-wave solution. A_1 and A_2 are constants and can be determined from the boundary conditions. The first term in the right hand side of equation 2.2 accounts for a wave propagating in the positive x direction with a velocity c_0 and the second term accounts for a wave propagating in the negative direction with the same velocity c_0. A physical example satisfying equation 2.1 is the unforced-motion of an undamped string [38]. Differential equations with different orders and added terms to equation 2.1 may result in non-dispersive wave-solution and/or existence of other type of waves which are associated with the source near-field response.

In this dissertation, the pipe-in-pipe "PiP" model is used in which an underground tunnel is modelled as a hollow cylinder and the surrounding soil is modelled as an infinite domain containing a cylindrical cavity. The model is used by Forrest [29] to model an underground tunnel and its surrounding soil and by Kopke [65] to model a gas pipe in an infinite soil, where in both the models only symmetrical loads are considered. The relevant literature of wave propagation related to this model is reviewed in the next sections, in which wave propagation in a full-space and a half-space media and wave propagation in cylindrical shells are discussed.

2.3.1 Wave propagation in a full-space and a half-space media

In an infinite isotropic elastic continuum, two types of non-dispersive waves can freely propagate and these are called the *body* waves. The first is a dilatational wave, or a *pressure* wave (known as the P-wave). This is a longitudinal wave, where the wave-front and the medium particles move in the same direction. The second is the equivoluminal wave or the *shear* wave (known as the S-wave). This is a transverse wave, where the wave-front and the medium particles move perpendicular to each other.

In an elastic half-space, both types of body waves decay at the surface and only *Rayleigh* wave propagates freely at the surface. These different waves can be realised by applying an impulsive load on the surface and observe the response away from the load. Three different waves are received at three different times. The pressure wave is the fastest and arrives first, the shear wave comes next and finally Rayleigh wave arrives and it is associated with large amplitudes. Rayleigh wave (known as the R-wave or the surface wave) is non-dispersive and it is confined near the surface to a depth approximately equal to the wavelength. The particles move in elliptical shape in the same plane as the wave-front. The vertical component of particle motion is greater than the horizontal component; both components decay exponentially with depth. Away from the surface where the Rayleigh wave disappears, motion of particle is attributed to body waves.

Pioneering work of Lamb [69] on the response of an isotropic elastic half-space to different kinds of impulsive and harmonic loads forms the basis of all contemporary understanding of wave propagation in elastic half-space. For the frequency range of interest, the distribution of energy between the three different kinds of waves are calculated by Miller and Pursey [80] for an elastic half-space excited by a vertically oscillating normal point force on the surface. Of the total input energy, 67% radiates as R-waves, 26% as S-waves and 7% P-waves. The calculations performed by Miller and Pursey is presented in more informative manner by Woods [118] as shown in Figure 2.3.

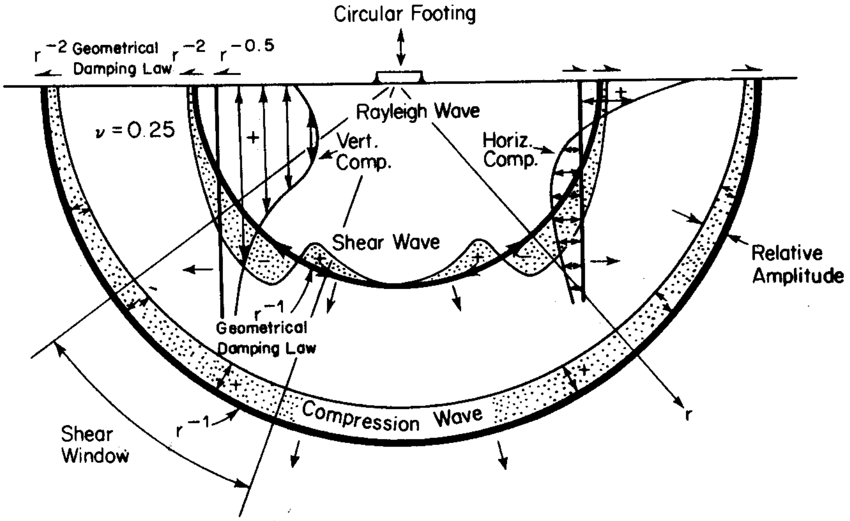

Figure 2.3: Wave propagation in an elastic half-space from a vertical surface load showing R- S- and P-waves (reproduced from [118]).

As P-and S-waves spread with hemispherical wave-fronts in the ground their decay rate is inversely proportional to the distance from the source. R-waves on the surface spread on a circular wave-front and with a decay rate inversely proportional to the root square of the distance from the source. Body waves do not propagate freely on the surface and their decay rate is inversely proportional to the square distance from the source.

In a layered half-space, where a layer with different properties is overlying a half-space, dispersive waves propagate on the surface of the upper layer. These waves propagate with velocities in the range between the Rayleigh wave speed of the upper layer and the shear wave speed of the half-space [101]. Waves propagate above and at some frequencies that are known as the cut-on frequencies. The types of propagating waves in the ground depend on the ground properties and the boundary conditions. The Stoneley wave is another example that appears at the interface of two half-spaces with different materials and the Love wave, which is the fastest surface wave, with motion perpendicular to the interface [38].

2.3.2 Wave propagation in cylindrical shells

Most of the papers reviewed in this context use the same procedure of analysis. Equations of motion are formulated and used to derive the stress equations. For the unforced vibration case, the stress equations are equated to zero to calculate the *dispersion equation.* The dispersion equation provides a relationship between the angular frequency and the wavenumber in the form $f(\xi,\omega)=0$, in which wave-solution in the form of equation 2.3 exists.

$$y = e^{i(\omega t+\xi x)} \tag{2.3}$$

where ω is the angular frequency and ξ is the wavenumber in the x direction. For a positive real value of ω, equation 2.3 represents a wave propagating in the negative x direction for a positive real ξ. Generally speaking, three types of waves can be found: free-propagating wave when ξ is pure real, evanescent wave when ξ is pure imaginary and leaky wave when ξ is complex (more discussions are given in Appendix B).

McFadden [76] investigates radial vibration of thick-walled hollow cylinders. The dispersion equation is formulated for the case of axisymmetrical motion and only real wavenumbers are considered. Analytical solution of the dispersion equation is calculated. Greenspon [39] and Gazis [33-35] investigate free-propagation in thick cylindrical shells and their results are published around the same time. Gazis provides a thorough investigation of the problem. The displacement equations are defined for different zones of wavenumbers and angular frequencies and written in terms of Bessel functions and modified Bessel functions. The dispersion equation, which is calculated to be always a real function, is derived in terms of quantities dependent on frequencies and wavenumbers and solved by the *interval halving iteration technique*. At a given real wavenumber, zeros of the dispersion equation are searched by evaluating the dispersion equation at frequencies with a fixed interval. When a change in the sign is recorded, the interval is halved and the direction of search is reversed to get closer to the root. Gazis produces dispersion curves for symmetrical and non-symmetrical motions and uses the same formulation to calculate dispersion curves for thin cylinders and for rods or what is known as Pochhammer's modes (The first author to formulate axially symmetric vibrations in rods). Gazis also discusses some simple cases degenerate from the dispersion equation, *e.g.* torsion waves and plane-strain motion. All the previous work of Gazis can also be found in a book entitled "Free vibrations of circular cylindrical shells" [3], where numerical values of the dispersion curves are provided.

Onoe *et al.* [89] investigate real, imaginary and complex solutions of the dispersion equation of axially symmetric waves in an elastic rod. They construct a mesh in the frequency wave-number coordinates through groups of curves that are used as bounds for solution branches. The method is ingenious, but perhaps less useful now that powerful computational techniques are available.

Bostrom and Burden [9] study surface waves along a cylindrical cavity. Displacement functions are calculated as a summation of the three wave components, namely transverse (SH and SV) and longitudinal P-waves. The dispersion equation is derived in a closed form. Simplified equations are presented to calculate the cut-on frequencies using the limiting forms of the modified Bessel functions. For a surface wave to take place along the cavity, its phase velocity should be less than the shear wave velocity, as a radial decaying displacement is obtained away from the surface in this case similar to surface waves in a half-space. It is found that surface-waves propagate along the cavity with a phase velocity in the range between the shear-wave velocity and Rayleigh-wave velocity. The effect of various point forces acting near the cavity is also investigated.

The literature on free wave propagation in composite cylindrical shells, cylindrical shells filled with water and cylindrical shells surrendered by water is intensive. Epstein [26] investigates circumferential waves in a cylindrical shell supported from inside by a continuum. The work considers only the two-dimensional plane-strain case. Greenspon [40] studies wave propagation of shells surrounded by water. Biot [6] investigates propagation of waves in a cylindrical shell containing a fluid, where only axially symmetrical waves are considered. Scott [97] calculates solutions of the dispersion equation of a thin cylindrical shell, loaded with a fluid from outside. He presents the dispersion equation in terms of the *fluid-loading parameter*. When the fluid-loading parameter is equal to zero, the dispersion equation of the shell without the surrounding water is generated. When the loading parameter is set to infinity, it gives the dispersion equation of a shell rigidly supported from outside. Starting from zero fluid loading at a given frequency, where the roots are calculable, the parameter is increased to full value (giving the case of the shell surrounded by fluid) in small steps and *Newton-Raphson* method is used to find new solutions in each step. Having determined the solutions for the full-loading parameter, a frequency step is used to determine the solutions for the range of frequency of interest.

Other methods are proposed to find solutions of dispersion equations. An example is the bisection method searching for minima of the absolute value of the dispersion equation. The method is slow compared with previous methods but it works better when two solutions lie in close proximity to each other [72]. It should be mentioned that each method has disadvantages and its own treatment for any numerical difficulties and there is no best method to find function roots [92].

2.4 Vibration countermeasures

There are many methods to decrease ground-borne vibration at buildings. They generally fall into three categories. Vibration isolation can be achieved by isolating the source, interrupting the vibration path and/or isolating the receiver *i.e.* the building. This section investigates and discusses the common methods in each category.

2.4.1 Vibration isolation at source

The main advantage of having a vibration countermeasure at the source is that larger number of buildings benefit from the countermeasure.

Source-vibration countermeasures include using low-stiffness train suspensions, continuous rail support, soft railpads, resiliently mounted sleepers and floating slab-tracks. Other countermeasures such as rail grinding, rail welding and wheel truing also reduce vibration. However, they are generally considered as maintenance issues rather than vibration countermeasures.

There are two types of railway track: ballasted track and slab track. Ballasted track is used for surface as well as underground railways. In this type, sleepers are supported on a layer of ballast on the ground. In the other type, *i.e.* the slab track, sleepers are supported on a concrete slab resting directly on the trackbed and known as directly fixed slab. Floating-slab track is widely known as an effective measure of vibration isolation for underground tunnels. Rubber bearings or steel springs are accommodated between the slab and the tunnel bed. The slab can be continuous or discontinuous. Continuous slab is cast in-situ and discontinuous slab is constructed in discrete pre-cast sections. Examples of floating-slab tracks are the 1.5m slab in Toronto, the 3.4m Eisenmann track in Munich and Frankfurt, the 7m slab in New York subway and the British VIPACT continuous slab system [29]. For surface trains, use of ballast mat underneath the normal ballast is analogous to the use of floating-slab track in underground tunnels. In some underground tunnels, where ballasted track is used, the ballast mat is used at sensitive areas, such as when the tunnel passes near the surface of the ground. An example of ballast mat used within a tunnel can be found in MBTA Boston in USA. Ballast mats are also used to improve electrical isolation, water drainage, or to reduce pulverisation of the ballast [94]. Modern designs of underground tunnels incorporate the two types of tracks in one assembly. Sleepers are supported on ballast filling a concrete tray, see Figure 2.4.

Figure 2.4: Installation of a floating-slab track in the form of precast reinforced concrete tray (courtesy of GERB, Germany [36]).

For old underground tunnels with directly-fixed slab or ballasted track, use of floating slab is not possible and hence rail pads may be the most economic solution for vibration problems. A recent advance in the railpad technology involves supporting the rail under the head and in the web with large rubber wedges, leaving the foot of the rail suspended, see Figure 2.5. This provides very low dynamic stiffness with minimal rail roll, very low profile and enables an easy maintenance of components [91]. The major disadvantage of using soft pads is that they permit greater rail vibration and consequently increased noise radiation [43]. Moreover, tracks will be more susceptible to corrugation growth, which may outweigh the benefit of resilient support [85].

Vibration isolation can also be achieved at the source by removal of wheel surface irregularities and by prevention of wheel surface irregularities. The latter is achieved by implementation of improved methods for lubrication at curves. Also rail grinding, rail welding, rail alignment, track foundation enhancement, widening of embankment, extra heavy tunnel structure and increasing the tunnel depth provide some extra vibration isolation [43,94,116].

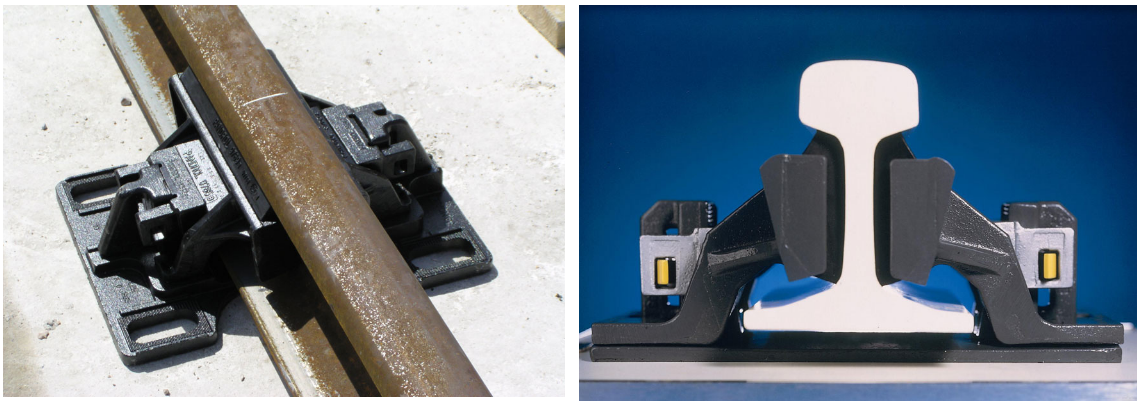

Figure 2.5: Vanguard resilient support of a rail (courtesy of Pandrol Ltd, UK [91]).

Many researchers study the effect of source countermeasures. For instance, Wilson *et al.* [115] discuss different methods for isolation of ground-borne vibration. They present values for the expected-isolation performance by using some of these countermeasures. Reducing resonance and unsprung mass of bogies lead to isolation up to 10-15dB of ground-borne vibration. Rail grinding and wheel truing lead to 10-15 dB isolation.

Lang [70] studies the effect of countermeasures on vibration from trams. This is a very special problem because of the very short distance between tracks and residential areas. Also, the normal type of track with sleepers-ballast system is not possible for tram rails which should be in the same level with the road surface. The work investigates the effect of floating slab on mineral wool on Vienna tramway.

Hildebrand [43] reports about some successful methods of vibration isolation. Among these methods, soil stabilisation is used in one site and in-track countermeasures (sleeper spacing is reduced, sleeper mass is redistributed so larger mass is directly underneath the rail and railpads are installed) are used in another site. It is likely that soil stabilisation reduces the vibration by decreasing the quasi-static effect.

2.4.2 Interrupting the path

Isolation of ground-borne vibration can be achieved by interrupting the vibration transmission-path with the use of open trenches, infilled trenches and tubular or solid row of piles. A trench is more effective in isolating the vibration than a row of piles. However, its use is limited to small depths due to soil-instability and water level considerations [57]. Trenches and piles diffract the waves and reduce the vibration amplitudes. They can be used near a source or near a receiver. Isolation near the source aims to reduce body waves and Rayleigh waves. Isolation near the receiver aims to reduce only Rayleigh waves, as body waves are rapidly attenuated at the surface away from the source. Researches on trenches include the work of Woods [118] who conducts full-scale experiments to assess the performance of trenches and sheet wall barriers. The trench geometry has a clear effect on the isolation performance. The work concludes that larger trenches are required at greater distance from the source to give a certain amplitude reduction. Magnification of amplitudes occurs in front (the source side) and to the side of trenches. Sheet wall barriers are not as effective as open trenches in screening surface waves.

Lang [70] reports a 6dB reduction in the velocity level near a tramway by using a trench filled with ballast. However, very small reduction is achieved away from the track.

Developments in numerical methods have advanced the work on modelling of trenches. The BEM is preferable for its ability to model an infinite domain and it only involves discretization of the surface. Klein *et al.* [63] use the BEM along with full-scale measurements to investigate the performance of trenches as a measure of vibration isolation. Plots of contours that have the same magnitude of the vibration performance are presented. These contours are called the isosurface and the vibration performance is defined as the ratio of the vertical response in presence of the trench over that response in the absence of the trench. As a general rule, the depth of the trench should be at least equal to Rayleigh wavelength in the ground for a good performance as most of the energy of the Rayleigh waves is confined to this depth. An existence of any sub-layers in the ground may worsen the performance of the trench due to reflection of waves at these layers. Kattis *et al.* [57] present a method to analyse a row of piles by transforming the piles into a continuous trench using the *homogenisation technique* which is well-known in the mechanics of fibre-reinforced composite materials. In this way, the running time of a BE code is greatly improved. The performance of open trenches or piles is found to be better than the concrete filled ones. Also it is found that the performance of open or concrete-filled trenches is better than performance of a barrier made up of discrete piles.

2.4.3 Vibration isolation of buildings

Base isolation is a common countermeasure to decrease ground-borne vibration in buildings. Steel springs or rubber blocks (called 'bearings') are placed between the building and its foundation to isolate the building from the motion of the ground. Bearings are provided in prestressed boxes which help in controlling differential settlements of the building and minimise the static deflection. Moreover, base isolators may be designed to isolate high levels of vibration from earthquakes. For earthquake isolation, systems can be used that are rigid except at extreme earth movements, when rigid links break and the isolation system is free to function [48].

A paper by Hunt [48] presents a review of base isolation of buildings. It discusses simple models of base-isolated buildings such as a single-degree-of-freedom system. It shows that the performance of such a model agrees with field measurements near the primary frequency of the building where the building moves as a rigid body. At higher frequencies, simple models do not work, as they do not account for the building flexibility and wave propagation characteristics. The paper also discusses the change of ground-vibration field due to base isolation of buildings. Constructing a building without an isolator decreases the ground vibration due to its added inertia effect. By using an isolator, the building is isolated but the ground vibration is not decreased. These counter-effects may decrease the total benefit of using base isolation of buildings.

Figure 2.6: Base isolation of buildings (courtesy of CDM, Belgium [12]).

Cryer [18] models vibration in a building with application to base isolation. He uses a computationally powerful model of an infinite building with a repeating-unit, analysed using the stiffness method and *Floquet's theorem*. The infinite model shows the same general characteristics as a finite model, though it does not show standing waves reflecting from the building's boundaries.

Talbot [107-109] presents a generic model using infinite models in the longitudinal direction to assess the performance of base-isolated buildings. He uses the stiffness method and Floquet's theorem to model a 2-dimensional multi-story building. This building is coupled to a row of piles in a 3-dimensional half-space modelled using the BEM and Floquet's theorem to account for periodicity in the longitudinal direction. He also introduces the power flow concept as a single useful measure of isolation performance. In a different paper, Talbot [110] investigates the effect of side-restraint bearings on the vibration isolation performance. The longitudinal, transverse and torsion stiffness of bearings including the side ones influence the isolation performance. The stiffness of side-restraint bearings should be minimised to keep the global resonance frequencies of buildings as low as possible. It is also found that damping in bearings has little effect on the isolation performance. The reader is referred to reference [112], for more details about base isolation of buildings.

2.5 Modelling of vibration from trains

Surface and underground railways are important sources of vibration in buildings near railway tracks. Large amplitudes of vibration generated by trains may cause instability of vehicles while low amplitudes may cause discomfort to passengers. For more than 100 years, many models of tracks have been presented. The purpose of work in this field is to provide an understanding of the behaviour of the wheel-rail interaction and the nature of noise and vibration generated by trains. This helps outlining the necessary conditions for stability of vehicles, comfort of people using vehicles and comfort of people live near railway tracks. This section discusses the literature of modelling of tracks, modelling of vibration from surface railways and modelling of vibration from underground railways respectively.

2.5.1 Modelling of tracks

This section reviews models of tracks on a ground modelled as a uniform stiffness or a rigid foundation. Models of tracks on elastic half-space or layered ground are considered in Section 2.5.2. The current models are important to investigate the effect of properties of the track, train speed, sleeper spacing, rail joints, wheel and rail roughness on the wheel-rail interaction. Two types of models are considered, continuous where the model is uniform along the track and discontinuous where the model is periodic due to sleeper spacing and/or rail joints.

Continuous models

A simple and widely accepted model of a track was first presented by Winkler in 1867. The model consists of a single infinite beam supported on a foundation with constant stiffness. Timoshenko proves its validity as a model of a railway track. In a paper entitled "History of Winkler foundation", Fryba [32] writes:

The Winkler foundation was many times cursed and refused, but the scientists return to this simple law again and again. I think that it shares the same lot as the other simple theories like Bernoulli-Euler beam, Palmgren-Miner rule etc.: Their simplicity wins against more precise formulations.

Many authors use a model of a beam on a Winkler foundation to investigate the dynamics of railway tracks. Two theories for the beam are used, Euler-Bernoulli and Timoshenko formulations. The former accounts only for the bending behaviour while the latter takes account also for shear deformations and rotary inertia of the beam. For a low frequency of excitation, where the propagating wave has a wavelength much greater than the beam-cross-sectional dimensions, both the formulations converge to the same solution. For a high frequency of excitation, Timoshenko formulation is necessary for an accurate solution.

Mathews [73] models the steady-state response of a beam on an elastic foundation under a moving oscillating load. He models the beam using Euler-Bernoulli formulation and solves the differential equation of the response using Fourier transformation techniques. He calculates a closed form solution for the beam response using the contour integrals and the residue theorem. In this paper, no damping is included and results are given for the case of complex poles, i.e. for velocities below the critical velocity. In a different paper [74], Mathews calculates the response, when viscous damping is included. For all velocities of moving load and excitation frequencies, it is found that all poles are complex values. A special consideration is required for calculating the response of a beam on elastic foundation with no damping, as purely real poles are produced above the critical velocity. Another aspect of the undamped beam is that the displacements are symmetrical about a non-oscillating moving load in a moving frame of reference.

Chonan [14] presents a model of a beam on an undamped elastic foundation using Timoshenko formulation for the beam. Small damping is introduced in the foundation to shift poles on the real axis to the complex domain. Bogacz *et al.* [8] present a generalisation of the problem comparing results of the beam response calculated by the two formulations; Euler-Bernoulli and Timoshenko. In the previous models, viscous damping is used whenever damping is introduced to the foundation. However, structural damping may also be used [59]. A detailed description for modelling of infinite beams under moving loads can be found in [31].

Duffy [25] presents a solution for a more complicated problem in which he calculates the complete solution (transient and steady state) of a beam on elastic foundation under a moving oscillating mass. Fourier transformation with respect to space is used to transform the differential equation. Laplace transformation is used with respect to time. This is because the beam response is equal to zero before applying the load, *i.e.* for $t \leq 0$ and it responds according to the load afterwards.

There are other types of foundations, *e.g.* Pasternak foundation [96] (Winkler foundation with a shear layer coupled from the top) but they are less popular in modelling of railway tracks.

Discrete-continuous models

To study the effect of rail joints and sleepers on the rail-wheel interaction, many studies have been conducted. The common feature of these studies is that the model is infinite in length with periodic discrete supports. In this section relevant literature of discrete-continuous models is reviewed.

Mead [77,78] provides a thorough study of wave propagation in mono-coupled and multi-coupled periodic structures. Due to periodicity, two types of zones are observed in the structure-response as a function of frequency. At one zone, energy does not propagate along the structure and this is known as the stopping-band zone. The other zone is known as the passing-band zone, where energy propagates along the structure.

Jezequel [55] introduces the *generalised Fourier method* to analyse an infinite beam supported periodically by lateral and torsion stiffness. The main characteristic of this method is that a single differential equation is used to describe the behaviour for all points of the beam with respect to time and space. To do this, a summation of a series of delta functions is used to account for discontinuities at periodic distances. Steady-state solutions are written as a summation of Fourier series with unknown coefficients. These solutions are substituted in equations of motion and the results are Fourier transformed to give a set of algebraic equations. The coefficients are found by solving this set of equations. Jezequel only considers non-oscillating moving loads. Kisilowski. *et al.* [60] present a mathematical solution based on the same method but including a moving wheel on a periodically supported rail. The wheel is modelled as a single-degree-of-freedom mass on a spring moving over a beam with constant velocity. A longitudinal compressive force is applied to the beam. Ilias and Muller [53] use the same method to analyse a discretely supported rail under a harmonic moving load and under a moving wheel-set. Krzyzynski [68] uses *Floquet's method* to model a harmonic moving load on an Euler-Bernoulli beam mounted on discrete infinite supports. Every discrete support consists of a spring-dash-pot to account for a rail-pad, a concentrated mass to account for a sleeper and another spring-dash-pot to account for ballast. This method takes advantage of periodicity in the longitudinal direction where Floquet's solution of the differential equation is used. Krzyzynski also provides a study of wave propagation in this periodic infinite structure. Muller *et al.* [82] provides comparison between the generalised Fourier and Floquet's methods. They apply the first method to model a rail using Timoshenko beam formulation and the second method using Euler-Bernoulli formulation. An undamped Euler-Bernoulli beam is compared with the corresponding Timoshenko beam with very high shear stiffness, very low rotational inertia and very low damping.

Hildebrand [42] uses a wave approach to study vibration attenuation in railway tracks. The model consists of two rails supported periodically by sleepers on ballast. The ballast is modelled as a continuous visco-elastic foundation. The method depends on considering a junction of the rail on the sleeper and calculates the displacements in terms of propagating and evanescent waves. The solution is calculated by considering three sets of equations expressing: the compatibility conditions, reflection of waves from the junction on the other rail and periodicity in the longitudinal direction using Floquet's method. It is concluded that at high frequencies (well above 200 Hz), a model lacking the second rail over-predicts the attenuation.

Nordborg [86] models an Euler-Bernoulli beam mounted on different kinds of discrete supports to calculate a closed-form solution of a track under non-moving oscillating loads. He transforms equations of motion to the wavenumber-frequency domain and these are solved using Floquet's theorem. In a second paper [87], he calculates the rail response for a moving oscillating load on the rail using results of *Green's function* in the frequency-space domain from [86]. To calculate the frequency domain response at a specific rail point, integration is performed in the space domain for Green's function multiplied by the frequency-domain force at a certain frequency. The response is then transformed to the time domain. He also uses this method to investigate vibration from a moving wheel on a railway with unevenness.

Smith and Wormley [103] use the *Fourier transform techniques* to model a moving constant load on an infinite Euler-Bernoulli beam supported periodically on rigid supports. The convolution integral is used to compute the beam response due to a spatially distributed load. Models of finite spans supported periodically are presented as an approximation for the infinite span model. In Fourier transform techniques, calculations are made only for one repeating unit. Response of any other unit is calculated using the periodicity condition. Equations of motion of the unit under consideration are transformed to the frequency domain. The resulting differential equations are solved as a summation of homogenous and particular solutions. The homogenous solution coefficients are found by considering the boundary condition at the end of the unit under consideration. These results are then transformed back to the time domain. In another paper, Smith *et al.* [104] couple a vehicle model to the track using an approximate modal analysis technique. In this technique a finite span approximation is used for the infinite beam.

Belotserkovskiy [5] uses Fourier transform techniques to analyse a rail modelled as an Euler-Bernoulli beam on a Winkler foundation with resilient hinges to represent rail joints under a harmonic-moving load. He also uses this method to analyse a Timoshenko beam on discrete supports to account for sleepers.

Forrest [29] models floating-slab tracks with continuous and discontinuous slabs under oscillating non-moving loads using the stiffness method along with the repeating-unit method. The stiffness method is used to write a relationship between deformations and forces on the left of any contiguous repeating-units. The stiffness matrix of the semi-infinite track on the right or left of the load is calculated using Floquet's method making use of the fact that responses decay to zero at infinity.

2.5.2 Modelling of vibration from surface trains

In the literature, many models for vibration from surface trains are presented. These range in complexity from simple models (including single-degree-of-freedom) to comprehensive three-dimensional models based on numerical techniques such as the FEM. The simple models lack accuracy and do not account for wave propagation in space, while the numerical models require long computation times. A successful model should satisfy both the accuracy and running-time efficiency. Due to the large number of mechanisms involved, most of the existing models address the contribution of certain mechanisms to the ground-borne vibration.

Early solutions of continuum and half-space problems under harmonic constant and harmonic moving loads have made great advances in modelling of vibration from surface trains. A thorough literature review about these solutions can be found in [31,38].

Many researchers use a beam on elastic half-space under non-moving or moving harmonic loads to model vibration from surface trains. An example is Ng [84] who models a railway track as an Euler- Bernoulli beam on an elastic half-space. The model considers non-moving loads and incorporates theory of random vibration to account for the input randomness. An early investigation of the response of a beam on elastic half-space under constant moving load is made by Filippov [28]. The work investigates moving loads with velocity up to Rayleigh wave speed in the half-space where damping is not modelled. A solution for all range of velocities of the moving load is presented by Kononov and Wolfert [64]. Metrikine and Popp [79] present a solution for vibration of periodically supported beam on elastic half-space. The solutions in the last three methods are calculated by transforming the differential equations to the wavenumber-frequency domain. The complex contour integrals are used to transform the results back to the original domain.

A theoretical model for both the generation and propagation of vibration from freight trains is presented by Jones and Block [56]. The model accounts for both the rail roughness and the quasi-static effect of moving axles. The input to the model is taken from measurements by using a track recording coach. The predicted vibration agrees well with the measured vibration in the frequency range 5-30Hz. It is found that heavy freight trains emit ground vibration with predominant frequency component in the range 4-30Hz.

Sheng *et al.* [98] present a model of a railway track coupled to a multi-layered half space. Both of the rails are modelled as a single Euler-Bernoulli beam and railpads are modelled as a continuous resilient layer. Sleepers are modelled as a continuous beam with no bending stiffness and ballast is modelled as a continuous layer of a linear spring with a consistent mass approximation. The effect of a harmonic moving load is investigated for moving load speeds higher than Rayleigh wave speed in the ground. A solution is calculated by using Fourier transform method. The vertical displacement spectrum of the ground is calculated for a harmonic moving load which moves passing the observation point. It is proved that the magnitude of the spectrum is independent of the longitudinal coordinate (the direction parallel to the track). Sheng *et al.* [100] compare the velocity and acceleration spectra calculated from this model with measurements taken at three different sites. The results show a good agreement and demonstrate the dominance of the quasi-static effect near the track at low frequencies.

In a third paper, Sheng *et al.* [101] use the same model to investigate the effect of track (track/embankment mass and bending stiffness) in ground vibration induced by quasi-static moving loads. Dispersion curves of the free-track, the rigid-bed track and the ground (half-space and layered half-space) without track are presented. These are used to predict some points in the dispersion curves for the coupled track-ground. An alternative method to identify dispersion curves is used and based on identifying the peaks for the response in the wavenumber-frequency domain. They use the *load speed lines* to determine the *peak response load speed* due to a quasi-static load. The peak response load speed or the critical speed is the speed at which the response due to a quasi-static moving load on the track exhibits a maximum. The load speed line is determined by transforming the term in the differential equation describing the quasi-static load *i.e.* $\delta(x - vt)$ to the wavenumber-frequency domain. If this line lies in tangency with the dispersion curves of the coupled track, an infinite response will occur in absence of damping or a peak if damping is included. For a track resting on a half space, it is found that a peak in the response might occur at a speed lower than Rayleigh wave speed in the ground. For a track resting on a layered half space, it is found that a peak in the response might occur for a speed lower than Rayleigh wave speed in the surface layer.

In another paper, Sheng *et al.* [102] investigate the effect of rail irregularities and the quasi-static effect on vibration from ballasted tracks and slab tracks. A moving single-axle vehicle model and other vehicle models are used to model a moving train on tracks with different forward velocities. They find that the vibration rate of attenuation with distance is much greater for the low-frequency range, *i.e.* 1.6-6 Hz than the middle frequency range, *i.e.* 6-20 Hz and the upper frequency range, *i.e.* 20-80 Hz. Due to its much greater bending stiffness, the slab track produces about 20dB lower vibration near the track than the ballasted tracks for frequencies up to 25 Hz. This is because slab track reduces the quasi-static effect which is dominant in the low frequency range. At the high-frequency range, it may increase vibration levels due to the increased forces at the wheel-rail interface.

Krylov [66] presents a model to investigate the effect of high-speed trains on ground vibration. The model accounts for sleeper spacing and the quasi-static forces of the moving train. The deflection of a beam on a Winkler foundation is used to calculate the force transmitted by a sleeper to the ground. The ground vibration is calculated in the frequency domain for a series of concentrated forces applied at the interface between sleepers and the ground. This model is used by Krylov *et al.* [67] to predict the vibration generated by TGV and Eurostar high-speed trains along tracks built on soft soils. Degrande and Lombaert [21] use the Betti-Rayleigh dynamic reciprocity theorem to increase efficiency of Krylov's model. Degrande and Schillemans [20] compare the results from this model with free field vibration measurements during the passage of a Thalys high-speed train at various speeds. The model gives good predictions at low frequencies where the quasi-static response dominates and at high frequencies where sleeper-passing response dominates. At the mid-frequency range where other mechanisms, *e.g.* rail roughness, are important the model underestimates the response. Another theoretical and experimental study on vibrations from high-speed trains is presented by Kaynia *et al.* [58] where a good match is shown between the predicted and measured results.

A generic methodology of modelling vibration from railways is presented by Hunt [46]. The method is based on models of infinite length for buildings and tracks and provides a tool to assess the performance of countermeasures. The load randomness is accounted for at the wheel-rail interface, where special attention is paid to the phasing between axle loads.

Numerical models are the ultimate choice to fully investigate the problem of ground vibration. The importance of these models is that they account for specific details of the prototype, but this is at the expense of the computational time. The continued development in computer storage and speed facilitates and attracts the rail industry to use numerical methods such as the FEM and the BEM, see [81] for example.

2.5.3 Modelling of vibration from underground trains

In this section, relevant literature on modelling of vibration from underground railways is reviewed. A detailed description of the work of Forrest [29] is given at the end, as it forms the basis for the work presented in this dissertation.

Cui and Chew [19] model underground tracks with rigid foundations to calculate the receptance under moving harmonic loads. They use two types of underground tracks: fixed track slab, where concrete slab is fixed to the tunnel and floating tracks with discontinuous slab. These two types are used in the Singapore Mass Rapid Transit (SMRT) system. The slab is modelled as continuous discrete masses, where no account is made for the slab length. Discrete models with stationary loads are presented as alternative models with smaller computation times.

Trochides [114] provides a simple model to predict vibration levels in buildings near subways. The model is based on energy consideration to formulate the impedance of the tunnel and the ground. Comparisons are made between calculations and measurements from a scaled model, which show a good agreement in the range 250-4000 Hz (higher than the range of frequency of interest for ground-borne vibration).

Many researchers use numerical methods such as BEM and FEM in modelling vibration from underground railways. Andersen and Jones [1] use a coupled FE and BE analysis to compare between 2D and 3D modelling. In their work, the load is applied at the bottom of a rectangular tunnel, where no account is made for a track. It is found that 2D modelling can give only quantitative results. Moreover, it provides a quick tool to assess vibration isolation measures. Hunt [49] states that 2D approaches do not work for tunnel modelling with acceptable accuracy, as they do not account for longitudinal and circumferential modes simultaneously.

Three-dimensional numerical models are developed by some researchers to model vibration from underground railways. The main disadvantage of these models is that they are computationally expensive. Powerful numerical models are developed under CONVURT [16], where a coupled FEM-BEM is used. The FEM is used to model tunnel walls while the BEM is used to model the surrounding soil. Taking account of periodicity in the tunnel direction using Floquet transformation makes a great improvement in the running time [15].

Sheng *et al.* [99] presents a numerical method based on the *discrete wavenumber fictitious force* method to model an underground tunnel embedded in a half-space. The method depends on writing the boundary integral equations of only the displacement Green's function. This is an advantage over the BEM as the traction Green's function is not required.

The Finite Difference method (FDM) [113] may also be used to model vibration from underground railways. The advantage of this method is that less effort is needed to write the code compared with other conventional methods such as the BEM and FEM.

The last part of this section is dedicated to describe the work of James Forrest [29] who presented a PhD dissertation on "Modelling of ground vibration from underground railways", in 1999 at Cambridge University. The main purpose of his work is to model floating-slab tracks and to assess their performance. The dissertation also includes some experimental work which is not discussed here. The modelling work lies in three chapters and is discussed in the following paragraphs.

In Chapter 3, Forrest models floating-slab tracks on rigid foundations. Euler-Bernoulli beam formulation is used to model both the rail and the slab. The two rails are modelled as a single beam as only the bending behaviour is considered. Railpads and slab bearings are modelled as continuous layers of resilient elements. Two types of slab are considered: continuous and discontinuous, under only non-moving oscillating loads. A direct solution based on separable functions in time and space is followed to solve the differential equation for a track with a continuous slab. For a track with a discontinuous slab, the repeating unit method is used in which Floquet's theorem is employed to account for periodicity in the longitudinal direction. A solution is presented for a concentrated load applied only over a slab discontinuity. A set of masses is coupled to the continuous slab track to simulate the effect of a train running on the track. For concentrated load acting on the track with continuous or discontinuous slab, it is found that the ratio between the total transmitted force to the ground and the input force is equal to the transmissibility calculated from a two-degree-of-freedom discrete system.

In Chapter 4, Forrest models a tunnel and its surrounding soil using the pipe-in-pipe model. The tunnel is modelled as a thin cylindrical shell and the ground is modelled as an infinite domain containing a cylindrical cavity using the 3D continuum theory. The coupling is performed in the wavenumber domain by satisfying stress equilibrium and displacement compatibility at the tunnel-soil interface. The discrete Fourier transform DFT is used to transform the results numerically to the space domain. The response of a free tunnel to a concentrated harmonic radial load is calculated using the theory of thin shell and then it is recalculated using both the theory of elastic continuum and a FE model. This is done to examine the validity of modelling the tunnel as a thin shell. All three models show good matching in the frequency range 1-100 Hz. At the end of this chapter, some results for the coupled tunnel-soil model are shown for a radial concentrated load applied at the tunnel wall. It should be noted that the response for tangential applied loads on the tunnel wall is not considered.

In Chapter 5, Forrest couples a floating-slab track to the pipe-in-pipe model. Two models are considered. In the first, the slab is coupled via a single longitudinal line of slab bearings (in the tunnel direction) and only the bending response of the track under concentrated harmonic loads is investigated. In the second model, the slab is coupled to the tunnel via two lines of slab bearings. This is a more precise model, as the torsion of the slab is included. However, it is assumed that the tunnel wall can only take radial loads. This is because tangential loads on the tunnel are not modelled. To assess the performance of floating-slab tracks as a measure of vibration isolation, Forrest couples a set of axles to the first track (a track coupled to the tunnel via single line of slab bearings). A white-noise random input is applied under each mass to simulate the roughness excitation for a moving train. The spectral density of the soil displacement is calculated as a function of frequency. This output is then weighted with an empirical roughness input calculated by Frederich [30] for a real rail roughness to calculate the root-mean-square displacement of the soil. The insertion gain method is used which gives the ratio between the root-mean-square displacements before and after floating the slab. Below the tunnel, the root-mean-square results show some little improvement (vibration isolation) by using floating-slab tracks instead of directly-fixed tracks. Away and above the tunnel, where most of buildings' foundations are found and isolation is needed, the results do not show a clear improvement and in some places vibration is increased. Forrest concludes that using slab bearings is not an effective measure of vibration isolation. However, this conclusion was based on root-mean-square results for floating-slabs with stiff slab-bearings (with natural frequencies down to 30Hz). Numerical problems are encountered with softer slab bearings.

Conclusions

There is a great need to develop a computational tool which can be used to evaluate the effectiveness of vibration countermeasures in underground tunnels. Many models for vibration from underground railways are presented in the literature. These models are either too simple based on 2D systems, or too precise based on numerical methods such as the FE and the BE methods. Simple models lack accuracy while precise numerical models lack the computational power. This dissertation is concerned with the development of such a model that accounts for the three-dimensional characteristic of the track, tunnel and soil and has the advantage of the short running time. The model will also be used to maintain a better understanding in the context of vibration from underground railways.

Chapter 3

MODELLING OF FLOATING-SLAB TRACKS

Introduction

Floating slab tracks are widely used to control vibration from underground trains. The track is mounted on a concrete slab that rests on rubber bearings, glass fibre or steel springs. The slab may be cast in-situ, resulting in a continuous length of concrete, or may be constructed in discrete pre-cast sections laid end to end. This chapter discusses modelling of such tracks with continuous and discontinuous slabs under harmonic moving loads. The track-bed is modelled as a rigid foundation and this is suitable for modelling of modern tracks where the stiffness of the slab bearings is much smaller than the stiffness of the track-bed. The rigid-bed models are known as the *excitation models* and are developed under CONVURT [16] to calculate forces at the wheel-rail interface for the different excitation mechanisms which are discussed in the literature review. These forces are then used as inputs to the precise model which comprises the track, the tunnel and the ground, to calculate vibration levels in the ground.

This chapter is organised in four sections. Modelling of tracks with continuous slabs is discussed in Section 3.1. Section 3.2 discusses modelling of tracks with discontinuous slabs. Sections 3.3 and 3.4 investigate the results for the models presented in Sections 3.1 and 3.2 respectively.

3.1 Modelling of tracks with continuous slabs

In this section, tracks with continuous slabs are modelled. The model is shown in Figure 3.1. It consists of an upper Euler-Bernoulli beam to account for both of the rails (with mass m_1 per unit length and bending stiffness EI_1) and a lower Euler-Bernoulli beam to account for the floating slab (with mass m_2 per unit length and bending stiffness EI_2). The model accounts for identical inputs on the two rails and hence a single beam is used to model both of the rails. Railpads are represented by a continuous layer of springs with stiffness k_1 per unit length and a viscous damping factor c_1 per unit length. Slab bearings are represented by a continuous layer of springs with stiffness k_2 per unit length and a viscous damping factor c_2 per unit length. Forrest [29] analyses this model under non-moving oscillating loads. The current work extends the formulation to account for moving oscillating loads. Modelling of tracks with continuous slabs under harmonic moving loads is presented in 3.1.1 while 3.1.2 discusses the effect of moving trains on such tracks.

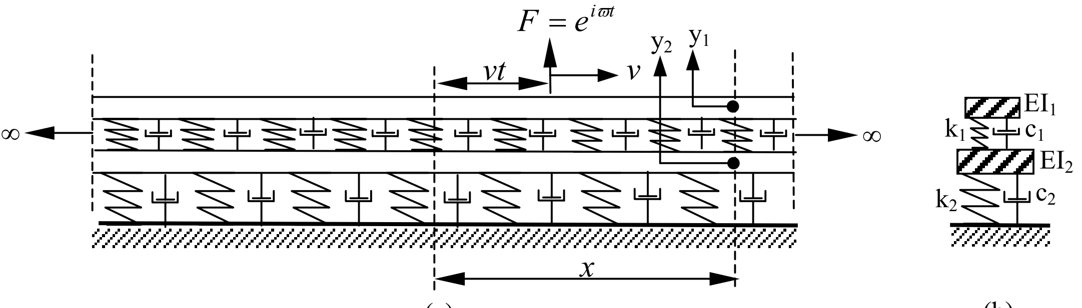

(a) (b)

Figure 3.1: (a) Floating-slab track on a rigid foundation, subjected to a unit moving harmonic load. (b) Side view.

3.1.1 Tracks under harmonic moving loads

Figure 3.1 shows a track with a continuous slab subjected to an oscillating moving load with angular frequency ϖ and velocity v. The load is defined such that it passes by $x = 0$ at time $t = 0$. The solution methodology depends on transforming the differential equations of the track to the wavenumber-frequency domain, where they are simplified and transformed back to the space-time domain. The reader is referred to Appendix B for a detailed explanation of the method.

The load on the upper beam in Figure 3.1 can be written in the space-time domain as

$$F(x,t) = e^{i\varpi t}\delta(x - vt) \tag{3.1}$$

where δ is the *Dirac delta* function, see [13] for example. Equation 3.1 is written in a complex notation for convenience. However, it should be remembered that only the real part is meant. This complex notation will be applied throughout this chapter. The generalised differential equations of the upper and the lower beams can be written as

$$EI_1 \frac{\partial^4 y_1}{\partial x^4} + m_1 \frac{\partial^2 y_1}{\partial t^2} + k_1(y_1 - y_2) + c_1(\frac{\partial y_1}{\partial t} - \frac{\partial y_2}{\partial t}) = e^{i\varpi t}\delta(x - vt) \tag{3.2}$$

and $$EI_2 \frac{\partial^4 y_2}{\partial x^4} + m_2 \frac{\partial^2 y_2}{\partial t^2} + k_2 y_2 - k_1(y_1 - y_2) + c_2 \frac{\partial y_2}{\partial t} - c_1(\frac{\partial y_1}{\partial t} - \frac{\partial y_2}{\partial t}) = 0\,. \tag{3.3}$$

When solving problems of moving loads, some authors prefer at this stage to replace the fixed frame of axis, *i.e.* (x,t), by the moving frame of axis, *i.e.* $(z = x - vt, t)$, see [31] for example. However, the derivation without following this approach leads to the same results at the end and has the advantage of giving more insight into defining the *critical velocity* which is discussed in Section 3.3. Equations 3.2, and 3.3 are transformed from the space-time domain (x,t) to the wavenumber-frequency domain (ξ,ω) using double Fourier transform defined by equations A.1 and A.2. The transformed equations read

$$EI_1\xi^4\tilde{y}_1 - m_1\omega^2\tilde{y}_1 + k_1(\tilde{y}_1 - \tilde{y}_2) + c_1 i\omega(\tilde{y}_1 - \tilde{y}_2) = 2\pi\delta(\omega + \xi v - \varpi) \tag{3.4}$$

and $$EI_2\xi^4\tilde{y}_2 - m_2\omega^2\tilde{y}_2 + k_2\tilde{y}_2 - k_1(\tilde{y}_1 - \tilde{y}_2) + c_2 i\omega\tilde{y}_2 - c_1 i\omega(\tilde{y}_1 - \tilde{y}_2) = 0 \tag{3.5}$$

where $\tilde{y}_1$ and $\tilde{y}_2$ are the transformation of y_1 and y_2 in the wavenumber-frequency domain. Equations 3.4 and 3.5 can be written in a matrix form as

$$[\mathbf{A}]\cdot\begin{bmatrix}\tilde{y}_1\\ \tilde{y}_2\end{bmatrix} = \begin{bmatrix}2\pi\delta(\omega + \xi v - \varpi)\\ 0\end{bmatrix} \tag{3.6}$$

where

$$[\mathbf{A}] = \begin{bmatrix} EI_1\xi^4 - m_1\omega^2 + k_1 + c_1 i\omega & -k_1 - c_1 i\omega \\ -k_1 - c_1 i\omega & EI_2\xi^4 - m_2\omega^2 + k_1 + k_2 + i\omega(c_1 + c_2) \end{bmatrix}.$$

Solving for $\tilde{y}_1, \tilde{y}_2$ from equation 3.6

$$\tilde{y}_1(\xi,\omega) = \frac{2\pi \cdot \delta(\omega + \xi v - \varpi) \cdot f_2(\xi,\omega)}{f_1(\xi,\omega)} \tag{3.7}$$

and

$$\tilde{y}_2(\xi,\omega) = \frac{2\pi \cdot \delta(\omega + \xi v - \varpi) \cdot f_3(\xi,\omega)}{f_1(\xi,\omega)} \tag{3.8}$$

where

$f_1(\xi,\omega) = |\mathbf{A}|$, $f_2(\xi,\omega) = EI_2\xi^4 - m_2\omega^2 + k_1 + k_2 + i\omega(c_1 + c_2)$, $f_3(\xi,\omega) = k_1 + c_1 i\omega$ and $|\mathbf{A}|$ is the determinant of matrix $\mathbf{A}$. Equations 3.7 and 3.8 are transformed to the wavenumber-time domain firstly using equation A.4, resulting in

$$\bar{y}_1(\xi,t) = \frac{f_2(\xi,\omega = \varpi - \xi v)}{f_1(\xi,\omega = \varpi - \xi v)} \cdot e^{i(\varpi - \xi v)t} \tag{3.9}$$

and

$$\bar{y}_2(\xi,t) = \frac{f_3(\xi,\omega = \varpi - \xi v)}{f_1(\xi,\omega = \varpi - \xi v)} \cdot e^{i(\varpi - \xi v)t}\,. \tag{3.10}$$

Equation A.3 is used to transform equations 3.9 and 3.10 from the wavenumber-time domain to the space-time domain and results in

$$y_1(x,t) = \frac{e^{i\varpi t}}{2\pi} \int_{-\infty}^{\infty} \frac{f_2(\xi,\omega = \varpi - \xi v)}{f_1(\xi,\omega = \varpi - \xi v)} \cdot e^{i\xi(x - vt)} d\xi \tag{3.11}$$

and

$$y_2(x,t) = \frac{e^{i\varpi t}}{2\pi} \int_{-\infty}^{\infty} \frac{f_3(\xi,\omega = \varpi - \xi v)}{f_1(\xi,\omega = \varpi - \xi v)} \cdot e^{i\xi(x - vt)} d\xi\,. \tag{3.12}$$

The previous integrations can be found numerically along the real ξ axis. Otherwise, this integration can be found analytically using the contour integrals, see Appendix B for more details. $f_1(\xi,\omega)$ is a polynomial of the eighth order and hence the integrated functions in equations 3.11 and 3.12 have eight poles. All these poles are complex values if any of c_1 or c_2 is not equal zero. The integrations in equations 3.11 and 3.12 can be written as

$$y_1(x,t) = \frac{ie^{i\varpi t}}{EI_1 EI_2} \sum_{j=1}^{4} \frac{e^{i\xi_j(x-vt)} \cdot f_2(\xi_j, \omega = \varpi - \xi_j v)}{\prod_j} \qquad \text{for } x - vt > 0, \tag{3.13}$$

$$y_2(x,t) = \frac{ie^{i\varpi t}}{EI_1 EI_2} \sum_{j=1}^{4} \frac{e^{i\xi_j(x-vt)} \cdot f_3(\xi_j, \omega = \varpi - \xi_j v)}{\prod_j} \qquad \text{for } x - vt > 0, \tag{3.14}$$

$$y_1(x,t) = \frac{-ie^{i\varpi t}}{EI_1 EI_2} \sum_{j=5}^{8} \frac{e^{i\xi_j(x-vt)} \cdot f_2(\xi_j, \omega = \varpi - \xi_j v)}{\prod_j} \qquad \text{for } x - vt < 0, \tag{3.15}$$

and

$$y_2(x,t) = \frac{-ie^{i\varpi t}}{EI_1 EI_2} \sum_{j=5}^{8} \frac{e^{i\xi_j(x-vt)} \cdot f_3(\xi_j, \omega = \varpi - \xi_j v)}{\prod_j} \qquad \text{for } x - vt < 0 \tag{3.16}$$

where $\prod_j = (\xi_j - \xi_1)(\xi_j - \xi_2)...(\xi_j - \xi_{j-1})(\xi_j - \xi_{j+1})...(\xi_j - \xi_8)$,

$\xi_1, \xi_2, ..., \xi_8$ are the roots of the equation $f_1(\xi, \omega = \varpi - \xi v) = 0$,

$\xi_1, \xi_2, \xi_3, \xi_4$ are the roots in the first and the second quadrants,

and $\xi_5, \xi_6, \xi_7, \xi_8$ are the roots in the third and the fourth quadrants.

The track displacements calculated by equations 3.13-3.16 are verified by computing the power transmission through the rails in Section 3.3. Other important aspects such as dispersion curves of the track and the critical velocity are also investigated.

3.1.2 Coupling a moving axle to the track

A simple model of a moving train is obtained by considering an axle moving over the track with constant velocity v. From equation 3.13-3.16, the displacements y_1, y_2 in a moving frame of axis ($z = x - vt$) under a moving load are invariant with time for $\varpi = 0$. This can be proved by substituting $x - vt = c$, where c is a constant. Thus, for a non-oscillating moving load with a constant velocity, an observer who is moving along the rail with velocity equal to the load velocity keeps seeing the same deflected shapes of the rail and the slab. As a linear model, the steady-state deflection of the rail under a constant moving load increases proportionally to any increase in the loading magnitude. Thus, for a moving axle on the track, the deflection of the rail at any point can be calculated by multiplying the deflection calculated for a unit load by the axle weight, *i.e.* $-Mg$, where *M* is the total axle mass and g is the gravity acceleration. Note that the axle inertia has an effect only on the transient displacement, *i.e.* when the axle starts to move. After some time, the transient effect disappears and only the steady-state effect remains.

As an introduction for the next section, one can prove the following relationship by referring to equations 3.13-3.16

$$y_{1,2}(x+L,t+\frac{L}{v}) = y_{1,2}(x,t)\cdot e^{i\varpi\frac{L}{v}}. \qquad (3.17)$$

This relationship is known as the periodicity condition and is discussed in the next section.

3.2 Modelling of tracks with discontinuous slabs

This section is divided into two parts. A track with a discontinuous slab under an oscillating moving load is analysed in the first part. In the second part, a train model is coupled to the track, and the dynamic force due to slab discontinuity is calculated. The reader is referred to Section 2.5.1 for literature on periodic structure theory which is useful for the work presented in this section.

3.2.1 Tracks under harmonic moving loads

The displacements of a track with a discontinuous slab under an oscillating moving load are calculated using three different methods:

- the Fourier–Repeating-unit method;
- the Periodic-Fourier method;
- the Modified-phase method.

As will be seen later, the first two methods are exact providing that careful consideration is taken when performing the numerical integration of the Fourier transform. The third method is approximate and only valid for velocities of moving loads lower than the critical velocity of the track. Each method is discussed separately in the following sections. The model is shown in Figure 3.2 and is similar to the model used in Section 3.1 except in that the slab is discontinuous with discrete length L. All track variables are the same as defined in Section 3.1.

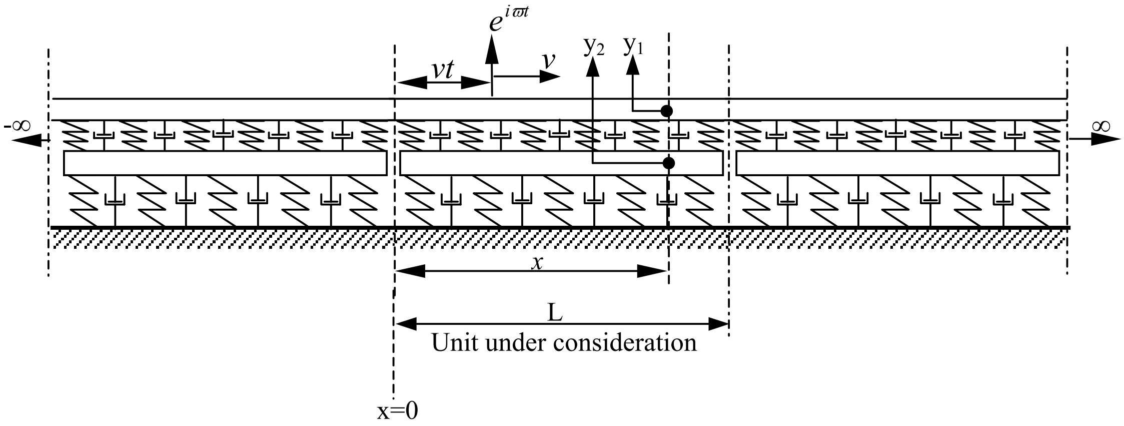

Figure 3.2: Floating-slab track with a discontinuous slab subjected to an oscillating moving load.

The Fourier–Repeating-unit method

This method is divided into two parts. The first is to calculate the track displacements for non-moving oscillating loads. The second is to integrate these displacements to calculate the track displacements for moving harmonic loads. Forrest [29] calculates the track displacements under a non-moving harmonic load applied on the rails, above the slab discontinuity (at x=0 in Figure 3.2). This is developed such that the load can be applied at any point in the rails.

To calculate the track displacements for an oscillating non-moving load, the track is divided into three blocks as shown in Figure 3.3; central block with length L, where the load is applied at distance x_0 from its left end, and two semi-infinite blocks on the right and the left of the central block and are called in this discussion the right and the left blocks respectively. For each block the stiffness matrix is written and matrices are assembled according to the compatibility conditions to calculate the track displacement at any point.

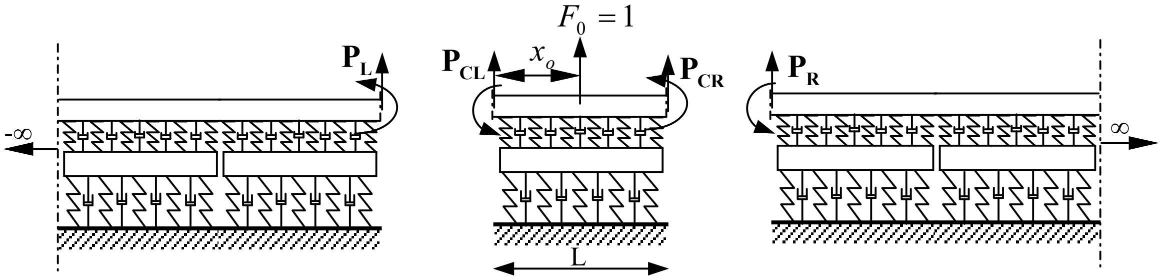

Figure 3.3: A floating-slab track divided into three blocks; central block and two semi-infinite blocks. The concentrated harmonic load is applied at the central block. The factor $e^{i\varpi t}$ is dropped from all forces.

For the right block in Figure 3.3, the force-displacement equation can be written as:

$$\mathbf{P_R} = \mathbf{K_R Y_R} \tag{3.18}$$

where $\mathbf{P_R}$ is a 2×1 vector, which comprises the shear force and bending moment at the upper beam on the left of the right block. $\mathbf{Y_R}$ is a 2×1 vector, which gives the vertical displacement and rotation at the upper beam on the left of the right block. $\mathbf{K_R}$ is the 2×2 stiffness matrix of the right block. Note that the factor $e^{i\varpi t}$ is dropped from all forces and displacements.

Similarly, for the left block, the following equation can be written

$$\mathbf{P_L} = \mathbf{K_L Y_L}\,. \tag{3.19}$$

For the central unit

$$\begin{bmatrix} \mathbf{P_{CL}} \\ \mathbf{P_{CR}} \\ F_0 \end{bmatrix} = \left[\mathbf{K_C}\right] \begin{bmatrix} \mathbf{Y_{CL}} \\ \mathbf{Y_{CR}} \\ Y_0 \end{bmatrix} \tag{3.20}$$

where the bold elements in the previous equation are 2×1 vectors giving forces (shear force and bending moment) or displacements (vertical displacement and rotation) as shown in Figure 3.3. F_0 and Y_0 are the amplitudes of the applied harmonic force and the displacement of the excitation point in the central unit. $\mathbf{K_C}$ is the stiffness matrix of the five-degree-of-freedom central unit. At the joints between the semi-infinite blocks and the central block, the equilibrium and compatibility conditions are

$$\mathbf{P_{CR}} = -\mathbf{P_R}\,,\ \mathbf{P_{CL}} = -\mathbf{P_L}\,,\ \mathbf{Y_{CR}} = \mathbf{Y_R} \text{ and } \mathbf{Y_{CL}} = \mathbf{Y_L}\,. \tag{3.21}$$

From equations 3.18, 3.19 and 3.21, equation 3.20 can be written as

$$\begin{bmatrix} -\mathbf{K_L Y_L} \\ -\mathbf{K_R Y_R} \\ F_0 \end{bmatrix} = [\mathbf{K_C}] \begin{bmatrix} \mathbf{Y_L} \\ \mathbf{Y_R} \\ Y_0 \end{bmatrix} \tag{3.22}$$

or

$$\left\{ \mathbf{K_C} - \begin{bmatrix} -\mathbf{K_L} & \mathbf{Z}(2,2) & \mathbf{Z}(2,1) \\ \mathbf{Z}(2,2) & -\mathbf{K_R} & \mathbf{Z}(2,1) \\ \mathbf{Z}(1,2) & \mathbf{Z}(1,2) & \mathbf{Z}(1,1) \end{bmatrix} \right\} \begin{bmatrix} \mathbf{Y_L} \\ \mathbf{Y_R} \\ Y_0 \end{bmatrix} = \begin{bmatrix} \mathbf{Z}(2,1) \\ \mathbf{Z}(2,1) \\ F_0 \end{bmatrix} \tag{3.23}$$

where $\mathbf{Z}(m,n)$ is a $m\times n$ matrix with zero elements.

Knowing the input value $F_0 = 1$, equation 3.23 is solved to determine the values of $\mathbf{Y_L}$, $\mathbf{Y_R}$ and Y_0. The first two vectors are used to determine $\mathbf{P_L}$ and $\mathbf{P_R}$ from equation 3.19 and 3.18 respectively. Forrest [29] uses the stiffness method to calculate the stiffness matrix for a block such as the central block but for loads and displacements which are only defined at the ends. Two contiguous blocks of these should be used to calculate the stiffness matrix of the central block in the current formulation, *i.e.* $\mathbf{K_C}$. The length of these two blocks are x_0 and $L - x_0$. To calculate the stiffness matrix of the semi-infinite blocks, Forrest uses the repeating-unit method. For details about the calculations see [29].

The previous procedure can be used to calculate *Green's function* $\hat{G}_\omega(x_o, x)$ which is defined as the response of the rail at x_o from a discontinuity for a non-moving oscillating unit load with an angular frequency ω applied at x from the same discontinuity. Employing the method presented by Nordborg [87], this function is used to calculate the track displacements under an oscillating moving load that moves crossing the observation point at x_0.

The response at x_o in the frequency domain can be calculated for a general input force in the frequency domain from the following equation

$$\hat{y}(x_o, \omega) = \int_{-\infty}^{\infty} \hat{G}_\omega(x_o, x) \cdot \hat{F}(x, \omega) \cdot dx \tag{3.24}$$

where $\hat{F}(x, \omega)$ is the input force in the space-frequency domain.

For a moving oscillating load with velocity v and angular frequency ϖ, the force can be written in the space-frequency domain as

$$\hat{F}(x, \omega) = \int_{-\infty}^{\infty} \delta(x - vt) \cdot e^{i\varpi t} \cdot e^{-i\omega t} dt = \frac{1}{v} e^{i(\varpi - \omega)x/v}. \tag{3.25}$$

Equation A.7 is used to calculate the integration in equation 3.25.
Substituting 3.25 into 3.24 gives

$$\hat{y}(x_o, \omega) = \frac{1}{v} \int_{-\infty}^{\infty} \hat{G}_\omega(x_o, x) \cdot e^{i\frac{(\varpi - \omega)}{v}x} \cdot dx. \tag{3.26}$$

This integration can be performed numerically using the trapezium rule [95] to give

$$\hat{y}(x_0, \omega) = \frac{1}{v} \sum_{j=1}^{j=M} a_j \hat{G}_\omega(x_o, x_j) \cdot e^{i\frac{(\varpi - \omega)}{v}x_j} \cdot \Delta x \tag{3.27}$$

where $a_j = 0.5$ for $j = 1, M$ and $a_j = 1$ for $j = 2, 3, ..., M-1$. An important criterion when calculating $\hat{y}$ in equation 3.27 is that the value of ω should be large enough to cover the range of frequency where $\hat{G}_\omega(x_o, x_j)$ is significant in order to have the right solution. The maximum and minimum values of ω control the value of Δx and vice versa. To avoid aliasing when calculating the summation in equation 3.27, the sampling frequency should be at least twice the signal bandwidth, which is known as Nyquist criterion [105]. This can be written mathematically as

$$\frac{1}{\Delta x} \geq \left| \frac{\varpi - \omega}{\pi \cdot v} \right| \quad \text{or} \quad \varpi - \frac{\pi \cdot v}{\Delta x} \leq \omega \leq \varpi + \frac{\pi \cdot v}{\Delta x}. \tag{3.28}$$

Having computed $\hat{y}(x_o, \omega)$, values of $y(x_o, t)$ are calculated by transforming 3.27 numerically to the time domain. Nyquist criterion in this case can be written as

$$\frac{1}{\Delta \omega} \geq \left| \frac{t}{\pi} \right| \quad \text{or} \quad \frac{-\pi}{\Delta \omega} \leq t \leq \frac{\pi}{\Delta \omega}. \tag{3.29}$$

For the purpose of summarising the Fourier–Repeating-unit method, the following steps are used to calculate the response $y(x_o, t)$:

1. calculate $\hat{G}_\omega(x_o, x)$ for the mesh shown in Figure 3.4, the mesh size should be large enough to include significant values of $\hat{G}_\omega(x_o, x)$ inside the mesh;

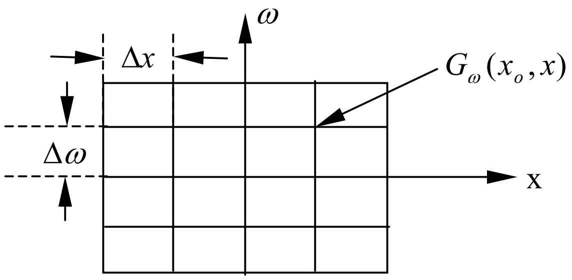

Figure 3.4: A 2D mesh to calculate $y(x_o, t)$

2. for each row of points, apply equation 3.27 to calculate the value of $\hat{y}(x_o, \omega)$;

3. having done step 2 for all the mesh rows, transform the resulted $\hat{y}(x_o, \omega)$ vector numerically to the time domain.

The Periodic-Fourier method

In this method, the periodic infinite structure theory is used to analyse a track under oscillating moving loads. The analysis follows the work presented by Belotserkovskiy [5] in analysing an infinite beam mounted on periodic supports.

To calculate the displacement for a periodic infinite structure, three sets of equations are required. The first comprises the differential equations which describe the motion for one of the repeating units of the structure. The second set describes the periodicity condition and is used to calculate the displacements at other units and to set a relationship between the boundary conditions in the third set. The third set contains the boundary conditions at the ends of the repeating unit.

Referring to Figure 3.2, the repeating unit under consideration is the one bounded by $x = 0$ and $x = L$. The load is defined as $\delta(x - vt) \cdot e^{i\varpi t}$. This means that it enters the unit at time $t = 0$, with a maximum magnitude because the real part of the load is $+1$ when $t = 0$. To explain the periodicity condition, a reference is made to two points in the space-time coordinate system. At the first point (a), the response $y(x_o, t_o)$ is measured at $x = x_o$ when the moving load $1 \cdot e^{i\varpi t_0}$ is at $x = vt_o$. The displacement $y(x_o, t_o)$ can be either the rail or the track displacement in this context. At the second point (b), the response $y(x_o + L, t_o + L/v)$ is measured at $x = x_0 + L$ when the moving load $1 \cdot e^{i\varpi (t_0 + L/v)}$ is at $x = vt_0 + L$. The excitation-measuring conditions at a and b are the same and the only difference is the load phase. Thus, one can write

$$F_b = F_a \cdot e^{i\varpi \frac{L}{v}} \quad \Rightarrow \quad y_b = y_a \cdot e^{i\varpi \frac{L}{v}}. \tag{3.30}$$

This leads directly to equation 3.17 which is known by the periodicity condition. Now, it is possible to write the three sets of equations as defined before.

1. The generalised differential equations, there are two fourth-order equations describing the motion of the upper and the lower beams. These are identical to equations 3.2 and 3.3.
2. This set consists of two equations (one for each beam) that result from equation 3.17

$$y_1(x+L, t+\frac{L}{v}) = y_1(x,t)\cdot e^{i\bar{\phi}} \tag{3.31}$$

and

$$y_2(x+L, t+\frac{L}{v}) = y_2(x,t)\cdot e^{i\bar{\phi}} \tag{3.32}$$

where $\bar{\phi} = \frac{\varpi L}{v}$ is the non-dimensional excitation frequency.

3. This set consists of eight equations and it relates the boundary conditions at the left and the right of the unit under consideration. For the upper beam, the displacement, slope, moment and shear are continuous. Using the periodicity condition, this can be written as

$$\frac{\partial^n y_1}{\partial x^n}(L, t+\frac{L}{v}) = e^{i\bar{\phi}}\cdot\frac{\partial^n y_1}{\partial x^n}(0,t) \qquad \text{n=0,1,2,3.} \tag{3.33}$$

For the lower beam, the end moments and shear forces are zero. This can be written as

$$\frac{\partial^m y_2}{\partial x^m}(L, t+\frac{L}{v}) = \frac{\partial^m y_2}{\partial x^m}(0,t) = 0 \qquad \text{m=2,3.} \tag{3.34}$$

It is convenient at this stage to use non-dimensional variables which are described by the following relationships

$$X = \frac{x}{L}, \tag{3.35}$$

$$T = \frac{vt}{L}, \tag{3.36}$$

and
$$Y_1(X,T) = \frac{y_1(x,t)}{L},\ Y_2(X,T) = \frac{y_2(x,t)}{L}. \tag{3.37}$$

Using the non-dimensional variables, the previous equations can be recast as:

1. the differential equations

$$\frac{\partial^4 Y_1}{\partial X^4} + \frac{m_1 v^2 L^2}{EI_1}\frac{\partial^2 Y_1}{\partial T^2} + \frac{k_1 L^4}{EI_1}(Y_1 - Y_2) + \frac{c_1 v L^3}{EI_1}\left(\frac{\partial Y_1}{\partial T} - \frac{\partial Y_2}{\partial T}\right) = \frac{L^2}{EI_1}\cdot e^{i\bar{\phi}t}\delta(X - T), \tag{3.38}$$

$$\frac{\partial^4 Y_2}{\partial X^4} + \frac{m_2 v^2 L^2}{EI_2}\frac{\partial^2 Y_2}{\partial T^2} + \frac{k_2 L^4}{EI_2}Y_2 - \frac{k_1 L^4}{EI_2}(Y_1 - Y_2) + \frac{c_2 v L^3}{EI_2}\frac{\partial Y_2}{\partial T} - \frac{c_1 v L^3}{EI_2}\left(\frac{\partial Y_1}{\partial T} - \frac{\partial Y_2}{\partial T}\right) = 0; \tag{3.39}$$

2. the periodicity conditions

$$Y_1(X+1, T+1) = Y_1(X,T)\cdot e^{i\bar{\phi}} \tag{3.40}$$

and
$$Y_2(X+1, T+1) = Y_2(X,T)\cdot e^{i\bar{\phi}}; \tag{3.41}$$

3. the boundary conditions

$$\frac{\partial^n Y_1}{\partial X^n}(1, T+1) = e^{i\bar{\phi}}\cdot\frac{\partial^n Y_1}{\partial X^n}(0,T) \qquad \text{n=0,1,2,3} \tag{3.42}$$

and
$$\frac{\partial^m Y_2}{\partial X^m}(1, T+1) = \frac{\partial^m Y_2}{\partial X^m}(0,T) = 0 \qquad \text{m=2,3.} \tag{3.43}$$

The first set consists of two differential equations of the fourth order that requires eight boundary conditions to be solved. The third set provides these eight boundary conditions. The solution is not calculable in the current domain due to the existence of a delta function in equation 3.38. However, transforming all equations to the space-frequency domain can solve this problem. The transformation for this case reads (compare with equation A.2)

$$\hat{Y}_{1,2}(x,\phi) = \int_{-\infty}^{\infty} Y_{1,2}(X,T) \cdot e^{-i\phi T} dT \,. \tag{3.44}$$

Transforming set 1 and 3 results in:

1.
$$\frac{\partial^4 \hat{Y}_1}{\partial X^4} + A_1 \hat{Y}_1 + A_2 \hat{Y}_2 = A_3 \cdot e^{m_9 X} \tag{3.45}$$

and
$$\frac{\partial^4 \hat{Y}_2}{\partial X^4} + B_1 \hat{Y}_2 + B_2 \hat{Y}_1 = 0 \,; \tag{3.46}$$

3.
$$\frac{\partial^n \hat{Y}_1}{\partial X^n}(1,\phi) = e^{i(\bar{\phi}-\phi)} \cdot \frac{\partial^n \hat{Y}_1}{\partial X^n}(0,\phi) \qquad \text{n=0,1,2,3} \tag{3.47}$$

and
$$\frac{\partial^m \hat{Y}_2}{\partial X^m}(1,\phi) = \frac{\partial^m \hat{Y}_2}{\partial X^m}(0,\phi) = 0 \qquad \text{m=2,3} \tag{3.48}$$

where A_1, A_2, A_3, B_1, B_2, and m_9 are independent of X and can be calculated from

$$A_1 = -\frac{m_1 v^2 L^2 \phi^2}{EI_1} + \frac{c_1 v L^3 i\phi}{EI_1} + \frac{k_1 L^4}{EI_1},\ A_2 = -\frac{c_1 v L^3 i\phi}{EI_1} - \frac{k_1 L^4}{EI_1},\ A_3 = \frac{L^2}{EI_1}$$

$$B_1 = -\frac{m_2 v^2 L^2 \phi^2}{EI_2} + \frac{(k_1+k_2)L^4}{EI_2} + \frac{(c_1+c_2) v L^3 i\phi}{EI_2},\ B_2 = -\frac{c_1 v L^3 i\phi}{EI_2} - \frac{k_1 L^4}{EI_2}$$

and $m_9 = i(\bar{\phi} - \phi)$.

Solving for $\hat{Y}_2$ from equations 3.45 and 3.46

$$\frac{\partial^8 \hat{Y}_2}{\partial X^8} + (A_1 + B_1)\frac{\partial^4 \hat{Y}_2}{\partial X^4} + (A_1 B_1 - A_2 B_2)\hat{Y}_2 = -A_3 B_2 \cdot e^{m_9 X} \,. \tag{3.49}$$

The general solution (homogenous and particular) of this differential equation can be written as

$$\hat{Y}_2 = r_1 e^{m_1 X} + r_2 e^{m_2 X} + r_3 e^{m_3 X} + ... + r_8 e^{m_8 X} + r_9 e^{m_9 X} \tag{3.50}$$

where m_1, m_2, $m_3,\ldots,m_8$ are the exponents of the homogenous solutions, and they form the roots of the following polynomial

$$m^8 + (A_1 + B_1)m^4 + (A_1 B_1 - A_2 B_2) = 0\,. \tag{3.51}$$

r_1, r_2, $r_3,\ldots,r_8$ are the coefficients of the homogenous solution and can be computed from the boundary conditions as will be shown below, r_9 is the coefficient of the particular solution and is calculated from

$$r_9 = \frac{-A_3 B_2}{m_9{}^8 + (A_1 + B_1)m_9{}^4 + (A_1 B_1 - A_2 B_2)}\,. \tag{3.52}$$

From equation 3.50 and equation 3.46

$$\hat{Y}_1 = r_1\left(\frac{-m_1{}^4 - B_1}{B_2}\right)e^{m_1 X} + \ldots + r_8\left(\frac{-m_8{}^4 - B_1}{B_2}\right)e^{m_8 X} + r_9\left(\frac{-m_9{}^4 - B_1}{B_2}\right)e^{m_9 X}\,. \tag{3.53}$$

Using equations 3.50, 3.53 and the boundary conditions defined by the third set (equations 3.47 and 3.48), the coefficients r_1, r_2, $r_3,\ldots,r_8$ can be found from the following relationship

$$[\mathbf{A}][\mathbf{R}] = [\mathbf{B}] \tag{3.54}$$

where

$$[\mathbf{R}] = [r_1 \quad r_2 \quad r_3 \quad r_4 \quad r_5 \quad r_6 \quad r_7 \quad r_8]^T \ ,$$

$$[\mathbf{B}] = [0 \quad 0 \quad 0 \quad 0 \quad -r_9 m_9{}^2 e^{m_9} \quad -r_9 m_9{}^3 e^{m_9} \quad -r_9 m_9{}^2 \quad -r_9 m_9{}^3]^T \ ,$$

and $[\mathbf{A}]$ is a 8×8 matrix, its first column is given by

$$[\mathbf{A}]_{first-column} = \begin{bmatrix} [m_1{}^4 + B_1][e^{m_1} - e^{i(\bar{\phi}-\phi)}] \\ [m_1{}^4 + B_1]m_1[e^{m_1} - e^{i(\bar{\phi}-\phi)}] \\ [m_1{}^4 + B_1]m_1{}^2[e^{m_1} - e^{i(\bar{\phi}-\phi)}] \\ [m_1{}^4 + B_1]m_1{}^3[e^{m_1} - e^{i(\bar{\phi}-\phi)}] \\ m_1{}^2 e^{m_1} \\ m_1{}^3 e^{m_1} \\ m_1{}^2 \\ m_1{}^3 \end{bmatrix} .$$

The jth column is calculated by replacing all m_1 by m_j; *e.g.* for the third column of $\mathbf{A}$ replace all m_1 in $[\mathbf{A}]_{first-column}$ by m_3.

For a given value of X, the coefficients r_1, r_2, $r_3, \ldots, r_8$ are calculated for a range of ϕ values to compute the displacements $\hat{Y}_1$ and $\hat{Y}_2$. These are transformed back numerically to the space-time domain using the inverse Fourier transform defined analytically as (see also equation A.4)

$$Y_{1,2}(X,T) = \frac{1}{2\pi} \int_{-\infty}^{\infty} \hat{Y}_{1,2}(x,\phi) \cdot e^{i\phi T} d\phi \ . \tag{3.55}$$

Equations 3.53 and 3.50 form the necessary equations to calculate the rail and slab displacements in the space-frequency domain for the chosen unit. For the purpose of coupling as will be explained in the next section, the procedure below shows the calculations of the rail displacement under an oscillating moving load, *i.e.* at T=X, for the range $0 \le X \le 1$ with interval ΔX:

1. calculate A_1, A_2, A_3, B_1, B_2, m_1, m_2, m_3, ..., m_8, and m_9 for N values of ϕ in the range $\phi_0 \le \phi \le \phi_f$ with interval $\Delta\phi$, the range is chosen in such that the excitation frequency $\overline{\phi}$ lies in the middle of this range. This is because most of the response activities occur at frequencies around the excitation frequency. This will be confirmed later in Section 3.4 and Figure 3.14;
2. calculate R in equation 3.54, using the variables values from step 1 for the range of frequency ϕ;
3. for a given X calculate $\hat{Y}_1$ using equation 3.53 and the values computed at step 1 and 2;
4. transform results to the time domain numerically, performing the integration using the trapezium rule [95]. From equation 3.55, Y_1 under the load can be computed from

$$Y_1 = \frac{1}{2\pi}\sum_{j=1}^{j=N} a_j \hat{Y}_1(X,\phi_j)\cdot e^{i\phi_j X}\Delta\phi \tag{3.56}$$

where $a_j = 0.5$ for $j = 1, N$ and $a_j = 1$ for $j = 2,3,...,N-1$;
5. repeat step 3 and 4 until covering all values of X.

The Modified-phase method

This method results as a direct application of the periodic infinite structure theory. The method is based on using the track displacements under an oscillating non-moving load to calculate the displacements for moving loads with the same excitation frequency. The method is approximate and only valid for relatively low velocities of moving loads compared to the track critical velocity. To explain the method, a reference is made to Figure 3.5.a. It shows an oscillating non-moving load that stands at $x = x_o$. The response underneath this load is $y_1 = c_1 e^{i\varpi t}$. Figure 3.5.b shows an oscillating moving load which passes x=0 with phase equal to zero. This load moves (slowly), until it gets to $x = x_o$. At this point the force will be $F = e^{i\varpi(t + x_o / v)}$. By comparing with the non-moving load displacement, the displacement underneath the moving load will be

$y_3 = c_1 e^{i\varpi t} e^{i\varpi x_o / v}$. Hence to calculate the moving load displacement, the non-moving load model can be used, but results should be modified by the factor $e^{i\varpi x_o / v}$. Results of this method will be compared with the previous two methods in Section 3.4.

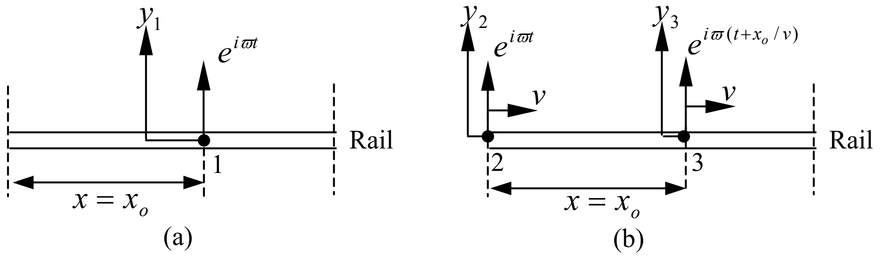

Figure 3.5: Demonstration of the Modified-phase method. (a) Response is measured under a non-moving load at point 1. (b) Response is measured under the load at point 3 where the phase is $\varpi x_0 / v$.

3.2.2 Coupling a train model to the track

Unlike moving axles on a track with a continuous slab, the inertial forces contribute to the steady-state displacements of a track with a discontinuous slab. As shown in Figure 3.6, a two-degree-of-freedom system is used to model a quarter of a train with four axles and two bogies moving on the track with constant velocity v. The unsprung mass M_1 accounts for a single axle, the sprung mass M_2 accounts for half a bogie, the static force $M_3 g$ accounts for the weight of quarter the carriage and chassis and k_u and c_u are the stiffness and damping factor of the primary suspension respectively.

The two-degree-of-freedom system is moving over a periodic structure. Thus, the steady-state displacements of the unsprung mass and the sprung mass can be written as a sum of Fourier series as

$$z_1 = \sum_{n=-s}^{+s} C_n \cdot e^{i\omega_n t} \tag{3.57}$$

and

$$z_2 = \sum_{n=-s}^{+s} G_n \cdot e^{i\omega_n t} \tag{3.58}$$

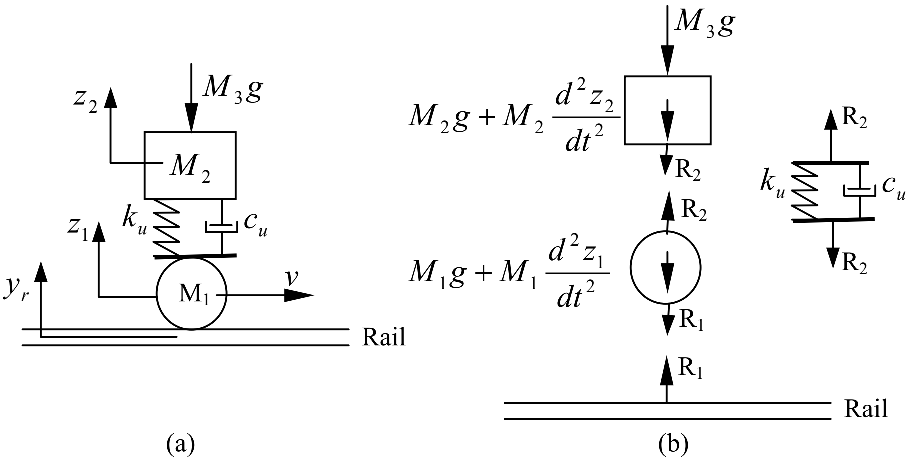

Figure 3.6: (a) Coupling a train model to the track. (b) Free body diagrams.

where z_1 and z_2 are the displacements of the unsprung mass and the sprung mass respectively, C_n and G_n are the amplitudes of the nth harmonic of the unsprung mass and the sprung mass respectively, ω_n is the angular frequency of the nth harmonic, *i.e.* $\omega_n = 2\pi(nv/L)$ and s is the maximum harmonic included in the summation.

The equilibrium equations of the sprung mass and the unsprung mass read

$$R_2 = -(M_2 + M_3)g - M_2\frac{d^2z_2}{dt^2} \tag{3.59}$$

and

$$R_1 = R_2 - M_1g - M_1\frac{d^2z_1}{dt^2} \tag{3.60}$$

where R_1 and R_2 are the axle-rail and the suspension forces respectively (see Figure 3.6.b).

The equilibrium equation of the suspension reads

$$R_2 = k_u(z_2 - z_1) + c_u(\frac{dz_2}{dt} - \frac{dz_1}{dt}). \tag{3.61}$$

By equating equations 3.59 and 3.61, and substituting z_1 and z_2 from equations 3.57 and 3.58, this results in

$$G_0 = \frac{k_u C_0 - (M_1 + M_3)g}{k_u} \quad \text{and}$$

$$G_n = \left[\frac{k_u + c_u i\omega_n}{k_u + c_u i\omega_n - M_2\omega_n^2}\right] C_n \quad \text{for } n \neq 0 . \qquad (3.62)$$

Solving for R_1 from equations 3.60 and 3.59 using the values of z_1 and z_2 from equations 3.57 and 3.58 gives

$$R_1 = -(M_1 + M_2 + M_3)g + \sum_{n=-s}^{+s} [M_1 C_n \omega_n^2 + M_2 G_n \omega_n^2] \cdot e^{i\omega_n t} . \qquad (3.63)$$

For an oscillating moving load on the track given by the relationship

$$R = e^{i\omega_n t} \text{ with } \omega_n = \frac{2\pi n v}{L} , \qquad (3.64)$$

the rail response under the moving load can be written in a Fourier series sum as

$$y_r = \sum_{q=-p}^{+p} h_{q,n} e^{i\omega_q t} \qquad (3.65)$$

where $h_{q,n}$ is the magnitude of the q$^{\text{th}}$ harmonic of the rail displacement when a unit oscillating load is moving on the rail with angular frequency ω_n. Calculations of rail displacements are presented in Section 3.2.1, from which values of $h_{q,n}$ can be computed.

The load R_1 in equation 3.63 is a sum of a number of oscillating loads with angular frequencies multiples of the track first frequency $2\pi(v/L)$. Hence, equation 3.65 can be used to write the rail displacement as

$$y_r = -(M_1 + M_2 + M_3)g \sum_{q=-p}^{+p} h_{q,0} e^{i\omega_q t} + \sum_{n=-s}^{+s} \sum_{q=-p}^{+p} (M_1 C_n + M_2 G_n)\omega_n^2 h_{q,n} e^{i\omega_q t} \,. \quad (3.66)$$

Swapping the summation of the second term in the right hand side and then replacing each q by n and vice-versa results in

$$y_r = -(M_1 + M_2 + M_3)g \sum_{n=-p}^{+p} h_{n,0} e^{i\omega_n t} + \sum_{n=-p}^{+p} \sum_{q=-s}^{+s} (M_1 C_q + M_2 G_q)\omega_q^2 h_{n,q} e^{i\omega_n t} \quad (3.67)$$

or

$$y_r = \sum_{n=-p}^{+p} [-(M_1 + M_2 + M_3)g \cdot h_{n,0} + \sum_{q=-s}^{+s} (M_1 C_q + M_2 G_q)\omega_q^2 h_{n,q}] e^{i\omega_n t} \,. \quad (3.68)$$

To satisfy the compatibility condition, displacements of the rail (equation 3.68) and the unsprung mass (equation 3.57) should be identical. Equating these two equations results in the following two relationships

$$p = s \quad (3.69)$$

and

$$C_n = [-(M_1 + M_2 + M_3)g \cdot h_{n,0} + \sum_{q=-s}^{+s} (M_1 C_q + M_2 G_q)\omega_q^2 h_{n,q}] \,. \quad (3.70)$$

Using equation 3.62, for $n = -s, -s+1, ..., 0, ..., s-1, s$ equation 3.70 can be written in matrix form as

$$[\mathbf{A}][\mathbf{C}] = [\mathbf{D}] \quad (3.71)$$

where $\mathbf{A}$ is a matrix with $(2 \times s + 1)$ rows and $(2 \times s + 1)$ columns. Its elements can be calculated from the following relationships

$$\mathbf{A}(i,j) = [\frac{k_u (M_1 + M_2) + c_u i\omega_{-s+j-1}(M_1 + M_2) - M_1 M_2 \omega_{-s+j-1}{}^2}{k_u + c_u i\omega_{-s+j-1} - M_2 \omega_{-s+j-1}{}^2}] \cdot \omega_{-s+j-1}{}^2 \cdot h_{-s+i-1,-s+j-1}$$

for $i \neq j$,

$$\mathbf{A}(i,j) = [\frac{k_u(M_1+M_2)+c_u i\omega_{-s+j-1}(M_1+M_2)-M_1M_2\omega_{-s+j-1}{}^2}{k_u+c_u i\omega_{-s+j-1}-M_2\omega_{-s+j-1}{}^2}]\cdot\omega_{-s+j-1}{}^2\cdot h_{-s+i-1,-s+j-1}-1$$

for $i = j$,

$[\mathbf{C}] = [C_{-s} \quad C_{-s+1} \quad .. \quad .. \quad C_s]^T$, $\omega_{-s+j-1} = 2\pi(-s+j-1)v/L$ and

$[\mathbf{D}] = [h_{-s,0}e \quad h_{-s+1,0}e \quad .. \quad .. \quad h_{s,0}e]^T$ with $e = (M_1+M_2+M_3)g$.

Having determined the coefficients $\mathbf{C}$ from equation 3.71, these are substituted in equation 3.62 to determine the coefficients $\mathbf{G}$. $\mathbf{C}$ and $\mathbf{G}$ are then used to determine the discrete model and the track displacements.

Note that when $v \to 0$, all diagonal elements in matrix $\mathbf{A}$ tend to the value -1, while non-diagonal elements tend to 0. From equation 3.71, the vector $\mathbf{C}$ becomes

$$[\mathbf{C}] = -(M_1+M_2+M_3)g\cdot[h_{-s,0} \quad h_{-s+1,0} \quad .. \quad .. \quad h_{s,0}]^T. \tag{3.72}$$

Substituting in equation 3.57

$$z_1 = -(M_1+M_2+M_3)g\sum_{n=-s}^{+s} h_{n,0}\cdot e^{i\omega_n t}. \tag{3.73}$$

The summation on the right hand side is equal to the rail displacement under a non-oscillating moving load. Hence, when $v \to 0$, the rail displacement is equal to the static displacement multiplied by the weight of the discrete model.

3.3 Results for tracks with continuous slabs

The parameters used to analyse floating-slab tracks are given in Table 3.1. These parameters are identical to the ones used by Forrest [29] except for the dampers. Smaller damping factors are used with 5% damping ratios. The damping factors can be calculated from the damping ratios from the following relationships

$$c_1 = 2\zeta_1 \cdot \sqrt{k_1 \cdot m_1} \text{ and } c_2 = 2\zeta_2 \cdot \sqrt{k_2 \cdot m_2} . \tag{3.74}$$

Rail	Slab
$EI_1 = 10 MPa/m^2$	$EI_2 = 1430 MPa/m^2$
$m_1 = 100 kg/m$	$m_2 = 3500 kg/m$
$k_1 = 40 MN/m/m$	$k_2 = 50 MN/m/m$
$c_1 = 6.3 kN/m/(m/s)$	$c_2 = 41.8 kN/m/(m/s)$

Table 3.1: Parameter values used for the floating-slab track.

The free-vibration equations of a floating-slab track are calculated from equation 3.6 by setting the force to zero, *i.e.*

$$[\mathbf{A}]\tilde{\mathbf{y}} = [\mathbf{A}]\begin{bmatrix} \tilde{y}_1 \\ \tilde{y}_2 \end{bmatrix} = \begin{bmatrix} 0 \\ 0 \end{bmatrix}. \tag{3.75}$$

The dispersion equation is calculated by the non-trivial solution of this equation, *i.e.* $|\mathbf{A}| = 0$ or $f_1(\xi, \omega) = 0$ as in equations 3.7 and 3.8 with $c_1 = 0$ and $c_2 = 0$ (compare with equation B.21). The vector $\tilde{\mathbf{y}}$ is the eigenvector describing the mode shape and can be calculated as explained in Appendix B. The dispersion curves are the real solutions of the dispersion equation and usually plotted for only positive frequencies due to symmetry about zero frequency. However, negative frequencies are important for calculation of critical velocities, which will be discussed later in this section.

Figure 3.7 shows the dispersion curves of the track. It has two positive cut-on frequencies. The first occurs at 18.75Hz, where waves start to propagate away from the excitation point. Note that cut-on frequencies of the track are associated with zero wavenumbers, *i.e.* infinite wavelengths, and hence the track behaves as a two-dimensional structure. As the slab is much heavier than the rails, the value of the first cut-on frequency can also be approximately calculated using the single-degree-of-freedom system consisting of a mass equal to the slab's mass per unit length and a spring with stiffness equal to the slab-bearings' stiffness per unit length, *i.e.* $f = 1/(2\pi)\sqrt{k_2 / m_2}$, which results in a cut-on frequency of 19.02Hz. By calculating $\tilde{\mathbf{y}}$ in equation 3.75 at the first cut-on frequency, the motion of the rails and the slab is observed to be in phase.

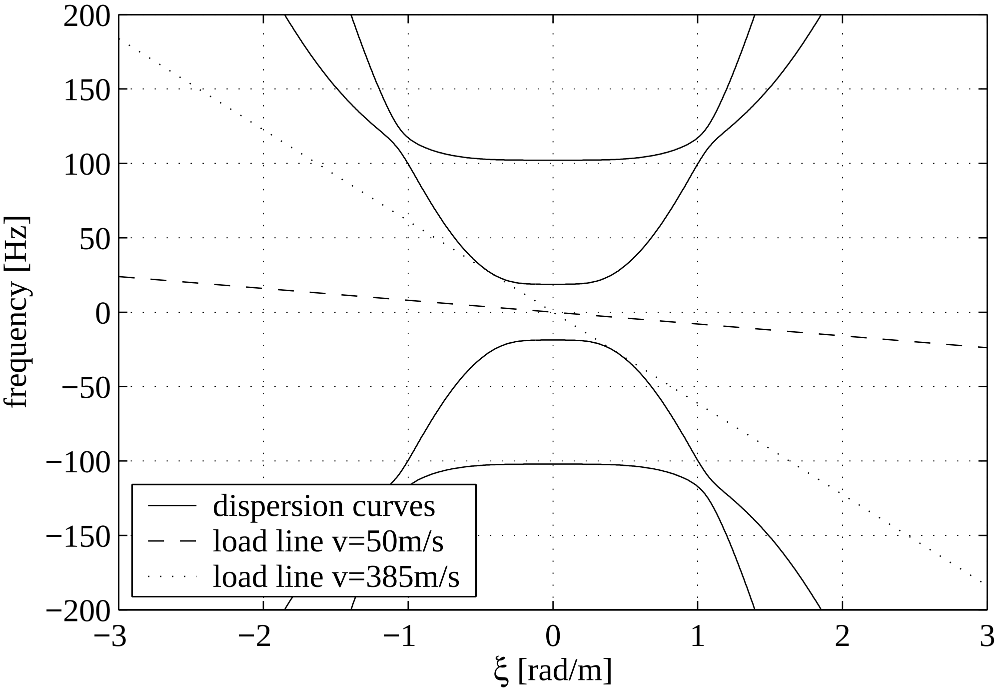

Figure 3.7: Dispersion curves of the floating-slab track calculated from the equation $f_1(\xi,\omega) = 0$. The load velocity lines are also shown for two velocities 50 m/s and 385 m/s.

The second cut-on frequency occurs at 102.15 Hz. At this cut-on frequency, waves propagate in which only the rails vibrate, while the slab does not move. Again the value of the second cut-on frequency can be approximately calculated using the single-degree-of-freedom system consisting of a mass equal to the rails' mass per unit length and a spring with stiffness equal to the railpads' stiffness per unit length, *i.e.* $f = 1/(2\pi)\sqrt{k_1 / m_1}$, which results in a cut-on frequency of 100.66Hz.

The track displacements under a static moving load, *i.e.* $\varpi = 0$, can be evaluated by performing the integrations in equations 3.11 and 3.12 numerically. Note that the integrated functions have infinite values at points where the denominator $f_1(\xi, \omega = -\xi v)$ is equal to zero. The dispersion curves in Figure 3.7 give the solutions of the equation $f_1(\xi, \omega) = 0$ in absence of damping. At the velocity when the line $\omega = -\xi v$ becomes tangential to the curve $f_1(\xi, \omega) = 0$, the displacement becomes infinite and this velocity is called the critical velocity.

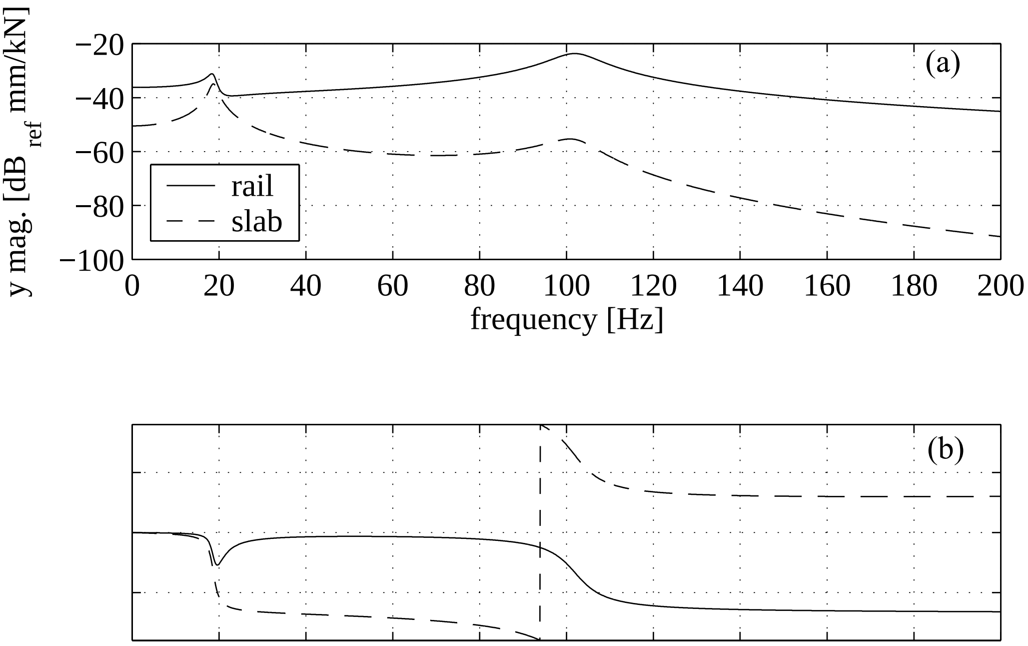

Figure 3.8: Rails and slab displacements under a non-moving harmonic load; (a) displacement, (b) phase.

In the absence of damping, the displacement is infinite at a velocity equal to the critical velocity. If damping is considered, the functions $f_2(\xi, \omega) / f_1(\xi, \omega)$ and $f_3(\xi, \omega) / f_1(\xi, \omega)$ will have peaks at the dispersion curves with higher values at lower angular frequencies ω. Hence, the track will have a finite peak at the critical velocity and smaller displacements at higher velocities. Figure 3.7 shows the line $\omega = -\xi v$ which is called the *load velocity line*, for two velocities; 50 m/s and 385 m/s. The latter is the track's critical load velocity.

Figure 3.8 (a and b) shows the track displacements and phases for a non-moving oscillating load. It can be seen that peaks occur at cut-on frequencies. This is because the load line $\omega = \varpi - \xi v$ (with $v = 0$ in this case) becomes tangential to one of the dispersion curves of the track in Figure 3.7 at cut-on frequencies. The importance of propagating waves can be realised away from the excitation point. Figure 3.9, shows the track responses at 40m away from the excitation point. It can be seen that the response below 19Hz is small as it is dominated by evanescent waves and leaky waves which decay dramatically with distance. Figure 3.9.b shows that at the range of frequency between the two cut-on frequencies, both the rails and slab move in phase. Above the second cut-on frequency, the picture is complicated as two propagating waves contribute to the track displacement as can be seen from Figure 3.7.

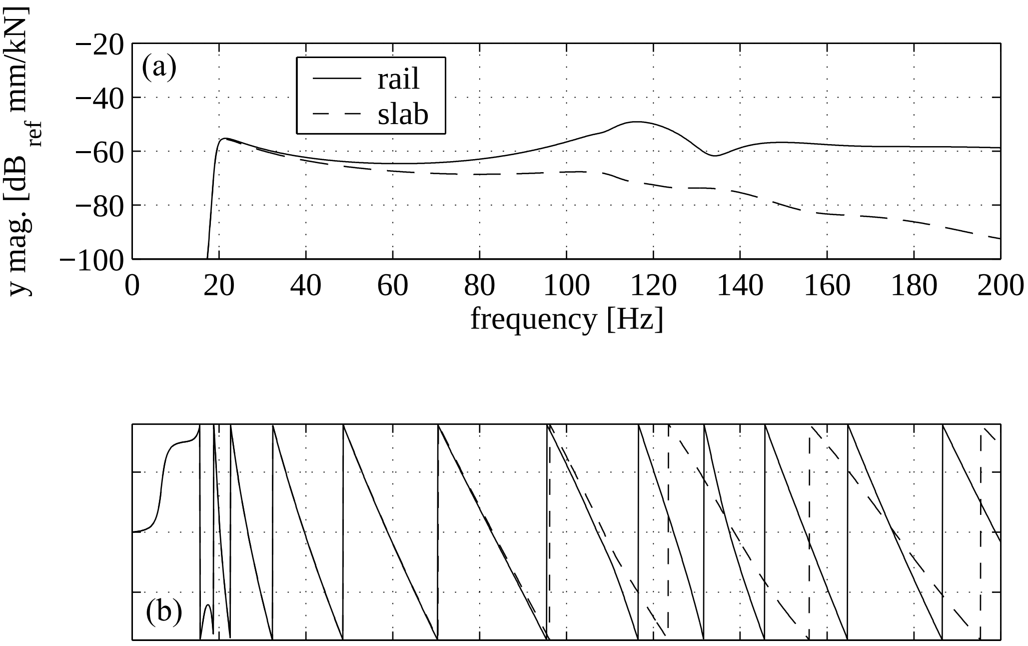

Figure 3.9: Rails and slab displacements at 40m away from a non-moving harmonic load; (a) displacement, (b) phase.

A different way of calculating the dispersion curves for a track under moving loads is by directly solving the equation $f_1(\xi, \omega = \varpi - \xi v) = 0$. At a given excitation frequency ϖ, this results in eight eigenvalues ($\xi_1, \xi_2, \xi_3, ..., \xi_8$). Due to the factor $e^{i\xi(x-vt)}e^{i\varpi t}$ in equations 3.13 to 3.16, the value of ξ determines the wave type, whether propagating, leaky or evanescent, but in a moving frame of reference $x - vt$ (see Appendix B for more details). At a given positive ϖ, a positive real root ξ represents a wave propagating to the right ahead of the moving load. In absence of damping, the velocity $v = 0$ gives the dispersion curves calculated before in Figure 3.7. Dispersion curves for $v = 0$ are symmetrical about $\xi = 0$. This means that waves that propagate to the left are identical to those that propagate to the right. When considering damping in the calculations (provided by c_1 and c_2) for non-moving loads, all roots shift to new positions by rotating counter clockwise in the complex ξ domain. Hence, positive real values of ξ gain small positive imaginary part and negative real values of ξ gain small negative imaginary part. Thus propagating waves transform to leaky waves with small coefficients of attenuation.

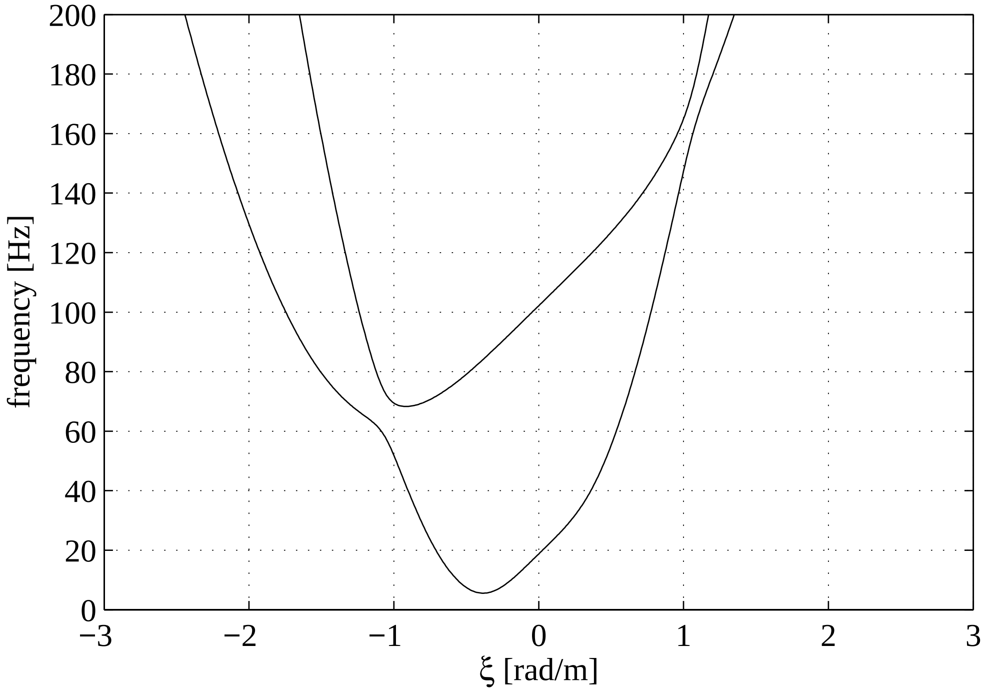

Figure 3.10: Dispersion curves for floating-slab track under an oscillating moving load with $v = 300m/s$.

Figure 3.10 shows the dispersion curves for $v = 300$ m/s, where only positive frequencies are plotted. The dispersion curves are no longer symmetrical about $\xi = 0$. Compared with the non-moving load, the curves have moved down and to the left. Cut-on frequencies are lower than before and wavenumbers are longer ahead of the load than behind the load. This means that wavelengths are shorter in front of the load. At frequencies just above the first cut-on, waves with longer wavelengths have negative phase velocities. However, these waves still propagate away from the load as they have positive group velocities, see [38] for more details.

By increasing the load velocity more and more, the lower dispersion curve heads toward the wavenumber axis and touches it around 385 m/s (the same critical velocity as calculated before from Figure 3.7). At this velocity, waves propagate from a static moving load, *i.e.* a load with $\varpi = 0$.

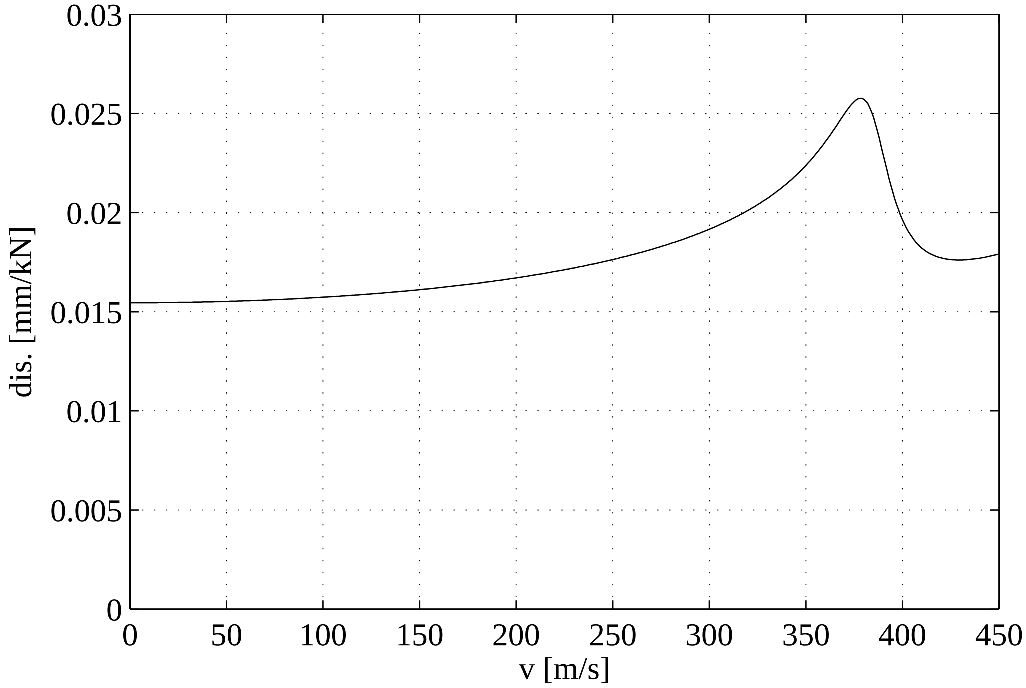

Figure 3.11: Rail displacement under non-oscillating moving load. Critical velocity occurs at 380 m/s.

The critical load velocity can also be calculated by plotting the displacement of the rail as a function of the load velocity as shown in Figure 3.11. The critical load velocity from this figure occurs at about 380m/s, *i.e.* slightly smaller than the value calculated before and the difference is attributed to damping which is modelled in the calculations of Figure 3.11. This figure also shows that the velocity effect is negligible when modelling non-oscillating moving loads on floating-slab tracks. This is true up to 100m/s, where no difference is observed between the static solution and the moving load solution. For underground trains, 100m/s is much higher than typical train velocities.

In the previous discussion, wave propagation is considered in a moving frame of reference. For a propagating wave with angular frequency ϖ and wavenumber ξ_j, the observation point oscillates with angular frequency ϖ in a moving frame of reference. However, in a fixed frame of reference, it oscillates with angular frequency $\varpi - \xi_j v$. This can be shown from the following relationship

$$e^{i\varpi t} \cdot e^{i\xi_j(x-vt)} = e^{i(\varpi-\xi_j v)t} \cdot e^{i\xi_j x}. \tag{3.76}$$

Hence, for a fixed frame of reference, the oscillation frequency ω_j of the observation point can be written as

$$\omega_j = \varpi - \xi_j v = \varpi(1 - \xi_j v/\varpi) = \varpi(1 - v/c_j)$$

or

$$f_j = \bar{f}(1 - v/c_j) \tag{3.77}$$

where f_j is the oscillation frequency for a fixed frame of reference, $\bar{f}$ is the oscillation frequency for a moving frame of reference, and c_j is the phase velocity of the propagating wave. Equation 3.77 is known physically as *Doppler effect*, see [117] for example. c_j can be positive or negative depending on the direction of propagation.

As mentioned in Section 3.1.1, calculations of the track displacements are verified by computing the power transmission through the rails. Figures 3.12 and 3.13 show the instantaneous power input in a longitudinal section of the rails bounded by $x = 0$ and $x = 6$. The power is calculated for a constant moving load in Figure 3.12 and 2 Hz harmonic load in Figure 3.13.

For conservation of power, the total input power is equal to the sum of the rate of change of kinetic and potential energies or in other words, the sum of kinetic and potential powers. This equality provides a check to the results presented in Section 3.1.1 and is confirmed by Figures 3.12 and 3.13. To calculate the input power to a section of the rails bounded by $x = x_0$ and $x = x_f$, where $x_f > x_0$, the following relationships are used:

1. The input power from the force

$$P_1(t) = \int_{x_0}^{x_f} \mathrm{Re}(\delta(x - vt)e^{i\varpi t}) \cdot \mathrm{Re}(\frac{\partial y_1}{\partial t})dx \; = \; \cos(\varpi t) \cdot \mathrm{Re}(\frac{\partial y_1}{\partial t})_{x=vt} \;\text{ if }\; (x_0 / v) \le t \le (x_f / v)$$

$$= 0 \text{ otherwise.} \tag{3.78}$$

2. The input power from the shear force and bending moment at $x = x_0$

$$P_2(t) = \mathrm{Re}(EI_1 \frac{\partial^3 y_1}{\partial x^3})_{x=x_0} \cdot \mathrm{Re}(\frac{\partial y_1}{\partial t})_{x=x_0} - \mathrm{Re}(EI_1 \frac{\partial^2 y_1}{\partial x^2})_{x=x_0} \cdot \mathrm{Re}(\frac{\partial^2 y_1}{\partial x \partial t})_{x=x_0} \tag{3.79}$$

where the first and the second terms express the power from the shear force and the bending moment respectively.

3. The input power from the shear force and bending moment at $x = x_f$

$$P_3(t) = -\mathrm{Re}(EI_1 \frac{\partial^3 y_1}{\partial x^3})_{x=x_f} \cdot \mathrm{Re}(\frac{\partial y_1}{\partial t})_{x=x_f} + \mathrm{Re}(EI_1 \frac{\partial^2 y_1}{\partial x^2})_{x=x_f} \cdot \mathrm{Re}(\frac{\partial^2 y_1}{\partial x \partial t})_{x=x_f} \,. \tag{3.80}$$

The sum $P_2(t)+P_3(t)$ is plotted in Figures 3.12 and 3.13 as a single quantity and called the boundary power.

4. The input power from the railpads' stiffness

$$P_4(t) = -\int_{x_0}^{x_f} \mathrm{Re}[k_1(y_1 - y_2)] \cdot \mathrm{Re}(\frac{\partial y_1}{\partial t})dx . \tag{3.81}$$

5. The input power from the railpads' damping

$$P_5(t) = -\int_{x_0}^{x_f} \mathrm{Re}[c_1(\frac{\partial y_1}{\partial t} - \frac{\partial y_2}{\partial t})] \cdot \mathrm{Re}(\frac{\partial y_1}{\partial t})dx . \tag{3.82}$$

The sum $P_4(t)+P_5(t)$ is plotted as a single quantity and called the railpads' power.

6. The kinetic power

$$P_6(t) = \int_{x_0}^{x_f} \mathrm{Re}(m_1 \frac{\partial^2 y_1}{\partial x^2}) \cdot \mathrm{Re}(\frac{\partial y_1}{\partial t})dx . \tag{3.83}$$

7. The potential power

$$P_7(t) = \int_{x_0}^{x_f} \mathrm{Re}(EI_1 \frac{\partial^2 y_1}{\partial x^2}) \cdot \mathrm{Re}(\frac{\partial^3 y_1}{\partial x^2 \partial t})dx . \tag{3.84}$$

As mentioned before, the sum of input power is equal to the sum of kinetic and potential powers. This can be written mathematically as

$$P_1(t) + P_2(t) + P_3(t) + P_4(t) + P_5(t) = P_6(t) + P_7(t) . \tag{3.85}$$

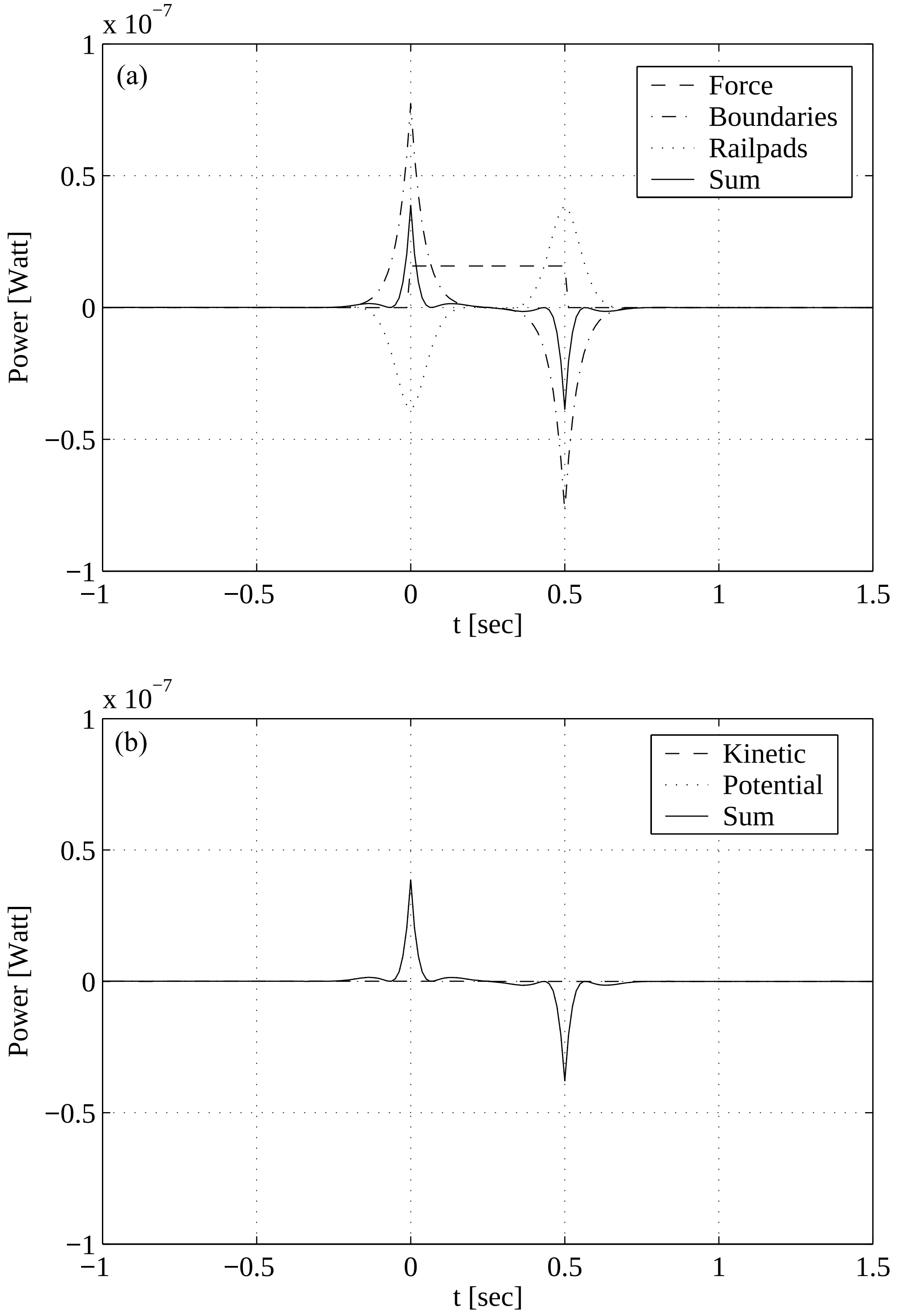

Figure 3.12: Instantaneous power in a 6m longitudinal section of the rails bounded between x=0m and x=6m, for a non-oscillating unit load moving with velocity 12m/s. The load passes x=0m at t=0s and x=6m at t=0.5s. (a) Different components of the power. (b) Kinetic and potential power. The input power from the force is multiplied by 100 to be clarified.

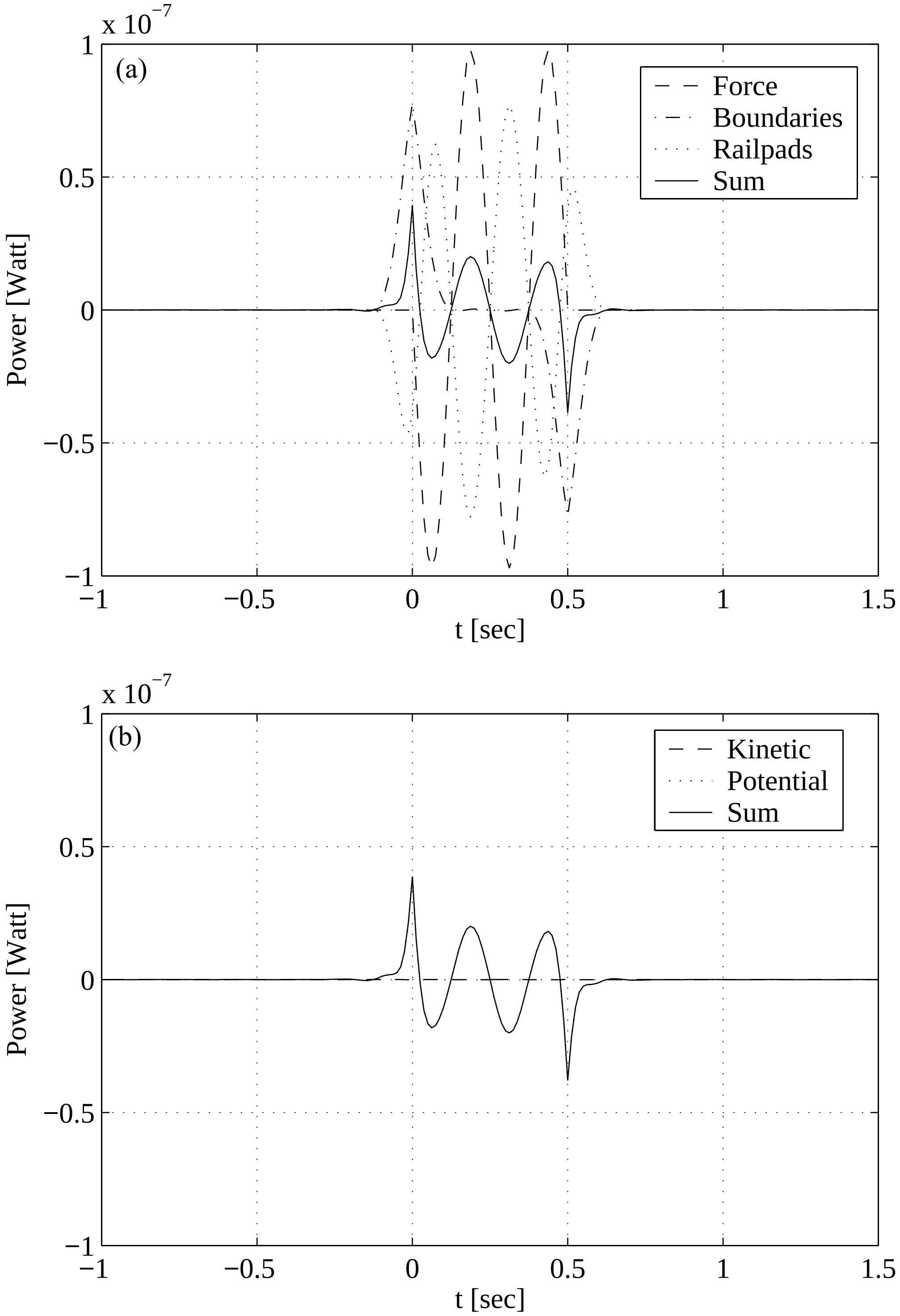

Figure 3.13: Instantaneous power in the same section as in Figure 3.12 but for a 2Hz oscillating unit load moving with velocity 12m/s. (a) Different components of the power. (b) Kinetic and potential power.

From Figures 3.12.b and 3.13.b, it can be seen that at low excitation frequency, most of the power is used to deform the beam rather than to vibrate it. This is the reason that the potential power dominates over the kinetic power.

The input power from a moving load to the entire track (see equation 3.78) for a non-oscillating moving load can be written using the moving frame of reference, *i.e.* $z = x - vt$ as

$$P_1(t) = \mathrm{Re}[-v\frac{\partial y_1(z=0,t)}{\partial z} + \frac{\partial y_1(z=0,t)}{\partial t}]. \tag{3.86}$$

In a moving frame of reference, the track deflection is independent of time and hence the second term in the right hand side is equal to zero, this enables writing

$$P_1(t) = -v\frac{\partial y_1(z=0,t)}{\partial z}. \tag{3.87}$$

The real symbol is not written in the last equation as all values of track responses are real values for a static-moving load. This means that the input power is equal to the load velocity multiplied by the slope of the rail deflection under the moving load.

3.4 Results for tracks with discontinuous slabs

The parameters given in Table 3.1 for a track with a continuous slab are used again in this section. Figure 3.14 shows the rail displacement at X=0.5 in the non-dimensional space-frequency domain. The Periodic-Fourier method is used to produce this result, which confirms the fact that most of the displacement activities lie near the excitation frequency.

Three Matlab [75] codes are developed to study the methods presented in Section 3.2.1. These codes are run on a PC computer with 1GB RAM and 2.4GHz processor. Figure 3.15 shows the time-history rail displacement for a track with slab length

$L = 6m$ at $X = 0.25$, *i.e.* $x = 1.5m$, for an oscillating moving load $(1.e^{i\varpi t})$ with $v = 10\ km/hr$ and $\varpi = 2\pi \times (2v/L)$ $= 5.82 rad/\sec$. The excitation frequency is chosen such that the load completes two cycles when it passes over one slab length. The three methods give identical results, although the third method is approximate. The running time to produce the results in Figure 3.14 using the Fourier–Repeating-unit method is 19 minutes where the Periodic-Fourier and the Modified-phase methods take only 2 and 1.2 seconds respectively.

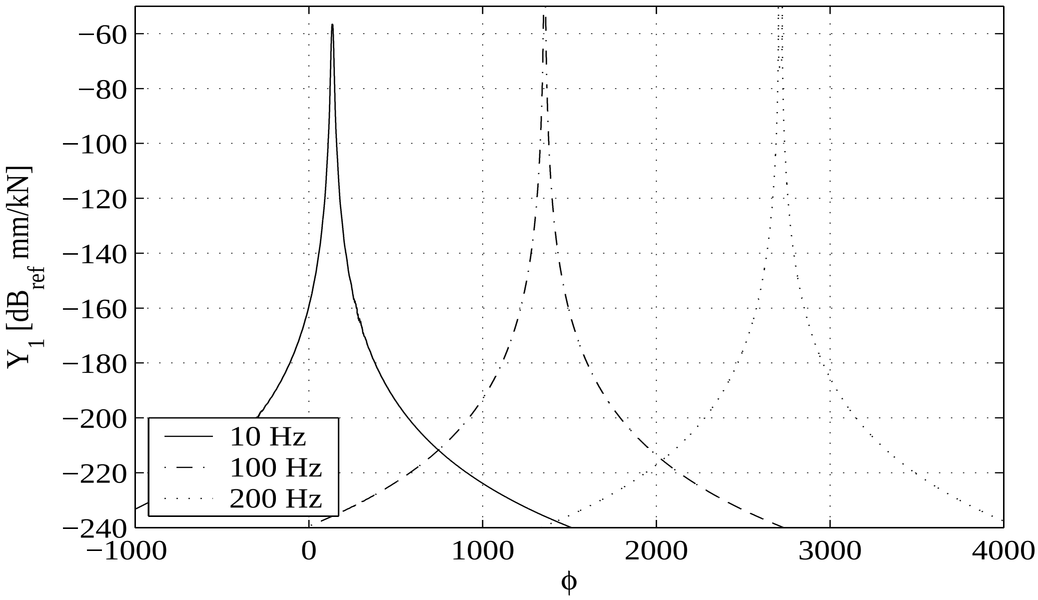

Figure 3.14: Spectrum of rail displacement for three values of $\bar{f}$=10Hz, 100Hz and 200Hz corresponding to $\bar{\phi}$ = 135.7, 1357.2 and 2714.3 respectively. For all curves v=10km/hr, L=6m, and X=0.5.

More improvement to the code of the first method could enhance the running time. For instance, values of $\hat{G}_{\omega}(x_o, x)$ in the lower half of the mesh in Figure 3.4, can be deduced from values of $\hat{G}_{\omega}(x_o, x)$ in the upper half using the relationship

$$\hat{G}_{-\omega}(x_o, x) = \hat{G}_{\omega}(x_o, x)^* . \tag{3.88}$$

This is because the input force for $\hat{G}_{-\omega}(x_o, x)$ is a complex conjugate of the input force for $\hat{G}_{\omega}(x_o, x)$. Under any improvement to the code of the Fourier–Repeating-unit method, it is not expected to be as efficient as the Periodic-Fourier method. This is because the first method involves computing results for non-moving loads in a two-dimensional mesh (see Figure 3.4), whereas in the second method the calculations need to be performed only along one column of points to produce the same results. This obviously gives the second method a computational advantage.

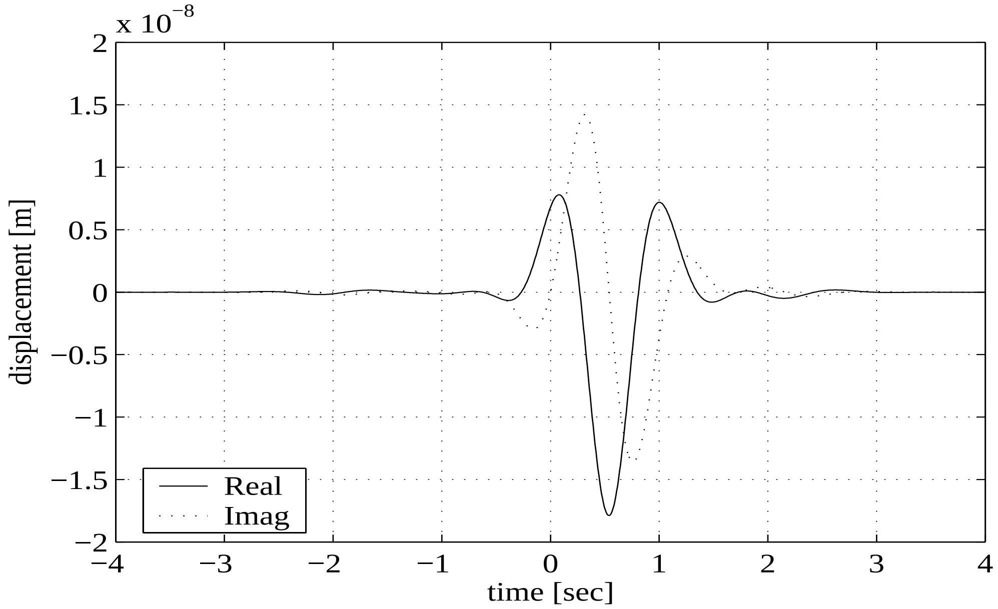

Figure 3.15: Displacement time-history at $X = 0.25$ in the rail, for a moving harmonic force with $\varpi = 5.82 rad/\sec$, $v = 10 km/hr$, and L= 6m. The three methods described in Section 3.2 are used and identical results are obtained.

In Figure 3.15, the real curve shows the response of the rail for a harmonic load which passes x=0 with a maximum magnitude ($\mathrm{Re}(1 \cdot e^{i\varpi t})_{t=0} = 1$). The imaginary curve shows the response of the same point in the rail but for a harmonic load that passes x=0 with zero magnitude ($\mathrm{Im}(1 \cdot e^{i\varpi t})_{t=0} = 0$).

Figure 3.16 shows the rail response under a non-oscillating moving load with velocities 1 km/hr, 80 km/hr and 300 km/hr. No significant differences are observed in the track response for velocities up to 80km/hr. For underground trains, the velocity is restricted (usually maximum of 60km/hr) to allow for train stopping at stations, and hence the static solution is sufficient in modelling of quasi-static moving loads. Figure 3.16 also shows that the stiffness under a moving load is not uniform. A parametric excitation occurs for a moving train due to this variable stiffness. This effect will be investigated at the end of this section.

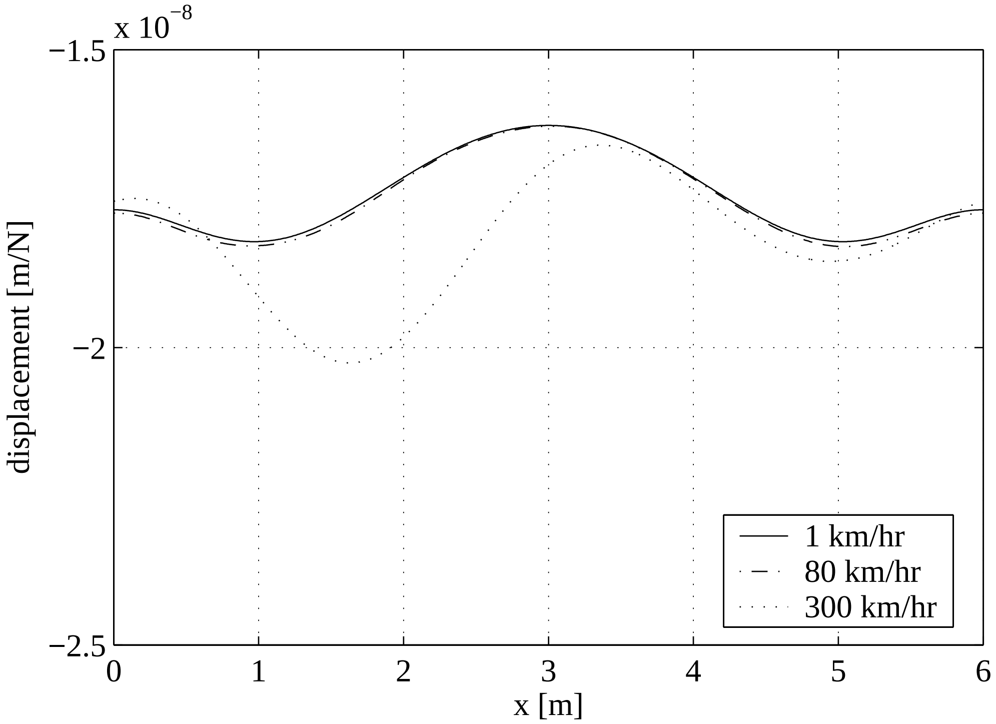

Figure 3.16: Rail displacement under a downward static-moving load for a track with 6m slab.

Figure 3.17 (a and b) shows the rail and slab displacements under a non-moving oscillating load applied at X=0.25 for three slab lengths L=3m, L=6m, and L=12m. By comparing the displacements at zero frequency, the stiffness of the track is higher for a longer slab length. This is expected as bending stiffness of the longer slab contributes more to the stiffness of the track. Two pronounced peaks occur at the same cut-on frequencies of the track with a continuous slab, which is discussed in Section 3.3.

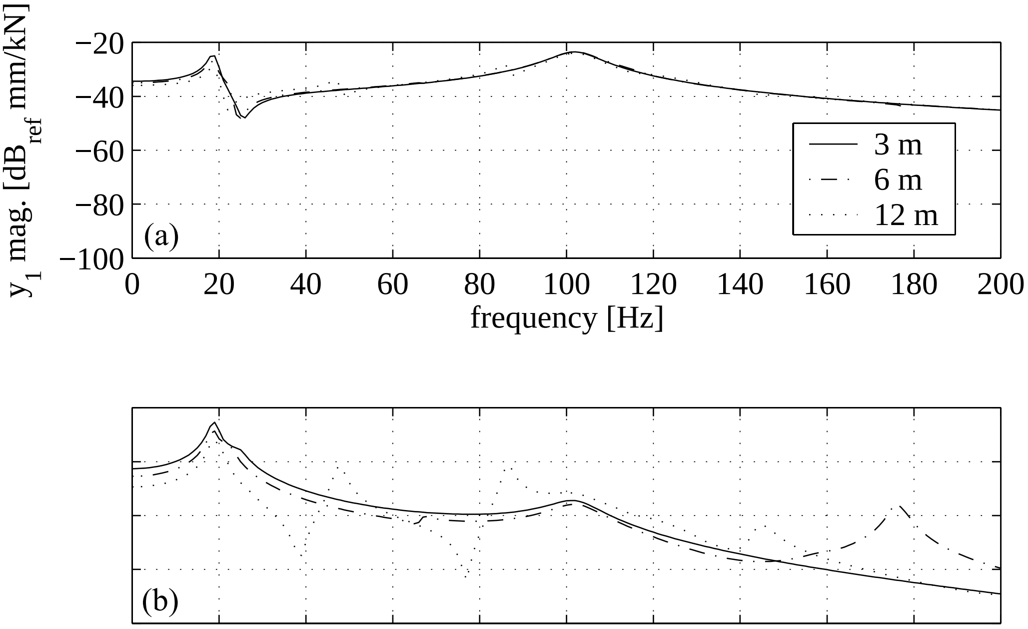

Figure 3.17: Track displacement under an oscillating non-moving load applied at X=0.25 for slab length L=3m, 6m and 12m. (a) rail displacement. (b) slab displacement.

Because of slab discontinuity, more peaks appear at the range of frequency of interest. These peaks are attributed to standing waves which are built by reflections of propagating waves at free ends of the slab. Frequencies at which peaks occur can be calculated from the free-free beam natural frequencies, see [7] for example, which reads

$$f_n = \sqrt{\frac{EI_2}{m_2}}\frac{\lambda_n^2}{2\pi L^2} \tag{3.89}$$

where $\lambda_1 = 4.73$, $\lambda_2 = 7.853$, $\lambda_3 = 10.996$, *etc...*

Using the parameters in Table 3.1, the peaks occur at 15.8, 43.6, 85.4 Hz for L=12m, which are in agreement with the results in Figure 3.17 (a and b).

Figure 3.18 shows the rail displacement under the load at X=0.25 for two velocities; 10 km/hr and 80 km/hr at the range of frequency of interest. It can be seen that the velocity has no significant influence on the absolute results up to 80 km/hr. This result confirms the validity of the Modified-phase method which assumes a change in the phase, not the magnitude of the displacement due to a change in the load velocity.

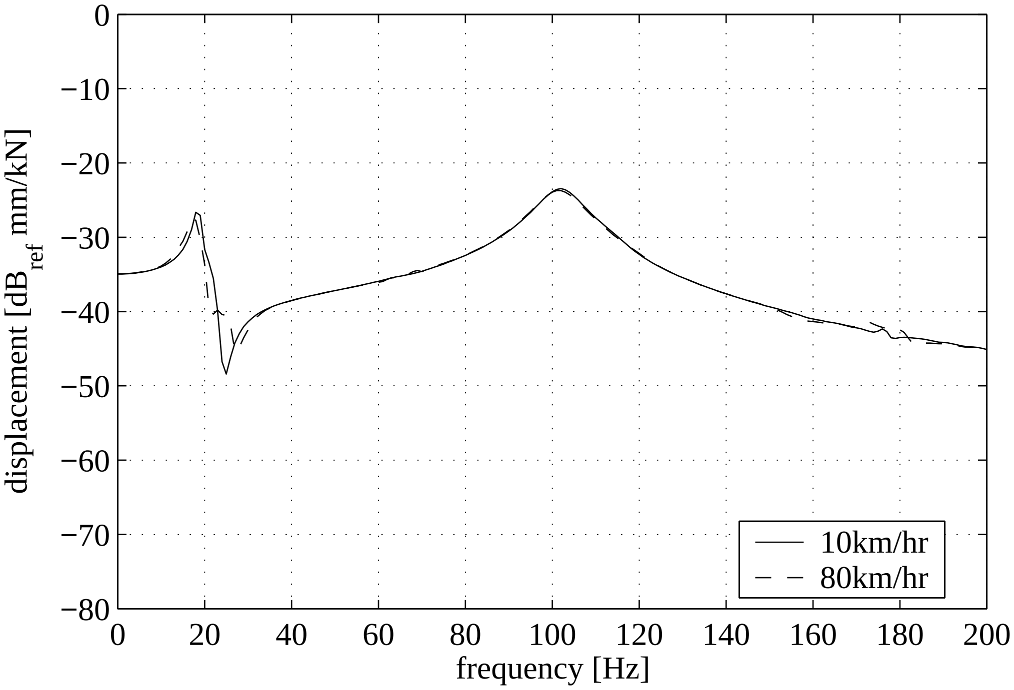

Figure 3.18: Rail displacement under a moving load at X=0.25, L=6m, for v=10km/hr and 80km/hr.

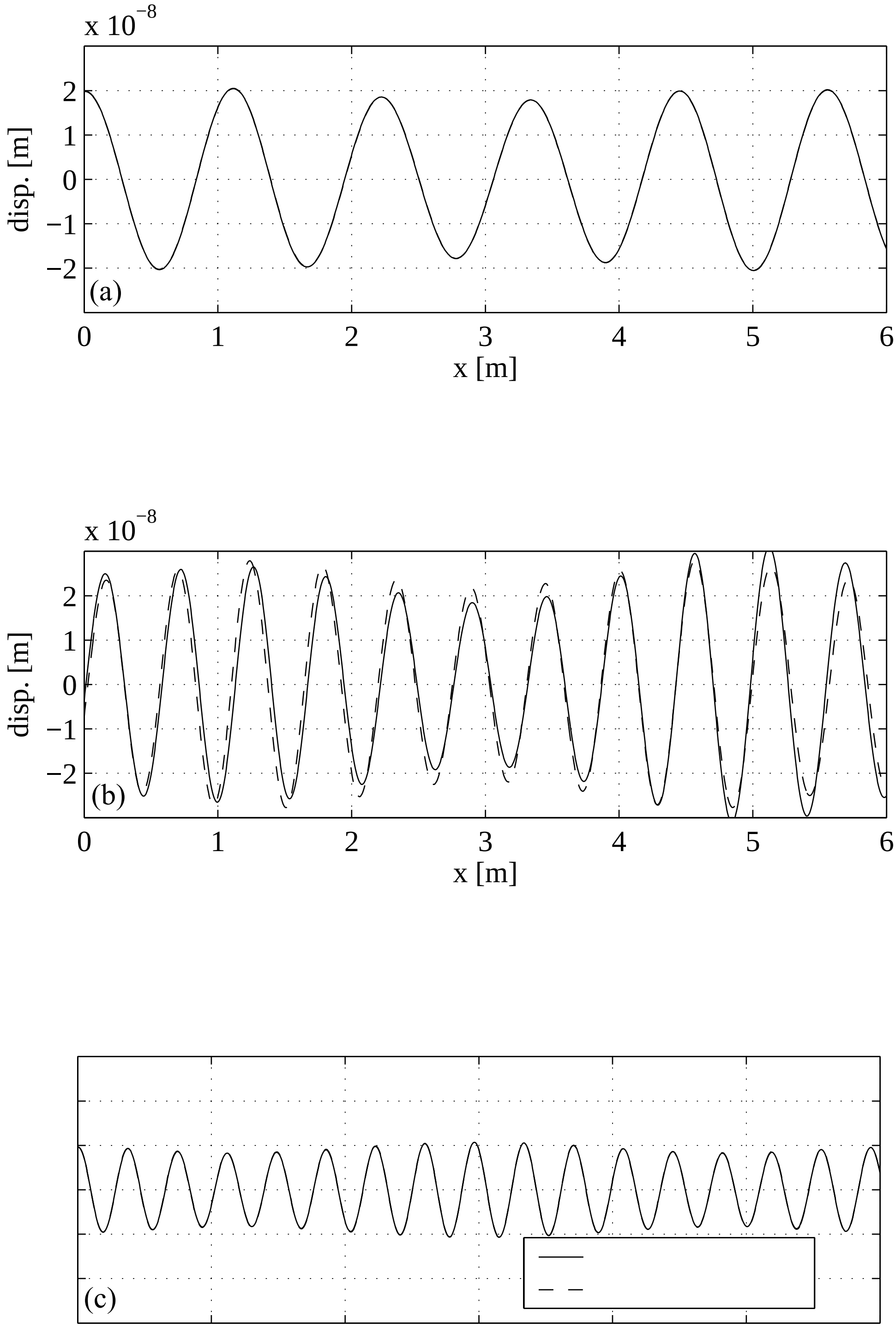

Figure 3.19: Rail displacement under an oscillating moving load calculated by the Periodic-Fourier method and the Modified-phase method for a slab length L=6m and velocity 40 km/hr. The excitation frequency is: (a) 10 Hz, (b) 20 Hz and (c) 30 Hz.

Figure 3.19 provides an additional check to the Modified-phase method. It shows the rail displacement under an oscillating moving load with velocity 40 km/hr and different excitation frequencies. From Figures 3.18 and 3.19, one can see that there is little difference between the results of the exact method, *i.e.* the Periodic-Fourier method and the approximate method, *i.e.* the Modified-phase method around the cut-on frequency. It has been shown so far that the Modified-phase method gives acceptable results to model tracks for typical velocities of underground trains. However, the Periodic-Fourier method will be used for the rest of the calculations in this section, as it gives more accurate results with no significant difference in the running time compared with the Modified-phase method.

Before coupling a train model to the track, it is important to calculate the function $h_{n,q}$ in equation 3.70. In Section 3.2.1, a summary of the Periodic-Fourier method to calculate the rail displacement under a harmonic moving load is given. The procedure is used for a given velocity v and a loading harmonic-number q, to calculate the rail displacement at N discrete space points ($X = 0, \Delta X, 2\Delta X, ..., 1$). These correspond to discrete time points [$t = 0, \Delta X(L/v), 2\Delta X(L/v), ..., (L/v)$]. Using the displacement results at these points, $h_{n,q}$ can be calculated from the following relation

$$h_{n,q} = \frac{v}{L} \sum_{k=1}^{N} a_k [L \cdot Y_1(X_k, X_k)] e^{-\frac{i2\pi q t_k}{(L/v)}} \Delta X(L/v) \tag{3.90}$$

where $a_k = 0.5$ for $k = 1, N$ and $a_k = 1$ for $k = 2, 3, ..., N-1$.

Equation 3.90 is a numerical form of the Fourier series' coefficients, see for example [95] and refer to equation 3.93 below. To satisfy Nyquist criterion

$$\frac{1}{\Delta t} \geq \frac{2q}{(L/v)} \quad \text{or} \quad \Delta X \leq \frac{1}{2q}. \tag{3.91}$$

A Matlab code [75] is developed to analyse the train-track model which is shown in Figure 3.6. The parameters used for the train model are $M_1 = 1000kg$, $M_2 = 2000kg$, $M_3 = 8000kg$ and $k_u = 2000kN/m$. It is found that a value of $s = 10$ is sufficient for convergence of results calculated by equations 3.57-3.60. The code involves computing $h_{n,q}$ for the calculations of equation 3.71 and the following relationship is used to improve the running time

$$h_{-n,-q} = h_{n,q}^{*} \tag{3.92}$$

where $h_{n,q}^{*}$ is the complex conjugate of $h_{n,q}$. In equation 3.71, it is enough to calculate values of $h_{n,q}$ for zero and positive q's, and use equation 3.92 to calculate $h_{n,q}$ for negative q's. In proving equation 3.92, $h_{q,n}$ can be defined from the following equation

$$h_{n,q} = \frac{1}{(L/v)} \int_{0}^{L/v} y_q \cdot e^{-i\omega_n t} dt \tag{3.93}$$

where y_q is the rail displacement under a moving oscillating load with angular frequency ω_q. If the load is oscillating with an angular frequency $\omega_{-q} = -\omega_q$, *i.e.* ($e^{-i\omega_q t} = \cos\omega_q t - \sin\omega_q t$), the displacement y_{-q} is just a complex conjugate of y_q. This is because the load in this case is just the complex conjugate of the load in the first case. Thus, it is possible to write

$$h_{-n,-q} = \frac{1}{(L/v)} \int_{0}^{L/v} y_{-q} \cdot e^{-i\omega_{-n} t} dt = \frac{1}{(L/v)} \int_{0}^{L/v} y_{-q} \cdot e^{i\omega_n t} dt = \frac{1}{(L/v)} \int_{0}^{L/v} [y_q \cdot e^{-i\omega_n t}]^{*} dt$$

and using equation 3.93

$$h_{-n,-q} = [\frac{1}{(L/v)} \int_{0}^{L/v} y_q \cdot e^{-i\omega_n t} dt]^{*} = h_{n,q}^{*} .$$

Figure 3.20 shows the *Dynamic magnification factor* DMF for two values of the suspension damping ratio ζ = 0.1 and 0.5. Results in this figure are calculated by using equation 3.60 to calculate the force at the unsprung-mass–rail interface as a function of time for a given velocity. The maximum and minimum values over the time are recorded, normalised and plotted as shown in the figure. The maximum recorded magnification is about 1%. It should be noted that the value of M_3 does not influence the DMF (see equation 3.63) as it only affects the static component of the force.

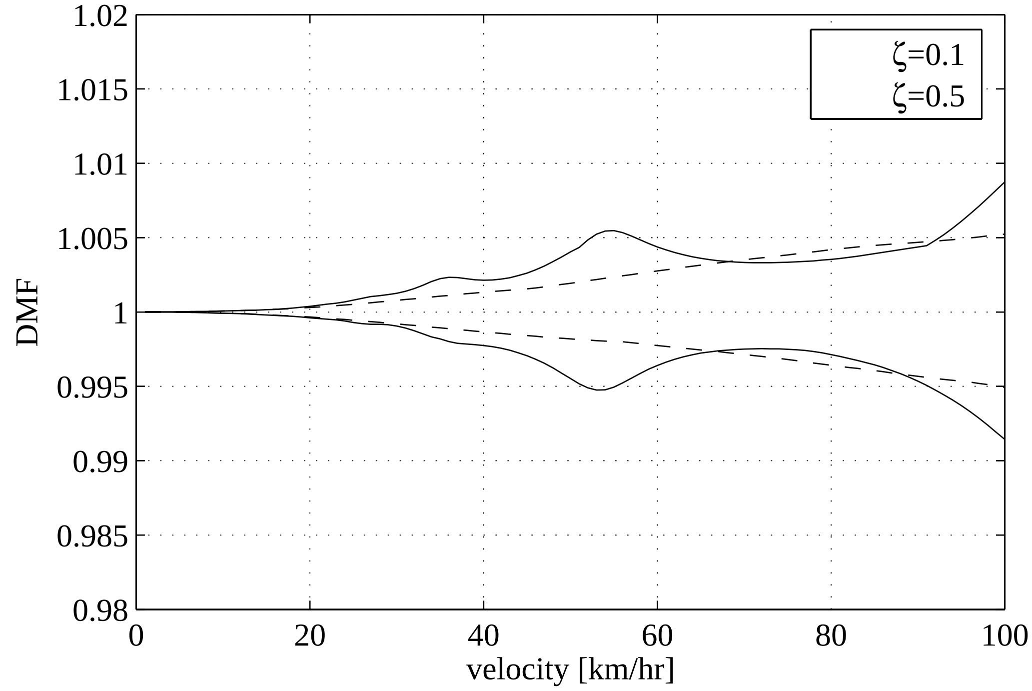

Figure 3.20: Dynamic magnification factor. This gives the maximum and the minimum of the mass-rail forces. These forces are normalised by dividing by $(M_1 + M_2 + M_3)g$. Values greater than 1 are for the maximum DMF, while those below 1 are for minimum DMF.

The figure shows some peaks at velocities 27, 36 and 54 km/hr for $\zeta = 0.1$. These three peaks correspond to the sprung mass resonance, which can be calculated by $f_r = (1/2\pi)\sqrt{k_u / M_2} = 5Hz$. From this frequency, resonance occurs when velocity is equal to $v_r = f_r L / n \quad m/\sec \; = 108/n \quad km/hr$, which agree with the values observed at n=4,3,2. These peaks are attenuated by increasing the damping ratio of the suspension to 0.5.

Figure 3.21 shows the effect of changing the suspension stiffness from $k_u = 2000 \ \ kN/m$ to $k_u = 2000 \times 10^6 \ \ kN/m$. The stiffness in the second case is so high that the train model behaves as a single mass (equal to 1000+2000=3000 kg) moving over the track. The figure shows that the DMF now exceeds 1.01 at velocities near 100km/hr.

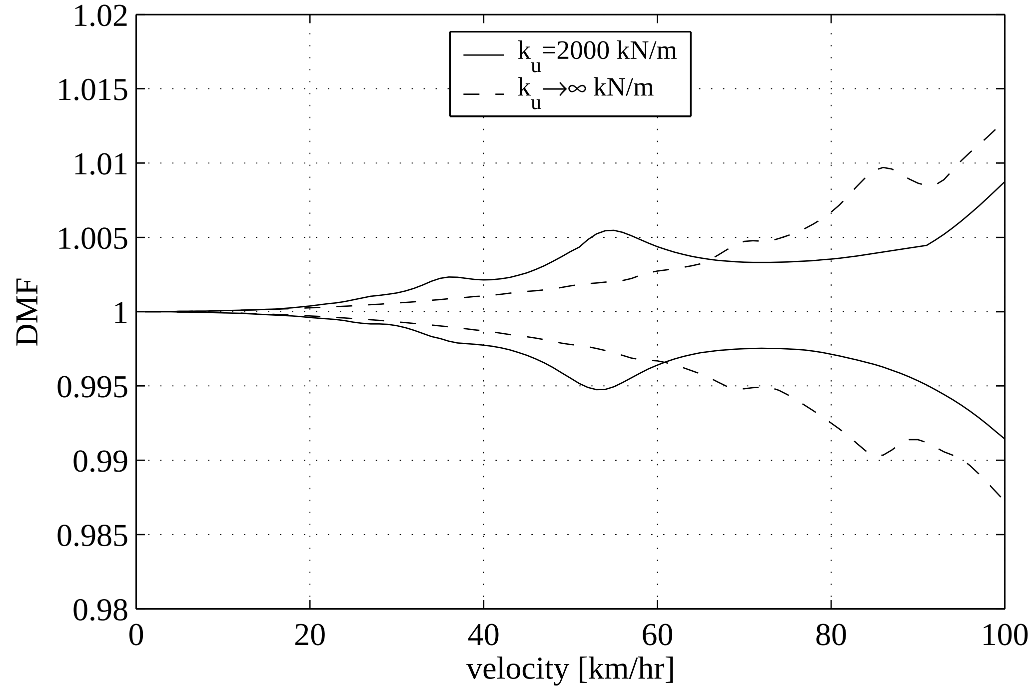

Figure 3.21: Dynamic magnification factor shows the maximum and the minimum of the mass-rail force. These forces are normalised by dividing by $(M_1 + M_2 + M_3)g$. Values greater than 1 are for the maximum DMF, while those below 1 are for minimum DMF.

In Figure 3.21 peaks occur at velocities 70, 87.5km/hr for $k_u = 2000 \times 10^6 \ \ kN/m$. These peaks can be explained by Figure 3.22 which shows the response of a mass $M = 3000kg$ coupled to a track with a discontinuous slab at $X = 0.25$, and excited by a unit harmonic load. The mass displacement is calculated by

$$y_r = \frac{H_r}{1 - M\varpi^2 H_r} e^{i\varpi t} \tag{3.94}$$

where H_r is the rail displacement under a non-moving unit harmonic load applied at $x = XL$ with ϖ excitation frequency.

From Figure 3.22, the first peak occurs at 16.25 Hz and this is the mass-track resonant frequency. Hence peaks are expected in Figure 3.21 at velocities equal to $v_r = f_r L/n \quad m/\sec \; = 329.4/n \quad km/hr$, which agree well with the values calculated at n=4,5.

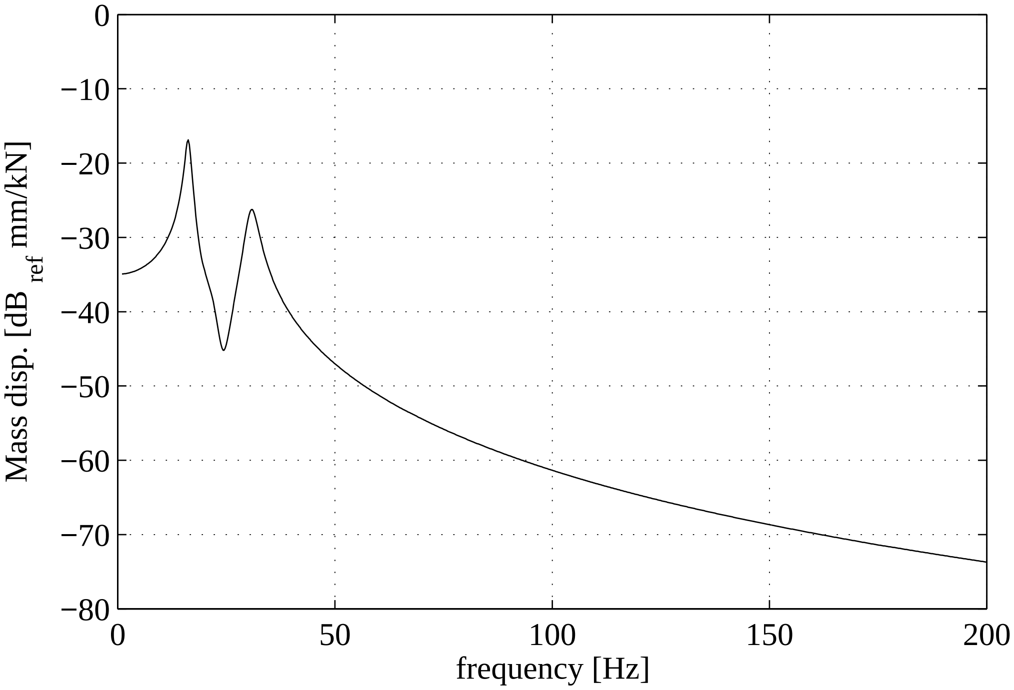

Figure 3.22: Displacement of a mass M=3000kg coupled to a track with a discontinuous slab with L=6m at X=0.25 and excited by a unit non-moving oscillating load.

Conclusions

Floating-slab tracks are modelled in this chapter. The track displacements under oscillating moving loads are calculated for tracks with continuous and discontinuous slabs. The purpose of the work is to calculate forces at the wheel-rail interaction due to moving trains on smooth rail-head.

A track with a continuous slab is modelled using the Fourier transform method. Analysis of the dispersion curves is carried out to identify the track resonant frequencies and the critical load velocity. Power calculations are presented to check the displacement results. It is shown that the input-power for a static moving load is equal to the load velocity multiplied by the slope of the rail deflection under the moving load. The velocity has no significant effect on the quasi-static displacement in the range of velocities 0-80km/hr for typical parameters of a track with a continuous slab. The dynamic effect of velocity on trains moving on such tracks is transient, *i.e.* vanishes after some time from the beginning of the movement. For a train moving with a constant velocity, the forces on the wheel-rail interface are only the quasi-static loads and this is of course in absence of any rail roughness.

Three different methods are presented to analyse tracks with discontinuous slabs. These are the Fourier–Repeating-unit method, the Periodic-Fourier method and the Modified-phase method. These methods may also be used to analyse other periodic infinite structure. The second method, *i.e.* the Periodic-Fourier method, gives accurate results in low running time.

In absence of roughness, slab discontinuity provides a parametric excitation to moving trains. A method is presented to analyse tracks with discontinuous slabs under moving trains with any velocity. However, the method is only used in this chapter for typical velocities of underground trains.

For underground trains, where velocity is less than 100km/hr to allow for train stopping at stations, the force at the wheel-rail interface is increased by 1% of its static value due to slab discontinuity for typical parameters of the train and the track. However, this effect can be more important in the future if faster or heavier-axles trains are used in underground tunnels.

While this chapter has investigated the dynamic effect of slab discontinuity on forces generated at the wheel-rail interface, the effect of slab discontinuity on ground-borne vibration is not considered in this dissertation. The focus of next chapters is on vibration generated by tracks with continuous slabs.

Chapter 4

MODELLING RAILWAY TRACKS IN TUNNELS

Introduction

The aim of this chapter is to develop a three-dimensional model of a railway track in an underground tunnel and to foster a better understanding of the context of vibration from underground railways. As described in Chapter 2, Forrest [29] presents the pipe-in-pipe model, abbreviated as PiP to model an underground tunnel and its surrounding soil. The inner pipe accounts for the tunnel wall which is formulated using the thin shell theory. The outer pipe with infinite outer radius is formulated using the elastic continuum theory and it accounts for the soil modelled as a full-space with a cylindrical cavity. Forrest calculates the displacements of the PiP model for only symmetrical loads (about one of the tunnel axis-of-symmetry in the cross-sectional plane). He couples floating-slab tracks to the PiP model via single line of support to account for bending loads and via two lines to account for the torsion of the slab. However, he assumes that forces are transmitted to the tunnel wall from the track only in the radial direction and does not consider tangential loads on the PiP model. This chapter improves on the work of Forrest by accounting for both the radial and tangential loads. The main features of the new work are:

- the displacements of the PiP model are calculated for anti-symmetrical inputs on the tunnel wall. This allows calculation of the response of the PiP model for tangential forces applied on the tunnel wall;
- three different arrangements of slab bearings are considered. The track is coupled to the PiP model via two lines, three lines and uniform support. This helps identifying the effect of slab connectivity on controlling the vibration propagating from tunnels as will be shown in Chapter 5. The uniform support is used to model the direct fixation case by setting the stiffness of slab bearings to infinity;

- dispersion curves of the PiP model and the track model are investigated. This provides a better understanding of the vibration results due to harmonic loads on the rails.

This chapter is divided into five sections. Section 4.1 presents the model and provides the necessary equations to calculate displacements of the track for different types of support distribution, *i.e.* slab-bearings distribution. Section 4.2 shows the calculation of FRFs, including those for the PiP model. Section 4.3 explains the method used to express the stiffness of slab bearings. Section 4.4 investigates the dispersion characteristics of the model and finally Section 4.5 discusses the code for calculating the soil displacements due to any input loads on the rails.

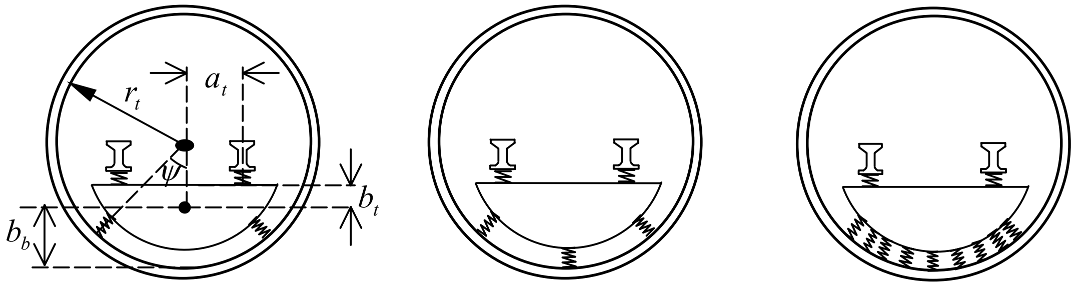

(a) (b) (c)

Figure 4.1: Floating-slab tracks attached to the tunnel wall via: (a) two lines of support, (b) three lines of support and (c) uniform layer. Railpads and slab bearings are continuous along the tunnel.

4.1 Formulation of the model

Three typical distribution of supports, *i.e.* slab bearings are considered in this chapter. Floating slabs are coupled to the tunnel via two lines, three lines or uniform support resulting in three different models. These models are shown in Figure 4.1 (a, b and c) and are analysed in the following three sections respectively. Note that the soil is considered in the formulation but not shown in the figure. The purpose of the analysis is to calculate the displacements of the rails, slab and PiP model in the wavenumber-frequency domain. The reader with little knowledge about coupling in the wavenumber-frequency domain is referred to Appendix B.3, in which a detailed explanation is given by using the method for coupling two Euler-Bernoulli beams to model floating-slab tracks on rigid foundations.

4.1.1 Track with two lines of support

Figure 4.2.a shows the model, where all forces are in the form $F = \tilde{F}e^{i(\omega t + \xi x)}$ and all displacements are in the form $y = \tilde{y}e^{i(\omega t + \xi x)}$. Two forces are applied on the left and the right rails denoted F_1 and F_2 respectively. The rails are assumed to vibrate only vertically and hence each rail has a single degree of freedom. The vertical displacements of the rails are described by y_1 and y_2. The vertical, horizontal and rotational displacements of the slab are described by y_3, y_4 and y_5 respectively.

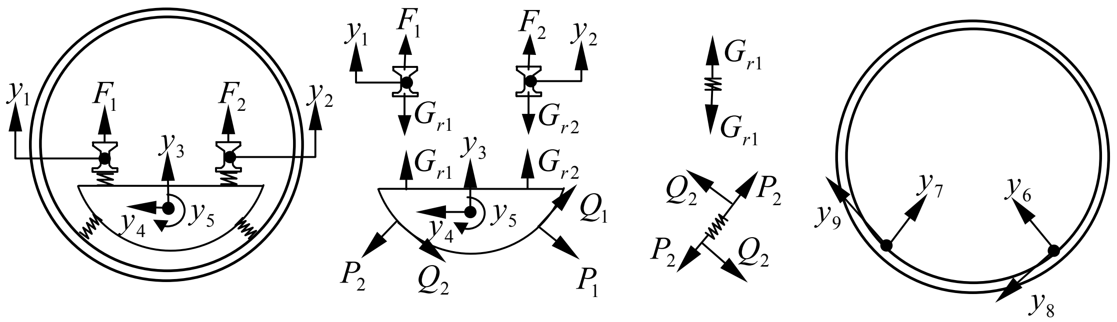

(a) (b) (c) (d)

Figure 4.2: Modelling a track on two lines of support: (a) external forces on the rails and degrees of freedom of the track, (b) free-body diagrams of the rails and the slab, (c) forces on the left railpad and left slab bearings and (d) the tunnel wall displacements at the interface.

Figure 4.2.b shows the forces and displacements on the free body diagrams of the rails and the slab. Figure 4.2.c shows the forces on the left railpads and the left support. The tunnel displacements at the contact points with the slab bearings are shown in Figure 4.2.d. The model has nine degrees of freedom and the input forces are only allowed at two degrees of freedom, *i.e.* on the rails. For given values of $\tilde{F}_1$ and $\tilde{F}_2$, the displacements and

induced forces are calculated by writing the equilibrium and compatibility equations in the wavenumber-frequency domain. Equations of equilibrium of the left and right rails read

$$\tilde{y}_1 = \tilde{H}_r(\tilde{F}_1 - \tilde{G}_{r1}) \tag{4.1}$$

and

$$\tilde{y}_2 = \tilde{H}_r(\tilde{F}_2 - \tilde{G}_{r2}) \tag{4.2}$$

where $\tilde{H}_r$ is the FRF of one of the rails in the vertical direction, as the two rails are identical, $\tilde{G}_{r1}$ and $\tilde{G}_{r2}$ are the forces transmitted to the slab from the left and the right rails respectively. The equations of equilibrium of the slab in the vertical, horizontal and rotational directions are

$$\tilde{y}_3 = \tilde{H}_v(-\tilde{P}_1\cos\psi - \tilde{P}_2\cos\psi + \tilde{Q}_1\sin\psi - \tilde{Q}_2\sin\psi + \tilde{G}_{r1} + \tilde{G}_{r2}), \tag{4.3}$$

$$\tilde{y}_4 = \tilde{H}_h(-\tilde{P}_1\sin\psi + \tilde{P}_2\sin\psi - \tilde{Q}_1\cos\psi - \tilde{Q}_2\cos\psi), \tag{4.4}$$

and

$$\tilde{y}_5 = \tilde{H}_\gamma\{(\tilde{G}_{r1} - \tilde{G}_{r2})a_t - (\tilde{Q}_1 + \tilde{Q}_2)[r_t - (r_t - b_b)\cos\psi] + (\tilde{P}_1 - \tilde{P}_2)(r_t - b_b)\sin\psi\} \tag{4.5}$$

where $\tilde{H}_v$, $\tilde{H}_h$ and $\tilde{H}_\gamma$ are the FRFs of the slab in the vertical, horizontal and rotational directions respectively and their calculations will be shown later, ψ is the central angle of the bearings (see Figure 4.1.a), r_t is inner radius of the tunnel, a_t is the horizontal distance between the slab centre and either the left or the right rail and b_b is the vertical distance between the slab centre and the bottom of the slab. Note that this is equivalent to the distance between the slab center and the tunnel invert as the bearing's height is relatively small.

The equilibrium equations of the railpads are given by

$$\tilde{G}_{r1} = k_r\tilde{y}_1 - k_r\tilde{y}_3 - k_r a_t\tilde{y}_5 \tag{4.6}$$

and

$$\tilde{G}_{r2} = k_r\tilde{y}_2 - k_r\tilde{y}_3 + k_r a_t\tilde{y}_5 \tag{4.7}$$

where k_r is the normal stiffness of the railpads.

The equilibrium equations of the slab bearings are given by

$$\widetilde{P}_1 = k_n[\widetilde{y}_3 \cos\psi + \widetilde{y}_4 \sin\psi - \widetilde{y}_5(r_t - b_b)\sin\psi - \widetilde{y}_6], \tag{4.8}$$

$$\widetilde{P}_2 = k_n[\widetilde{y}_3 \cos\psi - \widetilde{y}_4 \sin\psi + \widetilde{y}_5(r_t - b_b)\sin\psi - \widetilde{y}_7], \tag{4.9}$$

$$\widetilde{Q}_1 = k_s\{-\widetilde{y}_3 \sin\psi + \widetilde{y}_4 \cos\psi + \widetilde{y}_5[r_t - (r_t - b_b)\cos\psi] - \widetilde{y}_8\}, \tag{4.10}$$

and

$$\widetilde{Q}_2 = k_s\{\widetilde{y}_3 \sin\psi + \widetilde{y}_4 \cos\psi + \widetilde{y}_5[r_t - (r_t - b_b)\cos\psi] - \widetilde{y}_9\} \tag{4.11}$$

where k_n and k_s are the normal and shear stiffness respectively of the slab bearings. The equilibrium equations at the inner surface of the tunnel for the PiP model are

$$\widetilde{y}_6 = \widetilde{H}_{6-6}\widetilde{P}_1 + \widetilde{H}_{6-7}\widetilde{P}_2 + \widetilde{H}_{6-8}\widetilde{Q}_1 + \widetilde{H}_{6-9}\widetilde{Q}_2, \tag{4.12}$$

$$\widetilde{y}_7 = \widetilde{H}_{7-6}\widetilde{P}_1 + \widetilde{H}_{7-7}\widetilde{P}_2 + \widetilde{H}_{7-8}\widetilde{Q}_1 + \widetilde{H}_{7-9}\widetilde{Q}_2, \tag{4.13}$$

$$\widetilde{y}_8 = \widetilde{H}_{8-6}\widetilde{P}_1 + \widetilde{H}_{8-7}\widetilde{P}_2 + \widetilde{H}_{8-8}\widetilde{Q}_1 + \widetilde{H}_{8-9}\widetilde{Q}_2, \tag{4.14}$$

and

$$\widetilde{y}_9 = \widetilde{H}_{9-6}\widetilde{P}_1 + \widetilde{H}_{9-7}\widetilde{P}_2 + \widetilde{H}_{9-8}\widetilde{Q}_1 + \widetilde{H}_{9-9}\widetilde{Q}_2 \tag{4.15}$$

where $\widetilde{H}_{j-k}$ is the FRF of the PiP model, which expresses the displacement of the j^{th} degree of freedom for a unit input applied on the k^{th} degree of freedom in the wavenumber-frequency domain. Calculations of these values will be shown in Section 4.2. To solve equations 4.1 to 4.15, they are rewritten in matrix form as follow

$$\widetilde{\mathbf{y}}_{\mathbf{R}} = \widetilde{\mathbf{H}}_{11}\widetilde{\mathbf{G}}_{\mathbf{R}} + \widetilde{\mathbf{H}}_{12}\widetilde{\mathbf{F}}_{\mathbf{R}}, \tag{4.16}$$

$$\widetilde{\mathbf{y}}_{\mathbf{S}} = \widetilde{\mathbf{H}}_{21}\widetilde{\mathbf{P}} + \widetilde{\mathbf{H}}_{22}\widetilde{\mathbf{G}}_{\mathbf{R}}, \tag{4.17}$$

$$\widetilde{\mathbf{G}}_{\mathbf{R}} = \widetilde{\mathbf{H}}_{31}\widetilde{\mathbf{y}}_{\mathbf{R}} + \widetilde{\mathbf{H}}_{32}\widetilde{\mathbf{y}}_{\mathbf{S}}, \tag{4.18}$$

$$\widetilde{\mathbf{P}} = \widetilde{\mathbf{H}}_{41}\widetilde{\mathbf{y}}_{\mathbf{S}} + \widetilde{\mathbf{H}}_{42}\widetilde{\mathbf{y}}_{\mathbf{T}}, \tag{4.19}$$

and

$$\widetilde{\mathbf{y}}_{\mathbf{T}} = \widetilde{\mathbf{H}}_{51}\widetilde{\mathbf{P}} \tag{4.20}$$

where

$$\tilde{\mathbf{y}}_{\mathbf{R}}=[\tilde{y}_1,\tilde{y}_2]^T,\ \tilde{\mathbf{G}}_{\mathbf{R}}=[\tilde{G}_{r1},\tilde{G}_{r2}]^T,\ \tilde{\mathbf{F}}_{\mathbf{R}}=[\tilde{F}_1,\tilde{F}_2]^T,\ \tilde{\mathbf{y}}_{\mathbf{S}}=[\tilde{y}_3,\tilde{y}_4,\tilde{y}_5]^T,$$

$$\tilde{\mathbf{P}}=[\tilde{P}_1,\tilde{P}_2,\tilde{Q}_1,\tilde{Q}_2]^T,\ \tilde{\mathbf{y}}_{\mathbf{T}}=[\tilde{y}_6,\tilde{y}_7,\tilde{y}_8,\tilde{y}_9]^T,\ \mathbf{H}_{11}=\begin{bmatrix}-\tilde{H}_r & 0\\ 0 & -\tilde{H}_r\end{bmatrix},$$

$$\mathbf{H}_{12}=\begin{bmatrix}\tilde{H}_r & 0\\ 0 & \tilde{H}_r\end{bmatrix},$$

$$\tilde{\mathbf{H}}_{21}=\begin{bmatrix}-\tilde{H}_v\cos\psi & -\tilde{H}_v\cos\psi & \tilde{H}_v\sin\psi & -\tilde{H}_v\sin\psi\\ -\tilde{H}_h\sin\psi & \tilde{H}_h\sin\psi & -\tilde{H}_h\cos\psi & -\tilde{H}_h\cos\psi\\ \tilde{H}_\gamma(r_t-b_b)\sin\psi & -\tilde{H}_\gamma(r_t-b_b)\sin\psi & -\tilde{H}_\gamma[r_t-(r_t-b_b)\cos\psi] & -\tilde{H}_\gamma[r_t-(r_t-b_b)\cos\psi]\end{bmatrix},$$

$$\tilde{\mathbf{H}}_{22}=\begin{bmatrix}\tilde{H}_v & \tilde{H}_v\\ 0 & 0\\ \tilde{H}_\gamma a_t & -\tilde{H}_\gamma a_t\end{bmatrix},\ \tilde{\mathbf{H}}_{31}=\begin{bmatrix}k_r & 0\\ 0 & k_r\end{bmatrix},\ \tilde{\mathbf{H}}_{32}=\begin{bmatrix}-k_r & 0 & -k_r a_t\\ -k_r & 0 & k_r a_t\end{bmatrix},$$

$$\tilde{\mathbf{H}}_{41}=\begin{bmatrix}k_n\cos\psi & k_n\sin\psi & -k_n(r_t-b_b)\sin\psi\\ k_n\cos\psi & -k_n\sin\psi & k_n(r_t-b_b)\sin\psi\\ -k_s\sin\psi & k_s\cos\psi & k_s[r_t-(r_t-b_b)\cos\psi]\\ k_s\sin\psi & k_s\cos\psi & k_s[r_t-(r_t-b_b)\cos\psi]\end{bmatrix},\ \tilde{\mathbf{H}}_{42}=\begin{bmatrix}-k_n & 0 & 0 & 0\\ 0 & -k_n & 0 & 0\\ 0 & 0 & -k_s & 0\\ 0 & 0 & 0 & -k_s\end{bmatrix}$$

$$\text{and } \tilde{\mathbf{H}}_{51}=\begin{bmatrix}\tilde{H}_{6-6} & \tilde{H}_{6-7} & \tilde{H}_{6-8} & \tilde{H}_{6-9}\\ \tilde{H}_{7-6} & \tilde{H}_{7-7} & \tilde{H}_{7-8} & \tilde{H}_{7-9}\\ \tilde{H}_{8-6} & \tilde{H}_{8-7} & \tilde{H}_{8-8} & \tilde{H}_{8-9}\\ \tilde{H}_{9-6} & \tilde{H}_{9-7} & \tilde{H}_{9-8} & \tilde{H}_{9-9}\end{bmatrix}.$$

Solving equations 4.19 and 4.20 for $\tilde{\mathbf{P}}$

$$\tilde{\mathbf{P}}=(\mathbf{I}_4-\tilde{\mathbf{H}}_{42}\tilde{\mathbf{H}}_{51})^{-1}\tilde{\mathbf{H}}_{41}\tilde{\mathbf{y}}_{\mathbf{s}} \tag{4.21}$$

where $\mathbf{I}_n$ is the identity matrix of size $n\times n$. Solving equations 4.16 and 4.18 for $\tilde{\mathbf{G}}_{\mathbf{R}}$

$$\tilde{\mathbf{G}}_{\mathbf{R}}=(\mathbf{I}_2-\tilde{\mathbf{H}}_{31}\tilde{\mathbf{H}}_{11})^{-1}(\tilde{\mathbf{H}}_{31}\tilde{\mathbf{H}}_{12}\tilde{\mathbf{F}}_{\mathbf{R}}+\tilde{\mathbf{H}}_{32}\tilde{\mathbf{y}}_{\mathbf{s}}). \tag{4.22}$$

Solving equations 4.22 and 4.17 for $\tilde{\mathbf{y}}_{\mathbf{s}}$ and substituting $\tilde{\mathbf{P}}$ from 4.21

$$\tilde{\mathbf{y}}_{\mathbf{s}} = [\mathbf{I}_3 - \tilde{\mathbf{H}}_{22}(\mathbf{I}_2 - \tilde{\mathbf{H}}_{31}\tilde{\mathbf{H}}_{11})^{-1}\tilde{\mathbf{H}}_{32} - \tilde{\mathbf{H}}_{21}(\mathbf{I}_4 - \tilde{\mathbf{H}}_{42}\tilde{\mathbf{H}}_{51})^{-1}\tilde{\mathbf{H}}_{41}]^{-1}\tilde{\mathbf{H}}_{22}(\mathbf{I}_2 - \tilde{\mathbf{H}}_{31}\tilde{\mathbf{H}}_{11})^{-1}\tilde{\mathbf{H}}_{31}\tilde{\mathbf{H}}_{12}\tilde{\mathbf{F}}_{\mathbf{R}} \,. \tag{4.23}$$

Equations 4.23, 4.21 and 4.20 form the necessary equations to calculate $\tilde{\mathbf{y}}_{\mathbf{s}}$, $\tilde{\mathbf{P}}$ and $\tilde{\mathbf{y}}_{\mathbf{T}}$ respectively.

4.1.2 Track with three lines of support

This model has two more degrees of freedom compared with the previous one. These are the radial and shear displacement of the PiP model at the tunnel invert. The model is shown in Figure 4.3, with three lines of support. The side slab bearings lie at a central angle ψ with the tunnel invert. The procedure followed in Section 4.1.1 is applied here to calculate the displacements for this model. The equivalent set of equations corresponding to equations 4.23, 4.21 and 4.20 is

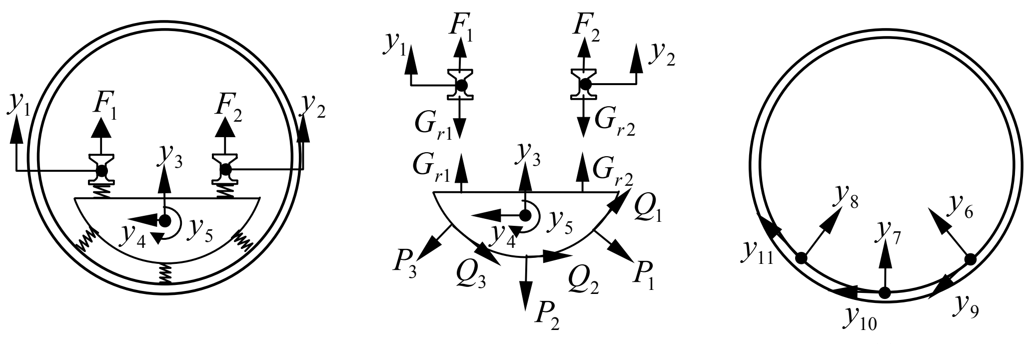

(a) (b) (c)

Figure 4.3: Modelling a track on three lines of support: (a) external forces on the rails and degrees of freedom of the track, (b) free-body diagrams of the rails and the slab and (c) the tunnel wall displacements at the interface.

$$\tilde{\mathbf{y}}_{\mathbf{s}} = [\mathbf{I}_3 - \tilde{\mathbf{H}}_{22}(\mathbf{I}_2 - \tilde{\mathbf{H}}_{31}\tilde{\mathbf{H}}_{11})^{-1}\tilde{\mathbf{H}}_{32} - \tilde{\mathbf{H}}_{21}(\mathbf{I}_6 - \tilde{\mathbf{H}}_{42}\tilde{\mathbf{H}}_{51})^{-1}\tilde{\mathbf{H}}_{41}]^{-1}\tilde{\mathbf{H}}_{22}(\mathbf{I}_2 - \tilde{\mathbf{H}}_{31}\tilde{\mathbf{H}}_{11})^{-1}\tilde{\mathbf{H}}_{31}\tilde{\mathbf{H}}_{12}\tilde{\mathbf{F}}_{\mathbf{R}} \tag{4.24}$$

$$\tilde{\mathbf{P}} = (\mathbf{I}_6 - \tilde{\mathbf{H}}_{42}\tilde{\mathbf{H}}_{51})^{-1}\tilde{\mathbf{H}}_{41}\tilde{\mathbf{y}}_{\mathbf{s}}, \tag{4.25}$$

and

$$\tilde{\mathbf{y}}_{\mathbf{T}} = \tilde{\mathbf{H}}_{51}\tilde{\mathbf{P}} \tag{4.26}$$

where

$$\tilde{\mathbf{H}}_{21} = \begin{bmatrix} -\tilde{H}_v\cos\psi & -\tilde{H}_v & -\tilde{H}_v\cos\psi & \tilde{H}_v\sin\psi & 0 & -\tilde{H}_v\sin\psi \\ -\tilde{H}_h\sin\psi & 0 & \tilde{H}_h\sin\psi & -\tilde{H}_h\cos\psi & -\tilde{H}_h & -\tilde{H}_h\cos\psi \\ \tilde{H}_\gamma(r_t-b_b)\sin\psi & 0 & -\tilde{H}_\gamma(r_t-b_b)\sin\psi & -\tilde{H}_\gamma[r_t-(r_t-b_b)\cos\psi] & -\tilde{H}_\gamma b_b & -\tilde{H}_\gamma[r_t-(r_t-b_b)\cos\psi] \end{bmatrix},$$

$$\tilde{\mathbf{H}}_{41} = \begin{bmatrix} k_n\cos\psi & k_n\sin\psi & -k_n(r_t-b_b)\sin\psi \\ k_n & 0 & 0 \\ k_n\cos\psi & -k_n\sin\psi & k_n(r_t-b_b)\sin\psi \\ -k_s\sin\psi & k_s\cos\psi & k_s[r_t-(r_t-b_b)\cos\psi] \\ 0 & k_s & k_s b_b \\ k_s\sin\psi & k_s\cos\psi & k_n[r_t-(r_t-b_b)\cos\psi] \end{bmatrix},$$

$$\tilde{\mathbf{H}}_{42} = \begin{bmatrix} -k_n & 0 & 0 & 0 & 0 & 0 \\ 0 & -k_n & 0 & 0 & 0 & 0 \\ 0 & 0 & -k_n & 0 & 0 & 0 \\ 0 & 0 & 0 & -k_s & 0 & 0 \\ 0 & 0 & 0 & 0 & -k_s & 0 \\ 0 & 0 & 0 & 0 & 0 & -k_s \end{bmatrix},$$

$$\text{and } \tilde{\mathbf{H}}_{51} = \begin{bmatrix} \tilde{H}_{6-6} & \tilde{H}_{6-7} & \tilde{H}_{6-8} & \tilde{H}_{6-9} & \tilde{H}_{6-10} & \tilde{H}_{6-11} \\ \tilde{H}_{7-6} & \tilde{H}_{7-7} & \tilde{H}_{7-8} & \tilde{H}_{7-9} & \tilde{H}_{7-10} & \tilde{H}_{7-11} \\ \tilde{H}_{8-6} & \tilde{H}_{8-7} & \tilde{H}_{8-8} & \tilde{H}_{8-9} & \tilde{H}_{8-10} & \tilde{H}_{8-11} \\ \tilde{H}_{9-6} & \tilde{H}_{9-7} & \tilde{H}_{9-8} & \tilde{H}_{9-9} & \tilde{H}_{9-10} & \tilde{H}_{9-11} \\ \tilde{H}_{10-6} & \tilde{H}_{10-7} & \tilde{H}_{10-8} & \tilde{H}_{10-9} & \tilde{H}_{10-10} & \tilde{H}_{10-11} \\ \tilde{H}_{11-6} & \tilde{H}_{11-7} & \tilde{H}_{11-8} & \tilde{H}_{11-9} & \tilde{H}_{11-10} & \tilde{H}_{11-11} \end{bmatrix}.$$

All the other matrices and vectors in equations 4.24-4.26, are same as defined in Section 4.1.1.

4.1.3 Track with uniform support

The floating slab in this case is connected to the PiP model via a uniform support as shown in Figure 4.4 with a central angle ψ between the tunnel invert and the bearings end. The normal and shear stiffness of the bearings have units of $N/m/m^2$ rather than $N/m/m$ as in the previous sections. Displacements of the track and the PiP model are calculated by writing the equilibrium equations in the wavenumber-frequency domain.

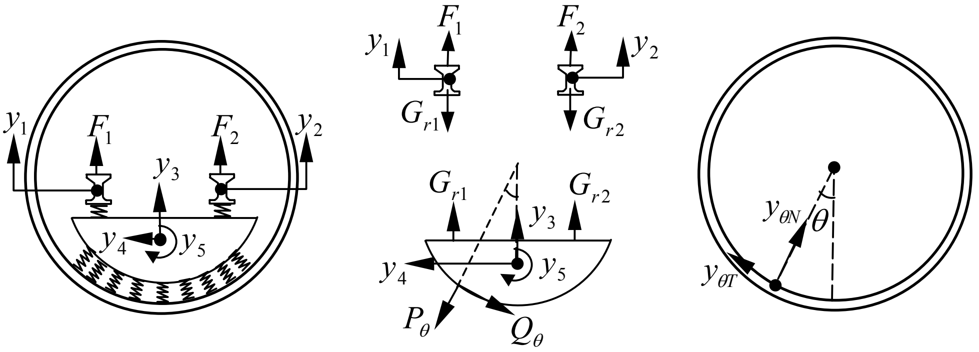

(a) (b) (c)

Figure 4.4: Modelling a track on a uniform support: (a) external forces on the rails and degrees of freedom of the track, (b) free-body diagrams of the rails and the slab and (c) the tunnel wall displacement at angle θ at the interface.

The equilibrium equations of the rails are identical to equations 4.1 and 4.2. The equilibrium equations of the slab are written as

$$\widetilde{y}_3 = \widetilde{H}_v(\widetilde{G}_{r1} + \widetilde{G}_{r2} - \int_{-\psi}^{\psi} \widetilde{P}_\theta \cos\theta \cdot r_t d\theta - \int_{-\psi}^{\psi} \widetilde{Q}_\theta \sin\theta \cdot r_t d\theta)\,, \tag{4.27}$$

$$\widetilde{y}_4 = \widetilde{H}_h(\int_{-\psi}^{\psi} \widetilde{P}_\theta \sin\theta \cdot r_t d\theta - \int_{-\psi}^{\psi} \widetilde{Q}_\theta \cos\theta \cdot r_t d\theta)\,, \tag{4.28}$$

and

$$\widetilde{y}_5 = \widetilde{H}_\gamma\{[\widetilde{G}_{r1} - \widetilde{G}_{r2}] \cdot a_t - \int_{-\psi}^{\psi} \widetilde{P}_\theta (r_t - b_b) \sin\theta \cdot r_t d\theta - \int_{-\psi}^{\psi} \widetilde{Q}_\theta [r_t - (r_t - b_b)\cos\theta] r_t d\theta\} \tag{4.29}$$

where $\tilde{P}_\theta$ and $\tilde{Q}_\theta$ are the induced forces for the PiP model on the tunnel wall at a central angle θ as shown in Figure 4.4.b. The equilibrium equations for the railpads are identical to equations 4.6 and 4.7. The equilibrium equations for slab bearings at angle θ are written as

$$\tilde{P}_\theta = k_n[\tilde{y}_3 \cos\theta - \tilde{y}_4 \sin\theta + \tilde{y}_5 (r_t - b_b)\sin\theta - \tilde{y}_{\theta N}] \tag{4.30}$$

and
$$\tilde{Q}_\theta = k_s\{\tilde{y}_3 \sin\theta + \tilde{y}_4 \cos\theta + \tilde{y}_5 [r_t - (r_t - b_b)\cos\theta] - \tilde{y}_{\theta T}] \tag{4.31}$$

where $\tilde{y}_{\theta N}$ and $\tilde{y}_{\theta T}$ are the displacements of the tunnel wall at a central angle θ as shown in Figure 4.4.c. The equilibrium equations of the PiP model are written as follows

$$\tilde{y}_{\theta N} = (\int_{-\psi}^{\psi} \tilde{P}_\tau \tilde{H}_{\theta\tau}^{NN} \cdot r_t d\tau + \int_{-\psi}^{\psi} \tilde{Q}_\tau \tilde{H}_{\theta\tau}^{NT} \cdot r_t d\tau) \tag{4.32}$$

and
$$\tilde{y}_{\theta T} = (\int_{-\psi}^{\psi} \tilde{P}_\tau \tilde{H}_{\theta\tau}^{TN} \cdot r_t d\tau + \int_{-\psi}^{\psi} \tilde{Q}_\tau \tilde{H}_{\theta\tau}^{TT} \cdot r_t d\tau) \tag{4.33}$$

where $\tilde{H}_{\theta\tau}^{NN}$, $\tilde{H}_{\theta\tau}^{NT}$, $\tilde{H}_{\theta\tau}^{TN}$, $\tilde{H}_{\theta\tau}^{TT}$ are the FRFs of the PiP model and express the displacement at angle θ for a unit load applied at angle τ. The left superscript determines the direction where the load at angle θ is applied. N is normal to the tunnel wall and T is tangential. The right superscript determines the direction of the calculated displacement at angle τ.

The integrations in the previous equations can be performed numerically. The trapezium rule [95] is used, where the collocation points are evenly distributed along the integration path. Equations 4.27-4.29 can be written as

$$\tilde{y}_3 = \tilde{H}_v (\tilde{G}_{r1} + \tilde{G}_{r2} - \sum_{j=1}^{M} c_j \tilde{P}_j \cos\theta_j \cdot r_t \Delta\theta - \sum_{j=1}^{M} c_j \tilde{Q}_j \sin\theta_j \cdot r_t \Delta\theta), \tag{4.34}$$

$$\tilde{y}_4 = \tilde{H}_h (\sum_{j=1}^{M} c_j \tilde{P}_j \sin\theta_j \cdot r_t \Delta\theta - \sum_{j=1}^{M} c_j \tilde{Q}_j \cos\theta_j \cdot r_t \Delta\theta), \text{ and} \tag{4.35}$$

$$\tilde{y}_5 = \tilde{H}_\gamma\{[\tilde{G}_{r1} - \tilde{G}_{r2}]a_t - \sum_{j=1}^{M} c_j \tilde{P}_j (r_t - b_b)\sin\theta_j \cdot r_t\Delta\theta - \sum_{j=1}^{M} c_j \tilde{Q}_j [r_t - (r_t - b_b)\cos\theta_j] r_t\Delta\theta\} \tag{4.36}$$

where M is the number of collocation points, $c_j = 0.5$ for $j = 1, M$ and $c_j = 1$ for all other j, $\Delta\theta = 2\psi/(M-1)$ and $\theta_j = -\psi + (j-1)\Delta\theta$.

Equations 4.32 and 4.33 can be written as

$$\tilde{y}_{iN} = (\sum_{j=1}^{M} c_j \tilde{P}_j \tilde{H}_{ij}^{NN} \cdot r_t\Delta\theta + \sum_{j=1}^{M} c_j \tilde{Q}_j \tilde{H}_{ij}^{NT} \cdot r_t\Delta\theta) \tag{4.37}$$

and

$$\tilde{y}_{iT} = (\sum_{j=1}^{M} c_j \tilde{P}_j \tilde{H}_{ij}^{TN} \cdot r_t\Delta\theta + \sum_{j=1}^{M} c_j \tilde{Q}_j \tilde{H}_{ij}^{TT} \cdot r_t\Delta\theta) \tag{4.38}$$

To calculate the displacements of the track and the PiP model, equations of equilibrium are written in matrix form as done in the previous two sections. Equations 4.16-4.20 can be written again here to calculate the model displacements. Some notation of these equations is different and is defined as

$\tilde{\mathbf{P}} = [\tilde{P}_1, \tilde{P}_2, ..., \tilde{P}_M, \tilde{Q}_1, \tilde{Q}_2, ..., \tilde{Q}_M]^T$, $\tilde{\mathbf{H}}_{21}$ is $3 \times 2M$ matrix and can be written as

$\tilde{\mathbf{H}}_{21} = [\tilde{\mathbf{H}}_{21}^{11}, \tilde{\mathbf{H}}_{21}^{12}]$ where

$$\tilde{\mathbf{H}}_{21}^{11} = r_t\Delta\theta \cdot \begin{bmatrix} -c_1 H_v \cos\theta_1 & -c_2 H_v \cos\theta_2 & ... & -c_M H_v \cos\theta_M \\ c_1 H_h \sin\theta_1 & c_2 H_h \sin\theta_2 & ... & c_M H_h \sin\theta_M \\ -c_1 \tilde{H}_\gamma (r_t - b_b)\sin\theta_1 & -c_2 \tilde{H}_\gamma (r_t - b_b)\sin\theta_2 & ... & -c_M \tilde{H}_\gamma (r_t - b_b)\sin\theta_M \end{bmatrix},$$

$$\tilde{\mathbf{H}}_{21}^{12} = r_t\Delta\theta \cdot \begin{bmatrix} -c_1 H_v \sin\theta_1 & -c_2 H_v \sin\theta_2 & ... & -c_M H_v \sin\theta_M \\ -c_1 H_h \cos\theta_1 & -c_2 H_h \cos\theta_2 & ... & -c_M H_h \cos\theta_M \\ -c_1 \tilde{H}_\gamma [r_t - (r_t - b_b)\cos\theta_1] & -c_2 \tilde{H}_\gamma [r_t - (r_t - b_b)\cos\theta_2] & ... & -c_M \tilde{H}_\gamma [r_t - (r_t - b_b)\cos\theta_M] \end{bmatrix}$$

$\tilde{\mathbf{H}}_{41}$ is $2M \times 3$ matrix and can be written as

$$\tilde{\mathbf{H}}_{41} = \begin{bmatrix} \tilde{\mathbf{H}}_{41}^{11} \\ \tilde{\mathbf{H}}_{41}^{21} \end{bmatrix} \text{ where}$$

$$\widetilde{\mathbf{H}}_{41}^{11} = k_n \cdot \begin{bmatrix} \cos\theta_1 & -\sin\theta_1 & (r_t - b_b)\sin\theta_1 \\ \cos\theta_2 & -\sin\theta_2 & (r_t - b_b)\sin\theta_2 \\ \vdots & \vdots & \vdots \\ \cos\theta_M & -\sin\theta_M & (r_t - b_b)\sin\theta_M \end{bmatrix},$$

$$\widetilde{\mathbf{H}}_{41}^{21} = k_s \cdot \begin{bmatrix} \sin\theta_1 & \cos\theta_1 & r_t - (r_t - b_b)\cos\theta_1 \\ \sin\theta_2 & \cos\theta_2 & r_t - (r_t - b_b)\cos\theta_2 \\ \vdots & \vdots & \vdots \\ \sin\theta_M & \cos\theta_M & r_t - (r_t - b_b)\cos\theta_M \end{bmatrix},$$

$\widetilde{\mathbf{H}}_{42}$ is $2M \times 2M$ matrix and can be written as

$$\widetilde{\mathbf{H}}_{42} = \begin{bmatrix} \widetilde{\mathbf{H}}_{42}^{11} & \widetilde{\mathbf{H}}_{42}^{12} \\ \widetilde{\mathbf{H}}_{42}^{21} & \widetilde{\mathbf{H}}_{42}^{22} \end{bmatrix}$$

where $\widetilde{\mathbf{H}}_{42}^{11} = -k_n \mathbf{I}_{2M}$, $\widetilde{\mathbf{H}}_{42}^{12} = \mathbf{Z}(M,M)$, $\widetilde{\mathbf{H}}_{42}^{21} = \mathbf{Z}(M,M)$ and $\widetilde{\mathbf{H}}_{42}^{22} = -k_s I_{2M}$. $\mathbf{Z}(M,M)$ is $M \times M$ matrix with zero elements.

$\widetilde{\mathbf{H}}_{51}$ is $2M \times 2M$ matrix and can be written as

$$\widetilde{\mathbf{H}}_{51} = \begin{bmatrix} \widetilde{\mathbf{H}}_{51}^{11} & \widetilde{\mathbf{H}}_{51}^{12} \\ \widetilde{\mathbf{H}}_{51}^{21} & \widetilde{\mathbf{H}}_{51}^{22} \end{bmatrix} \text{ where}$$

$$\widetilde{\mathbf{H}}_{51}^{11} = r_t \Delta\theta \cdot \begin{bmatrix} c_1 H_{11}^{NN} & c_2 H_{12}^{NN} & \ldots & c_M H_{1M}^{NN} \\ c_1 H_{21}^{NN} & c_2 H_{22}^{NN} & \ldots & c_M H_{2M}^{NN} \\ \vdots & \vdots & \vdots & \vdots \\ c_1 H_{M1}^{NN} & c_2 H_{M2}^{NN} & \cdots & c_{MM} H_{MM}^{NN} \end{bmatrix}$$

$$\widetilde{\mathbf{H}}_{51}^{12} = r_t \Delta\theta \cdot \begin{bmatrix} c_1 H_{11}^{NT} & c_2 H_{12}^{NT} & \ldots & c_M H_{1M}^{NT} \\ c_1 H_{21}^{NT} & c_2 H_{22}^{NT} & \ldots & c_M H_{2M}^{NT} \\ \vdots & \vdots & \vdots & \vdots \\ c_1 H_{M1}^{NT} & c_2 H_{M2}^{NT} & \cdots & c_{MM} H_{MM}^{NT} \end{bmatrix}$$

$$\widetilde{\mathbf{H}}_{51}^{21} = r_t \Delta\theta \cdot \begin{bmatrix} c_1 H_{11}^{TN} & c_2 H_{12}^{TN} & \dots & c_M H_{1M}^{TN} \\ c_1 H_{21}^{TN} & c_2 H_{22}^{TN} & \dots & c_M H_{2M}^{TN} \\ \vdots & \vdots & \vdots & \vdots \\ c_1 H_{M1}^{TN} & c_2 H_{M2}^{TN} & \cdots & c_{MM} H_{MM}^{TN} \end{bmatrix}$$

$$\widetilde{\mathbf{H}}_{51}^{22} = r_t \Delta\theta \cdot \begin{bmatrix} c_1 H_{11}^{TT} & c_2 H_{12}^{TT} & \dots & c_M H_{1M}^{TT} \\ c_1 H_{21}^{TT} & c_2 H_{22}^{TT} & \dots & c_M H_{2M}^{TT} \\ \vdots & \vdots & \vdots & \vdots \\ c_1 H_{M1}^{TT} & c_2 H_{M2}^{TT} & \cdots & c_{MM} H_{MM}^{TT} \end{bmatrix}$$

The model displacements can now be calculated from the following equations (compare with equations 4.24-4.26)

$$\widetilde{\mathbf{y}}_{\mathbf{s}} = [\mathbf{I}_3 - \widetilde{\mathbf{H}}_{22}(\mathbf{I}_2 - \widetilde{\mathbf{H}}_{31}\widetilde{\mathbf{H}}_{11})^{-1}\widetilde{\mathbf{H}}_{32} - \widetilde{\mathbf{H}}_{21}(\mathbf{I}_{2M} - \widetilde{\mathbf{H}}_{42}\widetilde{\mathbf{H}}_{51})^{-1}\widetilde{\mathbf{H}}_{41}]^{-1}\widetilde{\mathbf{H}}_{22}(\mathbf{I}_2 - \widetilde{\mathbf{H}}_{31}\widetilde{\mathbf{H}}_{11})^{-1}\widetilde{\mathbf{H}}_{31}\widetilde{\mathbf{H}}_{12}\widetilde{\mathbf{F}}_{\mathbf{R}}, \tag{4.39}$$

$$\widetilde{\mathbf{P}} = (\mathbf{I}_{2M} - \widetilde{\mathbf{H}}_{42}\widetilde{\mathbf{H}}_{51})^{-1}\widetilde{\mathbf{H}}_{41}\widetilde{\mathbf{y}}_{\mathbf{s}}, \tag{4.40}$$

and

$$\widetilde{\mathbf{y}}_{\mathbf{T}} = \widetilde{\mathbf{H}}_{51}\widetilde{\mathbf{P}}. \tag{4.41}$$

4.2 Evaluation of FRFs

To calculate the displacements at a given wavenumber and angular frequency (ξ, ω) for any of the models described in the previous sections, values of FRFs are to be calculated firstly at the same wavenumber and angular frequency. FRFs of the rails and the slab are calculated using Euler-Bernoulli beam theory. FRFs of the coupled tunnel and the surrounding soil are calculated using the PiP model.

4.2.1 FRFs of the rails and slab

The rails and the slab are modelled as Euler-Bernoulli beams. The governing differential equation for an infinite Euler-Bernoulli beam subjected to external torque $T(x,t)$ is given by

$$J\frac{\partial^2\gamma}{\partial t^2} - GK\frac{\partial^2\gamma}{\partial x^2} = T(x,t) \tag{4.42}$$

where GK is the torsional rigidity of the beam (G is the shear modulus, K is the torsion constant of the beam section), J is the polar moment of inertia. Transforming this equation to the wavenumber-frequency domain using equations A.1 and A.2 results in

$$-J\omega^2\tilde{\gamma} + GK\xi^2\tilde{\gamma} = \tilde{T} . \tag{4.43}$$

The FRF for the beam torsion is defined as the beam rotation for a unit torque in the wavenumber-frequency domain. Applying this definition results in

$$H_\gamma = \frac{\tilde{\gamma}}{\tilde{T}} = \frac{1}{GK\xi^2 - J\omega^2} . \tag{4.44}$$

Calculation of the bending FRF of the beam is shown in Appendix B and given by equation B.26.

4.2.2 FRFs of the PiP model

Unlike FRFs of beams, calculating FRFs of the PiP model are not straightforward. This is because another coordinate is involved in the calculations. This coordinate is θ and it describes the variation around the tunnel. There are two types of FRFs according to the input load. In the first type, the input load is applied radially to the tunnel wall, for instance to calculate $\tilde{H}_{6-6}$, $\tilde{H}_{7-6}$, $\tilde{H}_{8-6}$ and $\tilde{H}_{9-6}$ in Section 4.1.1 (see Figure 4.2.d). In the second type, the input load is applied tangentially to the tunnel wall, for instance to calculate $\widetilde{H}_{6-8}$, $\widetilde{H}_{7-8}$, $\widetilde{H}_{8-8}$ and $\widetilde{H}_{9-8}$ in Section 4.1.1 (see Figure 4.2.d). The difference between the two types is that the load and displacements in the first type decompose into symmetrical-sinusoidal Fourier-series-components, while the second results in anti-symmetrical–sinusoidal Fourier-series-components about the axis-of-symmetry of the PiP model at the load position. To explain this point, consider calculations of $\widetilde{H}_{7-8}$. This FRF can be evaluated by the following:

- apply a unit force in the position and the direction of y_8 (see Figure 4.2.d) in the form $F(x,t) = 1.e^{(i\xi x+\omega t)}$;
- calculate the displacement in the position and the direction of y_7 (see Figure 4.2.d). The displacement takes the form $y_7(x,t) = \widetilde{H}_{78}.e^{(i\xi x+\omega t)}$.

As discussed in Appendix B, a unit load in the wavenumber-frequency domain at [$\xi = \overline{\xi}$ and $\omega = \overline{\omega}$] corresponds to a load with space and time variation $e^{(i\overline{\xi}x+\overline{\omega}t)}$ in the space-time domain. Transforming the quantity $[1\cdot\delta(\xi-\overline{\xi})\cdot\delta(\omega-\overline{\omega})]$ to the space-time domain confirms this result.

To include the variation around the tunnel wall, the load $F(x,t) = 1.e^{(i\xi x+\omega t)}$ can be written in a vector form to express the longitudinal, the tangential and the radial load distribution in terms of θ as

$$\mathbf{F}(x,\theta,t) = \begin{bmatrix} 0 \\ \delta(\theta)/r_t \\ 0 \end{bmatrix} .e^{(i\xi x+\omega t)} \tag{4.45}$$

where θ is measured in a clockwise direction and is equal to zero at the position of the applied load. The distribution with respect to θ can be written as a summation of Fourier series, see [95] for example, with periodicity 2π. This is because the load does not change by moving from θ to $\theta+2\pi$ around the tunnel. Thus equation 4.45 can be written as

$$\mathbf{F}(x,\theta,t)=\sum_{n=0}^{\infty}\begin{bmatrix} c_{xn}\sin n\theta \\ c_{\theta n}\cos n\theta \\ c_{rn}\sin n\theta \end{bmatrix} e^{i(\xi x+\omega t)} \tag{4.46}$$

where $c_{\theta 0}=\dfrac{1}{2\pi\cdot r_t}$ and $c_{\theta n}=\dfrac{1}{\pi\cdot r_t}$ for n=1,2…∞, $c_{xn}=0$ and $c_{rn}=0$ for all n.

It should be noted that the load components in equation 4.46 for a given cross-sectional wavenumber n, is anti-symmetrical about $\theta=0$ and is identified in this context as the second loading combination. The first loading combination, *i.e.* a symmetrical input load, is calculated by replacing any $\cos n\theta$ in equation 4.46 by $\sin n\theta$ and vice versa. For general anti-symmetrical stresses applied on the PiP model in the form

$$\mathbf{q}(x,\theta,t)=\begin{bmatrix} q_x \\ q_\theta \\ q_r \end{bmatrix}=\begin{bmatrix} \tilde{q}_x(n,\xi,\omega)\cdot\sin n\theta \\ \tilde{q}_\theta(n,\xi,\omega)\cdot\cos n\theta \\ \tilde{q}_r(n,\xi,\omega)\cdot\sin n\theta \end{bmatrix}.e^{(i\xi x+\omega t)}. \tag{4.47}$$

The displacement of the PiP model at the inner surface of the tunnel wall can be written in the form

$$\mathbf{u}(x,\theta,t)=\begin{bmatrix} u_x \\ u_\theta \\ u_r \end{bmatrix}=\begin{bmatrix} \tilde{u}_x(n,\xi,\omega)\cdot\sin n\theta \\ \tilde{u}_\theta(n,\xi,\omega)\cdot\cos n\theta \\ \tilde{u}_r(n,\xi,\omega)\cdot\sin n\theta \end{bmatrix}.e^{(i\xi x+\omega t)}. \tag{4.48}$$

Figure 4.5 shows the sign convention for the stresses and displacements in equation 4.47 and 4.48. It also shows the composition of a tangential load applied at the tunnel invert into its Fourier components. The PiP model displacements due to the load in equation 4.46 can be calculated using equations 4.47 and 4.48 for each n, in which $\tilde{u}_x$, $\tilde{u}_\theta$ and $\tilde{u}_z$ are significant. The total displacement is calculated by summing the displacements for all values of n. The PiP model displacement given by equation 4.48 decreases by increasing the value of n and hence a limited number of n should be included in the calculations to get a converged solution. Further details about the calculations of anti-symmetrical displacements in the form of equation 4.48 due to input stresses in the form of equation 4.47 are given in Appendix C.

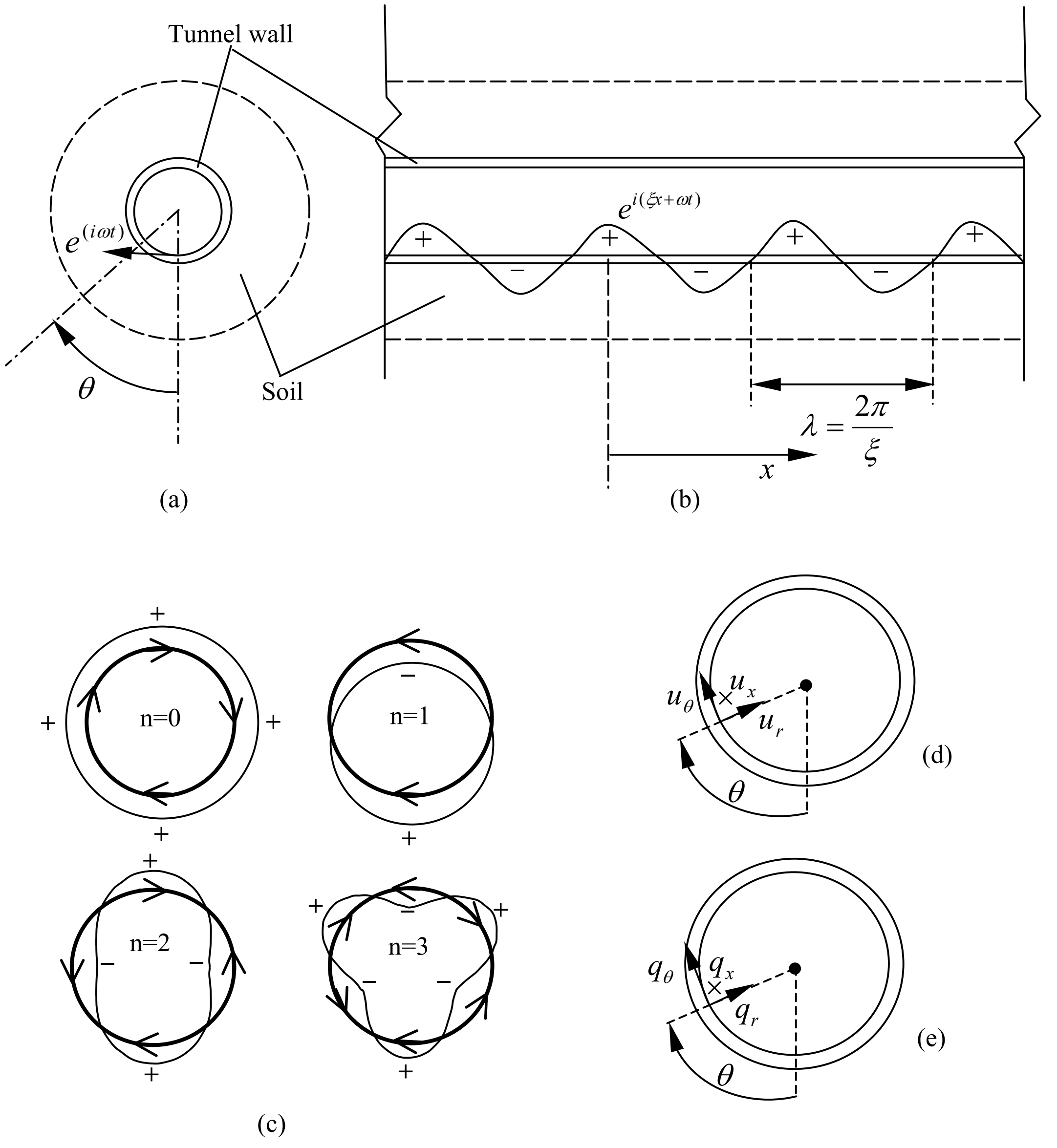

Figure 4.5: Schematic showing the decomposition of a load $e^{i(\omega t+\xi x)}$ applied tangentially at the tunnel invert. (a) and (b) show the spatial distribution of the load, (c) shows the steady state and the first three Fourier components of the load. (d) and (e) show the sign convention of the displacements and stresses respectively. The cross sign means perpendicular to the page, into it.

4.3 Stiffness of slab bearings

The stiffness of slab bearings is expressed in terms of the vertical natural frequency of the slab modelled as a beam on Winkler foundation, where the foundation stiffness is equal to the stiffness of the slab bearings. This is a widely accepted way in the industry to describe floating-slab tracks. A f_n Hz floating slab is a slab that has a cut-on frequency at f_n Hz for a rigid tunnel wall. It should be noted that in reality the vertical cut-on frequency of the slab is shifted due to the influence of the rails, tunnel and ground, which are not considered when calculating the cut-on frequency. However, this shift is typically small for soft slab bearings and much lighter rails compared with the slab. For a floating slab with a mass m_s and vertical stiffness of slab bearings k_v, the cut-on frequency is calculated from the following relationship

$$f_n = \frac{1}{2\pi}\sqrt{\frac{k_v}{m_s}}\,. \tag{4.49}$$

Using equation 4.49 for the models shown in Figure 4.6, the natural frequency of the floating slabs are calculated by:

for two lines of support

$$f_n = \frac{1}{2\pi}\sqrt{\frac{k_n(2\cos^2\psi + 2\Re\sin^2\psi)}{m_s}}\,; \tag{4.50}$$

for three lines of support

$$f_n = \frac{1}{2\pi}\sqrt{\frac{k_n(2\cos^2\psi + 1 + 2\Re\sin^2\psi)}{m_s}}\,; \tag{4.51}$$

for uniform support

$$f_n = \frac{1}{2\pi}\sqrt{\frac{r_t k_n[\psi(1+\Re)+0.5(1-\Re)\sin 2\psi]}{m_s}} \tag{4.52}$$

where $\Re$ is the ratio of the shear stiffness to the normal stiffness of the slab bearings, *i.e.* $\Re = k_s / k_n$.

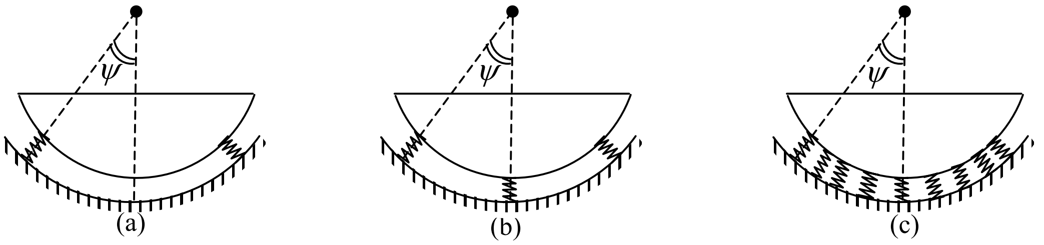

Figure 4.6: 2D models of floating slabs connected to the tunnel wall via: (a) two lines of support, (b) three lines of support and (c) uniform support.

4.4 Dispersion characteristics of the model

In this section, FRFs of the model are investigated by studying the dispersion characteristics of the PiP model and the track on rigid foundation model. It is useful before that to study the dispersion behaviour of the separate components of the PiP model, *i.e.* the free tunnel modelled as a thin shell and the free soil modelled as a full-space with a cylindrical cavity. The reader is referred to Appendix B which provides a good introduction about wave propagation and dispersion equations by modelling a track as double beams on rigid foundation.

Table 4.1 shows the parameters of the tunnel, soil and track, which are used for the analysis in the following sections. The parameters used in the table are defined as follows: E is the Elastic modulus; ν is Poisson's ratio; ρ is the density; r_c is the cavity radius; λ

and μ are Lame's constants; c_p and c_s are the compression and shear wave velocities; r_t is the tunnel inner radius and h is the tunnel thickness. The track parameters are defined in Section 4.1.

Soil	Tunnel	Track
$E = 550 \times 10^6 Pa$ $\nu = 0.44$ $\rho = 2000 kg/m^3$ $r_c = 3.00m$ $\lambda = 1.4 \times 10^9 Pa$ $\mu = 191 \times 10^6 Pa$ $c_p = 944 m/s$ $c_s = 309 m/s$	$E = 50 \times 10^9 Pa$ $\nu = 0.3$ $\rho = 2500 kg/m^3$ $r_t = 2.75m$ $h = 0.25m$ $\lambda = 28.8 \times 10^9 Pa$ $\mu = 19.2 \times 10^9 Pa$ $c_p = 5189 m/s$ $c_s = 2774 m/s$	$EI_r = 5 \times 10^6 Pa \cdot m^4$ $m_r = 50 kg/m$ $k_r = 20 \times 10^6 N/m/m$ $EI_v = 1430 \times 10^6 Pa \cdot m^4$ $EI_h = 41699 \times 10^6 Pa.m^4$ $m_s = 3500 kg/m$ $GK = 1.875 \times 10^9 Pa \cdot m^4$ $J = 1310 kg \cdot m^2/m$ $a_t = 0.75m$ $b_t = 0.2m$ $b_b = 0.3m$ $\Re$ =1.0 for $f_n \to \infty$ and $\Re$ =0.5 otherwise

Table 4.1: Parameter values used to model a railway track in a tunnel.

4.4.1 Dispersion characteristics of the PiP model

This section is divided into three parts discussing the solution of the dispersion equations for: the tunnel wall modelled as a thin shell, the surrounding soil modelled as a thick shell (using the elastic continuum theory) and the coupled tunnel wall and soil.

The tunnel wall modelled as a thin shell

The equilibrium equation of a thin cylindrical shell in the wavenumber-frequency domain is given by

$$[\mathbf{A}]\begin{bmatrix}\tilde{u}_{xn}\\ \tilde{u}_{\theta n}\\ \tilde{u}_{rn}\end{bmatrix}=\frac{-r_a(1-\nu^2)}{Eh}\begin{bmatrix}\tilde{q}_{xn}\\ \tilde{q}_{\theta n}\\ \tilde{q}_{rn}\end{bmatrix} \tag{4.53}$$

where $\mathbf{A}=\mathbf{A}_1$ for the first loading combination, *i.e.* symmetrical input and $\mathbf{A}=\mathbf{A}_2$ for the second loading combination, *i.e.* anti-symmetrical input. The elements of $\mathbf{A}_2$ are calculated by the author and given in Appendix C, while the elements of $\mathbf{A}_1$ are calculated by Forrest [29] and can be written in terms of $\mathbf{A}_2$ elements (see equation C.4) as follows

$$\mathbf{A}_1=\begin{bmatrix}1 & -1 & 1\\ -1 & 1 & -1\\ 1 & -1 & 1\end{bmatrix}*\mathbf{A}_2 \tag{4.54}$$

where $(*)$ means an element to element multiplication. The unforced vibration (free vibration) solution of equation 4.53 is calculated by setting the stress vector to zero, this results in two possible solutions:

- a trivial solution, *i.e.* $\tilde{u}_{xn}=0$, $\tilde{u}_{\theta n}=0$, $\tilde{u}_{rn}=0$;
- a non-trivial solution, $D(\xi,\omega)=|\mathbf{A}|=0$. (4.55)

It can be shown that the determinants of $\mathbf{A}_1$ and $\mathbf{A}_2$ are identical. Calculating the determinants of both the matrices can prove this. It can be alternatively proved by using the following determinants property. For two square matrices $\mathbf{B}$ and $\mathbf{G}$ of the same size, if $\mathbf{B}$ results from multiplying one of $\mathbf{G}$'s rows or columns by a constant c, then the relationship between the determinants of the two matrices is, see [106] for example

$$|\mathbf{B}| = c \cdot |\mathbf{G}| . \tag{4.56}$$

Note that $\mathbf{A}_1$ is calculated by multiplying the second row and then the second column of $\mathbf{A}_2$ by –1 and hence the two matrices have the same determinant. Equation 4.55 is known as the dispersion equation. This equation can be written as a polynomial of the eighth degree as

$$D(\xi,\omega) = a_1\xi^8 + a_2\xi^6 + a_3\xi^4 + a_4\xi^2 + a_5 \tag{4.57}$$

where a_1, a_2, a_3, a_4 and a_5 are real quantities (for no damping) and are functions of the angular frequency ω, the cross-sectional wavenumber *n* and the shell parameters.

For given *n* and ω, there are 8 roots for equation 4.57. If ξ is a root, $-\xi$ is also a root due to absence of odd powers in (4.57). Also ξ^* is another root because the coefficients a_1, a_2, $\dots a_5$ are real quantities. This means for each root ξ, there are three other roots $[-\xi, \xi^*, -\xi^*]$.

Figure 4.7 shows the solutions of the dispersion equation calculated by Matlab [75] built-in function “roots” for the tunnel parameters given in Table 4.1. For *n*=0, there are no evanescent waves at the frequency range of interest. Two non-dispersive waves can propagate freely at all frequencies: the compression wave and the shear wave (torsional wave). The compression wave propagates with phase velocity equal to $\sqrt{E/\rho}$ = 4472 m/s and this is equal to the pressure wave velocity of cylinders [38] and is slower than the velocity of compression wave in a full-space (5189m/s) with the same material properties as the shell (see Table 4.1). This is because Poisson’s effect is restraint in a full-space while it is not in the shell case. Unlike the compression wave, the torsional wave propagates with velocity equal to the shear wave velocity in a full-space, which is equal to 2774 m/s.

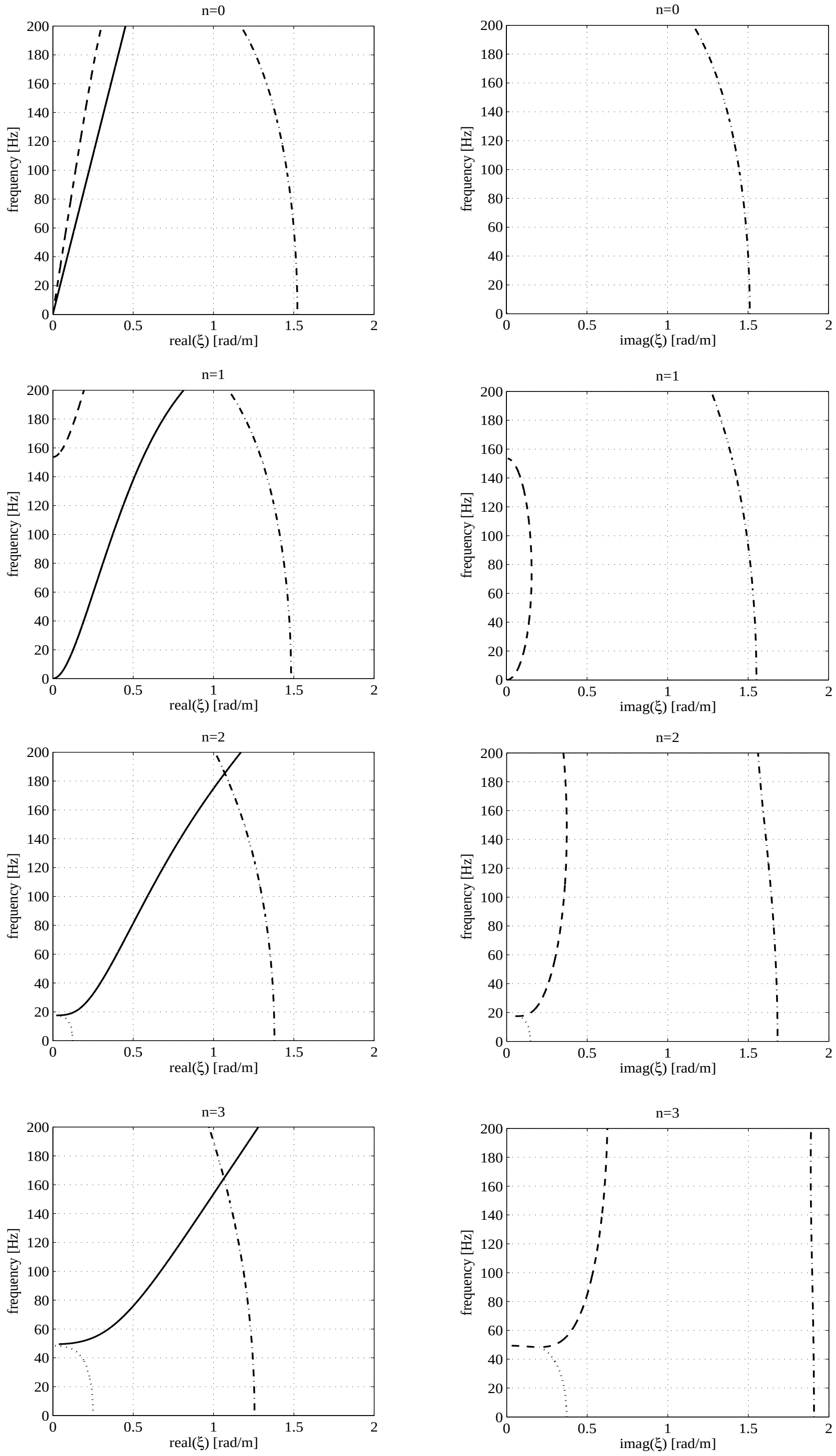

Figure 4.7: Solutions of the dispersion equation of a thin shell, where only roots in the first quarter of the complex wavenumbers for $n = [0,1,2,3]$ are plotted. The left column of subfigures shows the real part of the roots, where the right column shows the imaginary part of the roots. Each root is plotted with different line style, *i.e.* (-), (--), (-.) and (..).

For *n*=1, there are propagating waves at all frequencies while evanescent waves exist below 153.5 Hz with wavenumbers smaller than 0.16 rad/m. Leaky waves exist at all frequencies. The real parts of wavenumbers associated with the leaky waves are greater than the wavenumbers of the propagating waves and hence leaky waves have smaller wavelengths compared with the propagating waves. The imaginary parts of wavenumbers associated with the leaky waves are greater than wavenumbers for evanescent waves and hence they are much attenuated. At 153.6 Hz there is a cut-on frequency, above which two waves with different wavelengths propagate. The case for *n*=2 is important, because it is the minimum cross-sectional wavenumber in which waves do not propagate below a certain frequency (17.5 Hz in this case).

Figure 4.8 shows the dispersion curves for all values of *n*. For values of *n* greater than 5, waves cannot propagate freely within the frequency range of interest. The curves in Figure 4.8 are assembled using the real solutions for the range *n*=0-5. As shown in Chapter 3, dispersion curves are of particular interest, as FRFs in the wavenumber-frequency domain exhibit peaks (or infinite response in absence of damping) at wavenumbers and angular frequencies along these curves. Also the velocity lines can be constructed to identify the peaks in the space-time domain.

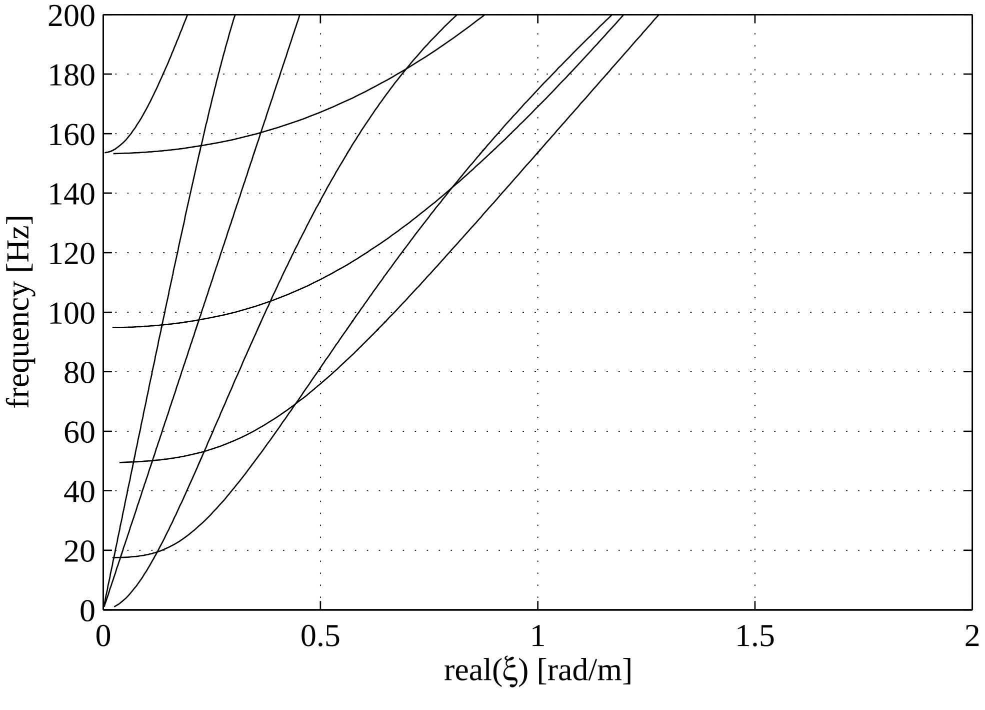

Figure 4.8: Dispersion curves of a free tunnel wall modelled as a thin shell.

The cut-on frequencies of the thin shell are associated with zero wavenumbers, *i.e.* a plane-strain problem. Hence, the shell behaves as a 2D ring and cut-on frequencies can be calculated from the corresponding natural frequencies of a ring as verified by Forrest [29].

Figure 4.9 shows the dispersion curves of the tunnel modelled as a thick cylindrical shell. The work of Gazis [33-35] is employed to calculate these results. Gazis uses the elastic continuum theory to calculate dispersion curves for cylindrical shells. The formulation is the same as presented by Forrest [29], but Forrest uses the modified Bessel functions to solve differential equations of the shell and this leads to dispersion equation with complex values at some wavenumbers and angular frequencies. Gazis uses both the Bessel and the modified Bessel functions to solve the differential equations and this leads to dispersion equation with pure-real values. Both formulations are used by the author; Gazis' formulation and Forrest's formulation. Identical results are obtained (see Figure 4.9). For Forrest's formulation, the dispersion equation is calculated by taking the determinant of matrix [**TT**] (equation C.7). The dispersion equation is solved by using Newton-Raphson method. Details of this method are found in the next section. By comparing Figures 4.8 and 4.9, it can be seen that the dispersion curves are calculated with good accuracy using the thin shell formulation in the range of frequency of interest.

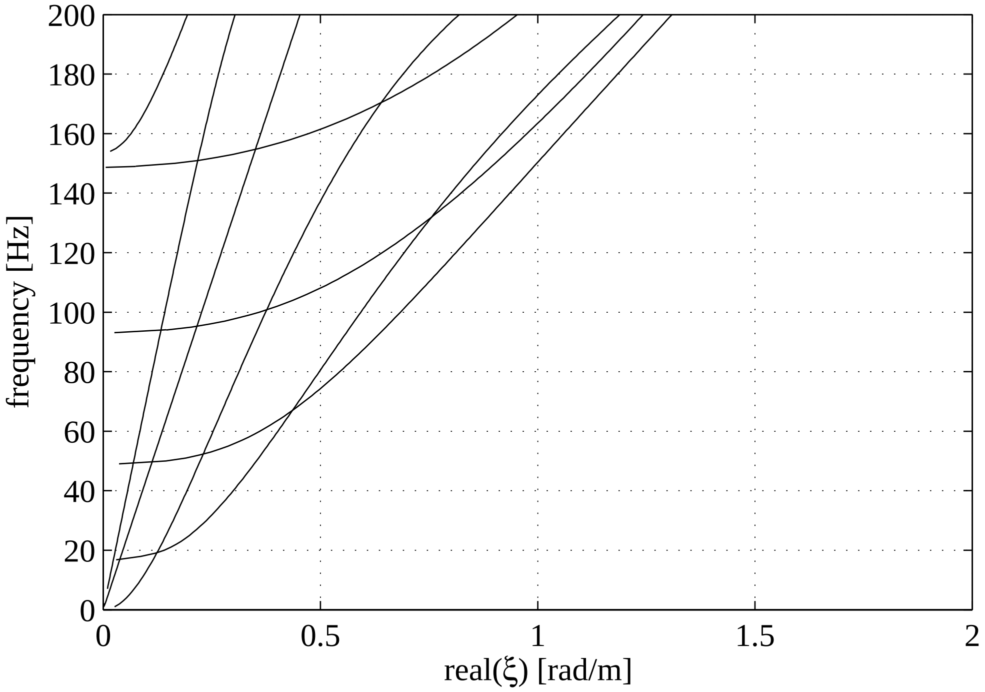

Figure 4.9: Dispersion curves of a free tunnel wall modelled as a thick shell.

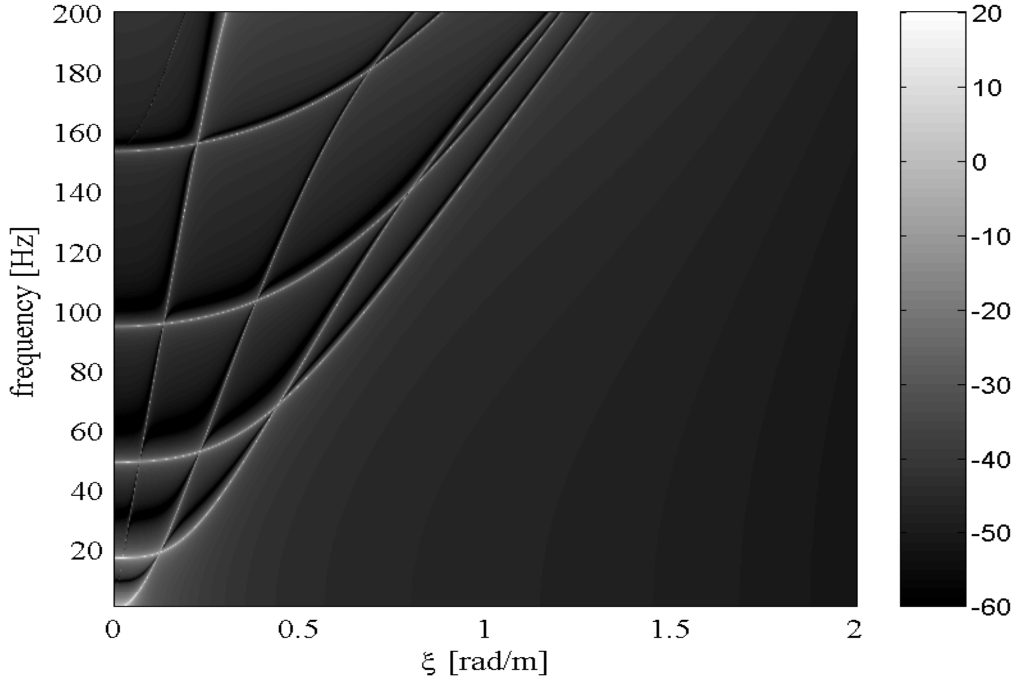

Figure 4.10: Radial displacement FRF of the free tunnel wall at $\theta = 0$ under a radial load.

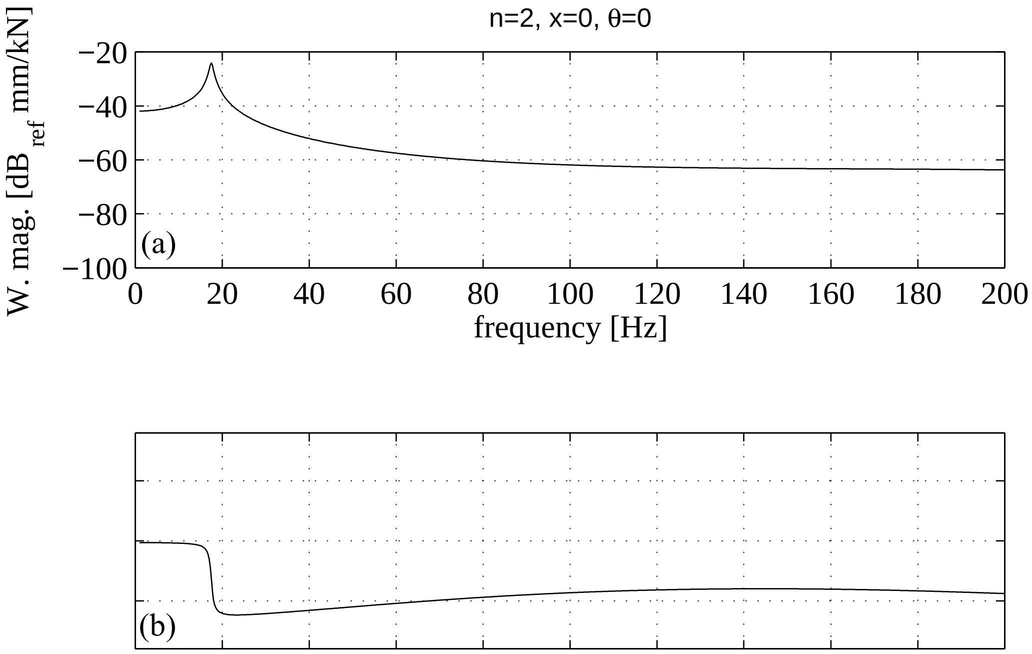

Figure 4.11: The response at the excitation point of a free tunnel wall modelled as a thin shell for radial input at *x*=0 with n=2; (a) displacement and (b) phase.

Figure 4.10 shows the radial FRF of a thin shell calculated for a radial load $e^{i(\omega t+\xi x)}$ applied at $\theta = 0$, where the response is measured at the excitation line. It can be seen that peaks occur at the dispersion curves as shown in Figure 4.8 with no torsional waves propagating for *n*=0 as shown in Figure 4.8. This is because torsional waves are not excited by radial loads.

Figure 4.11.a shows the displacement at $x = 0$, $\theta = 0$, for a radial harmonic load applied at $x = 0$ with circumferential distribution $\cos(2\theta)$. Damping is introduced to the shell by using a complex modulus of elasticity. This is done by replacing E by E_2 in equation 4.53, where $E_2 = E(1 + i\eta_E)$, η_E is the hysteretic loss factor and is taken to equal 5%. The discrete Fourier transform DFT [105] is used to transform results from the wavenumber domain to the space domain with $dx = 0.25m$ and $N = 2^{14}$. A peak occurs at 17.5 Hz corresponding to the cut-on frequency for *n*=2 in Figure 4.7.

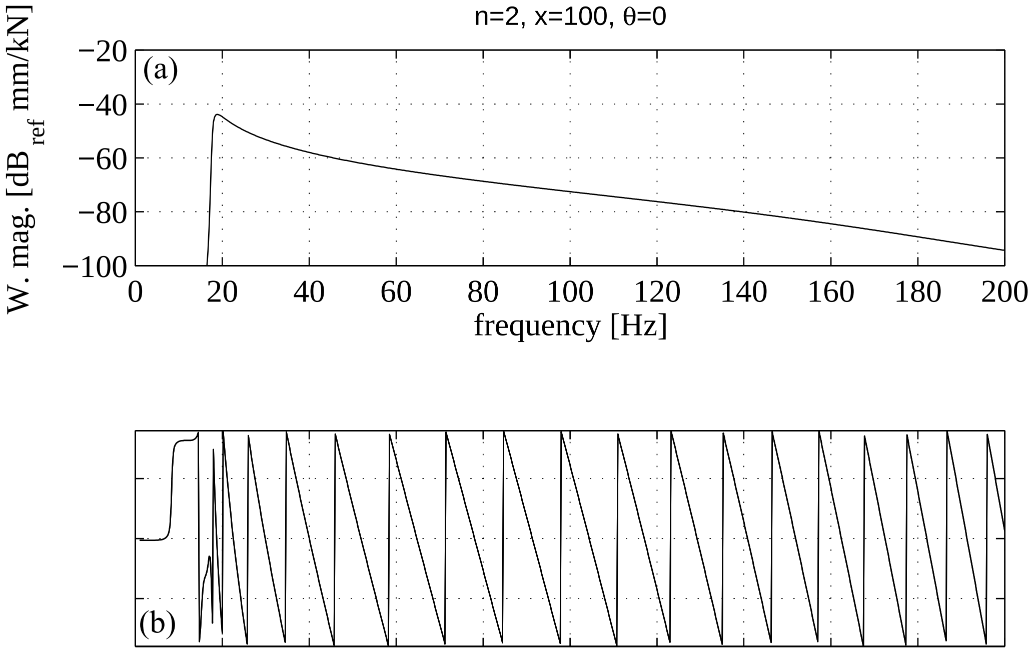

Figure 4.12: The response at 100m away from the excitation point of an isolated tunnel wall modelled as a thin shell for radial input with n=2; (a) displacement and (b) phase.

To examine the existence of propagating waves, the response is measured away from the excitation point with a distance sufficient to allow decaying of evanescent and leaky waves. In Figure 4.12.a, the displacement is measured at 100m away from the excitation point. It is clear that the response is small below the cut-on frequency. Figure 4.12.b shows the phase measured at this point. The phase fluctuates around the zero value and less fluctuation is expected for results measured at further distance from the excitation point. This can be explained by calculating the rate of change of phase with respect to frequency, which can be expressed as

$$\frac{d\varphi}{df} = -\frac{d(2\pi L/\lambda)}{df} = \frac{-2\pi L}{c_{ph}} \tag{4.58}$$

where φ is the phase of the measuring point, c_{ph} is the phase velocity, λ is the wavenumber and L is the distance between the excitation point and the measuring point. Equation 4.58 is true providing that at the excitation point the rate of change of the phase is small and the propagating wave is dominating the response. Applying this equation for instance for *n*=2, *L*=100m, *f*=102Hz and c_{ph} = 1300.15m/s from Figure 4.7, results in a rate of change of the phase equal to –0.483rad/Hz which matches with the results calculated from Figure 4.12.b.

Figure 4.13 (a,b) shows the tunnel radial displacement along its length. At frequency below the cut-on frequency where the response is dominated by the leaky waves, see also Figure 4.7 (for *n*=2), the curve has minima at 20.4, 48.25, 76 and 103.6 m, and hence with approximately 27.7m periodicity. These are due to interference between leaky waves. For a displacement described by two leaky waves with complex wavenumbers $\xi_1 = \gamma_1 + i\eta_1$ and $\xi_2 = \gamma_2 + i\eta_2$, the response y can be written as

$$y = c_1 e^{i(\gamma_1 + i\eta_1)x} + c_2 e^{i(\gamma_2 + i\eta_2)x} \tag{4.59}$$

where c_1 and c_2 are the coefficients associated with each wave and can be complex quantities. Equation 4.59 can be written in different form as

$$y = |c_1| e^{i(\gamma_1 + i\eta_1)x + i\phi_1} + |c_2| e^{i(\gamma_2 + i\eta_2)x + i\phi_2} \tag{4.60}$$

where ϕ_1 and ϕ_2 are the phase of c_1 and c_2 respectively. Equation 4.60 can be written as

$$\begin{aligned} y = {} & |c_1| e^{-\eta_1 x}[\cos(\gamma_1 x + \phi_1) + i\sin(\gamma_1 x + \phi_1)] \\ & + |c_2| e^{-\eta_2 x}[\cos(\gamma_2 x + \phi_2) + i\sin(\gamma_2 x + \phi_2)] \end{aligned} . \tag{4.61}$$

Multiplying by the conjugate and simplifying results in

$$\begin{aligned} y \cdot y^* = |y|^2 = {} & |A_1|^2 e^{-2\eta_1 x} + |A_2|^2 e^{-2\eta_2 x} \\ & + 2|A_1| \cdot |A_2| \cdot e^{-(\eta_2 + \eta_2)x} \cos[(\gamma_1 - \gamma_2)x + \phi_1 - \phi_2]. \end{aligned} \tag{4.62}$$

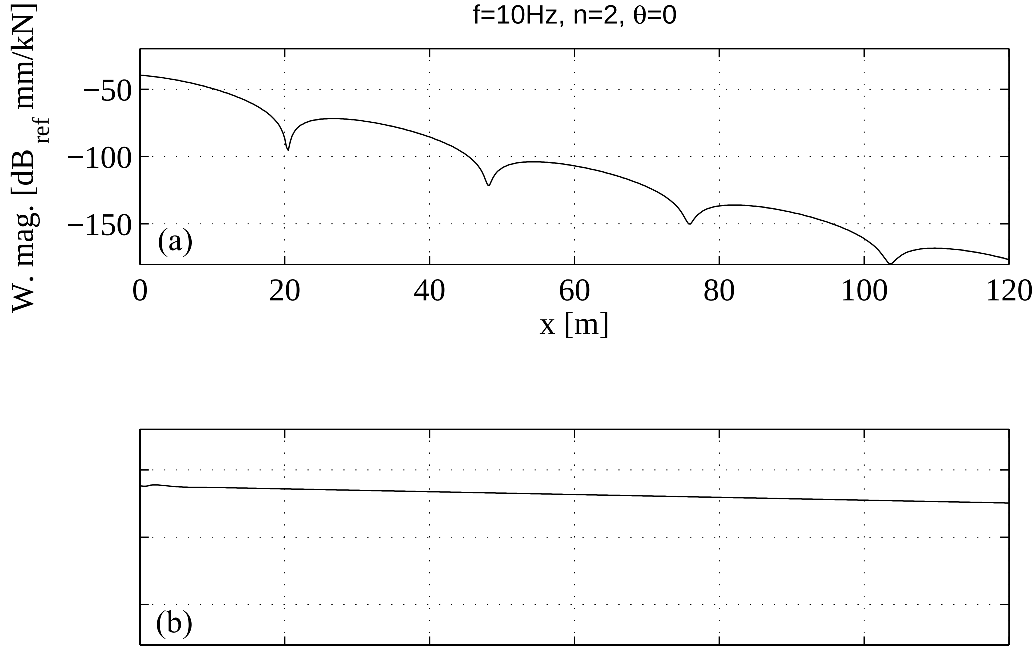

Figure 4.13: The isolated shell response along the shell with $\theta = 0$ for a radial harmonic load applied at x=0 with n=2 and excitation frequency; (a) 10Hz and (b) 100Hz.

The oscillation in the previous equation arises from the cosine term with a period equal to $2\pi/(\gamma_1-\gamma_2)$. From Figure 4.7 and for *n*=2, there are 4 leaky waves at $f=10Hz$ with wavenumbers $\pm 0.113+0.133i$, $\pm 1.375+1.678i$. Leaky waves with wavenumbers $\pm 0.113+0.133i$ are dominating the response away from the load as those with wavenumbers $\pm 1.375+1.678i$ have higher decaying factors (due to the higher imaginary parts). Substituting γ_1=0.113 and γ_2= – 0.113, the oscillation period is 27.8m which agrees with the results in Figure 4.13.a.

The response at a frequency below the cut-on frequency decays rapidly compared with a frequency above the cut-on frequency. This can be confirmed by comparing Figure 4.13.a and 4.13.b, and also by comparing Figure 4.14.a and 4.14.b, which show the real part of the response at frequencies of 10Hz and 100Hz, *i.e.* below and above the cut-on frequency. The wavelength in Figure 4.14.b is 10.58m; equal to wavenumber 0.59 rad/m which matches with the propagating wavenumber for *f*=100Hz, *n*=2 in Figure 4.7.

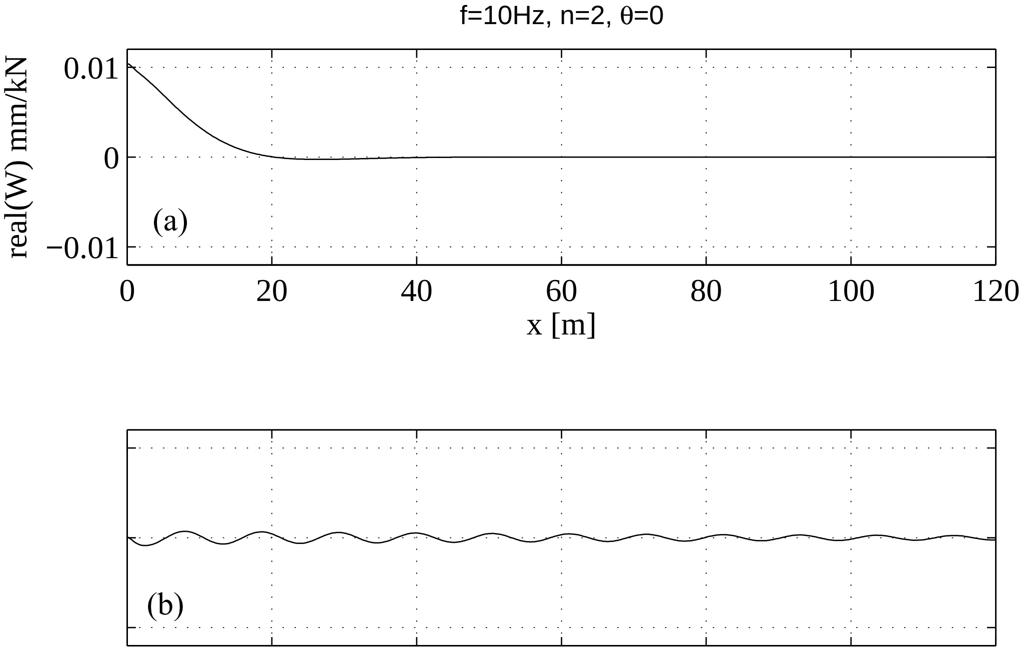

Figure 4.14: The real part of the isolated shell response along the shell with $\theta = 0$ for a radial harmonic load applied at x=0 with n=2 and excitation frequency; (a) 10Hz and (b) 100Hz.

The surrounding soil modelled as a thick shell

The free-vibration equation of a full-space with a cylindrical cavity is calculated by the following equation

$$[\mathbf{T_m}]\cdot\mathbf{B} = Z(3,1) \tag{4.63}$$

where $Z(3,1)$ is a 3×1 vector with zero elements, $\mathbf{T_m} = \mathbf{T_{m1}}$ for the first loading combination and $\mathbf{T_m} = \mathbf{T_{m2}}$ for the second loading combination, see equation C.11. The elements of $\mathbf{T_{m2}}$ are given in Appendix C, while the elements of $\mathbf{T_{m1}}$ are derived by Forrest and can be calculated from the following relationship (see equation C.9)

$$[\mathbf{T_{m1}}] = \begin{bmatrix} 1 & -1 & -1 \\ -1 & 1 & 1 \\ 1 & -1 & -1 \end{bmatrix} * [\mathbf{T_{m2}}]. \tag{4.64}$$

Using the same argument which leads to equation 4.56, one can prove that $|\mathbf{T_{m1}}| = -|\mathbf{T_{m2}}|$. Equating these determinants to zero, both matrices lead to the same dispersion equation. Two main characteristics are associated with the current problem:

- the dispersion equation is not in polynomial form but it comprises of the modified Bessel function of the second kind and hence a different numerical method should be used to calculate the roots;
- Unlike the floating slab track in Chapter 3 and the thin shell in the previous section, the forced vibration solution does not consists only of the normal wave solutions (propagating, evanescent and leaky waves), but additional solutions arise due to the integration along the branch cuts. Note that due to the terms $\alpha = \sqrt{\xi^2 - \omega^2 / c_1^2}$ and $\beta = \sqrt{\xi^2 - \omega^2 / c_2^2}$ in equation C.8, branch points occur at $\xi = \pm\xi_c$ and $\xi = \pm\xi_s$, where $\xi_c = \omega / c_1$ is the wavenumber of the compression wave and $\xi_s = \omega / c_2$ is the wavenumber of the shear wave, see Appendix C.

In this section, only the real solutions of the dispersion equation are searched. Newton-Raphson method [92] is used to find the roots of the dispersion equation. At a given frequency and cross-sectional wavenumber *n*, the iterative formula for Newton-Raphson reads

$$\xi_{j+1} = \xi_j + \Delta \text{ with } \Delta = -D(\xi_j)/D'(\xi_j) \tag{4.65}$$

where $D(\xi_j)$ is the dispersion equation calculated at ξ_j and $D'(\xi_j)$ is the derivative of the dispersion equation evaluated at ξ_j. The iteration in equation 4.65 converges if the starting guess ξ_1 lies near a root. The derivative is calculated using the following relationship [120]

$$\begin{aligned}\frac{d}{d\xi}\left|\mathbf{T_m}(\xi)\right| &= \frac{d}{d\xi}\left|\mathbf{T_m}(1), \mathbf{T_m}(2), \mathbf{T_m}(3)\right| \\ &= \left|\dot{\mathbf{T}}_\mathbf{m}(1), \mathbf{T_m}(2), \mathbf{T_m}(3)\right| + \left|\mathbf{T_m}(1), \dot{\mathbf{T}}_\mathbf{m}(2), \mathbf{T_m}(3)\right| + \left|\mathbf{T_m}(1), \mathbf{T_m}(2), \dot{\mathbf{T}}_\mathbf{m}(3)\right|\end{aligned} \tag{4.66}$$

where $\mathbf{T_m}(1), \mathbf{T_m}(2), \mathbf{T_m}(3)$ are the columns of matrix $\mathbf{T_m}$ and $\dot{\mathbf{T}}_\mathbf{m}(j)$ is a column vector which contains the first derivative of the elements of $\mathbf{T_m}(j)$. The advantage of equation 4.66 is that only closed-form expressions are required for derivatives of individual elements rather than calculating a closed-form expression of the determinant and then differentiating term by term.

It is found that at a given frequency, the dispersion equation satisfies $\left|\mathbf{T}_m(-\xi)\right| = \left|\mathbf{T}_m(\xi)\right|$ and $\left|\mathbf{T}_m(\xi^*)\right| = \left|\mathbf{T}_m(\xi)\right|^*$. Hence if ξ is a root, then $-\xi$ and ξ^* are also roots. Thus for real roots, only positive values are searched.

A Matlab [75] code is written to calculate the real positive roots of the dispersion equation. To decrease the running time, the use of "for loops" is minimised. At a given frequency, a vector of M values of ξ is used; each element represents a starting point. Two Matlab functions are coded to calculate the dispersion equation and its derivative, which result into two vectors with M elements. Instead of calculating a 3×3 matrix for each point of the vector and then calculating the determinant, the vector is processed at once. The dispersion-equation-function calculates 9 vectors (each with M elements) corresponding to the elements of $\mathbf{T}_m$, and the determinant is calculated at once using a closed-form expression for the determinant of a 3×3 matrix. Similarly, the dispersion-equation-derivative function calculates additional 9 vectors corresponding to the elements of the matrix derivative in equation 4.66. After some iterations, the elements of the vector from the last iteration are compared with those from the iteration before. Those elements which have converged are taken as solutions of the dispersion equation.

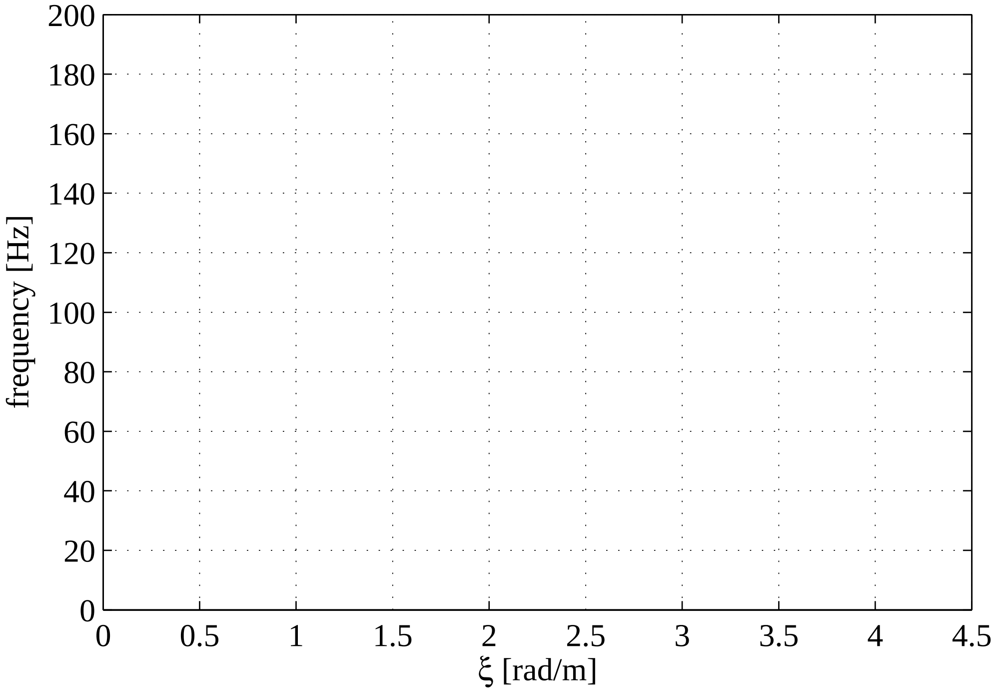

Figure 4.15: Dispersion curves of an infinite domain with a cylindrical cavity.

Figure 4.15 shows the dispersion curves of the soil with a cylindrical cavity for the parameters given in Table 4.1. In the frequency range of interest, waves with cross-sectional wavenumbers n from 0-5 can propagate freely with phase velocities in the range between the shear wave velocity and the Rayleigh wave velocity. For each cross-sectional wavenumber n, waves have cut-on frequencies at velocity equal to the shear wave velocity. By increasing the frequencies, the phase velocity of the propagating waves decreases and approaches the Rayleigh wave velocity. This is expected, because the wavelength of the propagating wave at high frequency is small compared to the cavity diameter. Hence, the cavity behaves as a free-surface equivalent to the free surface of a half-space. Figure 4.16 shows the phase velocities of the propagating waves. The Rayleigh wave velocity is calculated by [38]

$$c_3 = c_2(0.87 + 1.12\nu)/(1+\nu)\,. \tag{4.67}$$

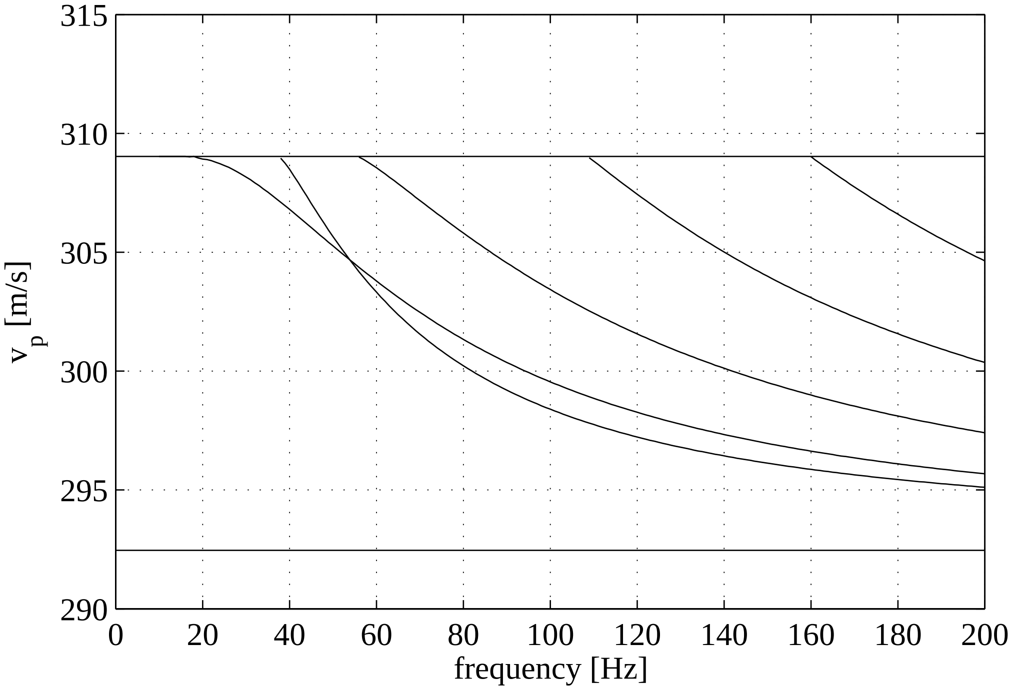

Figure 4.16: The phase velocity for the dispersion curves of an infinite domain with a cylindrical cavity.

It can be seen from Figure 4.16 that there is a cut-on frequency for each cross-sectional wavenumber. The cut-on frequencies are given in Table 4.2. The results given in this section are compared with the results of Bostrom and Burden [9]. They present a study on propagation of surface waves along a cylindrical cavity. They calculate the displacement in terms of the transverse (SH and SV) and compression components. The dispersion equation is derived in a closed form. Using the limiting forms of the modified Bessel functions, two simplified equations are presented to calculate the cut-on frequencies; an equation for $n = 0$ and another equation for $n \geq 2$. These equations are used by the author to recalculate the cut-on frequencies using the soil parameters in Table 4.1. Identical results are obtained for $n = 0,2,3,4$. However, Bostrom and Burden claims that there is no cut-on frequency for $n = 1$, which does not agree with the result of this work. To check this, the dispersion equation derived by Bostrom and Burden is investigated for $n = 1$ and it is found that it has a cut-on frequency at the same value given in Table 4.2.

n	f_n
0	$37.5 Hz$
1	$9.93 Hz$
2	$55.52 Hz$
3	$108.57 Hz$
4	$159.89 Hz$

Table 4.2: Cut-on frequencies of the soil model.

Figure 4.17 shows the displacement FRF for $n = 4$ calculated at the cavity surface. The sharp curve follows the dispersion curve for $n = 4$ in Figure 4.15 for frequencies from $200 Hz$ down to the cut-on frequency. The peaks continue below the cut-on frequency until it gets to $\xi = 0$ at about $f = 40 Hz$. Above the cut-on frequency, the sharp curve has infinite values that are attributed to zero values of the dispersion equation. However, peaks below the cut-on frequency have finite values and are attributed to maximal values of the FRF (for the forced vibration).

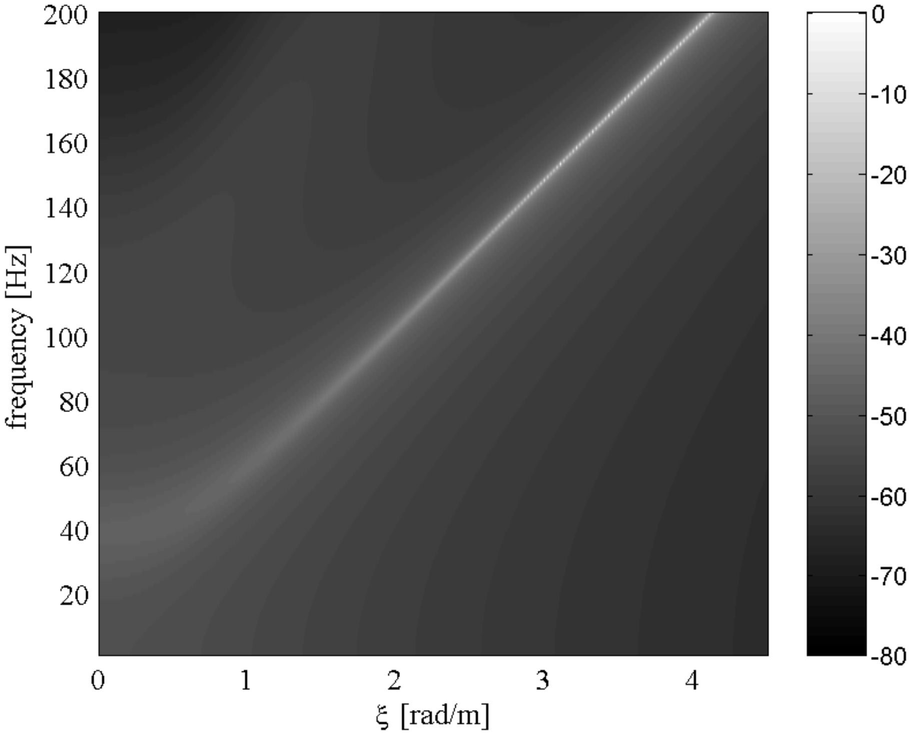

Figure 4.17: FRF of the soil model for n=4 measured at the cavity surface.

The PiP model

The dispersion equation of the PiP model is calculated by the following equation (see equation C.14)

$$\left| \frac{r_a}{r_t} \mathbf{A_E} [\mathbf{U_m}]_{r=r_c} + \frac{r_c}{r_t} [\mathbf{T_m}]_{r=r_c} \right| = 0 \, . \tag{4.68}$$

As same as the dispersion equation of the thin shell model and the soil model, the dispersion equation of the PiP model is independent of the loading combination and this has been confirmed by comparing the dispersion equations resulting from both of the loading combinations.

Newton-Raphson method is used again for this case to calculate the solutions of the dispersion equation. No real roots are found for the parameters given in Table 4.1 in the frequency range of interest. This means that beside its importance in supporting the soil, the tunnel wall does not allow waves to propagate freely.

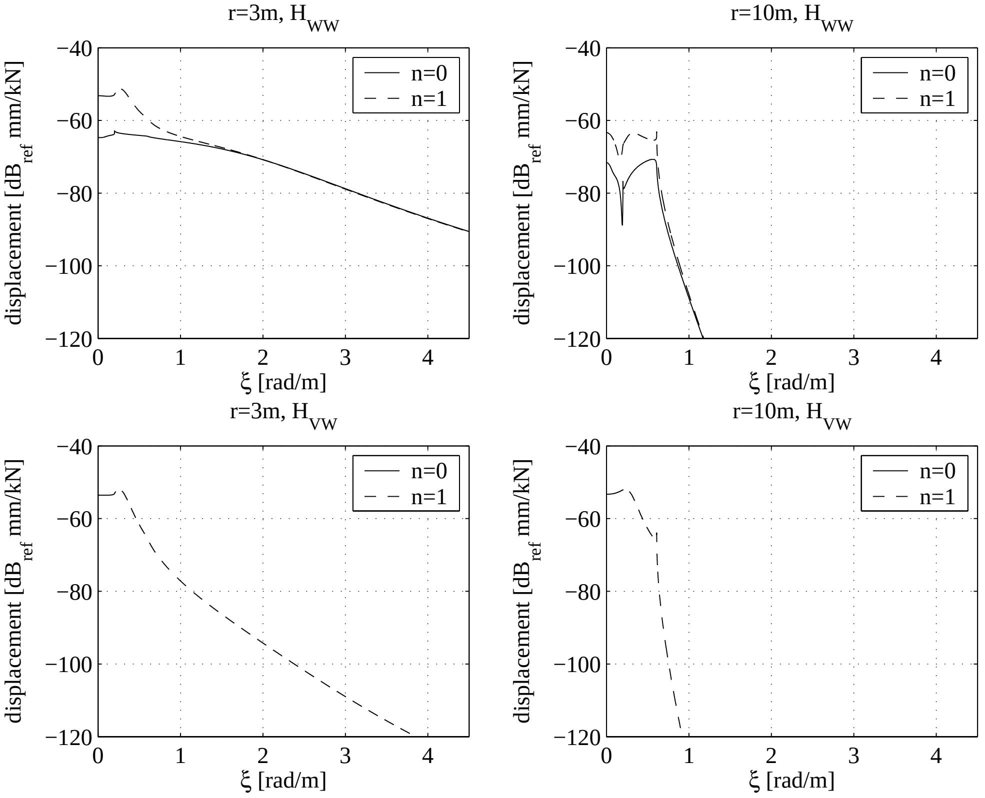

Figure 4.18: FRF of the PiP model for *n*=0 and *n*=1 for a radial input on the inner surface of the tunnel. H_{WW} is the radial displacement FRF (equivalent to $\tilde{u}_r(n,\xi,\omega = 2\pi \times 30 rad/s)$) due to a radial input while H_{VW} is the tangential displacement FRF (equivalent to $\tilde{u}_\theta(n,\xi,\omega = 2\pi \times 30 rad/s)$) due to a radial input. The tunnel-soil interface lies at *r*=3.

Figures 4.18 and 4.19 show the PiP model response for a radial input and tangential input respectively for a frequency of 30Hz and for cross-sectional wavenumbers *n*=0,1. The results in Figure 4.18 are calculated using $\tilde{q}_x(n,\xi,\omega) = 0$, $\tilde{q}_\theta(n,\xi,\omega) = 0$ and $\tilde{q}_r(n,\xi,\omega) = 1$, and the formulation for the first loading combination. The results in Figure 4.19 are calculated using equation 4.47 and 4.48, substituting $\tilde{q}_x(n,\xi,\omega) = 0$, $\tilde{q}_\theta(n,\xi,\omega) = 1$ and $\tilde{q}_r(n,\xi,\omega) = 0$, and the formulation for the second loading combination (see Appendix C). Near and at the tunnel-soil interface, the response is distributed over a wide range of wavenumbers, while away from the tunnel the response is confined to a narrow band of wavenumbers. For *n*=0, the PiP model has no tangential response for the radial input and vice versa, *i.e.* $H_{WV} = H_{VW} = 0$. Note also that because of reciprocity [93], the relationship $H_{WV} = H_{VW}$ holds for any value of *n* at the tunnel-soil interface (compare H_{VW} for r=3m in Figures 4.18.c with H_{WV} for r=3m in 4.19.c).

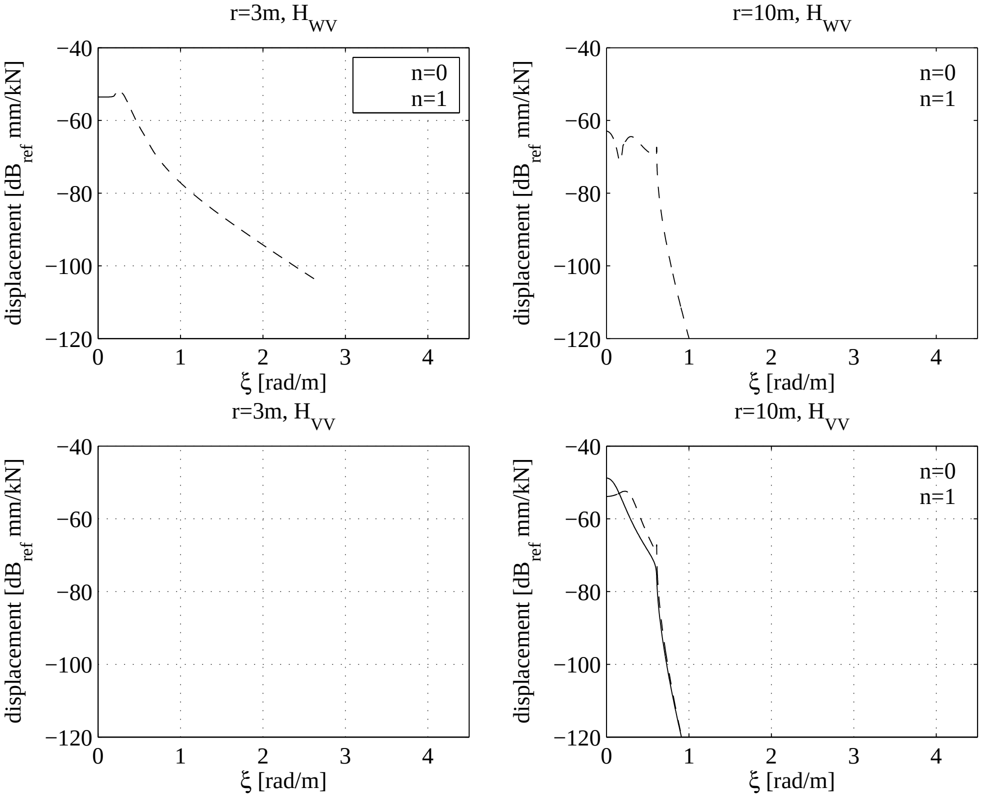

Figure 4.19: FRF of the PiP model for *n*=0 and *n*=1 for a tangential input on the inner surface of the tunnel. H_{WV} is the radial displacement FRF (equivalent to $\tilde{u}_r(n,\xi,\omega = 2\pi \times 30 rad/s)$) due to a tangential input while H_{VV} is the tangential displacement FRF (equivalent to $\tilde{u}_\theta(n,\xi,\omega = 2\pi \times 30 rad/s)$) due to a tangential input. The tunnel-soil interface lies at *r*=3.

The wave propagation study in this chapter has addressed the PiP model so far. In the next section, the dispersion equations of tracks on rigid foundations will be investigated. When the stiffness of track's support, i.e. the slab bearings, is much smaller that the stiffness of the PiP model, it is possible to calculate the forces generated on the tunnel wall due to any loading on the rails from a model of a track coupled to a rigid tunnel wall, *i.e.* a track on rigid foundation. These forces can then be used as input to the PiP model as formulated in Appendix C to calculate the vibration levels around the tunnel. Such a procedure may be accurate but it will not be used in this dissertation, as the direct formulation in Section 4.1 does not take long time to be performed. However attention should be drawn to the importance of dispersion curves of a track on rigid foundation, in which force magnification happens. This will be discussed in the next section.

4.4.2 Dispersion characteristics of the track

Figure 4.20 shows a floating-slab track attached to a rigid foundation via two lines of support. The track has five degrees of freedom. The force-displacement relationship is calculated by the following equation

$$\widetilde{\mathbf{F}} = [\widetilde{\mathbf{K}}]\widetilde{\mathbf{y}} \tag{4.69}$$

where $\widetilde{\mathbf{F}} = [\widetilde{F}_1, \widetilde{F}_2, \widetilde{F}_3, \widetilde{F}_4, \widetilde{F}_5]^T$, $\widetilde{\mathbf{y}} = [\widetilde{y}_1, \widetilde{y}_2, \widetilde{y}_3, \widetilde{y}_4, \widetilde{y}_5]^T$,

$$\widetilde{\mathbf{K}} = \begin{bmatrix} \widetilde{K}_r + k_r & 0 & -k_r & 0 & -k_r \cdot a_t \\ 0 & \widetilde{K}_r + k_r & -k_r & 0 & k_r \cdot a_t \\ -k_r & -kr & \begin{matrix} \widetilde{K}_v + 2k_r + 2k_n c^2 \\ + 2k_s s^2 \end{matrix} & 0 & 0 \\ 0 & 0 & 0 & \begin{matrix} \widetilde{K}_h + 2k_n s^2 \\ + 2k_s c^2 \end{matrix} & \begin{matrix} -2k_n(r_t - b_b)s^2 \\ + 2k_s c[r_t - (r_t - b_b)c] \end{matrix} \\ -k_r \cdot a_t & k_r \cdot a_t & 0 & \begin{matrix} -2k_n(r_t - b_b)s^2 \\ + 2k_s c[r_t - (r_t - b_b)c] \end{matrix} & \begin{matrix} \widetilde{K}_\gamma + 2k_s[r_t - (r_t - b_b)c]^2 \\ + 2k_r a_t^2 + 2k_n(r_t - b_b)^2 s^2 \end{matrix} \end{bmatrix}$$

$\tilde{K}_r = 1/\tilde{H}_r = EI_r\xi^4 - m_r\omega^2$, $\tilde{K}_v = 1/\tilde{H}_v = EI_v\xi^4 - m_s\omega^2$, $\tilde{K}_h = 1/\tilde{H}_h = EI_h\xi^4 - m_s\omega^2$, $\tilde{K}_\gamma = 1/\tilde{H}_\gamma = GK\xi^2 - J\omega^2$, $c = \cos\psi$, $s = \sin\psi$, EI_h is the bending stiffness of the slab in the horizontal direction and all the other parameters are defined in Section 4.1.

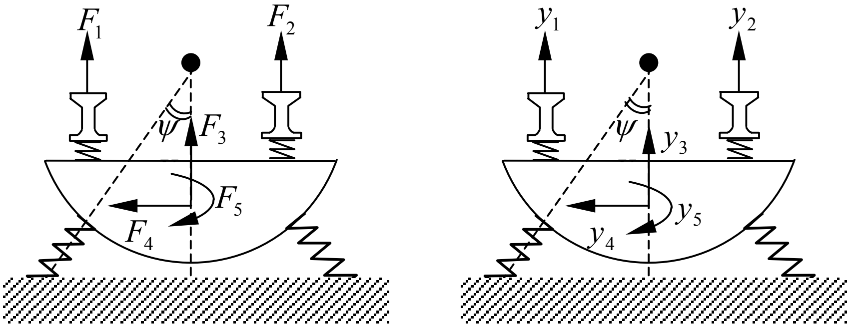

(a) (b)

Figure 4.20: Floating-slab track on rigid bed; (a) forces, (b) displacements.

The stiffness matrix $\tilde{\mathbf{K}}$ in equation 4.69 is assembled using the direct stiffness method which is usually used to calculate stiffness matrices for structures under static loads [4]. For instance $\tilde{\mathbf{K}}(3,2)$ is calculated by applying a unit displacement at the second degree of freedom, fixing the other degrees of freedom and measuring the force at the third degree of freedom. Alternatively, the stiffness matrix can be calculated by using the formulation in Section 4.1.1 and setting the FRFs of the PiP model to zero.

To calculate the dispersion equation, the determinant of $\tilde{\mathbf{K}}$ is set to zero. Again, only real roots are searched. The Matlab function "roots" is used to calculate the solutions. Figure 4.21 shows the dispersion curves of a 20 Hz floating-slab track for the frequency range 0-200 Hz and using the track parameters given in Table 4.1 with $\psi = 15^\circ$. Table 4.3 shows the cut-on frequencies of this track along with the propagating modes (the eigenvectors) at the cut-on frequencies.

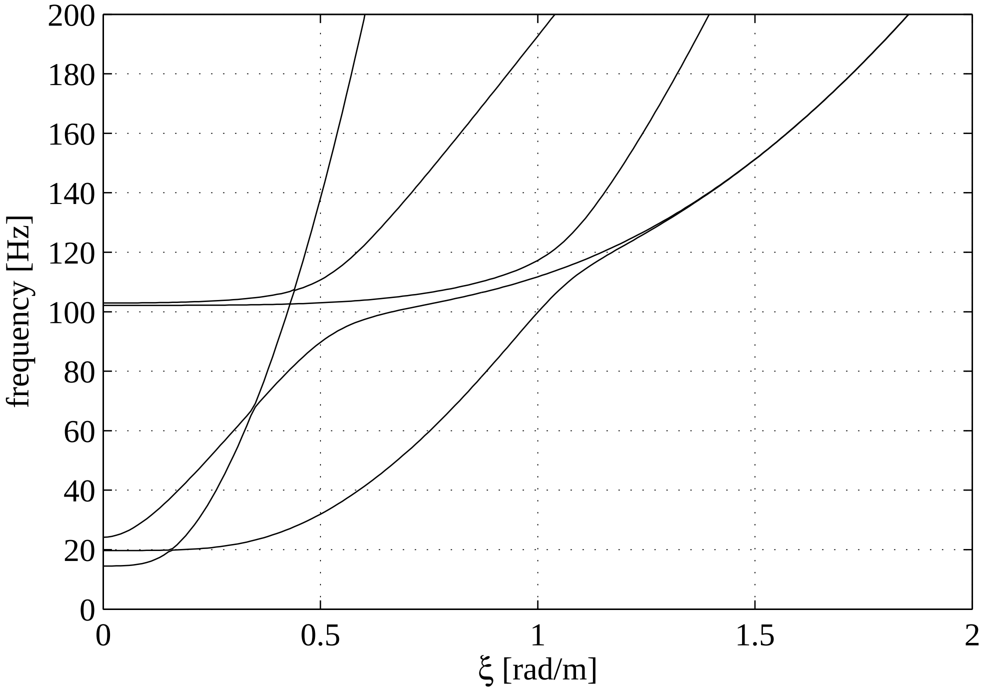

Figure 4.21: Dispersion curves of a floating-slab track on rigid bed.

The modes from the first to the fifth are called: the horizontal-slab mode, the vertical-slab mode, the torsional-slab mode, the in-phase-rails mode and the out-of-phase-rails mode respectively. The horizontal-slab mode has rails' displacements and rotational displacement of the slab, which vanish if $\psi = 0$.

Mode	1	2	3	4	5
Cut-on frequency Hz	14.50	19.71	24.20	102.14	102.92
$\tilde{y}_1$	0.02	1.00	0.80	1.00	1.00
$\tilde{y}_2$	-0.02	1.00	-0.80	1.00	-1.00
$\tilde{y}_3$	0.00	0.96	0.00	-0.03	0.00
$\tilde{y}_4$	1.00	0.00	-0.11	0.00	0.00
$\tilde{y}_5$	0.27	0.00	1.00	0.00	-0.06

Table 4.3: Cut-on frequencies and mode shapes for a track on rigid bed.

Two cases are of significant importance and will be discussed more in Chapter 5. The first is when $\widetilde{F}_1 = \widetilde{F}_2$. In this case only two modes can propagate; these are the second and the fourth modes. The second case is when $\widetilde{F}_1 = -\widetilde{F}_2$. This time three modes can propagate; the first, the third and the fifth.

Calculating the dispersion curves for the full track model (consisting of the track and the PiP model) is complicated. However, the dispersion curves of the track on a rigid bed are important and help identifying the peaks of the FRFs of the full track-tunnel-soil model.

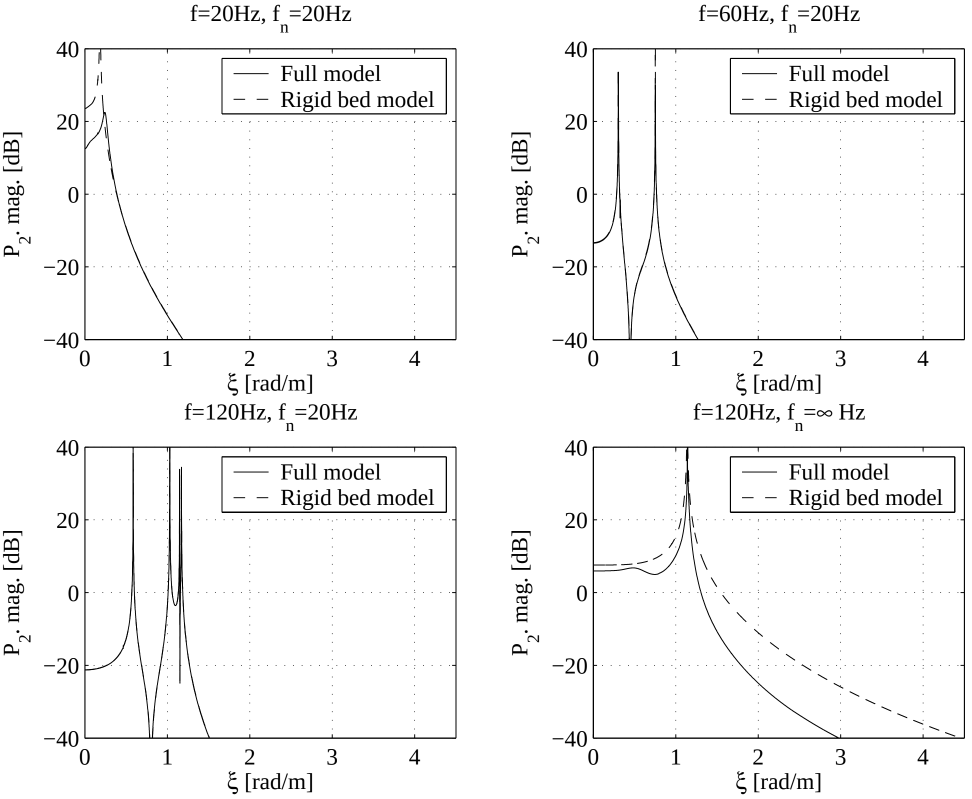

Figure 4.22: $\widetilde{P}_2$ calculated by the full track model and the rigid-bed model for a loading $\widetilde{F}_1 = 1$, $\widetilde{F}_2 = 0$, for different excitation frequencies and different slabs. (a) f=20Hz, f_n=20Hz (b) f =60Hz, f_n =20Hz (c) f=120Hz, f_n =20Hz (d) f =120Hz, f_n =∞Hz.

Figure 4.22 shows the normal force of the left slab bearing calculated by the full track model as described in Section 4.1.1 (Figure 4.2) and by the rigid-bed model as calculated by equation 4.69 (Figure 4.20). The results are for applied forces $\widetilde{F}_1 = 1$ and $\widetilde{F}_2 = 0$ with $\psi = 15^\circ$ and $\Re = 0.5$. Figures 4.22 (a, b and c) are calculated for a 20Hz slab with excitation frequencies 20, 60 and 120Hz respectively, while a directly-fixed slab (∞ Hz) with 120Hz excitation frequency is used to produce the results in Figure 4.22.d.

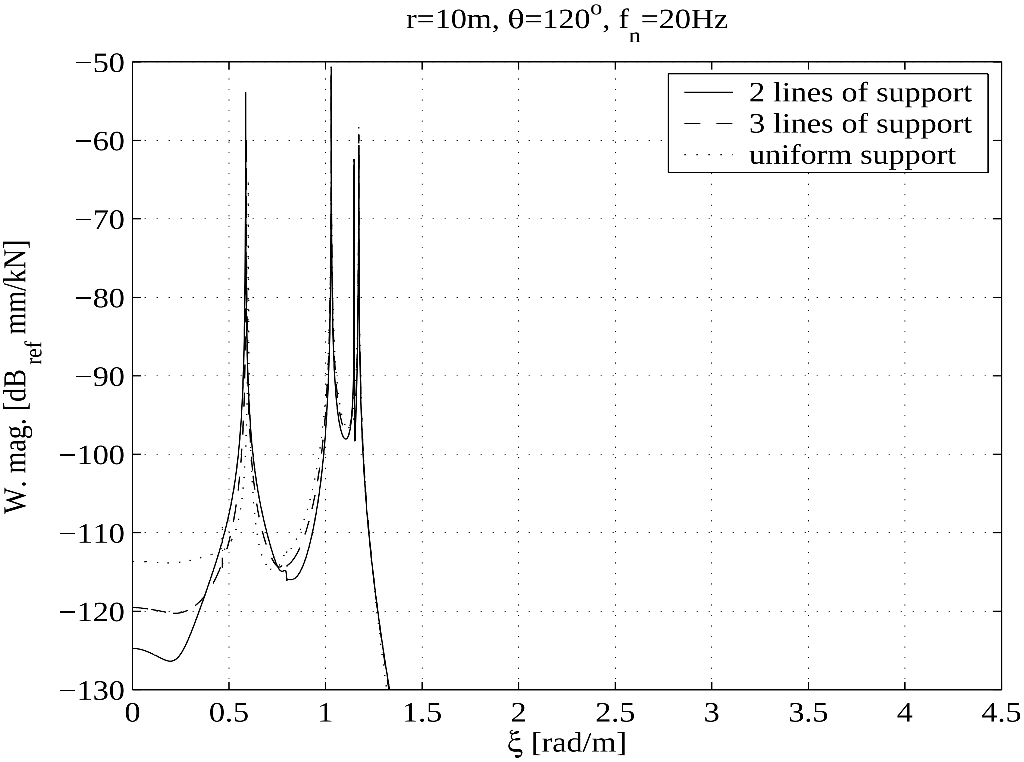

Figure 4.23: The radial displacement calculated at r=10m and θ=120° for the track supported on: two lines of support, three lines of support and uniform support. The loads are $\widetilde{F}_1 = 1$, $\widetilde{F}_2 = 0$ with 120 Hz excitation frequency.

It can be seen that the forces on the tunnel invert can be calculated approximately using the rigid-bed model. The accuracy of this approximation decreases at frequencies and wavenumbers on the track dispersion curves (Figure 4.22.a) and also decreases by increasing the stiffness of the slab bearings (Figure 4.22.d). Note that peaks occur at wavenumbers defined by the dispersion curves of the track on rigid-bed, this is confirmed by comparing the wavenumbers in which peaks occur in a, b and c with the corresponding wavenumbers as plotted in Figure 4.21. These peaks appear in the displacement FRF of the soil as in Figure 4.23 which shows the soil displacement FRFs at angle θ=120° and 10m away from the tunnel centre for $\widetilde{F}_1 = 1$, $\widetilde{F}_2 = 0$, $\psi = 15^\circ$, $\Re = 0.5$, f_n=20Hz and 60Hz excitation frequency. The number of collocation points for the uniform support is taken as M=10 which is found to be accurate for the current parameters. Note that some modes have little contribution to the response and hence no pronounced peaks are observed at their eigen frequencies.

4.5 Computations of the soil displacement

A Matlab code is written to calculate the soil displacement at any radius r and angle θ for any input load on the rails defined by $\widetilde{F}_1$ and $\widetilde{F}_2$. The code is summarised in the following paragraphs.

For a range of frequency $\mathbf{f} = [1,2,...,200]$, the ultimate task of the code is to calculate the soil displacement in the wavenumbers $\boldsymbol{\xi} = [0,0.01,0.02,...,4.5]$. The spacing and the maximum value of the frequency and wavenumber vectors may be changed according the required resolution and results accuracy. For instance, if the displacement results are to be calculated in the space domain, the Nyquist criterion plays an important role in determining the values of the maximum and interval of the wavenumber vector. The code is divided into the following four subroutines and functions.

1. Calculations of matrix $\mathbf{B}$

The purpose of this subroutine is to calculate and save the soil vectors of coefficients $\mathbf{B}_1$ for the first loading combination and $\mathbf{B}_2$ for the second loading combination (see Appendix C), for frequencies and wavenumbers as defined by $\mathbf{f}$ and $\boldsymbol{\xi}$ above. For a given frequency, 22 vectors (each of 3×1 elements) are saved for each wavenumber ξ and cross-sectional wavenumbers n. Each vector gives $\mathbf{B}_1$ or $\mathbf{B}_2$ for values of n from 0-10 and for the PiP model parameters in Table 4.1. This means that for each frequency a total number of $22 \times \Lambda$ vectors are saved by this subroutine, where Λ is the total number of wavenumbers. It should be noted that this subroutine would not be run again unless new parameters of the PiP model, *i.e.* the tunnel or the soil parameters, are to be considered.

2. Displacement FRF function of the PiP model

This function takes the form $H_{PiP}(f, r, \theta, ii, jj)$ and calculates the radial, tangential or longitudinal displacement FRF of the PiP model for a radial or tangential input load applied on the tunnel invert. The inputs to this function are the frequency f, the measuring point radius *r*, the measuring point angle θ, and two indices ii and jj. The index ii determines the direction of the input; 3 if radial and 2 if tangential. The index jj determines the output direction; 3 if radial, 2 if tangential and 1 if longitudinal. For instance to calculate $\tilde{H}_{7-8}$ in Section 4.1.1 (see Figure 4.2.d), use $ii = 2$ and $jj = 3$. The output from this function is a $\Lambda \times 1$ vector of the displacement calculated at the wavenumbers $\boldsymbol{\xi}$.

In this function, values of $\mathbf{B}_1$ or $\mathbf{B}_2$ are called depending on the input on the tunnel wall; whether radial or tangential, and the procedure described in Section 4.2.2 and Appendix C.4 is used to calculate the FRF at the required radius and angle. It should be noted that the FRF depends on the relative angle between the measuring point and the excitation point, *i.e.* if the load is applied at θ_1 on the tunnel wall and the measuring point lies at θ_2, the angle ($\theta_2 - \theta_1$) should be used as an input angle to this function.

3. Forces on the tunnel wall from the full track model

This function calculates the forces on the tunnel wall $\tilde{\mathbf{P}}$ using the formulations in Sections 4.1.1, 4.1.2 and 4.1.3 for the track supported on two lines, three lines and uniform support respectively. The Reciprocal theorem [93] is used and an advantage is taken of symmetrical and anti-symmetrical FRFs to speed up the running time. For instance, in equation 4.20 matrix $\tilde{\mathbf{H}}_{51}$ can be alternatively calculated by the following relationship

$$\widetilde{\mathbf{H}}_{51} = \begin{bmatrix} \widetilde{H}_{6-6} & \widetilde{H}_{6-7} & 0 & \widetilde{H}_{6-9} \\ \widetilde{H}_{6-7} & \widetilde{H}_{6-6} & -\widetilde{H}_{6-9} & 0 \\ 0 & -\widetilde{H}_{6-9} & \widetilde{H}_{8-8} & \widetilde{H}_{8-9} \\ \widetilde{H}_{6-9} & 0 & \widetilde{H}_{8-9} & \widetilde{H}_{8-8} \end{bmatrix}. \tag{4.70}$$

4. The soil displacement

Having calculated the normal and tangential forces on the tunnel wall, the soil displacement at the wavenumbers ξ can be calculated by the following relationships:

(a) for two lines of support:

$$\begin{aligned} \widetilde{u} = {} & \widetilde{H}_{PiP}(f,r,\theta+\psi,3,jj)\cdot\widetilde{P}_1 + \widetilde{H}_{PiP}(f,r,\theta-\psi,3,jj)\cdot\widetilde{P}_2 \\ & +\widetilde{H}_{PiP}(f,r,\theta+\psi,2,jj)\cdot\widetilde{Q}_1 + \widetilde{H}_{PiP}(f,r,\theta-\psi,2,jj)\cdot\widetilde{Q}_2 \end{aligned}; \tag{4.71}$$

(b) for three lines of support:

$$\begin{aligned} \widetilde{u} = {} & \widetilde{H}_{PiP}(f,r,\theta+\psi,3,jj)\cdot\widetilde{P}_1 + \widetilde{H}_{PiP}(f,r,\theta,3,jj)\cdot\widetilde{P}_2 \\ & +\widetilde{H}_{PiP}(f,r,\theta-\psi,3,jj)\cdot\widetilde{P}_3 + \widetilde{H}_{PiP}(f,r,\theta+\psi,2,jj)\cdot\widetilde{Q}_1\,; \\ & +\widetilde{H}_{PiP}(f,r,\theta,2,jj)\cdot\widetilde{Q}_2 + \widetilde{H}_{PiP}(f,r,\theta+\psi,2,jj)\cdot\widetilde{Q}_3 \end{aligned} \tag{4.72}$$

(c) for uniform support:

$$\widetilde{u} = \sum_{j=1}^{M} c_j \widetilde{H}_{PiP}(f,r,\theta-\theta_j,3,jj)\widetilde{P}_j \cdot r_t\Delta\theta + \sum_{j=1}^{M} c_j \widetilde{H}_{PiP}(f,r,\theta-\theta_j,2,jj)\widetilde{Q}_j \cdot r_t\Delta\theta \tag{4.73}$$

where the value of jj is 1,2 or 3 for the soil displacement in the longitudinal, tangential or the radial directions respectively.

Conclusions

In this chapter a formulation for a full model of a track in an underground railway tunnel is presented. The model comprises of a floating-slab track coupled via slab bearings to the PiP model which accounts for a tunnel wall and its surrounding soil. Special attention is given to the slab support, slabs are attached to the tunnel wall in one of three ways; via two lines, three lines or a uniform support. An important aspect of the uniform support is that it allows modelling of a directly-fixed slab by setting the support stiffness to infinity.

Wave propagation in the PiP model and its separate components is investigated. The dispersion curves for a tunnel wall modelled as a thin shell are compared with a tunnel modelled as a thick shell and a good agreement is obtained in the frequency range 0-200Hz. For the soil with a cylindrical cavity, waves propagate near the surface with velocities between the Rayleigh wave velocity and the shear wave velocity. At high frequencies, these waves behave as surface waves in a half-space. The results calculated for the soil are compared with published results in the context of wave propagation.

Waves can propagate in a free tunnel wall and in a full-space with a cylindrical cavity, but due to coupling there is no free wave propagation in the PiP model for the parameters of the tunnel and soil considered here.

The dispersion curves of a floating-slab track on rigid foundation are also calculated. These curves have a great effect on the FRFs of the full track-tunnel-soil system. The generated forces on the tunnel exhibit peaks at wavenumbers and frequencies along these curves. A good knowledge of dispersion curves of the track helps in identify the effect of the track parameters on vibration from underground railways, as will be shown in Chapter 5.

Chapter 5

POWER FLOW FROM UNDERGROUND RAILWAY TUNNELS

Introduction

Rail roughness is an important source of the vibration generated at the wheel-rail interface. For a train moving with a constant velocity of 36 km/hr, a rail roughness with wavelengths in the range between 0.1-10 m is responsible for the vibration generated in the frequency range between 1-100 Hz.

Existing models of underground railways use the displacement, velocity or acceleration power spectral density (PSD) calculated at some points in the track, the tunnel or the ground as measures of vibration, see [52] for example. The PSD should be calculated in different directions and at many points to show the vibration environment at and away from the tunnel.

In this chapter, a different measure of vibration is used which is based on the mean power flow from the tunnel, paying particular attention to the part of the power which radiates upwards to places where buildings' foundations are expected to be found. This measure has many advantages over the conventional approach, for instance:

- it provides a single measure of the vibration by calculating the power radiated upwards (the PSD at a single point is not representative for all places around the tunnel);

- it accounts for vibration in the vertical, horizontal and longitudinal directions at once (the PSD must be computed for each direction separately);

- the power-flow measure accounts for both the velocity and stress states around the tunnel.

This chapter is divided into five sections. Section 5.1 shows the calculation of the rail displacement for two different models of moving-trains on rails with in-phase roughness. Section 5.2 derives expressions for the stress and velocity at the soil and performs the power calculations. Typical results of the power flow for floating slabs with different natural frequencies are given in Section 5.3, and by means of a parametric survey Section 5.4 provides some insight into the effect of track properties on mean power flow. Finally calculations of power flow due to rails with out-of-phase roughness are presented to evaluate the effect of roughness phase-delay on the isolation performance.

5.1 Rail displacement due to an infinite moving-train

The power flow is calculated due to a train with infinite length, which moves along a tunnel with a constant forward velocity v on rails with some sinusoidal roughness.

Two train models are used in this chapter and are shown in Figures 5.1 and 5.2. The first model comprises a set of single-degree-of-freedom moving axles, infinite in number and with fixed spacing L. In the second model, a second mass and a spring-damper system is used to account for a bogie and a primary suspension. In this context rails with in-phase roughness are assumed and the beam in Figure 5.1 and 5.2 represents both rails of the track. The derivation will be extended to rails with out-of-phase roughness in Section 5.5.

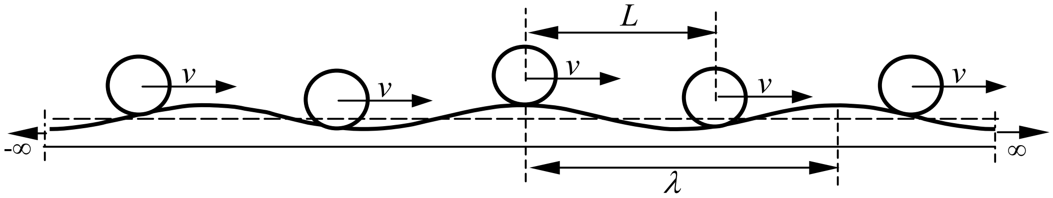

Figure 5.1: A snapshot at time $t = 0$ for infinite number of axles moving over a rail with sinusoidal roughness of wavelength λ and magnitude Δ. Rail displacements are not shown.

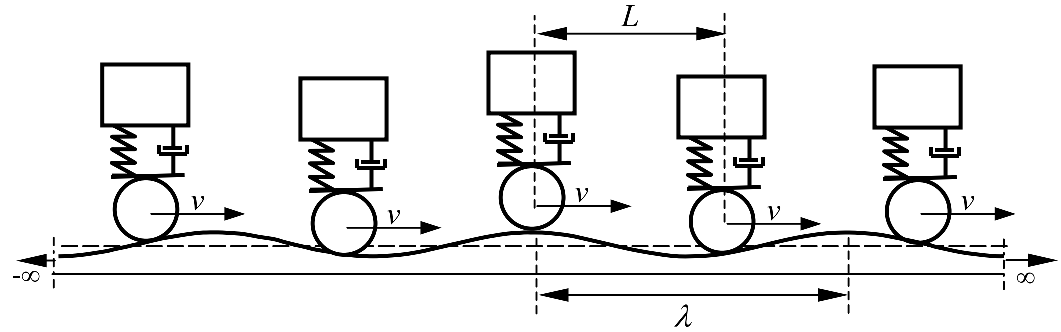

Figure 5.2: A snapshot at time $t = 0$ for infinite number of two degree-of-freedom systems moving over a rail with sinusoidal roughness of wavelength λ and magnitude Δ. Rail displacements are not shown.

Due to a given sinusoidal rail roughness of magnitude Δ and wavelength λ, both of the train models apply dynamic forces on the rail, which are equivalent to a set of infinite number of harmonic loads G as shown in Figure 5.3. The loads move with the same velocity v of the train and have the same excitation angular frequency $\varpi = (2\pi v/\lambda)$ with a phase difference $(\varpi L/v)$ between successive loads. The value of G as will be shown later is the dynamic force at the wheel-rail interface for the two rails and its value depends on the train model, whether the first or the second. The total load on the rail can be written in the space-time domain as a summation of delta functions

$$F(x,t) = \sum_{k=-\infty}^{\infty} G \cdot e^{i\varpi t} e^{ik\varpi L/v} \cdot \delta(x - vt - kL). \tag{5.1}$$

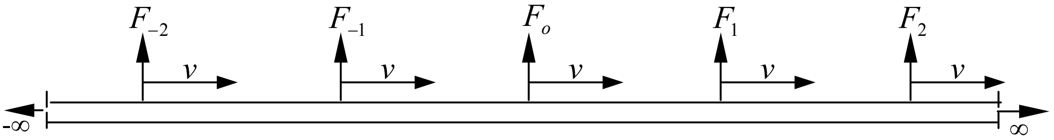

Figure 5.3: Infinite number of harmonic loads applied on the rail in the form $F_k = G \cdot e^{i\varpi t} e^{ik(\varpi L/v)}$.

This equation is transformed to the wavenumber-frequency domain using equations A.1 and A.2 to give

$$\tilde{F}(\xi,\omega) = 2\pi \sum_{k=-\infty}^{\infty} G \cdot e^{-i\xi kL} e^{ik\varpi L/v} \cdot \delta(\omega + \xi v - \varpi)\,. \tag{5.2}$$

The displacement of the rail under this loading in the wavenumber-frequency domain $\tilde{y}_r$ is equal to the displacement FRF multiplied by the force. Hence

$$\tilde{y}_r(\xi,\omega) = 2\pi \cdot \tilde{H}_r(\xi,\omega) \sum_{k=-\infty}^{\infty} G \cdot e^{-i\xi kL} e^{ik(\varpi L/v)} \cdot \delta(\omega + \xi v - \varpi) \tag{5.3}$$

where $\tilde{H}_r(\xi,\omega)$ is the displacement FRF of the rail. It is calculated from the models described in Section 4.1, 4.2 or 4.3 by substituting $\tilde{F}_1 = 0.5$, $\tilde{F}_2 = 0.5$ and computing the value of $\tilde{y}_1$ or $\tilde{y}_2$. Transforming equation 5.3 to the wavenumber-time domain (see equation A.4) results in

$$\bar{y}_r(\xi,t) = \tilde{H}_r(\xi,\varpi - \xi v) \cdot G \cdot e^{i(\varpi - \xi v)t} \sum_{k=-\infty}^{\infty} e^{ikL(\varpi/v - \xi)}\,. \tag{5.4}$$

Equation 5.4 in its current form does not result in a closed-form expression once it is transformed to the space-time domain. Using equation A.8, the infinite sum of exponential functions is written in an equivalent sum of delta functions to give

$$\bar{y}_r(\xi,t) = \tilde{H}_r(\xi,\varpi - \xi v) \cdot e^{i(\varpi - \xi v)t} \cdot G \cdot \frac{2\pi}{L} \sum_{p=-\infty}^{\infty} \delta\Big(\xi - \frac{\varpi}{v} + \frac{2\pi \cdot p}{L}\Big)\,. \tag{5.5}$$

Transforming equation 5.5 to the space-time domain (see equation A.3) results in

$$y_r(x,t) = \frac{e^{i\varpi t}}{L} \cdot G \cdot \sum_{p=-\infty}^{\infty} e^{i\xi_p(x-vt)} \tilde{H}_r(\xi_p,\omega_p) \tag{5.6}$$

where $\xi_p = \frac{\varpi}{v} - \frac{2\pi p}{L}$ and $\omega_p = \frac{2\pi p v}{L}$.

For an observation point which moves along the rail with a velocity v, the rail displacement is merely a harmonic function with frequency equal to the excitation frequency ϖ (substitute $x - vt$ = constant). Equation 5.6 can also be written as a summation of separated time and space functions as

$$y_r(x,t) = G \cdot \sum_{p=-\infty}^{\infty} \frac{\widetilde{H}_r(\xi_p, \omega_p)}{L} e^{i\xi_p x} e^{i\omega_p t} . \tag{5.7}$$

This important result expresses the displacement of the rail as a sum of infinite convecting waves. Each wave is described with its angular frequency ω_p and a wavenumber ξ_p which will be called the *wavenumber deficit.*

The infinite sum in equation 5.7 can be approximated as a finite sum performed over the region with large $\widetilde{H}_r(\xi,\omega)$ response. This is made clear in Figure 5.4 where the significant values of wavenumber deficit ξ_p are those that map onto regions of high $\widetilde{H}_r(\xi,\omega)$.

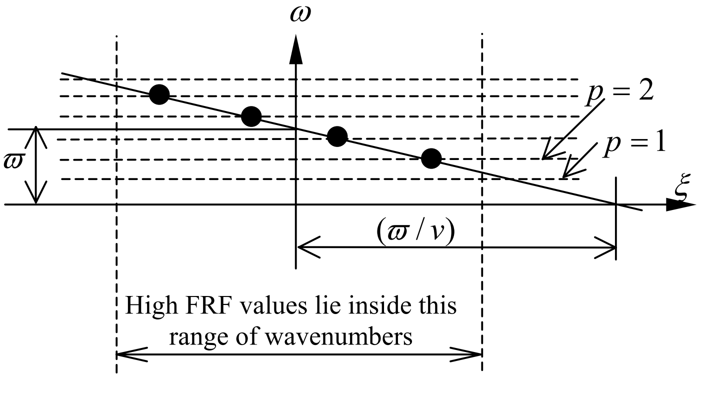

Figure 5.4: Demonstration of the wavenumber region used in calculating equation 5.6. Points with p outside this region are not included in the summation where those included are shown with small filled circles.

The value of G which describes the dynamic load at the wheel-rail interface, depends on the train model used to perform the calculations. By considering the single-degree-of-freedom model first, the roughness under the middle axle in Figure 5.1 can be written as a function of time in the form

$$y_{\Delta} = \Delta \cdot e^{i\varpi t} . \tag{5.8}$$

For this axle the induced force on the wheel-rail interface (see Figure 5.3) is calculated by

$$F_0 = G \cdot e^{i\varpi t} . \tag{5.9}$$

The displacement of the rail under this axle can be calculated from equation 5.6 as

$$y_0 = G \sum_{p=-\infty}^{\infty} \frac{\widetilde{H}_r(\xi_p, \omega_p)}{L} \cdot e^{i\varpi t} . \tag{5.10}$$

The relationship between the dynamic force of the axle and the axle displacement is calculated from the axle equilibrium and given by

$$F_0 = -M_a \frac{d^2(y_{\Delta} + y_0)}{dt^2} \tag{5.11}$$

where M_a is the axle mass. Substituting y_{Δ}, y_0 and F_0 from equations 5.8, 5.10 and 5.9 respectively in equation 5.11 results in

$$G = \frac{-\Psi \cdot \Delta}{1 + (\Psi / L) \cdot \sum\limits_{p=-\infty}^{\infty} \widetilde{H}_r(\xi_p, \omega_p)} \quad \text{with } \Psi = -M_a \varpi^2 . \tag{5.12}$$

This relationship calculates the value of G for the first train model. Note that Ψ is the force-displacement transfer function for an axle. Similarly, the value of G for the second train model in Figure 5.2 can be calculated by using the force-displacement transfer function calculated by solving the equations of motion of the two-degree-of-freedom system with an unsprung mass M_a, sprung mass M_b and a stiffness-damping system of a stiffness k_u and a viscous damping factor c_u. The transfer function is given by

$$\Psi = -M_a \varpi^2 - \frac{M_b \varpi^2 (k_u + c_u i \varpi)}{(k_u + c_u i \varpi - M_b \varpi^2)}. \tag{5.13}$$

5.2 Mean power flow calculations

To calculate the power flow from an underground tunnel due to a moving train, it is important first to provide some expressions for the soil's velocity and stress around the tunnel. To calculate the displacement, the velocity or the stress at any point in the surrounding soil, the displacement FRF of the rail in equation 5.7 is replaced by the appropriate transfer function between the rails and the required position in the soil. For instance, using the coordinate system in Figure C.3, the radial displacement, velocity and stress at a point in the soil with coordinates (r,θ) are calculated by

$$u_r(r,\theta,x,t) = \sum_{p=-\infty}^{\infty} e^{i\xi_p x} e^{i\omega_p t} [\frac{G \cdot \widetilde{u}_r(r,\theta,\xi_p,\omega_p)}{L}], \tag{5.14}$$

$$v_r(r,\theta,x,t) = \sum_{p=-\infty}^{\infty} e^{i\xi_p x} e^{i\omega_p t} [\frac{G \cdot \widetilde{v}_r(r,\theta,\xi_p,\omega_p)}{L}], \tag{5.15}$$

and

$$\tau_{rr}(r,\theta,x,t) = \sum_{p=-\infty}^{\infty} e^{i\xi_p x} e^{i\omega_p t} [\frac{G \cdot \widetilde{\tau}_{rr}(r,\theta,\xi_p,\omega_p)}{L}] \tag{5.16}$$

where $\widetilde{u}_r$, $\widetilde{v}_r$ and $\widetilde{\tau}_{rr}$ are the radial displacement, velocity and stress FRFs respectively of the soil at (r,θ). They are calculated from the models described in Section 4.1, 4.2 or 4.3 by substituting $\widetilde{F}_1 = 0.5$, $\widetilde{F}_2 = 0.5$ and following the procedure in Section 4.5. The relationship between the displacement and the velocity FRF is calculated by equating equation 5.15 to the derivative of equation 5.14 with respect to time to get

$$\tilde{v}_r(r,\theta,\xi_p,\omega_p) = i\omega_p \tilde{u}_r(r,\theta,\xi_p,\omega_p)\,. \tag{5.17}$$

To perform the power calculations, it should be noted that the soil response is a periodic function of time with periodicity (L/v). This period is used to calculate the mean power. For instance, the mean power flow per unit area from the radial stress component is calculated by the following relationship

$$p_r(x,r,\theta) = \frac{1}{(L/v)} \int_{t=0}^{t=L/v} \mathrm{Re}(v_r(r,\theta,x,t)) \cdot \mathrm{Re}(\tau_{rr}(r,\theta,x,t)) \cdot dt\,. \tag{5.18}$$

This integration involves multiplying the real part of equation 5.15 by the real part of equation 5.16. Each of these real parts is made up of a sum of sinusoidal functions with a period of

$$T = \frac{2\pi}{\omega_p} = \frac{L/v}{p}\,. \tag{5.19}$$

To perform the integration in equation 5.18, a single term from the velocity expression in equation 5.15 should be taken and multiplied by all terms of the stress expression in equation 5.16 and perform the integration. Then take the next velocity term and repeat the process. The following relationship is useful to perform the integrations

$$\int_{t_o}^{t_o+T} \sin(\frac{2\pi}{T_1}t+\phi_1)\cdot\sin(\frac{2\pi}{T_2}t+\phi_2)\cdot dt \;= 0 \;\text{ if }\; T = nT_1 = mT_2,\; T_1 \neq T_2 \tag{5.20}$$

$$= \frac{T}{2}\cos(\phi_1-\phi_2) \;\text{ if }\; T = T_1 = T_2 \tag{5.21}$$

where n and m are integers, t_o, ϕ_1, ϕ_2 are arbitrary.

Applying equation 5.20 on the integration in equation 5.18, the non-zero terms in the integration are those which involve the multiplication of sinusoidal functions with the same periods. Hence equation 5.18 can be written as

$$p_r(x,r,\theta)=\frac{v}{L}\sum_{p=-\infty}^{\infty}\int_{t=0}^{t=L/v}\mathrm{Re}(e^{i(\xi_p x+\omega_p t)}\cdot\tilde{v}_p)\cdot\mathrm{Re}(e^{i(\xi_p x+\omega_p t)}\cdot\tilde{\tau}_p)dt \tag{5.22}$$

where $\tilde{v}_p$ and $\tilde{\tau}_p$ are the amplitudes of the velocity and stress waves respectively and are calculated by

$$\tilde{v}_p=\frac{G\cdot\tilde{v}_r(r,\theta,\xi_p,\omega_p)}{L} \tag{5.23}$$

and
$$\tilde{\tau}_p=G\cdot\frac{\tilde{\tau}_{rr}(r,\theta,\xi_p,\omega_p)}{L}. \tag{5.24}$$

Equation 5.22 can be simplified further to

$$p_r(x,r,\theta)=\frac{v}{L}\sum_{p=-\infty}^{\infty}\int_{t=0}^{t=(L/v)}\{\tilde{v}_{pR}\tilde{\tau}_{pR}\cos^2(\xi_p x+\omega_p t)+\tilde{v}_{pI}\tilde{\tau}_{pI}\sin^2(\xi_p x+\omega_p t) \\ -0.5(\tilde{v}_{pR}\tilde{\tau}_{pI}+\tilde{v}_{pI}\tilde{\tau}_{pR})\sin[2(\xi_p x+\omega_p t)]\}\cdot dt \tag{5.25}$$

where the subscripts R and I are used to express the real and the imaginary parts respectively.

Using equation 5.21, the integration of the first two terms in the right hand side is zero and hence

$$p_r(x,r,\theta)=\frac{1}{2}\sum_{p=-\infty}^{\infty}[\tilde{v}_{pR}\tilde{\tau}_{pR}+\tilde{v}_{pI}\tilde{\tau}_{pI}]=\frac{1}{2}\sum_{p=-\infty}^{\infty}\mathrm{Re}[\tilde{v}_p\cdot\tilde{\tau}_p^*] \tag{5.26}$$

or

$$p_r(x,r,\theta)=\frac{|G|^2}{2L^2}\mathrm{Re}\{\sum_{p=-\infty}^{\infty}[\tilde{v}_r(r,\theta,\xi_p,\omega_p)\cdot\tilde{\tau}_{rr}^*(r,\theta,\xi_p,\omega_p)]\} \tag{5.27}$$

where (*) denotes the conjugate of the complex quantity. The significance of this result is its independence of the longitudinal coordinate x. This confines the problem to the two-dimensional plane perpendicular to the longitudinal direction.

As mentioned in Section 5.1, the infinite sum in (5.27) can be approximated as a finite sum performed over the region with large FRFs.

The power radiated through a circular sector with radius r and bounded by the two angles θ_1 and θ_2 can be calculated from the following expressions

$$\begin{aligned}P(\theta_1,\theta_2)=\frac{|G|^2}{2L^2}\int_{\theta_1}^{\theta_2}\sum_{p=-\infty}^{\infty}&\mathrm{Re}[\tilde{v}_x(r,\theta,\xi_p,\omega_p)\cdot\tilde{\tau}_{rx}^*(r,\theta,\xi_p,\omega_p)\\&+\tilde{v}_\theta(r,\theta,\xi_p,\omega_p)\cdot\tilde{\tau}_{r\theta}^*(r,\theta,\xi_p,\omega_p)+\tilde{v}_r(r,\theta,\xi_p,\omega_p)\cdot\tilde{\tau}_{rr}^*(r,\theta,\xi_p,\omega_p)]rd\theta.\end{aligned} \tag{5.28}$$

The three components in this expression take account of the power contributions from the longitudinal, tangential and radial stresses respectively.

5.3 Results for rails with in-phase roughness

Typical results for mean power flow from an underground tunnel are presented in this section. The parameter values used for the track, tunnel and soil are given in Table 4.1.

Figure 5.5(a, b) shows the magnitude of the radial and tangential velocity FRFs at r=10m and θ=120° for a 20Hz floating-slab on uniform support with $\psi=35^\circ$. The FRFs are calculated using the track model in Section 4.1.3 with $\tilde{F}_1=0.5$ and $\tilde{F}_2=0.5$. Only positive frequencies are plotted for no damping in both the track and the PiP models. Note that the significant FRF values lie at wavenumbers close to zero and the zero frequency has no contribution to the response even for low excitation angular frequencies ϖ (see equation 5.17).

The two distinct white curves in Figure 5.5 (a, b) correspond to the track dispersion curves in bending (see also Figure 3.7). In Section 3.2, the dispersion curves are presented for a double beam model which accounts only for the bending behaviour of the track and hence is equivalent to the results presented here. There are two cut-on frequencies which occur at 20Hz and 102Hz. These correspond to the slab resonance and the rail resonance respectively.

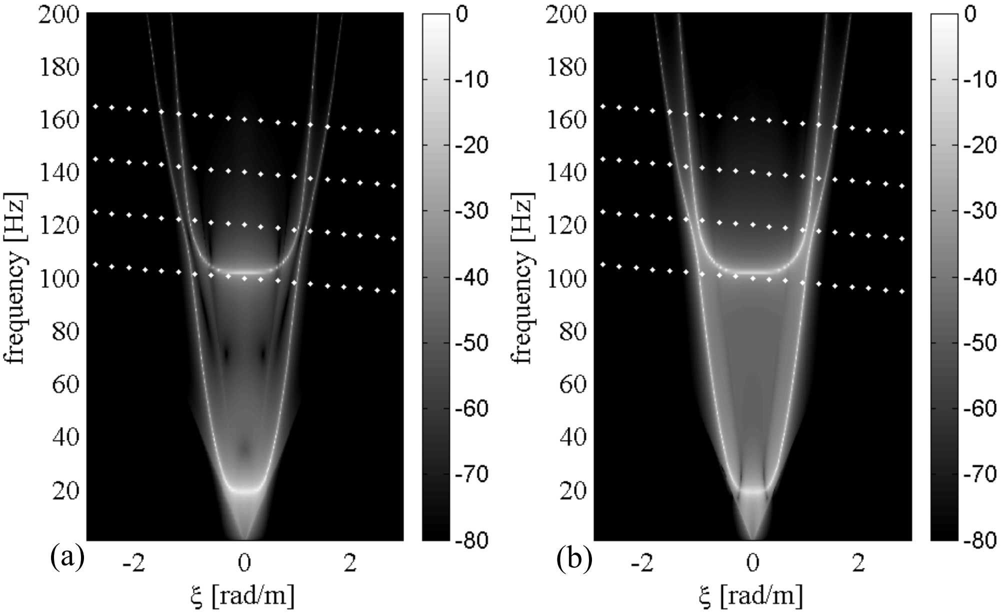

Figure 5.5: The radial and tangential velocity FRFs (dB $_{\text{ref}}$ m/s/N) at r=10m and θ=120° (a) radial velocity FRF, (b) tangential velocity FRF. The results are for a unit input at the rail where the slab has a natural frequency f_n=20 Hz and is supported uniformly with $\psi = 35^\circ$, (No damping is considered). The four parallel dotted lines give $\left|\tilde{v}_r(10,120^\circ,\xi_p,\omega_p)\right|$ and $\left|\tilde{v}_\theta(10,120^\circ,\xi_p,\omega_p)\right|$ in equation (5.28) for velocity $v = 40km/hr$ and excitation frequencies $\bar{f}$ =100,120,140 and 160Hz.

Figure 5.6 shows the longitudinal, tangential and radial mean power flow calculated at r=10m and integrated over a full circle enclosing the tunnel. The curves are calculated for a 20Hz floating-slab on uniform support with $\psi = 35^\circ$ and for a train modelled as unsprung axles with M_a=1000kg, L=20m and moving with velocity v=40km/hr over a roughness with a unit magnitude $\Delta = 1$. The results are calculated at every 1Hz (from 1-200Hz) by averaging the results within 1Hz band (0.5Hz on either side). In each band the results are calculated for every 0.1Hz increment. Averaging is used to smooth curves which fluctuate more severely otherwise. This is on account of discrete sampling of the FRFs (see Figures 5.4 and 5.5). Fluctuations are attributed to the high levels of the FRFs at points along the dispersion curves. At a given excitation frequency, some values of (ξ_p, ω_p) lie on or near the track's dispersion curves, which leads to a peak in the calculated velocity and stress. At another frequency, none of the values of (ξ_p, ω_p) lie on or near the track's dispersion curves, which leads to a trough. Introducing some damping in the track leads to more curve smoothing. This is because damping attenuates the high levels of FRF at dispersion curves of the track. However damping is not introduced in the track in Figures 5.5-5.8 which are presented to verify the power calculations.

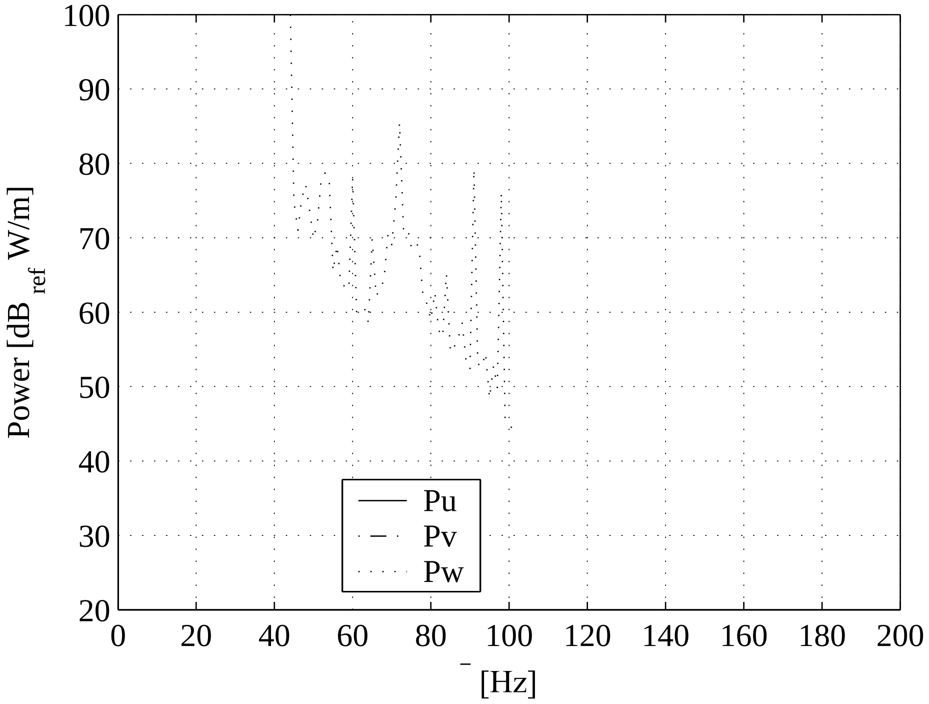

Figure 5.6: The longitudinal P_u, tangential P_v and radial P_w components of the power flow calculated at a circle enclosing the tunnel with radius r =10 m. The results are for train modelled as unsprung-axles moving with velocity 40km/hr over a 20Hz floating-slab track supported uniformly with $\psi = 35^\circ$ (No damping is included).

It can be seen from Figure 5.6 that all components have significant contribution to the power flow at frequencies above 100Hz. However, the longitudinal component has less effect for frequencies below 100Hz.

The power flow method provides an effective tool for checking the PiP model calculations presented in Chapter 4 and Appendix C. The mean power calculated for all closed boundaries enclosing the tunnel wall must be identical if there are no internal sources of power in the soil and no losses for the case of zero soil damping. When no damping is considered for both the track and the PiP model, the mean input-power on the rails should equal the mean output-power radiated from any boundaries enclosing the tunnel. This is confirmed in Figure 5.7 which shows the mean output-power calculated by summing the power components in Figure 5.6 and the mean power input on the rails.

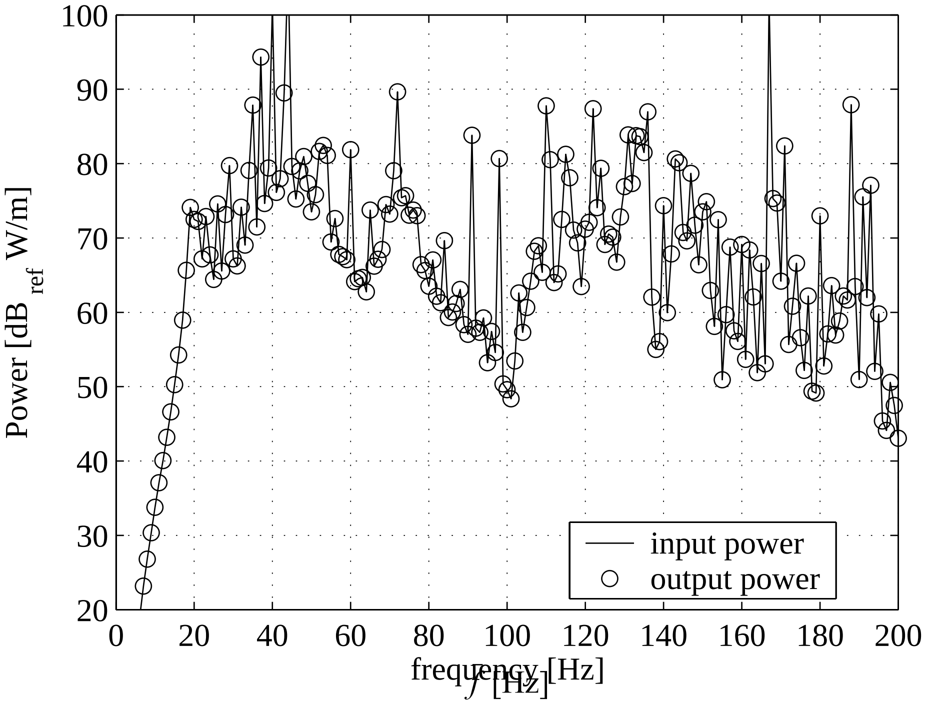

Figure 5.7: Verifying that the input power on the rails is equal to the output power from a circle enclosing the tunnel. The output power is calculated by summing the power components in Figure 5.6.

The mean power flow at any point x in the rail is calculated by integrating the product of the force (equation 5.1) and the rail velocity (calculated from equation 5.7) as follows

$$P_r(x) = \frac{v}{L}\int_{t=0}^{L/v} \mathrm{Re}[\sum_{k=-\infty}^{\infty} G \cdot e^{i\varpi t} e^{ik\varpi L/v} \cdot \delta(x - vt - kL)] \cdot \\ \mathrm{Re}[G \cdot \sum_{p=-\infty}^{\infty} \frac{\widetilde{V}_r(\xi_p,\omega_p)}{L} e^{i\xi_p x} e^{i\omega_p t}]dt \tag{5.29}$$

where $\widetilde{V}_r(\xi_p,\omega_p)$ is the rail velocity FRF at (ξ_p,ω_p) and is calculated from the displacement FRF $\widetilde{H}_r(\xi_p,\omega_p)$ using the following relationship

$$\widetilde{V}_r(\xi_p,\omega_p) = i\omega_p \widetilde{H}_r(\xi_p,\omega_p)\,. \tag{5.30}$$

Rearranging the integration and the summation symbols in equation 5.29 results in

$$P_r(x) = \frac{v}{L}\sum_{p=-\infty}^{\infty}\int_{t=0}^{L/v} \mathrm{Re}[\sum_{k=-\infty}^{\infty} G \cdot e^{i\varpi t} e^{ik\varpi L/v} \cdot \delta(x - vt - kL)] \\ \mathrm{Re}[G \cdot \frac{\widetilde{V}_r(\xi_p,\omega_p)}{L} e^{i\xi_p x} e^{i\omega_p t}]dt \quad . \tag{5.31}$$

In the last expression, only a single delta function of the delta-functions train lies in the range $0 \le t \le (L/v)$. This is the one described by the integer value $k = (x - vt)/L$ in which $0 \le t \le (L/v)$. By using equation A.7, the integration is zero everywhere except at $t = (x - kL)/v$ and hence reduces to

$$P_r(x) = \frac{1}{L}\sum_{p=-\infty}^{\infty} \mathrm{Re}[G \cdot e^{i\varpi(x-kL)/v} e^{ik\varpi L/v}] \cdot \mathrm{Re}[G \cdot \frac{\widetilde{V}_r(\xi_p,\omega_p)}{L} e^{i\xi_p x} e^{i\omega_p (x-kL)/v}]\,. \tag{5.32}$$

Substituting the values of ξ_p and ω_p from equation 5.6 and simplifying

$$P_r(x) = \frac{1}{L}\sum_{p=-\infty}^{\infty} \mathrm{Re}[G \cdot e^{i\varpi x/v}] \cdot \mathrm{Re}[G \cdot \frac{\widetilde{V}_r(\xi_p, \omega_p)}{L} e^{i\varpi x/v}]. \tag{5.33}$$

This result gives the mean input power at any point along the rail. This varies from point to point due to the sinusoidal profile of the roughness. The mean power along the rail P_{rm} is calculated by averaging equation 5.31 along a single wavelength of the roughness $\lambda = (2\pi v / \varpi)$, hence

$$P_{rm} = \frac{\varpi}{2\pi v} \int_{x=0}^{2\pi v/\varpi} \frac{1}{L}\sum_{p=-\infty}^{\infty} \mathrm{Re}[G \cdot e^{i\varpi x/v}] \cdot \mathrm{Re}[G \cdot \frac{\widetilde{V}_r(\xi_p, \omega_p)}{L} e^{i\varpi x/v}] \cdot dx. \tag{5.34}$$

Similar to the integration in equation 5.22, the current integration is evaluated by writing the exponential terms as summations of real and imaginary parts and then using equation 5.21 to evaluate the integrations. This results in

$$P_{rm} = \frac{|G|^2}{2L^2} \sum_{p=-\infty}^{\infty} \mathrm{Re}[\frac{\widetilde{V}_r(\xi_p, \omega_p)}{L}] \tag{5.35}$$

which is used to calculate the input power on the rails in Figure 5.7.

Figure 5.8 shows another comparison, where the mean power flow at a circle enclosing the tunnel wall with radius r=10m due to a moving train modelled as unsprung axles is compared with the corresponding results from the two degree-of-freedom model. The unsprung-axles results are those presented in Figure 5.7. The parameter values used for the two degree-of-freedom systems are an unsprung mass $M_a = 1000kg$, sprung mass $M_b = 3000kg$ and a stiffness-damping system of $k_u = 470kN/m$ and $c_u = 73.55kN/(m/s)$. The suspension parameters are chosen to give a natural frequency of the sprung mass of 2 Hz and viscous damping factor of 0.5.

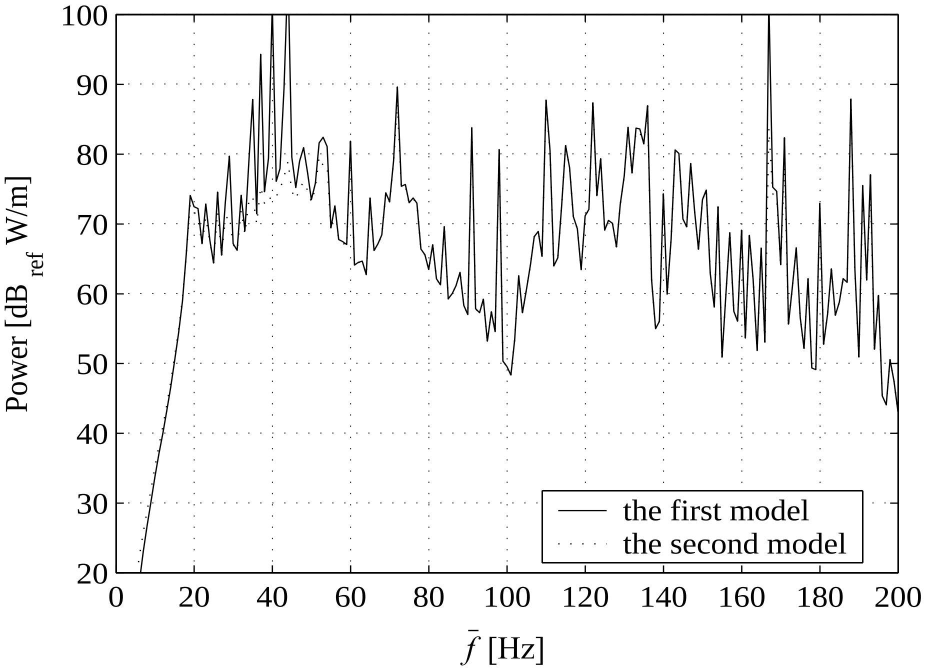

Figure 5.8: The power flow calculated at a circle enclosing the tunnel at 10m using the unsprung-axles model (the first model) shown in Figure 5.1 and the two degree-of-freedom model (the second model) shown in Figure 5.2.

It can be seen that the unsprung-axles model is a good model for a moving train. At high frequencies, *i.e.* above 50Hz, the two models give identical results. This is because the suspension-system isolates the dynamic force of the sprung mass. Some difference can be observed around 42 Hz, at which the sprung mass acts as a tuned-mass that decreases the response around the axle-track resonant frequency as will be discussed later. The unsprung-axles model will be used in the next section to illustrate the effect of various track parameters on the mean power flow.

5.4 Effect of track properties on power flow

The region of most interest for vibration in buildings is that part of the soil above the tunnel since this is where foundations of buildings are located. Power radiated downwards is generally of no interest except perhaps in the case of rigid bedrock, which is not considered here. Hence the mean power radiated upwards from the tunnel is calculated and for the best design of a track this value should be minimised.

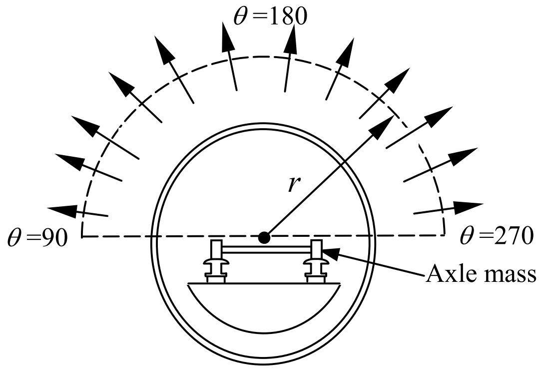

Figure 5.9: Power flow radiated upward calculated at distance r=10 m from the tunnel center due to infinite number of axles moving on the rails. The slab supports are not shown in the diagram.

The power radiated upwards is evaluated using a semicircular boundary of radius r as shown in Figure 5.9. The parameter values of the track and PiP models are same as before (see Table 4.1) but hysteretic damping [17] is now introduced to the track by using complex stiffness for the railpads and the normal and shear slab-bearings, which are calculated at (ξ_p, ω_p) in the form

$$\begin{aligned} &k_{r2} = k_r[1 + i\eta_r \operatorname{sgn}(\omega_p)], \\ &k_{n2} = k_n[1 + i\eta_s \operatorname{sgn}(\omega_p)], \\ \text{and} \quad &k_{s2} = k_s[1 + i\eta_s \operatorname{sgn}(\omega_p)] \end{aligned} \tag{5.36}$$

where $\operatorname{sgn}(\omega_p)$ gives the sign of the angular frequency at p, *i.e.* equal –1 for negative angular frequencies and +1 for positive angular frequencies. Note that the response at zero frequency does not contribute to the power as discussed before (see equation 5.17). The structural damping is used by many authors in modelling of railway tracks under moving loads, see for example [101].

In the forthcoming results, the loss factors of the railpads and slab-bearings are η_r =0.3 and η_s =0.5 respectively. These are the values used by Forrest [29]. For the PiP model, no damping is introduced to maintain a generic behaviour for the calculated results.

The next step before investigating the effect of track parameters is to determine the radius r of the semicircle at which the mean power will be calculated. Figure 5.10 shows the mean power flow for a directly-fixed slab and a 20Hz floating slab uniformly supported with $\psi = 35^\circ$. The results are calculated for excitation frequencies 30Hz and 100Hz. It can be seen that the mean power is effectively invariant for values of $r \geq 10m$ because there is no significant change of power flow across the horizontal part of the boundary. At semicircles near the tunnel wall, *i.e.* $r \approx 3m$, it becomes necessary to account for power flow through the horizontal part of the boundary.

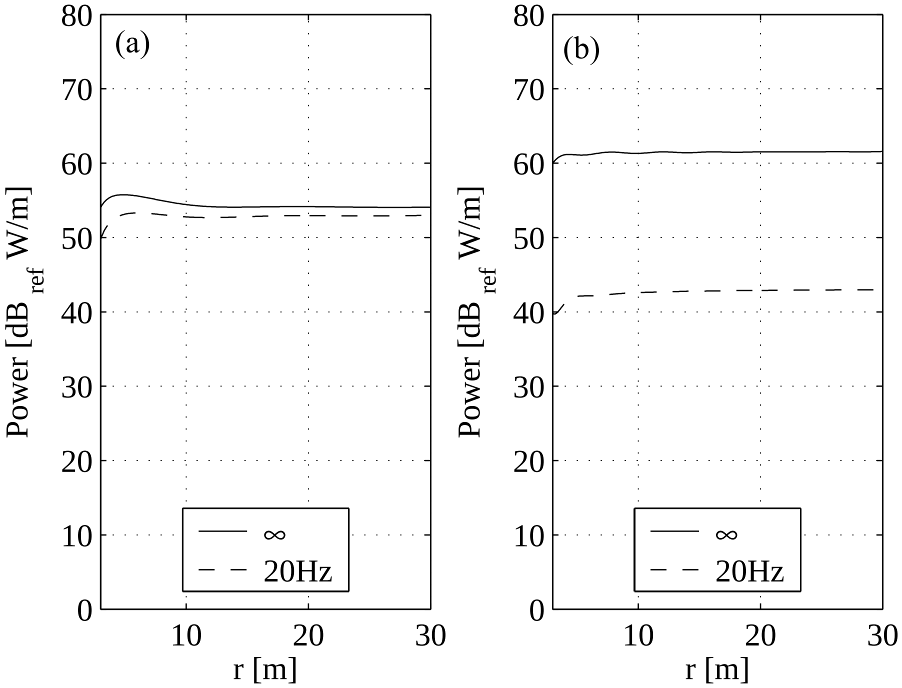

Figure 5.10: Distance effect on the mean power flow radiated upward and calculated along semicircles with $3m \leq r \leq 30m$ from the tunnel center for a directly-fixed slab and 20Hz floating slab of uniform support with $\psi = 35^\circ$. The results are for train velocity 40km/hr and a roughness of excitations: (a) 30Hz and (b) 100Hz.

Figure 5.11 shows the mean power flow for a directly-fixed, 40Hz, 20Hz and 5Hz slab with $\psi = 35^\circ$. The train parameters are M_a = 1000kg, v = 40km/hr and L =20m, where a sinusoidal rail roughness is used with unit magnitude $\Delta = 1$. The most distinguishable peaks for all curves occur at 42 Hz. This frequency is the axle–track resonant frequency. The parameters which control this peak are discussed in Section 5.4.1. Another peak occurs approximately at the cut-on frequency of the slab. For a 40Hz floating-slab, this happens to coincide closely with the axle resonant frequency.

In the following sections, the effects of changing parameters such as the unsprung mass, the bending stiffness of the rail and the slab, the stiffness of the railpads and the slab bearings and the distribution of slab bearings are studied.

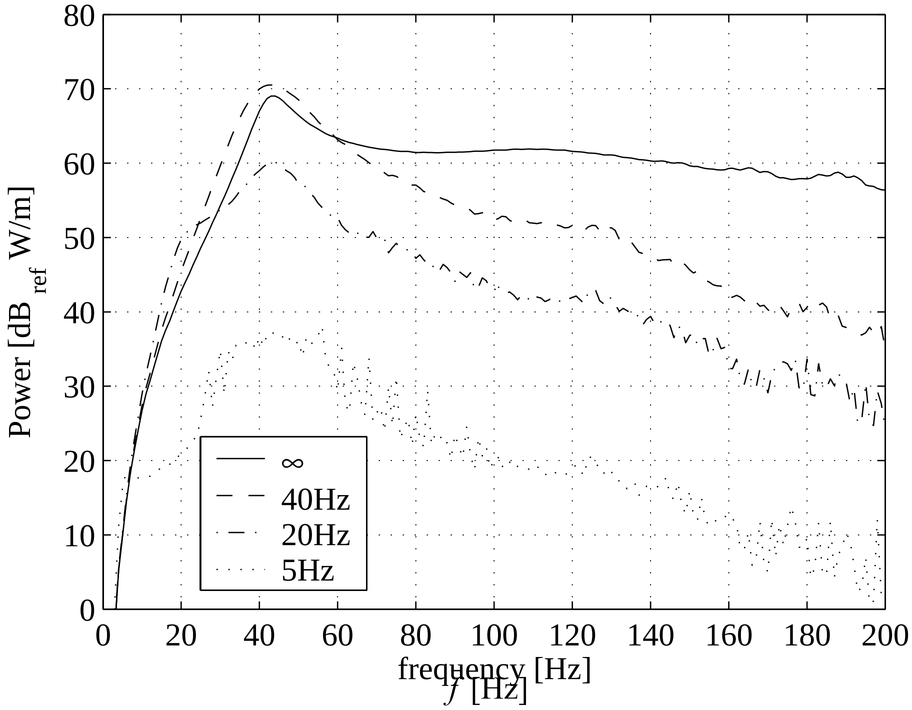

Figure 5.11: Power flow radiated upwards for different slab-bearings stiffness for a train moving with velocity 40km/hr. The slab is supported uniformly with $\psi = 35^\circ$.

5.4.1 Effect of the unsprung-axle mass (axle–track resonance*)*

The axle–track system at resonance can be considered as a single-degree-of-freedom system with a mass equal to the axle mass plus the part of the rails which move up and down with the axle and a stiffness equal to the track stiffness underneath the axle. A closed form equation for calculating the resonance frequency is derived from the resonance of a mass coupled to a beam on Winkler foundation and can be written as

$$(m_b\varpi^2 - k_f)^3 + \frac{{M_a}^4}{64EI_b}\varpi^8 = 0 \tag{5.37}$$

where m_b is the beam mass per unit length, EI_b is the beam bending stiffness, k_f is the foundation stiffness and M_a is the coupled mass. One can prove equation 5.36 by using the displacement of a beam on an elastic foundation under a unit harmonic load with angular frequency ϖ applied at $x = 0$ and given by equation 5.37 which is calculated by [29]

$$y_b(x,t) = \frac{1}{4\alpha^3 EI_b}(e^{\alpha|x|} + ie^{i\alpha|x|})e^{i\varpi t} \text{ with } \alpha^4 = \frac{m_b\varpi^2 - k_f}{EI_b}. \tag{5.38}$$

The value of α in equation 5.38 should be chosen to be with a negative real value if α^4 is positive, while it should be chosen in the third quarter if α^4 is negative. The direct method described in Appendix B can be used to derive equation 5.38. If a mass M_a is coupled to the beam at $x = 0$ and excited by a unit harmonic load with angular frequency ϖ, the mass displacement can be calculated by

$$y_{M_a}(t) = \frac{1}{1/y_b(0,0) - M_a\varpi^2}e^{i\varpi t}. \tag{5.39}$$

From equation 5.39, a resonance occurs when $1/y_b(0,0) = M_a\varpi^2$. Substituting for $y_b(0,0)$ from equation 5.38 and simplifying, results in equation 5.37.

Using the parameters of two rails from Table 4.1, the axle–track resonance occurs at 42 Hz which matches with the results in Figure 5.11. Doubling the unsprung mass to M_a=2000kg leads to the results in Figure 5.12 with an axle-track resonance at 31 Hz. The same value is again calculated by equation 5.36.

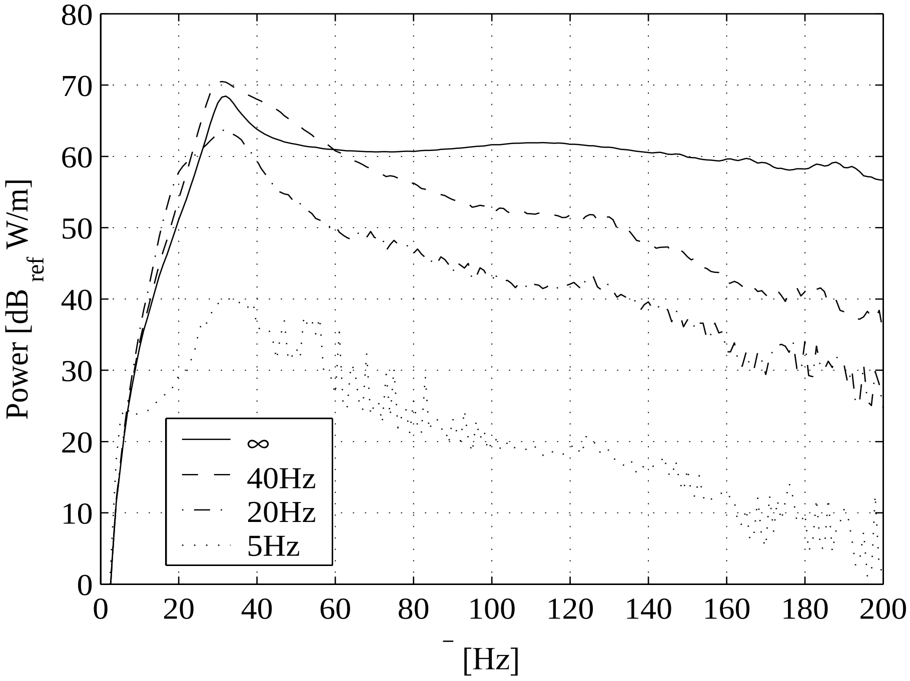

Figure 5.12: The effect of doubling the unsprung axle mass used in Figure 5.11.

5.4.2 Effect of slab bearings

To develop a simple understanding, a train moving on a directly-fixed-slab track can be modelled as a single-degree-of-freedom system. The mass of this system is equal to the equivalent unsprung-axle and the rails, and the stiffness is equal to the equivalent stiffness of the railpads. For such a system, the force at the base is magnified around the natural frequency f_n and vibration isolation is achieved above $\sqrt{2}f_n$. More isolation can be achieved by providing a second mass and spring between the original system and the base. This new two degree-of-freedom system corresponds to a floating-slab track. As mentioned in the literature review, simple systems help understand some of the basic principles, but they do not accurately model tracks in which wave propagation in the track and soil should be considered.

To calculate the effect of using a vibration countermeasure such as a floating slab, the Power Flow Insertion Gain (PFIG) is used and defined by

$$PFIG = 10\log_{10}\left(\frac{P_{after}}{P_{before}}\right) \tag{5.40}$$

where P_{before} and P_{after} are the mean power radiated upwards before and after using the vibration countermeasure. A negative value of the PFIG means a power reduction, *i.e.* vibration isolation, while a positive value means a power magnification. The PFIG is used throughout the rest of this section to evaluate the effect of changing the track parameters and strictly speaking it calculates the change in the mean power rather than the instantaneous power. However it is conventional to be called power flow insertion gain PFIG rather than mean power insertion gain [109].

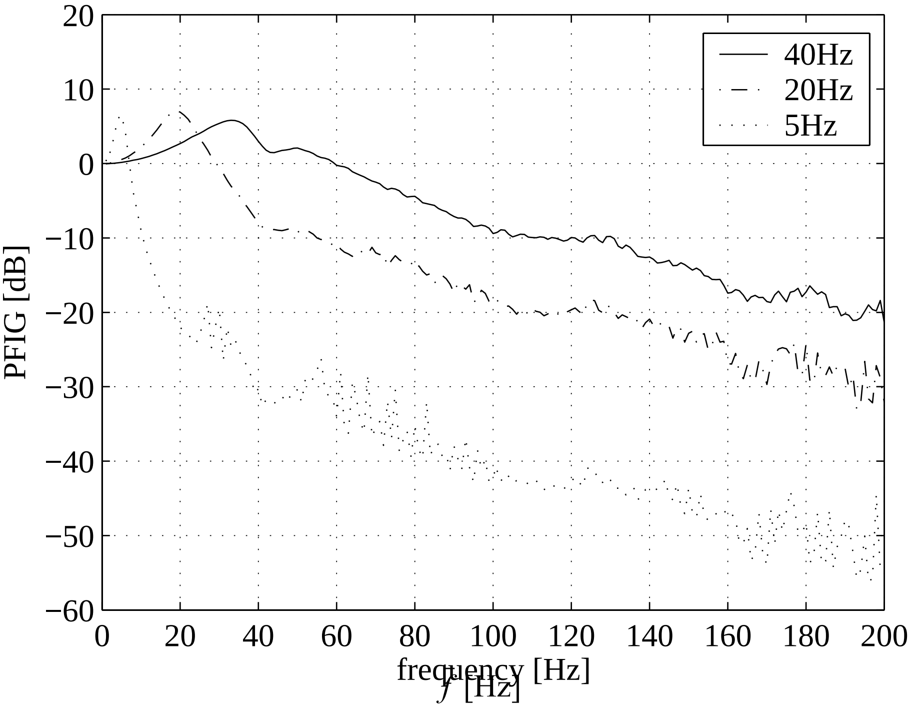

Figure 5.13: The power-flow insertion gain calculated for the results in Figure 5.11.

Figure 5.13 shows the PFIG by floating-slab tracks with frequencies 40 Hz, 20 Hz and 5 Hz respectively. These curves are calculated by equation 5.40 using the results presented in Figure 5.11. The performance of the floating-slab is good at frequencies well above the cut-on frequency of the slab, but it leads to vibration magnification at the cut-on frequency of the slab.

5.4.3 Effect of stiffness of railpads

Figure 5.14 shows the effect of changing the railpad stiffness from 20MN/m/m to 2MN/m/m. In this case four tracks with the same railpads stiffness (20MN/m/m) but with different slab-bearings stiffness are used as a reference, *i.e.* P_{before}. Only the railpads' stiffness for all tracks are changed to (2MN/m/m). Changing the stiffness of railpad leads to a change in the axle–track resonance (from 42Hz to 24Hz) and decreases the power radiation at high frequencies (above 70Hz) by an average of 14dB. The other peaks and troughs are attributed to the periodic-infinite structure behaviour which leads to passing bands and stopping bands [78].

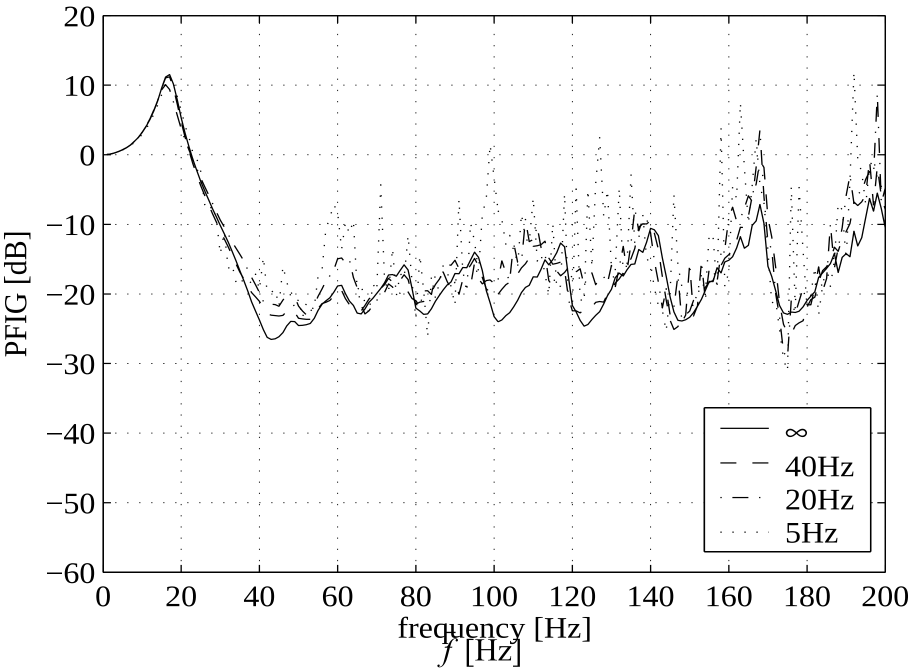

Figure 5.14: Insertion gain due to changing the railpad stiffness from 20MN/m/m to 2MN/m/m for a slab supported uniformly with $\psi = 35^\circ$.

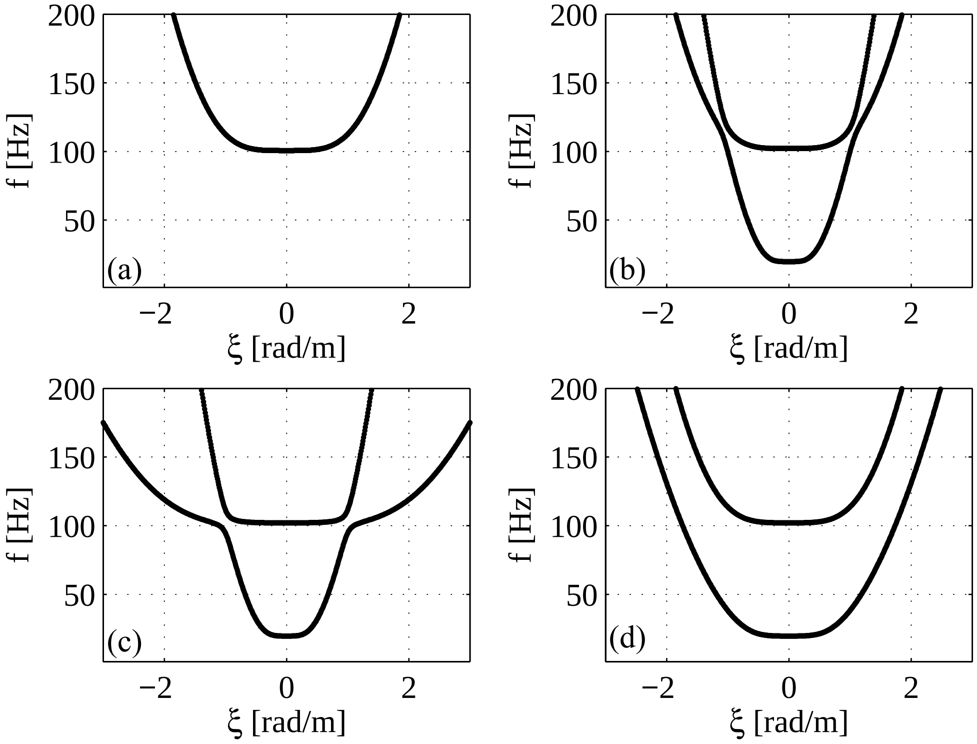

Figure 5.15: Dispersion curves of a track on rigid foundation for bending case. (a) ∞ Hz slab. (b) 20 Hz slab. (c) Same parameters as used in (b) but with 1/10 bending stiffness of rail. (d) Same parameters as used in (b) but with 1/10 bending stiffness of slab.

5.4.4 Effect of bending stiffness of the rails and slab

Figure 5.15.a shows the dispersion curves for a track on rigid foundation with slab bearings of infinite stiffness. Only one mode can propagate along the rails with a cut-on frequency at 102 Hz. Two modes can propagate by using a 20 Hz floating slab; the slab mode and the in-phase-rails mode.

According to equation 5.37, changing the bending stiffness of the rail affects the axle-track resonant frequency because it changes the track stiffness under the axle. Comparing Figures 5.15(b) and 5.15(c) reveals that another effect of decreasing the rail bending-stiffness is the broadening of the rail dispersion curve. The same effect can be seen for the slab dispersion curve by changing the slab bending-stiffness (compare Figure 5.15(d) with 5.15(b)). As shown in Chapter 4, the PiP model strongly attenuates large wavenumbers and its FRFs are confined to small values of wavenumbers. The input-power at the tunnel wall can be decreased by broadening the dispersion curves of the track such that they lie away from the region magnified by the PiP model. This is confirmed by Figure 5.16 (a, b) which shows the PFIG by decreasing the bending stiffness of the rail and the slab respectively to the tenth of their original values.

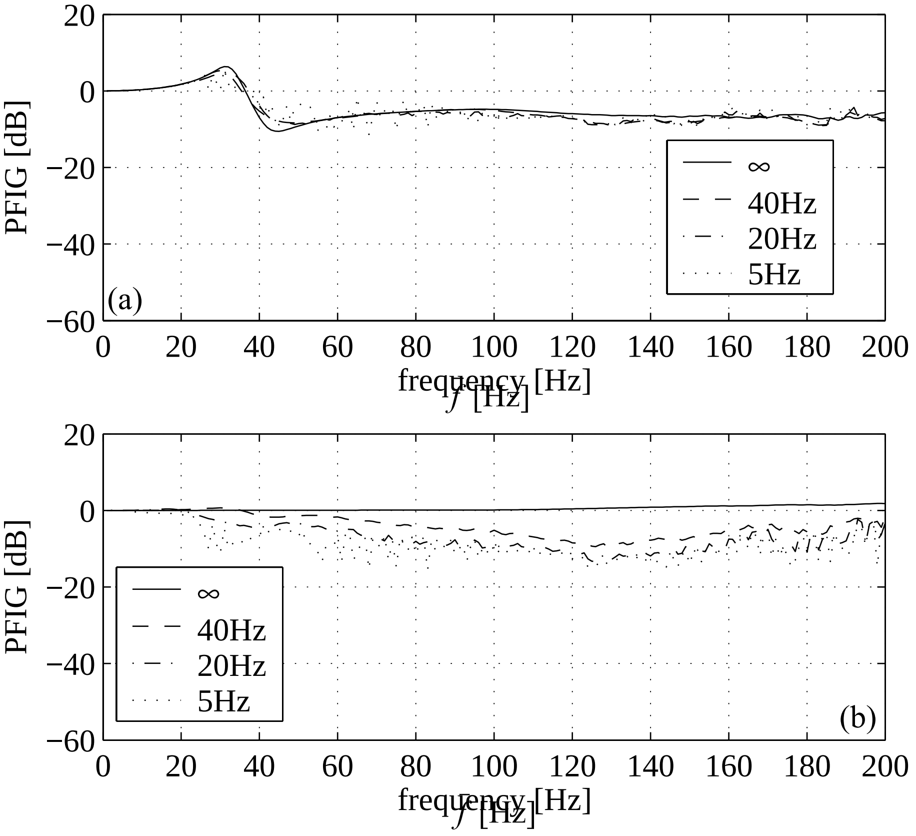

Figure 5.16: Insertion gain due to (a) changing the bending stiffness of rail from 5MPa.m^4 to 0.5MPa.m^4. (b) changing the bending stiffness of slab from 1430MPa.m^4 to 143MPa.m^4. The slab is supported uniformly with $\psi = 35^\circ$.

5.4.5 Effect of distribution of slab bearings

The support distribution controls the Fourier components of the input-load around the tunnel. Generally speaking, more power flow is expected by using a discrete support than a uniform support. This is because the PiP model displacements are more constrained by the latter support.

Figures 5.17.a and 5.17.b show examples of controlling the power radiated upwards by redistributing the supports. The slab bearings are discretely supported via three lines and two lines with $\psi = 35^\circ$ and the PFIG is calculated by using the uniform support with $\psi = 35^\circ$ as a reference. For a discretely supported slab, it is possible to control the angle ψ, such that one of Fourier components (the input-load components) around the tunnel becomes zero. However, this is a subject of further research.

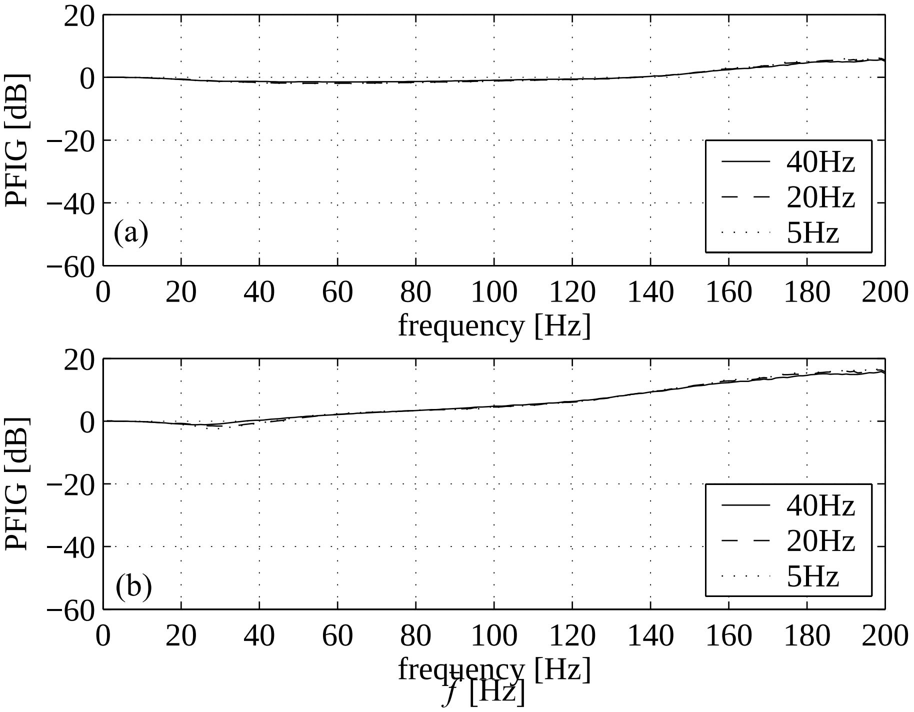

Figure 5.17: Insertion gain due to changing the uniform support to (a) three lines of supports and (b) two lines of supports. The slab bearings angle is constant in all cases and equal to $\psi = 35^\circ$.

Before finishing this section, it is worthwhile to give a general idea about the computational efficiency of the codes which are run using Matlab [75] on a PC computer with 1GB RAM and 2.4GHz processor.

The calculation and saving of matrix $\mathbf{B}_1$ or $\mathbf{B}_2$ (see Appendix C) for a single frequency and for values of $-5 \le \xi \le 5$ take about 0.0475 seconds. This means that for the range of frequency $0 \le f \le 200Hz$ and with spacing 0.1Hz, a total time of 190 seconds is needed to save all values of $\mathbf{B}_1$ and $\mathbf{B}_2$. The rest of the calculation takes: 0.53 seconds for two lines of support, 0.625 seconds for three lines of support and 3.672 seconds for uniform support using $M = 16$ (see equation 4.34-4.38 and equation 4.73). These times are for a single excitation frequency and for all the four slabs used in this section, *i.e.* ∞, 40, 20 and 5Hz.

The codes are written in a way to avoid "for loops" as much as possible to speed up the running times of Matlab. The previous times include calculations of stress and displacements in the radial, horizontal and longitudinal directions on a semicircle above the tunnel with 10m radius and performing the numerical integration in equation 5.28.

Using the running times given above, the results in Figure 5.11 are calculated in 2 hours and 3 minutes (including $\mathbf{B}_1$ and $\mathbf{B}_2$ calculations). The same results for three lines and two lines of supports are calculated in 23.5 minutes and 21.9 minutes respectively.

5.5 Rails with out-of-phase roughness

The derivation for out-of-phase roughness is similar to the one for in-phase roughness in Section 5.1. Figure 5.18 shows the forces on the wheel-rail interface, where 180° phase difference is observed between forces on the two rails. The total force on the left rail $F_L(x,t)$ and the right rail $F_R(x,t)$ can be written as

$$F_L(x,t) = \sum_{k=-\infty}^{\infty} G_w \cdot e^{i\varpi t} e^{ik\varpi L/v} \cdot \delta(x - vt - kL) \tag{5.41}$$

and

$$F_R(x,t) = -\sum_{k=-\infty}^{\infty} G_w \cdot e^{i\varpi t} e^{ik\varpi L/v} \cdot \delta(x - vt - kL). \tag{5.42}$$

where G_w is the wheel force at the wheel-rail interface. In Section 5.1, the force G is used, which expresses the axle force, *i.e.* for two wheels.

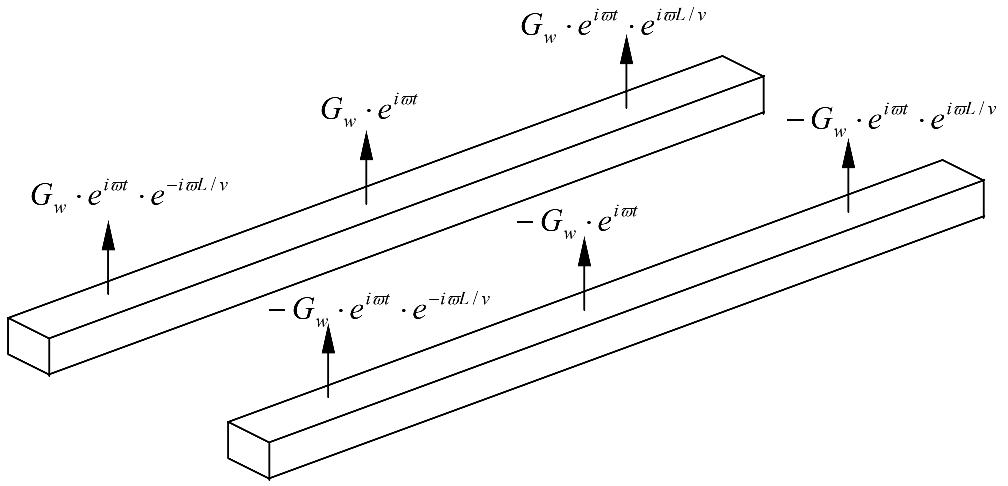

Figure 5.18: Schematic showing the loads on the wheel-rail interface due to out-of-phase sinusoidal roughness.

Following the derivation in Section 5.1, the displacement of the left rail in the wavenumber-frequency domain is written as

$$\tilde{y}_L(\xi,\omega) = 2\pi \sum_{k=-\infty}^{\infty} G_w \cdot [\tilde{H}_{LL}(\xi,\omega) - \tilde{H}_{LR}(\xi,\omega)] e^{-i\xi kL} \cdot e^{-i\varpi kL/v} \cdot \delta(\omega + \xi v - \varpi) \qquad (5.43)$$

where $\tilde{H}_{LL}(\xi,\omega)$ is the displacement FRF of the left rail and is equal to the value of $\tilde{y}_1$ calculated from the full track model in Section 4.1 for $\tilde{F}_1 = 1$ and $\tilde{F}_2 = 0$. $\tilde{H}_{LR}(\xi,\omega)$ is the displacement FRF of the left rail and is equal to the value of $\tilde{y}_1$ in Section 4.1 for $\tilde{F}_1 = 0$ and $\tilde{F}_2 = -1$. Note that the sum $[\tilde{H}_{LL}(\xi,\omega) - \tilde{H}_{LR}(\xi,\omega)]$ can be calculated directly by computing $\tilde{y}_1$ for $\tilde{F}_1 = 1$ and $\tilde{F}_2 = -1$.

Similarly the displacement of the right rail in the wavenumber-frequency domain can be written as

$$\tilde{y}_R(\xi,\omega) = 2\pi \sum_{k=-\infty}^{\infty} G_w \cdot [\tilde{H}_{RL}(\xi,\omega) - \tilde{H}_{RR}(\xi,\omega)] e^{-i\xi kL} \cdot e^{-i\varpi kL/v} \cdot \delta(\omega + \xi v - \varpi). \qquad (5.44)$$

The sum $[\widetilde{H}_{RL}(\xi,\omega)-\widetilde{H}_{RR}(\xi,\omega)]$ is equal to $\widetilde{y}_2$ in Section 4.1 for $\widetilde{F}_1=1$ and $\widetilde{F}_2=-1$.

The wheel force can be calculated from the following equation (compare with equation 5.32)

$$G_w=\frac{-\Psi\cdot\Delta}{1+(\Psi/L)\cdot\sum_{p=-\infty}^{\infty}[\widetilde{H}_{LL}(\xi_p,\omega_p)-\widetilde{H}_{LR}(\xi_p,\omega_p)]}\quad\text{with } \Psi=-M_w\varpi^2. \tag{5.45}$$

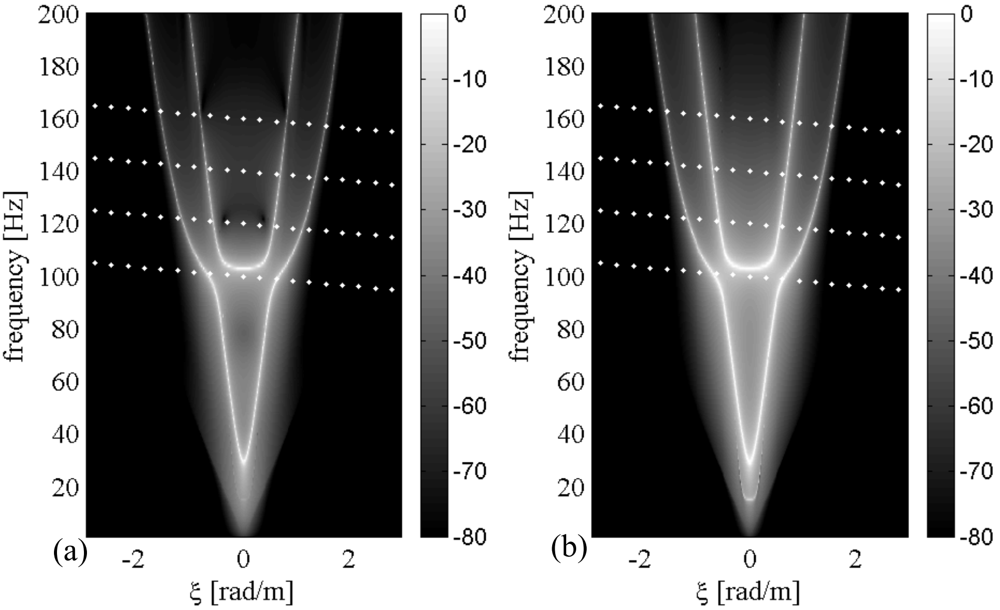

Figure 5.19: The radial and tangential velocity FRFs (dB $_{\text{ref}}$ m/s/N) at r=10m and θ=120° (a) radial velocity FRF, (b) tangential velocity FRF. The results are for a 20 Hz floating-slab uniformly supported with $\psi=35^\circ$ under the rails input-load $\widetilde{F}_1=1$ and $\widetilde{F}_2=-1$ and no damping is considered. The four parallel dotted lines give $\left|\widetilde{v}_r(10,120^\circ,\xi_p,\omega_p)\right|$ and $\left|\widetilde{v}_\theta(10,120^\circ,\xi_p,\omega_p)\right|$ for excitation frequencies $\bar{f}$=100,120,140 and 160Hz.

To calculate the power flow from an underground tunnel for a moving train on rails with out-of-phase roughness, equation 5.28 is used again noting that all the FRFs such as $\tilde{v}_x(r,\theta,\xi_p,\omega_p),\tilde{\tau}_{rx}(r,\theta,\xi_p,\omega_p)$ are calculated for $\tilde{F}_1 = 1$ and $\tilde{F}_2 = -1$ instead of $\tilde{F}_1 = 0.5$ and $\tilde{F}_2 = 0.5$ which are used for rails with in-phase roughness.

Figure 5.19 shows the radial and tangential velocity FRFs at 10m away from the tunnel centre with angle θ=120°, for a 20Hz floating-slab supported uniformly with $\psi = 35^\circ$ under the rail loads $\tilde{F}_1 = 1$ and $\tilde{F}_2 = -1$. The two distinct white curves correspond to the track dispersion curves in torsion with cut-on frequencies occur at 30Hz and 103Hz. These correspond to the slab-torsion mode and the out-of-phase-rails mode respectively. A close look at Figure 5.19.b shows that there is another mode with cut-on frequency at 15Hz. This corresponds to the slab-horizontal mode. However, this mode is much less significant due to the weak coupling between the torsion and the horizontal bending of the slab.

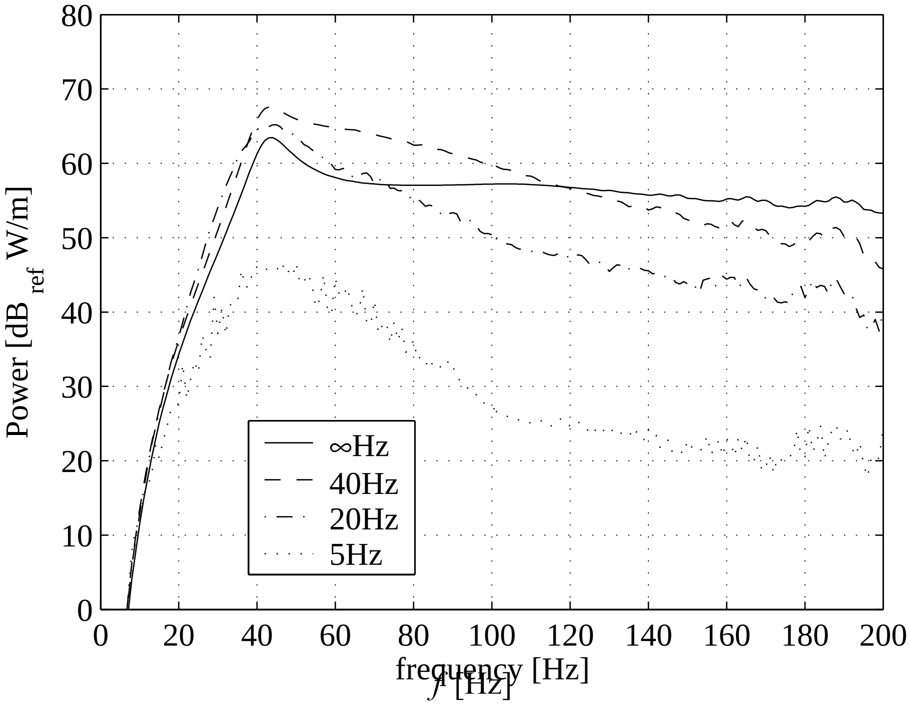

Figure 5.20: Power flow radiated upwards for rails with out-of-phase roughness. The results are for different slab-bearings stiffness and the slab is uniformly supported with $\psi = 35^\circ$.

Figure 5.20 shows the mean power-flow for rails with out-of-phase roughness. The axle-track resonance (or the wheel-track resonance) is still clear and occurs at frequency

42Hz. However, the slab cut-on frequency is now higher than the slab vertical cut-on frequency and this affects the isolation performance at high frequencies. Figure 5.21 shows the PFIG for the results in Figure 5.21. It can be seen that vibration isolation occurs at frequencies 118Hz, 73Hz and 11.4 Hz for 40 Hz, 20 Hz and 5 Hz floating slabs respectively (compare with the results in Figure 5.13 for rails with in-phase roughness). This indicates that the isolation performance can be strongly influenced by the delay of roughness phase.

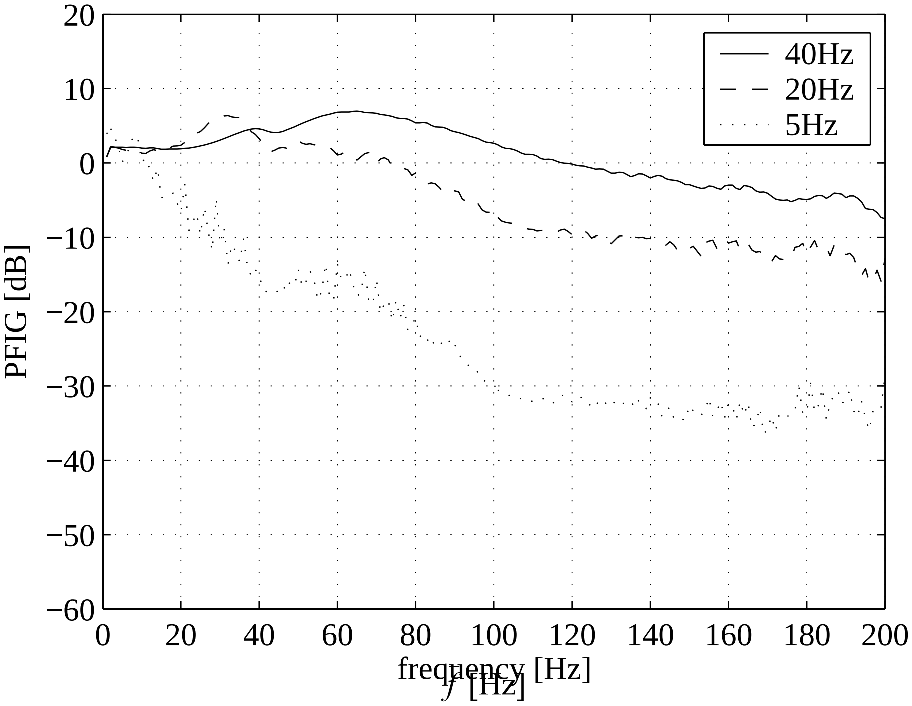

Figure 5.21: The power-flow insertion gain calculated for the results in Figure 5.20.

Conclusions

A new method is presented in this chapter to calculate vibration from underground railways. The method is based on calculating the power flow which radiates upwards due to an infinite train moving along the tunnel. The importance of the infinite-train model is that the power flow is independent of the longitudinal coordinates (in the tunnel direction) and hence reduces the 3D problem to a 2D one. The method incorporates the 3D track-tunnel-soil model developed in Chapter 4 to give a powerful computational tool for designing of tunnels and assessing the performance of vibration countermeasures.

The power-flow insertion gain (PFIG) is used to understand the effects of track properties and vibration countermeasures on power flow. It is shown that the track dispersion curves are a key factor in understanding the isolation performance.

The effects of unsprung mass, railpads, slab bearings, bending stiffness of rails and slab and the support distribution are studied for an in-phase roughness-excitation. The effect of out-of-phase roughness is also investigated and it shows a clear influence on the isolation performance.

Chapter 6

CONCLUSIONS AND FURTHER WORK

This chapter summarises the conclusions reached from the work described in this dissertation and gives some recommendations for further work.

6.1 Conclusions

The main objectives of the work presented in this dissertation are to prosper a better understanding in the context of vibration from underground railways and to develop a computational tool which can be used in the design of tracks in tunnels and to assess the performance of vibration countermeasures. These objectives are addressed in Chapters 3, 4 and 5.

In Chapter 3, floating-slab tracks with continuous and discontinuous slabs are modelled. This is done to understand the effect of harmonic-moving loads on such tracks. The tunnel wall is modelled as a rigid foundation. For a track with a continuous slab, analysis of the dispersion curves is carried out to identify the track resonant frequencies and the critical load velocity. Power calculations are presented to verify the displacement results. For a train moving on such a track with a smooth rail-head, only quasi-static loads arise at the wheel-rail interface, which can be analysed using the static-load solution and this is valid for typical velocities of underground trains.

For a track with a discontinuous slab, three different methods are presented. Two of these are exact and the third is approximate. The approximate method is based on the fact that the load velocity affects the phase of the track response rather than the magnitude for typical velocities of underground trains. A method is also presented to couple a moving train on a track with a discontinuous slab, where dynamic loads are generated at the wheel-rail interface due to slab discontinuity.

A more comprehensive model of a railway track in an underground railway tunnel is presented in Chapter 4. The model is three-dimensional, analytical and accounts for the essential dynamics of the track, tunnel and soil. It comprises a floating-slab track coupled to a tunnel wall which is embedded in an infinite homogenous soil (the pipe-in-pipe model). The coupling is performed in the wavenumber-frequency domain. The waveguide solution is investigated for the different components of the model in order to provide a better understanding of the vibration due to general loads on the rails.

In Chapter 5, a powerful computational tool for the design of tunnels and assessment of vibration countermeasures is developed. The tool incorporates the three-dimensional model of the track, tunnel and soil and calculates power flow due to an infinite train moving along the tunnel. The power-flow insertion gain (PFIG) is used to understand the effects of track properties on vibration from underground railways. The effects of unsprung mass, railpads, slab bearings, bending stiffness of rails and slab, support distribution and the roughness phase are studied. In the work presented in this dissertation, it is found that dispersion curves of the track play an important role in understanding the isolation performance of vibration countermeasures.

6.2 Further work

The models in Chapter 3 consider the effect of oscillating-moving loads on tracks with smooth rail-heads. It will be useful to account for rail roughness, particularly to evaluate the dynamic effect of slab discontinuity on underground moving trains.

The tunnel and soil are modelled in this dissertation using the PiP model, where a thin shell formulation is used to account for the tunnel wall. Further verification of this model can be done by using the elastic continuum formulation to account for the tunnel wall.

The power-flow method developed in Chapter 5 can be used to examine some innovative countermeasures, such as using a concentric layer around the tunnel to reduce the propagating vibration. There is also the effect of support distribution; the computational procedure described in Chapter 5 can be used to find the angle of distribution for the best vibration isolation.

The power-flow results in this dissertation are presented for a roughness excitation with unit magnitude. It is more useful to weight these results with some real measured roughness to identify frequencies leading to high values of power. Having done this, the effect of train velocity can be investigated. Note that the train velocity changes the spectrum of the rail roughness [29] as well as the power results due to a rail roughness with unit magnitude (see Figure 5.4).

Power flow in this dissertation is based on the total mean power which is integrated along some semicircle above the tunnel. It will be useful to investigate the variation of power flow with angle along this semicircle. This is important especially if a specific sector of the semicircle or position in the soil is meant to be *vibration-isolated*.

The PFIG presented in Chapter 5 shows that vibration magnification occurs at low frequencies around the cut-on frequency of the slab (Figure 5.13). This does not usually happen in practice where countermeasures provide an isolation performance even at low excitation frequencies. A recent work by Hunt [51] has explained the reason for this low-frequency isolation. The rail roughness responsible for low excitation frequencies is associated with long wavelengths. This roughness is attributed to the uneven track-bed profile rather than the rail corrugation. By using a vibration countermeasure such as floating-slab track or softer railpads, the rail roughness undergoes a considerable reduction at low frequencies. This means that the rail roughness at low frequencies is decreased by using the vibration countermeasure and hence a negative value of the PFIG is observed. Note that in Chapter 5, the PFIG is calculated for a rail roughness with a unit magnitude before and after using the vibration countermeasure. The work of Hunt can be incorporated with the power-flow method to calculate more practical results for the PFIG.

The PiP model in its current form does not account for a free surface. Some subtle techniques might be used to account for a free-surface using the PiP model. For example the stresses around the tunnel wall due to a moving train can be integrated and used as a line-load in a half-space model, see [111] for more details. Such a model can be used to evaluate the effect of reflection at the free surface on the PFIG.

References

[1] L. Andersen and C.J.C. Jones, *Vibration from a railway tunnel predicted by coupled finite element and boundary element analysis in two and three dimensions.* Proceedings of the Fourth International Conference on Structural Dynamics - EURODYN2002, 2002, Munich, Germany, pp. 1131-1136.

[2] H.E. Apud and A.J. Brammer, *Effects of shock and vibration on humans*. Chapter 44 in the book: Shock and Vibration handbook, 4th edition, C.M. Harris, 1998.

[3] A.E. Armenakas, D.C. Gazis and G. Herrmann, *Free vibrations of circular cylindrical shells*. First edition, Pergamon Press Inc, 1969.

[4] J.J. Azar, *Matrix structural analysis*. Pergamon Press INC, 1972.

[5] P.M. Belotserkovskiy, *Forced oscillations of infinite periodic structures. Applications to railway track dynamics*. Vehicle System Dynamics Supplement, 1998, 28, pp. 85-103.

[6] M.A. Biot, *Propagation of elastic waves in a cylindrical bore containing a fluid.* Journal of Applied Physics, 1952, 23(9), pp. 997-1005.

[7] R.D. Blevins, *Formulas for natural frequency and mode shape*. 4th edition, Krieger Publishing company, Florida.

[8] R. Bogacz, T. Krzyzynski and K. Popp, *On the generalization of Mathew's problem of the vibrations of a beam on elastic foundation*. ZAAM. Z. angew. Math. Mech, 1989, 69(8), pp. 243-252.

[9] A. Bostrom and A. Burden, *Propagation of elastic surface waves along a cylindrical cavity and their excitation by a point force*. Journal of the Acoustical Society of America, 1982, 72(3), pp. 998-1004.

[10] BS 6472:1992, *Guide to evaluation of human exposure to vibration in buildings (1 Hz to 80 Hz)*.

[11] BS 6841:1987, *Guide to measurement and evaluation of human exposure to whole body mechanical vibration and repeated shock*.

[12] CDM: www.cdm.be.

[13] J.S. Chisholm and R.M. Morris, *Mathematical methods in physics.* North-Holand publishing company, Amsterdam, 1964.

[14] S. Chonan, *Moving harmonic load on an elastically supported Timoshenko beam*. ZAAM. Z. angew. Math. Mech, 1978, 58, pp. 9-15.

[15] D. Clouteau, M. Arnst, T.M. Al-Hussaini and G. Degrande, *Freefield vibrations due to dynamic loading on a tunnel embedded in a stratified medium.* Accepted for publication in Journal of Sound and Vibration.

[16] CONVURT: *Control of vibration from underground railway traffic*. www.convurt.com.

[17] S.H. Crandall, *The hysteretic damping model in vibration theory.* Proceedings of the Institution of Mechanical Engineers, Part C: Journal of Mechanical Engineering Science, 1991, 205, pp. 23-28.

[18] D. Cryer, *Modeling of Vibration in Buildings with application to Base Isolation.* PhD Dissertation, University of Cambridge, 1994.

[19] F. Cui, C.H. Chew, *The effectiveness of floating slab track system, Part I. Receptance method*. Applied Acoustics, 2000, 61, pp. 441-453.

[20] G. Degrande and L. Schillemans, *Free field vibrations during the passage of a Thalys high-speed train at variable speed*. Journal of Sound and Vibration, 2001, 247(1), pp. 131-144.

[21] G. Degrande and G. Lombaert, *An efficient formulation of Krylov's prediction model for train induced vibrations based on the dynamic reciprocity theorem*. Journal of the Acoustical Society of America, 2001, 110(3). pp. 1379-1390.

[22] G. Degrande, P. Chatterjee, W.V. Velde, P. Hoelscher, V. Hopman, A. Wang, N. Dadkah and R. Klein, *Vibrations due to a test train at variable speeds in a deep bored tunnel embedded in London clay*. Proceedings of the Eleventh International Congress on Sound and Vibration, 2004, pp. 3055-3062.

[23] J. Dominguez, *Boundary elements in dynamics*. Computational mechanics publications and Elsevier applied science, 1993.

[24] M.L.M. Duarte and M. R. Filho, *Perception threshold of people exposed to sinusoidal vibration*. Proceedings of the Tenth International Congress on Sound and Vibration, 2003, pp. 3791-3798.

[25] D.G. Duffy, *The response of an infinite railroad track to a moving, vibrating mass*. Journal of Applied Mechanics, Transaction of the ASME, 1990, 57, pp. 66-73.

[26] H.I. Epstein, *Circumferential waves for a cylindrical shell supported by a continuum.* Journal of Sound and Vibration, 1978, 58(2), pp. 155-166.

[27] J.M. Fields, *Railway noise and vibration annoyance in residential areas*. Journal of Sound and Vibration, 1979, 66(3). pp. 445-485.

[28] A.P. Filippov, *Steady-state vibrations of an infinite beam on elastic half-space under moving load*. Izvestija AN SSSR OTN Mehanica I Mashinostroenie, 1961, 6, pp. 97-105.

[29] J.A. Forrest, *Modelling of ground vibration from underground railways*. PhD dissertation, Cambridge University, 1999.

[30] F. Frederich, *Die Gleislage – aus fahrzeugtechnischer Sicht [Effect of track geometry on vehicle performance]*. Zeitschrift fur Eisenbahnwesen und Vekehrstechnik – Glaser Annalen, 1984, 108(12), pp. 355-362.

[31] L. Fryba, *Vibration of solids and structures under moving loads*. Noordhoff Publishing, Groningen, 1972.

[32] L. Fryba, *History of Winkler foundation*. Vehicle System Dynamics Supplement, 1995, 24, pp. 7-12.

[33] D.C. Gazis, *Exact analysis of the plane-strain vibrations of thick-walled hollow cylinders*. Journal of the Acoustical Society of America, 1958, 30(8), pp. 786-794.

[34] D.C. Gazis, *Three-dimensional investigation of the propagation of waves in hollow circular cylinders. I. Analytical foundation*. Journal of the Acoustical Society of America. 1959, 31(5), pp. 568-573.

[35] D.C. Gazis, *Three-dimensional investigation of the propagation of waves in hollow circular cylinders. II. Numerical results*. Journal of the Acoustical Society of America, 1959, 31(5), pp. 573-578.

[36] GERB: www.gerb.com.

[37] C.G. Gordon, *Generic vibration criteria for vibration-sensitive equipment*. Proc. SPIE, 1999, 3786, pp. 22-39.

[38] K.F. Graff, *Wave motion in Elastic Solids*, Oxford University Press, London, 1975.

[39] J.E. Greenspon, *Vibrations of thick cylindrical shells.* A letter to the editor. Journal of the Acoustical Society of America, 1959, 31, pp. 1682-1683.

[40] J.E. Greenspon, *Vibrations of thick and thin cylindrical shells surrounded by water*. Journal of the Acoustical Society of America, 1961, 33(10), pp. 1321-1328.

[41] M. Heckl, G. Hauk and R. Wettschureck, *Structure-borne sound and vibration from rail traffic*. Journal of Sound and Vibration, 1996, 193(1), pp. 175-184.

[42] R. Hildebrand, *Vertical vibration attenuation in railway track: a wave approach*. Journal of Sound and Vibration, 2001, 247(5), pp. 857-874.

[43] R. Hildebrand, *Countermeasures against railway ground and track vibrations*. Report at Department of Vehicle Engineering. Stockholm. 2001. (www.lib.kth.se/Sammanfattningar/hildebrand011210.pdf).

[44] H.H. Hung and Y. B. Yang, *A review of researches on ground-borne vibrations with emphasis on those induced by trains*. Proc. Natl. Sci. Counc, 2001, 25(1), pp. 1-16.

[45] H.E.M. Hunt, *Measurement and modelling of traffic-induced ground vibration.* PhD Dissertation, University of Cambridge, 1988.

[46] H.E.M. Hunt, *Modelling of rail vehicles and track for calculation of ground-vibration transmission into buildings*. Journal of Sound and Vibration. 1996, 193(1). pp. 185-194.

[47] H.E.M. Hunt, *Settlement of railway track near bridge abutment.* Proc. Instn Civ. Engrs, Transp., 1997, 123, pp. 68-73.

[48] H.E.M. Hunt, *Base Isolation of buildings: a review*. Proceedings of the Institute of Acoustics, 2000, 22(2), pp. 205-211.

[49] H.E.M. Hunt, *Measures for reducing ground vibration generated by trains in tunnels*. In Noise and vibration from high-speed trains, V.V. Krylov, Thomas Telford, 2001.

[50] H.E.M. Hunt and M.F.M. Hussein, *Ground-borne vibration transmission from road and rail systems - prediction and control*. Chapter 117.a in Handbook of noise and vibration control. To be published by John Wiley & Sons, New York. Edited by M. J. Crocker.

[51] H.E.M. Hunt, *Classification of rail roughness for calculation of ground-vibration and the evaluation of countermeasures*. To appear in Journal of Sound and Vibration.

[52] M.F.M. Hussein and H.E.M. Hunt, *An insertion loss model for evaluating the performance of floating-slab track for underground railway tunnels*. Proceedings of the Tenth International Congress on Sound and Vibration, 2003, pp. 419-426.

[53] H. Ilias and S. Muller, *A discrete-continuous track-model for wheelsets rolling over short wavelength sinusoidal rail irregularities*. Vehicle System Dynamics Supplement, 1994, 23, pp. 221-233.

[54] ISO 2631-2:2003, *Mechanical vibration and shock - Evaluation of human exposure to whole-body vibration - Part 2: Vibration in buildings (1 Hz to 80 Hz).*

[55] L. Jezequel, *Response of periodic systems to a moving load*. Journal of Applied Mechanics. Transaction of the ASME, 1981, 48(3), pp. 613-618.

[56] C.J.C. Jones and J.R. Block, *Prediction of ground vibration from freight trains*. Journal of Sound and Vibration, 1996, 193(1), pp. 205-213.

[57] S.E. Kattis, D. Polyzos and D.E. Beskos, *Modelling of pile wave barriers by effective trenches and their screening effectiveness*. Soil Dynamics and Earthquake Engineering, 1999, 18, pp. 1-10.

[58] A.M. Kaynia, C. Madshus and P. Zackrisson, *Ground vibration from high-speed trains: prediction and countermeasure*. Journal of Geotechnical and Geoenvironmental Engineering, 2001, 126(6), pp. 531-537.

[59] S. Kim and J.M. Roesset, *Dynamic response of a beam on a frequency-independent damped elastic foundation to moving load*. Can. J. Civ. Eng, 2003, 30, pp. 460-467.

[60] J. Kisilowski, Z. Strzyzakowski and B. Sowinski, *Application of discrete-continuous model systems in investigating dynamics of wheelset-track system vertical vibration*. ZAAM. Z. angew. Math. Mech, 1988, 68(4), pp. 70-71.

[61] R. Klaboe, I. H. Turunen-Rise, L. Harvik and C. Madshus, *Vibration in dwellings from road and rail traffic - Part II: Exposure-effect relationships based on ordinal logit and logistic regression models*. Applied Acoustics, 2003, 64(1), pp. 89-109.

[62] R. Klaboe, E. Ohrstrom, I.H. Turunen-Rise, H. Bendtsen and H. Nykanen, *Vibration in dwellings from road and rail traffic - Part III: Towards a common methodology for socio-vibrational surveys*. Applied Acoustics, 2003, 64(1), pp. 111-120.

[63] R. Klein, H. Antest and D. Le Houedec, *Efficient 3D modelling of vibration isolation by open trenches*. Computers and Structures, 1997, 64(1-4), pp. 809-817.

[64] A.V. Kononov and R.A.M. Wolfert, *Load motion on a viscoelastic half-space*. European Journal of Mechanics, A/Solids, 2000, 19, pp. 361-371.

[65] U.G. Kopke, *Condition monitoring of buried gas pipes using a vibrating pig*. PhD Dissertation, University of Cambridge, 1992.

[66] V.V. Krylov, *Effects of track properties on Ground vibrations generated by high-speed trains*. Acta Acustica, 1998, 84, pp. 78-90.

[67] V.V. Krylov, A.R. Dawson, M.E. Heelis and A.C. Collop, *Rail movement and ground waves caused by high-speed trains approaching track-soil critical velocities*. Proc Instn Mech Engrs, 2000, 214, pp. 107-116.

[68] T. Krzyzynski, *On continuous subsystem modelling in the dynamic interaction problem of a train-track-system*. Vehicle System Dynamics Supplement, 1995, 24, pp. 311-324.

[69] H. Lamb, *On the propagation of tremors over the surface of an elastic solid*. Phil. Trans. Roy. Soc., 1904, Ser. A, CCIII 1, pp. 1-42.

[70] J. Lang, *Ground borne vibrations caused by trams and control measures*. Journal of Sound and Vibration, 1988, 120(2), pp. 407-412.

[71] K.T. Lo, *Measurement and modelling of vibration transmission through piled foundation*. PhD Dissertation, University of Cambridge, 1994.

[72] M.J.S. Lowe, *Matrix techniques for modelling ultrasonic waves in multilayered media*. IEEE Transaction on Ultrasonics, Ferroelectrics and Frequency Control, 1995, 42(4), pp. 525-542.

[73] P.M. Mathews, *Vibrations of a beam on elastic foundation*. ZAAM. Z. angew. Math. Mech, 1958, 38, pp. 105-115.

[74] P.M. Mathews, *Vibrations of a beam on elastic foundation II*. ZAAM. Z. angew. Math. Mech, 1959, 39, pp. 13-19.

[75] Matlab 6.5.0.18091 3a, Release 13. the Mathworks, Inc., 2002.

[76] J.A. McFadden, *Radial vibrations of thick-walled hollow cylinders*. Journal of the Acoustical Society of America, 1954, 26(5), pp. 714-715.

[77] D.J. Mead, *Wave propagation and natural modes in periodic systems: I. Mono-coupled systems*. Journal of Sound and Vibration, 1975, 40(1), pp. 1-18.

[78] D.J. Mead, *Wave propagation and natural modes in periodic systems: II. Multi-coupled systems, with and without damping*. Journal of Sound and Vibration, 1975, 40(1), pp. 19-39.

[79] A.V. Metrikine and K. Popp, *Vibration of a periodically supported beam on an elastic half-space*. European Journal of Mechanics. A/Solids, 1999, 18, pp. 679-701.

[80] G.F Miller and H. Pursey, *On the partition of energy between elastic waves in a semi-infinite soild*. Proc. Royal Soc., 1955, 233 Series A, pp. 55-69.

[81] M. Mohammadi and D.L. Karabalis, *Dynamic 3-D soil-railway track interaction by BEM-FEM*. Earthquake Engineering and Structural Dynamics, 1995, 24(9), pp. 1177-1193.

[82] S. Muller, T. Krzyzynski and H. Ilias, *Comparison of semi-analytical methods of analysing periodic structures under a moving load*. Vehicle System Dynamics supplement, 1995, 24, pp. 325-339.

[83] D.E. Newland, *An introduction to random vibrations, spectral and wavelet analysis*. Longman Singapore Publishers Ltd, 1975.

[84] S.L.D. Ng, *Transmission of ground-borne vibration from surface railway trains*. PhD Dissertation, University of Cambridge, 1995.

[85] J.C.O. Nielsen, *Numerical prediction of rail roughness growth on tangent railway track.* Journal of Sound and Vibration, 2003, 267(3), pp. 537-548.

[86] A. Nordborg, *Vertical rail vibration: point force excitation*. Acta Acustica, 1998, 84(2), pp. 280-288.

[87] A. Nordborg, *Vertical rail vibration: parametric excitation*. Acta Acustica, 1998, 84(2), pp. 289-300.

[88] Y. Okumura and K. Kuno, *Statistical analysis of field data of railway noise and vibration collected in an urban area*. Applied Acoustics, 1991, 33, pp. 263-280.

[89] M. Onoe, H.D. McNiven and R.D. Mindlin, *Dispersion of axially symmetric waves in elastic rods*. Journal of Applied Mechanics, Transaction of the ASME, 1962, 29, pp. 729-734.

[90] O.R.E. D151 Specialists' Committee, *Effect of vibration on buildings and their occupants- analysis of the literature and commentary. Report no 4, Question D151: vibrations transmitted through the ground*, 1982. Office for research and experiments of the international union of railways, Utrecht, Netherlands.

[91] Pandrol: www.Pandrol.com.

[92] W.H. Press, B.P. Flannery, S.A. Teukolsky and W.T. Vetterling, *Numerical recipes in Pascal*. Cambridge University Press, Cambridge, 1998.

[93] J.W. Rayleigh, *The theory of sound*. vol. 1, Dover. New York, 1894, Reprint 1945.

[94] P.J. Remington, L.G. Kurzweil and D.A. Towers, *Low-frequency noise and vibration from trains*. Ch.16 from Transportation noise reference book, ed.Nelson, P.M. Butterworth & Co.Ltd., 1987.

[95] K.F. Riley, M.P. Hobson and S.J. Bence, *Mathematical methods for physics and engineering*. Cambridge University Press, Cambridge, 2000.

[96] H. Saito and T. Terasawa, *Steady-state vibrations of a beam on a Pasternak foundation for moving loads*. Journal of Applied Mechanics, Transaction ASME, 1980, 47(4), pp. 879-883.

[97] J.F.M. Scott, *The free modes of propagation of an infinite fluid-loaded thin cylindrical shell*. Journal of Sound and Vibration, 1988, 125(2), pp. 241-280.

[98] X. Sheng, C.J.C. Jones and M. Petyt, *Ground vibration generated by a load moving along a railway track*. Journal of Sound and Vibration, 1999, 228(1), pp. 129-156.

[99] X. Sheng, C.J.C. Jones and D.J. Thompson, *Ground vibration generated by a harmonic load moving in a circular tunnel in a layered ground*. Proceedings of the 10th international meeting on low frequency noise and vibration and its control, 2002, pp. 161-176.

[100] X. Sheng, C.J.C. Jones and D.J. Thompson, *A comparison of a theoretical model for quasi-statically and dynamically induced environmental vibration from trains with measurements*. Journal of Sound and Vibration, 2003, 267(3), pp. 621-635.

[101] X. Sheng, C.J.C. Jones and D.J. Thompson, *A theoretical study on the influence of the track on train-induced ground vibration*. Journal of Sound and Vibration, 2004, 272, pp. 909-936.

[102] X. Sheng, C.J.C. Jones and D.J. Thompson, *A theoretical model for ground vibration from trains generated by vertical track irregularities.* Journal of Sound and Vibration, 2004, 272, pp. 937-965.

[103] C.C. Smith and D.N. Wormley, *Response of continuous periodically supported guideway beams to travelling vehicle loads*. Journal of Dynamic Systems, Measurements and Control, Transaction of the ASME, 1975, 97, pp. 21-29.

[104] C.C. Smith, A.J. Gilchrist and D.N. Wormley, *Multiple and continuous span elevated guideway-vehicle dynamic performance*. Journal of Dynamic Systems, Measurements and Control, Transaction of the ASME, 1975, 97, pp. 30-40.

[105] S. Stearns, *Digital Signal Analysis*. Hayden Book Company, Inc., New Jersey, 1983.

[106] G. Strang, *Linear Algebra and its application*. Third Edition, Harcourt Brace Jovanovich College Publishers, 1988.

[107] J.P. Talbot, *On the performance of base-isolated buildings: A generic model*. PhD Dissertation, University of Cambridge, 2001.

[108] J.P. Talbot and H.E.M. Hunt, *A computationally efficient piled-foundation model for studying the effects of ground-borne vibration on buildings*. Proc. Instn Mech. Engrs. Part C: Journal of Mechanical Engineering Science, 2003, 217, pp. 975-989.

[109] J.P. Talbot and H.E.M. Hunt, *A generic model for evaluating the performance of base-isolated buildings*. Journal of Low Frequency Noise, Vibration and Active Control, 2003, 22(3), pp. 149-160.

[110] J.P. Talbot and H.E.M. Hunt, *The effect of side-restraint bearings on the performance of base-isolated buildings*. Proc. Instn Mech. Engrs, Part C: Journal of Mechanical Engineering Science, 2003, 217, pp. 849-859.

[111] J.P. Talbot, H.E.M. Hunt and M.F.M. Hussein, *A prediction tool for optimisation of maintenance activity to reduce disturbance due to ground-borne vibration from underground railways*. Proceedings of the eighth International Workshop on Railway Noise, 2004, 2, pp. 409-420.

[112] J.P. Talbot, *Base isolation of buildings for control of ground-borne vibration*. Chapter 117.b in Handbook of noise and vibration control. To be published by John Wiley & Sons, New York. Edited by M. J. Crocker.

[113] R.M. Thornely-Taylor, *The prediction of vibration, ground-borne and structure-radiated noise from railways using finite difference method- Part1- theory*. Proceeding of the Institute of Acoustics, 2004, 26(2), pp. 69-79.

[114] A. Trochides, *Ground-borne vibrations in buildings near subways*. Applied Acoustics, 1991, 32, pp. 289-296.

[115] I.H. Turunen-Rise, A. Brekke, L. Harvik, C. Madshus and R. Klaboe, *Vibration in dwellings from road and rail traffic - Part I: A new Norwegian measurement standard and classification system*. Applied Acoustics, 2003, 64(1), pp. 71-87.

[116] G.P. Wilson, H.J. Saurenman and J.T. Nelson, *Control of ground-borne noise and vibration*. Journal of Sound and Vibration, 1983, 87(2), pp. 339-350.

[117] A.B. Wood, *A textbook of sound*. G. Bell and Son Ltd., 1946.

[118] R.D. Woods, *Screening of surface waves in soils*. Journal of the Soil Mechanics and Foundations Division, Proceedings of the American society of Civil Engineers, 1968, SM4, pp. 951-979.

[119] A.D. Wunsch, *Complex variables with applications*. Addison-Wesley Publishing Company, Inc.

[120] D. Zeitlin, *On several applications of the first derivative of a determinant* (in Mathematical Notes). American Mathematical Monthly, 1963, 70(1), pp. 58-60.

Appendix A

BASIC RELATIONSHIPS

The purpose of this appendix is to provide a quick reference to some of the mathematical relationships which are used throughout this dissertation.

1. To transform a function $f(x)$ from the space domain x to the wavenumber domain ξ, see [105] for example

$$F(\xi) = \int_{-\infty}^{\infty} f(x) \cdot e^{-i\xi x} dx \,. \tag{A.1}$$

Equivalently to transform $g(t)$ from the time domain t to the frequency domain ω

$$G(\omega) = \int_{-\infty}^{\infty} g(t) \cdot e^{-i\omega t} dt \,. \tag{A.2}$$

2. To transform the function $F(\xi)$ back to the space domain

$$f(x) = \frac{1}{2\pi} \int_{-\infty}^{\infty} F(\xi) \cdot e^{i\xi x} d\xi \,. \tag{A.3}$$

Equivalently to transform $G(\omega)$ back to the time domain

$$g(t) = \frac{1}{2\pi} \int_{-\infty}^{\infty} G(\omega) \cdot e^{i\omega t} d\omega \,. \tag{A.4}$$

3. Some general Fourier transform relationships

$$\int_{-\infty}^{\infty} 1 \cdot e^{-i\omega t} dt = 2\pi\delta(\omega) . \tag{A.5}$$

$$\int_{-\infty}^{\infty} \frac{d^n g(t)}{dt^n} \cdot e^{-i\omega t} dt = (i\omega)^n G(\omega) \tag{A.6}$$

where $G(\omega)$ is defined by equation A.2.

4. Useful relationships for the delta function, see [83]

$$\int_{-\infty}^{\infty} \delta(t - t_o) F(t) dt = F(t_o) . \tag{A.7}$$

$$\sum_{k=-\infty}^{\infty} \delta(\omega - \frac{2\pi k}{T}) = \frac{T}{2\pi} \sum_{m=-\infty}^{\infty} e^{-i\omega m T} . \tag{A.8}$$

Appendix B

WAVENUMBER-FREQUENCY DOMAIN ANALYSIS

The purpose of this appendix is to demonstrate some basic concepts about wave propagation and coupling of structures in the wavenumber-frequency domain. This is done by analysing a model of a railway track, which comprises of two infinite Euler-Bernoulli beams on an elastic foundation. The model is used in Chapter 3 to account for a floating-slab track with identical inputs on the two rails. Three methods are presented in this appendix: the direct method, the Fourier transformation method and the coupling in the wavenumber-frequency domain method. It is hoped that this appendix will form a good introduction for readers with little knowledge on the subject of wave propagation and/or the analysis in the wavenumber-frequency domain to help understand the contents of this dissertation.

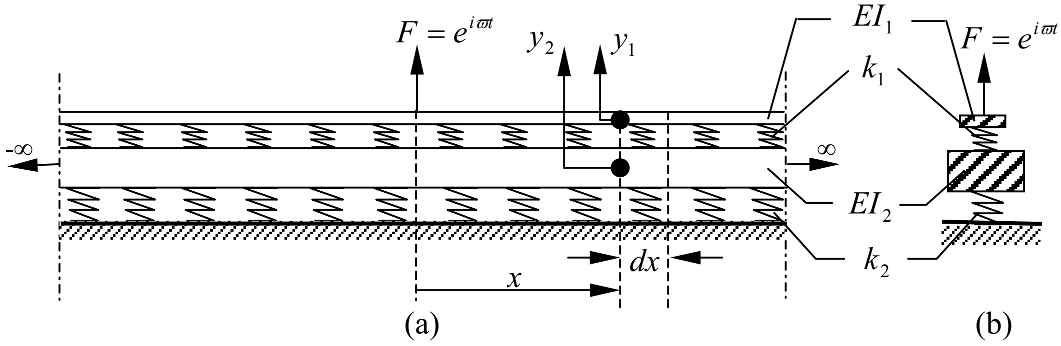

Figure B.1: A floating-slab track subjected to a harmonic load at x=0. (a) Front view. (b) Side view at x=0.

B.1 The direct method

This method treats the input force as a boundary condition for the problem. The model is shown in Figure B.1 with a concentrated harmonic load applied at x=0. The model is split into two semi-infinite structures (left and right of x=0). The input force is described for the right semi-infinite structure as a boundary condition on its left end. For the left semi-infinite structure the input force is described as a boundary condition on its right end. In this way, no forces are applied along the structures apart from at their ends. Due to symmetry, it is enough to analyse only the right semi-infinite structure.

For a two degree-of-freedom element at distance x and with length dx (see Figure B.1.a), equations of motion of this element read

$$EI_1 \frac{\partial^4 y_1}{\partial x^4} + m_1 \frac{\partial^2 y_1}{\partial t^2} = -k_1 (y_1 - y_2) \tag{B.1}$$

and

$$EI_2 \frac{\partial^4 y_2}{\partial x^4} + m_2 \frac{\partial^2 y_2}{\partial t^2} = k_1 (y_1 - y_2) - k_2 y_2 \tag{B.2}$$

where EI_1 is the bending stiffness of both of the rails, EI_2 is the bending stiffness of the floating slab, k_1 is the stiffness of the railpads per unit length, k_2 is the stiffness of the slab bearings per unit length, m_1 is mass of the rails per unit length, m_2 is the mass of the floating slab per unit length, y_1 is the upper beam displacement, *i.e.* the rails displacement, and y_2 is the lower beam displacement, *i.e.* the slab displacement. Equations B.1 and B.2 can be written in matrix form as

$$\begin{bmatrix} EI_1 & 0 \\ 0 & EI_2 \end{bmatrix} \frac{\partial^4 \mathbf{y}}{\partial x^4} + \begin{bmatrix} m_1 & 0 \\ 0 & m_2 \end{bmatrix} \frac{\partial^2 \mathbf{y}}{\partial t^2} + \begin{bmatrix} k_1 & -k_1 \\ -k_1 & k_1 + k_2 \end{bmatrix} \mathbf{y} = \begin{bmatrix} 0 \\ 0 \end{bmatrix} \tag{B.3}$$

where $\mathbf{y} = [y_1, y_2]^T$.

Assuming the following wave form solution for $\mathbf{y}$

$$\mathbf{y} = \begin{bmatrix} y_1 \\ y_2 \end{bmatrix} = \begin{bmatrix} Y_1 \\ Y_2 \end{bmatrix} \cdot e^{i(\omega t + \xi x)} = \mathbf{Y} \cdot e^{i(\omega t + \xi x)}. \tag{B.4}$$

Note that in the theory of differential equations, the solution B.4 is known as a homogeneous solution of the equations in B.3. This also forms a general solution, as the particular solution is equal to zero (due to the zero vector on the right hand side of equation B.3).

Substituting $\mathbf{y}$ from equation B.4 in equation B.3 results in

$$\begin{bmatrix} EI_1\xi^4 + k_1 - m_1\omega^2 & -k_1 \\ -k_1 & EI_2\xi^4 + k_1 + k_2 - m_2\omega^2 \end{bmatrix}\mathbf{Y} = \begin{bmatrix} 0 \\ 0 \end{bmatrix}, \text{ or } [\mathbf{A}]\mathbf{Y} = 0\,. \qquad \text{(B.5)}$$

Equation B.5 has two possible solutions:

- a trivial solution, *i.e.* $\mathbf{Y} = 0$, where there are no displacements;
- a non-trivial solution, for this case $|\mathbf{A}| = 0$, *i.e.* the determinant of matrix $\mathbf{A}$ is equal to zero.

The determinant of matrix $\mathbf{A}$, is a function of ω, ξ and the track parameters: EI_1, EI_2, m_1, m_2, k_1 and k_2. The equation $|\mathbf{A}| = 0$ is known as the *Dispersion equation*. For prescribed track parameters, it is a function of ξ and ω. It will be seen later that the angular frequency ω must equal the excitation frequency ϖ, see Figure B.1. For a positive real value of ω, there are three different wave-type solutions according to the value of ξ in equation B.4:

1. *propagating wave*: this solution arises when ξ is a real quantity. Positive real ξ results in a wave propagating to the left, while negative value results in a wave propagating to the right due to the factor $e^{i(\omega t + \xi x)}$ in equation B.4;

2. *evanescent waves*: this solution arises when ξ is an imaginary quantity. Positive imaginary ξ results in a decaying solution with distance *x*, while negative imaginary ξ results in an increasing solution with *x*;

3. *leaky waves*: this solution arises when ξ is a complex quantity. The solution is propagating (oscillating) but with some decay/increase with distance. The sign of the real part of ξ determines the wave direction while the sign of the imaginary part of ξ determines whether the solution decays or increases with distance.

For the current problem and for a given angular frequency $\omega = \varpi$, the dispersion equation is a polynomial of the eighth order in ξ. The general displacements of the track can be written as

$$\mathbf{y} = (c_1 \mathbf{E}_1 e^{i\xi_1 x} + c_2 \mathbf{E}_2 e^{i\xi_2 x} + \ldots + c_8 \mathbf{E}_8 e^{i\xi_8 x}) e^{i\omega t} . \tag{B.6}$$

The eigenvector $\mathbf{E}_j$ ($j = 1,2,\ldots,8$) is calculated from the following relationship

$$\mathbf{E}_j = \mathbf{D}(2) \tag{B.7}$$

where $\mathbf{D}(2)$ is the second column of the 2×2 matrix $\mathbf{D}$ which is calculated by

$$[\mathbf{S}, \mathbf{V}, \mathbf{D}] = svd(\mathbf{A}_j) \tag{B.8}$$

where the right hand side is the singular value decomposition of matrix $\mathbf{A}$ evaluated at the solution (ξ_j, ω), see [106] for more details.

In Figure B.2.a, solutions of the dispersion equation are plotted at each frequency $f = \omega/(2\pi)$ for the range of frequency 0-100 Hz, using the following track parameters: $EI_1{=}10 MPa.m^2$; $m_1{=}100 kg/m$; $k_1{=}40 MN/m/m$; $EI_2{=}1430 MPa.m^2$; $m_2{=}3500 kg/m$ and $k_2{=}\ 50 MN/m/m$.

At low frequencies, it can be seen from Figure B.2.a, and B.2.b that there are no real solutions ξ and hence the track displacements do not include propagating waves. For higher frequencies, (see Figure B.2.a and B.2.c), real solutions of ξ appear. The frequency at which waves start to propagate is known as the *cut-on frequency*. This frequency is 18.75 Hz for the current parameters.

The final step in this method is to find the coefficients $c_1, c_2, \ldots, c_8$ in equation B.6 by using the boundary conditions.

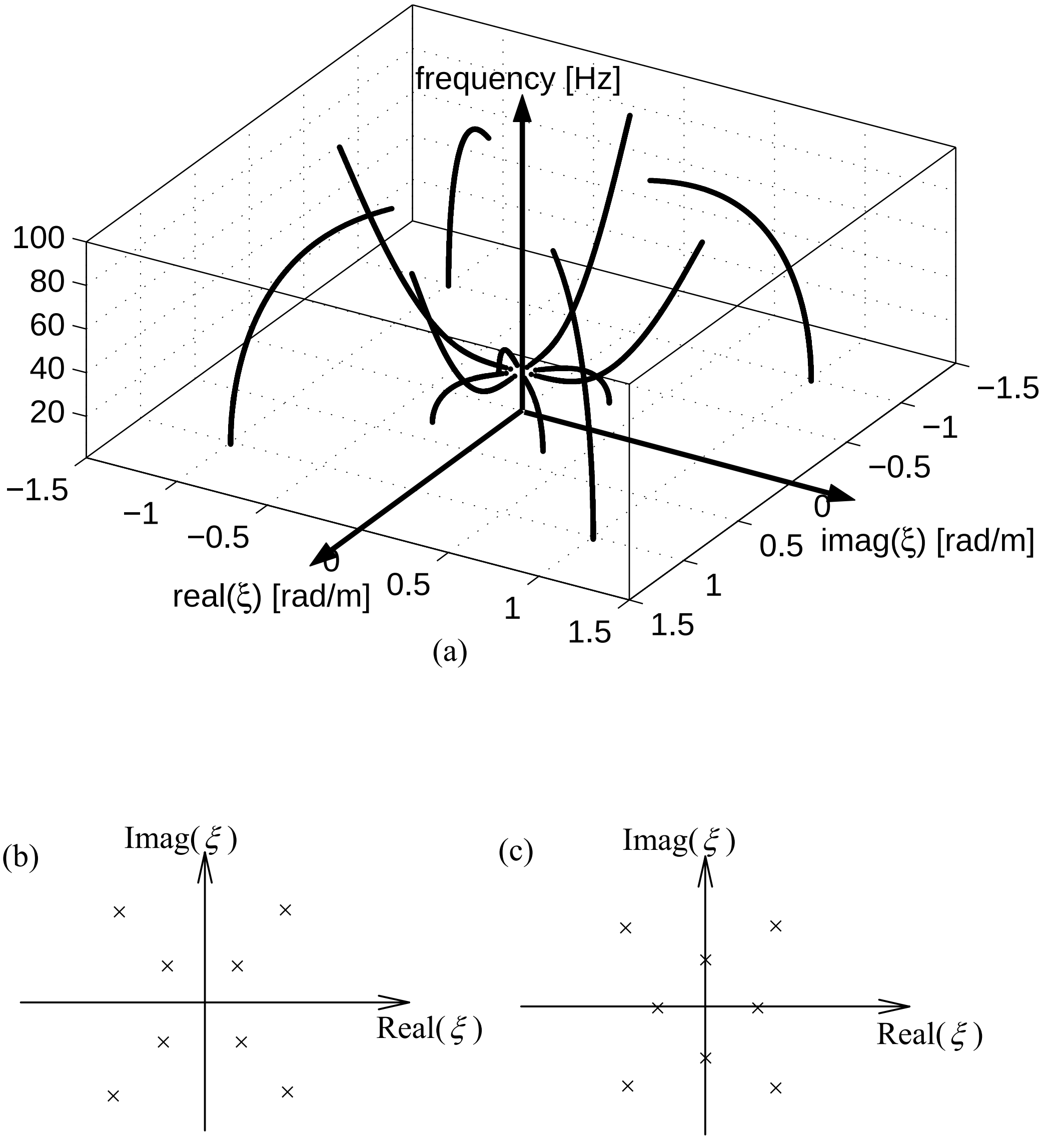

Figure B.2: (a) Roots of the dispersion equation of a floating-slab track on rigid foundation. (b) Cross-sectional view of (a) at frequency below the cut-on frequency, where all solutions are complex quantities. (c) Cross-sectional view of (a) at frequency above the cut-on frequency, where four solutions are complex, two are real and two are imaginary quantities. The (×) sign shows a root position.

For the right semi-infinite structure, *i.e.* for $x > 0$, any coefficient c_j associated with solutions increasing with x should be set to zero, as the displacement does not increase with distance away from the excitation point. Moreover, purely propagating waves should travel only to the right due to absence of sources at $x > 0$, and hence any coefficient associated with real ξ should be set to zero. This means for x>0, only solutions associated with ξ which lie in the first and the second quarter excluding the positive real axis are included in the displacement, which is applicable on four roots (see Figure B.1). A similar argument can be used for the left semi-infinite beams, where in this time only roots which lie in the third and the forth quarter excluding the negative real axis are included in the displacement.

The remaining four coefficients in equation B.6 are determined by using the boundary conditions at x=0. There are four boundary conditions at x=0 due to symmetry and are expressed mathematically in equation B.9: the slope is zero for the upper and the lower beams and the shear force is equal to half of the applied force for the upper and the lower beam. Note that the shear force condition at x=0 for the upper beam is only satisfied if $\omega = \varpi$.

$$\frac{\partial y_1(x=0,t)}{\partial x} = 0, \tag{B.9.a}$$

$$\frac{\partial y_2(x=0,t)}{\partial x} = 0, \tag{B.9.b}$$

$$EI_1 \frac{\partial^3 y_1(x=0,t)}{\partial x^3} = \frac{F}{2}, \tag{B.9.c}$$

and

$$EI_2 \frac{\partial^3 y_2(x=0,t)}{\partial x^3} = 0. \tag{B.9.d}$$

B.2 The Fourier transformation method

Unlike the direct method, this method treats the load as a part of the differential equation rather than a boundary condition. In this method, the governing differential equations of the track are transformed to the wavenumber-frequency domain (ξ, ω). The transformed equations are then simplified and transformed back to the space-time domain (x, t). For the model shown in Figure B.1, the governing differential equations (equivalent to equations B.1 and B.2) read

$$EI_1\frac{\partial^4 y_1}{\partial x^4}+m_1\frac{\partial^2 y_1}{\partial t^2}+k_1(y_1-y_2)=\delta(x)e^{i\varpi t} \tag{B.10}$$

and
$$EI_2\frac{\partial^4 y_2}{\partial x^4}+m_2\frac{\partial^2 y_2}{\partial t^2}-k_1(y_1-y_2)+k_2y_2=0\,. \tag{B.11}$$

Equations A.1 and A.2 are used to transform equations B.10 and B.11 to the wavenumber-frequency domain. The transformed equations read

$$EI_1\xi^4\tilde{y}_1-m_1\omega^2\tilde{y}_1+k_1(\tilde{y}_1-\tilde{y}_2)=2\pi\delta(\omega-\varpi) \tag{B.12}$$

and
$$EI_2\xi^4\tilde{y}_2-m_2\omega^2\tilde{y}_2-k_1(\tilde{y}_1-\tilde{y}_2)+k_2\tilde{y}_2=0\,. \tag{B.13}$$

Equations B.12 and B.13 can be written in matrix form as

$$\begin{bmatrix} EI_1\xi^4+k_1-m_1\omega^2 & -k_1 \\ -k_1 & EI_2\xi^4+k_1+k_2-m_2\omega^2 \end{bmatrix}\tilde{\mathbf{y}}=\begin{bmatrix} 2\pi\delta(\omega-\varpi) \\ 0 \end{bmatrix} \tag{B.14}$$

where $\tilde{\mathbf{y}}=[\tilde{y}_1,\tilde{y}_2]^T$. Note that the matrix on the left hand side is matrix $\mathbf{A}$ in equation B.5. The inverse of matrix $\mathbf{A}$ can be written as

$$[\mathbf{A}]^{-1}=\frac{1}{|\mathbf{A}|}\begin{bmatrix} EI_2\xi^4+k_1+k_2-m_2\omega^2 & k_1 \\ k_1 & EI_1\xi^4+k_1-m_1\omega^2 \end{bmatrix}. \tag{B.15}$$

Equation B.14 can be written as

$$\tilde{\mathbf{y}}(\xi,\omega)=\frac{2\pi\delta(\omega-\varpi)}{|\mathbf{A}|}\begin{bmatrix} EI_2\xi^4+k_1+k_2-m_2\omega^2 \\ k_1 \end{bmatrix}. \tag{B.16}$$

Transforming equation B.16 firstly to the wavenumber-time domain using equation A.4 results in

$$\hat{\mathbf{y}}(\xi,t)=\frac{e^{i\varpi t}}{\left|\mathbf{A}\right|_{@\,\omega=\varpi}}\begin{bmatrix}EI_2\xi^4+k_1+k_2-m_2\varpi^2\\ k_1\end{bmatrix}. \tag{B.17}$$

Now, equation B.17 is transformed to the space-time domain using equation A.3

$$\mathbf{y}(x,t)=\frac{e^{i\varpi t}}{2\pi}\int_{-\infty}^{\infty}\frac{1}{\left|\mathbf{A}\right|_{@\,\omega=\varpi}}\cdot\begin{bmatrix}EI_2\xi^4+k_1+k_2-m_2\varpi^2\\ k_1\end{bmatrix}\cdot e^{i\xi x}d\xi\,. \tag{B.18}$$

It is sufficient for the purpose of demonstration to solve for $y_1(x,t)$ as $y_2(x,t)$ can be found using the same method. From equation B.18, $y_1(x,t)$ can be written as

$$y_1(x,t)=\frac{e^{i\varpi t}}{2\pi}\int_{-\infty}^{\infty}f(\xi)\cdot e^{i\xi x}d\xi \tag{B.19}$$

where $f(\xi)=[(EI_2\xi^4+k_1+k_2-m_2\varpi^2)/(\left|A\right|_{@\,\omega=\varpi})]$. There are two methods for evaluating the integration in equation B.19. The first is by performing the integration directly on the real ξ axis. This is difficult to undertake analytically and hence it can be calculated numerically using the IDFT, *i.e.* the inverse discrete Fourier transform. The other method is to use the results of contour integration from the theory of complex variables, see [119] for example. As shown in Figure B.3, the integration of the function $f(\xi)\cdot e^{i\xi x}$ along the real axis from $\xi_a\rightarrow-\infty$ to $\xi_b\rightarrow\infty$, is equivalent to the closed-path integration along the real axis from ξ_a to ξ_b plus the integration along the semicircle from ξ_b to ξ_a, provided that the integration along the semicircle is zero. This integration along this closed path of integration is equal to the summation of residues evaluated at the poles of the function $f(\xi)\cdot e^{i\xi x}$, *i.e.*

$$\int_{-\infty}^{\infty}f(\xi)\cdot e^{i\xi x}d\xi=2\pi\cdot i\cdot\sum_{j=1}^{j=pp}R[f(\xi)\cdot e^{i\xi x},\xi_j] \tag{B.20}$$

where $R[f(\xi)\cdot e^{i\xi x},\xi_j]$ is the residue of $f(\xi)\cdot e^{i\xi x}$ at the pole ξ_j, pp is the total number of poles enclosed by the contour. The poles of $f(\xi)\cdot e^{i\xi x}$ are the singular points of the function and can be calculated by equating the denominator of $f(\xi)$ to zero, *i.e.*

$$\left|A\right|_{@\,\omega=\varpi}=0\,. \tag{B.21}$$

The last equation is identical to the dispersion equation as calculated in the previous section (note in the previous section that $\omega=\varpi$). As mentioned before, this equation has eight solutions at any angular frequency $\omega=\varpi$ and they are plotted in Figure B.2. The integration along the semicircle in Figure B.3 (substituting $\xi=R\cdot e^{i\theta}$) is

$$\int f(\xi)d\xi=\int_{\theta=0}^{\theta=\pi}\frac{EI_2(R\cdot e^{i\theta})^4+k_1+k_2-m_2\omega^2}{\left|A\right|_{@\,\omega=\varpi}}\cdot(R\cdot i\theta)(e^{i(R\cos\theta+iR\sin\theta)x})d\theta\,. \tag{B.22}$$

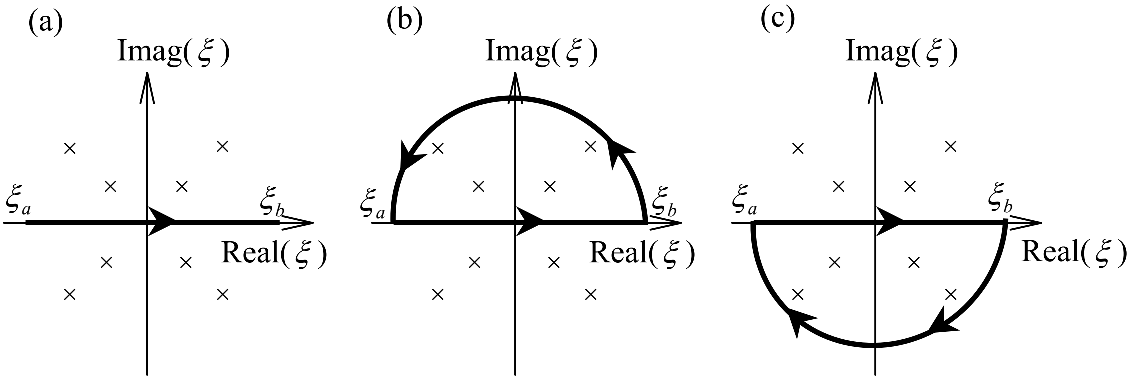

Figure B.3: The integration of the function $f(\xi)e^{i\xi x}$ along the real axis from $\xi_a\to-\infty$ to $\xi_b\to\infty$ in (a) is equivalent to the integration along the real axis from ξ_a to ξ_b plus the semicircle from ξ_b to ξ_a in (b) or (c). The choice depends upon whether the integration along the semicircle is zero.

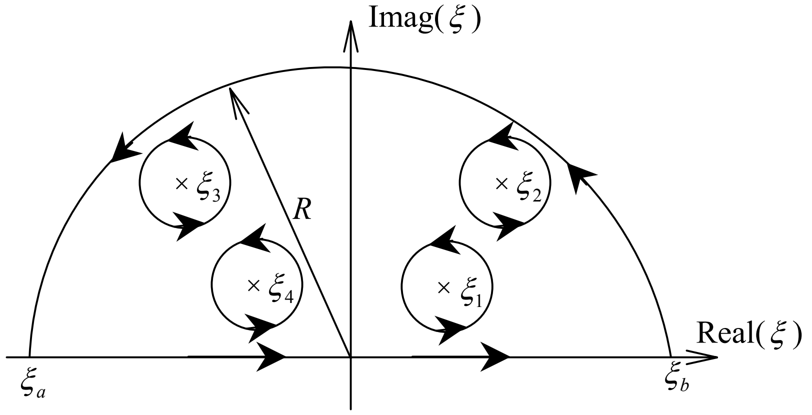

Figure B.4: The integration of the function $f(\xi)e^{i\xi x}$ on the closed contour along the real axis from ξ_a to ξ_b plus the semicircle from ξ_b to ξ_a is equivalent to the sum of integrations along the closed paths around the poles which lie inside the closed contour. The integration around a pole ξ_j is calculated by $2\pi \cdot i \cdot R[f(\xi)e^{i\xi x}, \xi_j]$.

The factor $e^{-Rx\sin\theta}$ in the last integration determines whether the integration will approach infinity or zero when R tends to infinity. In the first and the second quarter $\sin\theta > 0$ and the integration only tends to zero for positive values of x. Thus for x>0, the closed integration in Figure B.3.b is used. For x<0 a different contour is used, in which the semicircle passes through the third and fourth quarter, see Figure B.3.c. In this way, the integration along the semicircle part always tends to zero when R tends to infinity.

Once the path is chosen, the integration along a closed contour is replaced by a summation of the residues at the interior poles [119]. For the current problem if none of the poles lie on the real axis (Figure B.4), equation B.19 can be simplified to

$$y_1(x,t) = 2\pi \cdot i \frac{e^{i\varpi t}}{2\pi} \sum_{j=1}^{j=4} \left(\frac{EI_2\xi_j^4 + k_1 + k_2 - m_2\varpi^2}{EI_1 EI_2 \prod_j} \right) e^{i\xi_j x} \quad \text{for } x \geq 0 \qquad \text{(B.23.a)}$$

and $$y_1(x,t) = -2\pi \cdot i \frac{e^{i\varpi t}}{2\pi} \sum_{j=5}^{j=8} \left(\frac{EI_2\xi_j^4 + k_1 + k_2 - m_2\varpi^2}{EI_1 EI_2 \prod_j} \right) e^{i\xi_j x} \quad \text{for } x < 0 \qquad \text{(B.23.b)}$$

where $\prod_j = (\xi_j - \xi_1)(\xi_j - \xi_2)\ldots(\xi_j - \xi_{j-1})(\xi_j - \xi_{j+1})\ldots(\xi_j - \xi_8)$,

$\xi_1, \xi_2, \ldots, \xi_8$ are the roots of dispersion equation at $\omega = \varpi$,

$\xi_1, \xi_2, \xi_3, \xi_4$ are the roots in the first and the second quadrants,

and $\xi_5, \xi_6, \xi_7, \xi_8$ are the roots in the third and the fourth quadrants.

The additional minus sign in equation B.23.b is to account for the clockwise direction of the contour around the poles, see Figure B.3.c.

Note that the displacement in equations B.23.a and B.23.b comprises of the three wave-type solutions discussed before, *i.e.* propagating, evanescent and leaky waves. It can be proved that this solution is identical to the one calculated by the direct method in the previous section.

For frequencies above the cut-on frequency some poles lie on the real axis and the integration path is modified to include or exclude the pole using the same physical argument used in the previous section. Figure B.5 shows the appropriate contour for $x \geq 0$ and $x < 0$ for the case in Figure B.2.c, *i.e.* for a frequency above the cut-on frequency. For instance, in Figure B.5.a the positive real value root is excluded by a small semicircle as it produces a propagating wave to the left due to the factor ($e^{i\varpi t} \cdot e^{i\xi x}$) in equation B.23.a.

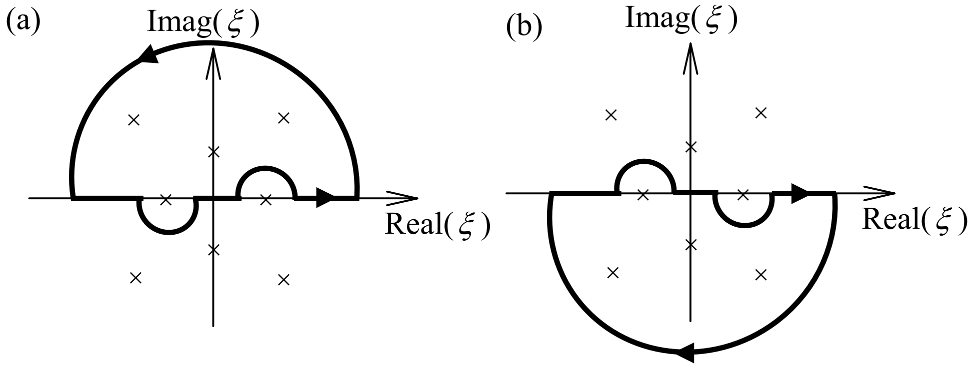

Figure B.5: The contour path for a frequency above the cut-on frequency, where some poles (solutions) lie on the real axis: (a) for $x \geq 0$ and (b) for $x < 0$.

B.3 Coupling in the wavenumber-frequency domain

The method of coupling in the wavenumber-frequency domain is demonstrated in this section by analysing the floating-slab track in Figure B.1. This section presents a good introduction to the theory which is used in Chapter 4 with a more complicated structure.

The model in Figure B.1 is split into two structures. The first structure is the upper beam as shown in Figure B.6.b, which accounts for the rails. The second structure is a beam on elastic foundation as shown in Figure B.6.c, which accounts for the floating slab and the slab bearings. These two structures are coupled via railpads which are uniformly distributed longitudinally throughout the length.

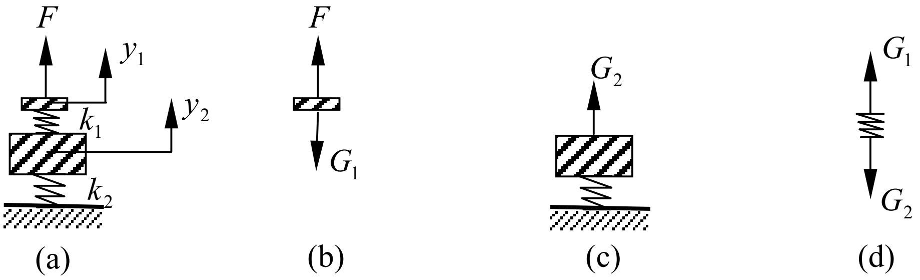

Figure B.6: Coupling of structures in the wavenumber-frequency domain. (a) The coupled structure. (b) The first structure; a free beam. (c) The second structure; a beam on an elastic foundation. (d) The railpads which connect the two structures.

An essential part of the analysis is to find the *frequency response functions* (FRFs) of the two structures separately in the wavenumber-frequency domain.

The generalised differential equation for the first structure, *i.e.* a free Euler-Bernoulli beam is

$$EI_1 \frac{\partial^4 z_1}{\partial x^4} + m_1 \frac{\partial^2 z_1}{\partial t^2} = P_1 \tag{B.24}$$

where z_1 is the vertical displacement of the free beam and P_1 is the total force on the beam in the vertical direction.

There are two methods for calculating the FRF of this structure:

1. Transforming the differential equation to the wavenumber-frequency domain directly using equations A.1, A.2 and A.6, which results in

$$EI_1\xi^4\tilde{z}_1 - m_1\omega^2\tilde{z}_1 = \tilde{P}_1. \tag{B.25}$$

The displacement FRF of the free beam is defined as the vertical displacement of the free beam for a unit vertical load in the wavenumber-frequency domain. Applying this definition on equation B.25, results in

$$\tilde{H}_{11} = \frac{\tilde{z}_1}{\tilde{P}_1} = \frac{1}{EI_1\xi^4 - m_1\omega^2}. \tag{B.26}$$

2. By using the following expressions for the displacement and force

$$z_1 = \tilde{z}_1 e^{i(\xi x+\omega t)} \text{ and } P_1 = \tilde{P}_1 e^{i(\xi x+\omega t)}. \tag{B.27}$$

Substituting these expressions of z_1 and P_1 in equation B.24, results in the displacement FRF of the free beam as in equation B.26.

To explain why the two methods lead to the FRF, consider the force in equation B.25, *i.e.* $\tilde{P}_1$. This force is in the wavenumber-frequency domain and concentrated at specific wavenumber ξ and angular frequency ω. It can be expressed as a function in the wavenumber-frequency domain $(\bar{\xi},\bar{\omega})$ as $\tilde{P}_1 \cdot \delta(\bar{\xi}-\xi)\cdot\delta(\bar{\omega}-\omega)$, where $(\bar{\xi},\bar{\omega})$ are used in this context to express the wavenumber-frequency coordinates. Transforming this expression to the space-time domain, using equation A.3 and A.4

$$\frac{1}{(2\pi)^2}\int_{\bar{\omega}=-\infty}^{\infty}\int_{\bar{\xi}=-\infty}^{\infty}\tilde{P}_1\cdot\delta(\bar{\xi}-\xi)\cdot\delta(\bar{\omega}-\omega)e^{i(\bar{\xi}x+\bar{\omega}t)}d\bar{\xi}d\bar{\omega} = \frac{1}{(2\pi)^2}\tilde{P}_1\cdot e^{i(\xi x+\omega t)}. \tag{B.28}$$

In the same way the transformation of the displacement in equation B.25 to the space-time domain gives

$$\frac{1}{(2\pi)^2}\int_{\overline{\omega}=-\infty}^{\infty}\int_{\overline{\xi}=-\infty}^{\infty}\tilde{z}_1\cdot\delta(\overline{\xi}-\xi)\cdot\delta(\overline{\omega}-\omega)e^{i(\overline{\xi}x+\overline{\omega}t)}d\overline{\xi}d\overline{\omega}=\frac{1}{(2\pi)^2}\tilde{z}_1\cdot e^{i(\xi x+\omega t)}. \tag{B.29}$$

By multiplying the input and the output in equations B.28 and B.29 by $(2\pi)^2$, it can be seen that the FRF calculated by the second method is equivalent to the one calculated by the first method.

For the second structure, *i.e.* a beam on elastic foundation, the generalised differential equation in the space-time domain reads

$$EI_2\frac{\partial^4 z_2}{\partial x^4}+m_2\frac{\partial^2 z_2}{\partial t^2}+k_2 z_2=P_2 \tag{B.30}$$

where z_2 is the vertical displacement of the beam and P_2 is the applied force on the beam in the vertical direction.

To calculate the FRF of this structure, substitute $z_2=\tilde{z}_2 e^{i(\xi x+\omega t)}$ and $P_2=\tilde{P}_2 e^{i(\xi x+\omega t)}$ and rearrange to get

$$\tilde{H}_{22}=\frac{\tilde{z}_2}{\tilde{P}_2}=\frac{1}{EI_2\xi^4-m_2\omega^2+k_2} \tag{B.31}$$

where $\tilde{H}_{22}$ is the FRF of the beam on elastic foundation in Figure B.6.c.

It is possible now to couple the two structures. For the vertical equilibrium of forces in the space-time domain, one can write (see Figure B.6.d)

$$G_1=G_2=G. \tag{B.32}$$

This equation is transformed to the wavenumber-frequency domain by substituting $G_1=\tilde{G}_1 e^{i(\xi x+\omega t)}$, $G_2=\tilde{G}_2 e^{i(\xi x+\omega t)}$ and $G=\tilde{G}e^{i(\xi x+\omega t)}$ to give

$$\widetilde{G}_1 = \widetilde{G}_2 = \widetilde{G}\,. \tag{B.33}$$

The rest of the analysis is carried out directly in the wavenumber-frequency. The equations of motion are written for the two structures and the railpads as follow

$$\widetilde{y}_1 = \widetilde{H}_{11}(\widetilde{F} - \widetilde{G})\,, \tag{B.34}$$

$$\widetilde{y}_2 = \widetilde{H}_{22}\widetilde{G}\,, \tag{B.35}$$

and

$$\widetilde{G} = k_1(\widetilde{y}_1 - \widetilde{y}_2)\,. \tag{B.36}$$

Solving equations B.34, B.35 and B.36 for $\widetilde{y}_1$ results in

$$\widetilde{y}_1 = \frac{\widetilde{H}_{11}(1 + k_1\widetilde{H}_{22})}{1 + k_1(\widetilde{H}_{11} + \widetilde{H}_{22})}\,. \tag{B.37}$$

Substituting $\widetilde{H}_{11}$ and $\widetilde{H}_{22}$ from equations B.26 and B.31 and for a unit harmonic load applied at *x*=0 with angular frequency ϖ, *i.e.* $\widetilde{F} = 2\pi\delta(\omega - \varpi)$, the equation reduces to the value of $\widetilde{y}_1$ as calculated by equation B.16.

Appendix C

THE PIPE-IN-PIPE (PiP) MODEL

The PiP model is used in Chapters 4 and 5 to model a tunnel wall and the surrounding soil. A detailed derivation of the response of this model to a symmetrical loading combination is presented by Forrest [29]. This appendix contains a brief summary of the formulation for the second loading combination, *i.e.* for anti-symmetrical loads. This appendix is divided into four sections. In the first two sections, a free tunnel wall is modelled as a thin shell and as a thick shell respectively. In the third section, the soil is modelled as a full-space with a cylindrical cavity. Finally, the PiP model is constructed by coupling a thin shell tunnel wall with the surrounding continuum soil.

C.1 Modelling the tunnel wall as a thin cylindrical shell

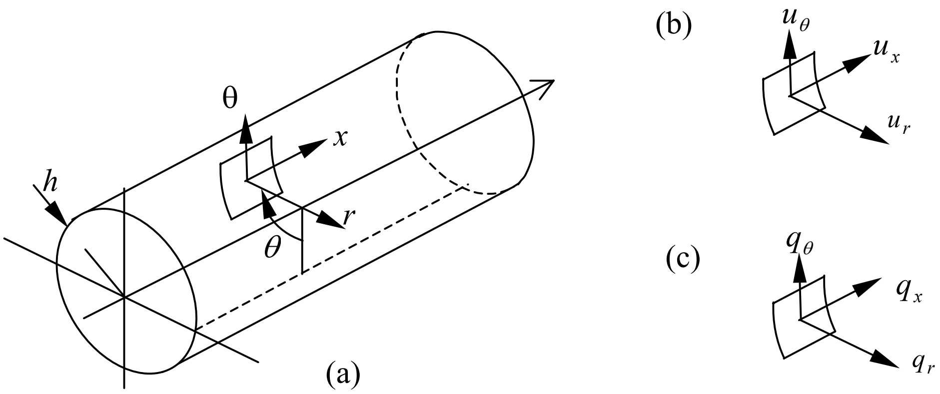

Figure C.1: Coordinate system for the cylindrical thin shell theory, showing (a) the principle directions for an element in the shell, (b) the displacement sign convention and (c) the corresponding sign convention of the applied surface stresses (this figure is reproduced from [29]).

Figure C.1 shows the sign conventions of the displacements and stresses for a free tunnel wall modelled as a thin cylindrical shell. The values of q_x, q_θ and q_r represent the applied stress in the middle surface of the shell in x, θ and r directions respectively.

The following form of the applied stresses and the resulting displacements are substituted in the governing differential equations of a thin shell: for the stresses

$$\begin{aligned} q_x &= \tilde{q}_{xn} \cdot \sin n\theta \cdot e^{i(\omega t+\xi x)}, \\ q_\theta &= \tilde{q}_{\theta n} \cdot \cos n\theta \cdot e^{i(\omega t+\xi x)}, \\ \text{and} \quad q_r &= \tilde{q}_{rn} \cdot \sin n\theta \cdot e^{i(\omega t+\xi x)}; \end{aligned} \tag{C.1}$$

for the displacements

$$\begin{aligned} u_x &= \tilde{u}_{xn} \cdot \sin n\theta \cdot e^{i(\omega t+\xi x)}, \\ u_\theta &= \tilde{u}_{\theta n} \cdot \cos n\theta \cdot e^{i(\omega t+\xi x)}, \\ \text{and} \quad u_r &= \tilde{u}_{rn} \cdot \sin n\theta \cdot e^{i(\omega t+\xi x)}. \end{aligned} \tag{C.2}$$

This leads to the following relationship between the amplitudes of the input-stresses and the output-displacements

$$[\mathbf{A}_2]\begin{bmatrix} \tilde{u}_{xn} \\ \tilde{u}_{\theta n} \\ \tilde{u}_{rn} \end{bmatrix} = \frac{-r_a(1-\nu^2)}{Eh}\begin{bmatrix} \tilde{q}_{xn} \\ \tilde{q}_{\theta n} \\ \tilde{q}_{rn} \end{bmatrix}. \tag{C.3}$$

Note that the loading combination in equation C.1 is the second loading combination which is anti-symmetrical around the shell. For the first loading combination, every cosine in equations C.2 and C.3 should be replaced by a sine and vice versa. In this case the resulting transfer matrix is $\mathbf{A}_1$, its elements are derived by Forrest [29] and given at the end of this section. In this dissertation the subscript 1 is used with transfer matrices of the first loading combination such as $\mathbf{A}_1$. The subscript 2 is used with transfer matrices of the second loading combination such as $\mathbf{A}_2$. Note that Forrest uses no subscripts at all as he only considers the first combination.

$[\mathbf{A}_2]$ is a 3×3 matrix and its elements are calculated by

$$\mathbf{A}_2(1,1) = \frac{\rho \cdot r_a(1-\nu^2)}{E}\omega^2 - r_a\xi^2 - \frac{(1-\nu)}{2r_a}n^2 - \frac{(1-\nu)}{2r_a}\frac{h^2}{12r_a{}^2}n^2$$

$$\mathbf{A}_2(1,2) = -\frac{(1+\nu)}{2}i\xi n$$

$$\mathbf{A}_2(1,3) = -\nu i\xi + \frac{h^2}{12}(i\xi)^3 + \frac{h^2}{12r_a{}^2}\frac{(1-\nu)}{2}i\xi n^2$$

$$\mathbf{A}_2(2,1) = \frac{(1+\nu)}{2}i\xi n$$

$$\mathbf{A}_2(2,2) = \frac{\rho \cdot r_a(1-\nu^2)}{E}\omega^2 - r_a\frac{(1-\nu)}{2}\xi^2 - \frac{1}{r_a}n^2 - \frac{r_a(1-\nu)}{2}\frac{h^2}{4r_a{}^2}\xi^2$$

$$\mathbf{A}_2(2,3) = -\frac{1}{r_a}n - \frac{h^2}{12}\frac{(3-\nu)}{2r_a}\xi^2 n$$

$$\mathbf{A}_2(3,1) = \nu i\xi - \frac{h^2}{12}(i\xi)^3 - \frac{h^2}{12r_a{}^2}\frac{(1-\nu)}{2}i\xi n^2$$

$$\mathbf{A}_2(3,2) = -\frac{1}{r_a}n - \frac{h^2}{12r_a}\frac{(3-\nu)}{2}\xi^2 n$$

$$\mathbf{A}_2(3,3) = \frac{\rho \cdot r_a(1-\nu^2)}{E}\omega^2 - \frac{h^2}{12}\left(r_a\xi^4 + \frac{2}{r_a}\xi^2 n^2 + \frac{1}{r_a{}^3}n^4 \right) - \frac{1}{r_a} + \frac{h^2}{6r_a{}^3}n^2 - \frac{h^2}{12r_a{}^3}$$

where r_a is the mean radius of the shell, *h* is the shell thickness, *E* is the elastic modulus, ρ is the shell's density, ν is Poisson's ratio and *n* is the cross-sectional wavenumber. The elements of $\mathbf{A}_1$ are calculated by [29]

$$\mathbf{A}_1 = \begin{bmatrix} \mathbf{A}_2(1,1) & -\mathbf{A}_2(1,2) & \mathbf{A}_2(1,3) \\ -\mathbf{A}_2(2,1) & \mathbf{A}_2(2,2) & -\mathbf{A}_2(2,3) \\ \mathbf{A}_2(3,1) & -\mathbf{A}_2(3,2) & \mathbf{A}_2(3,3) \end{bmatrix}. \tag{C.4}$$

C.2 Modelling the tunnel wall as a thick cylindrical shell

Using the elastic continuum theory with a cylindrical geometry as shown in Figure C.2, two sets of equations can be written for the stress-displacement relationship at any radius *r* as follows

$$\begin{bmatrix} \tilde{u}_{rn} \\ \tilde{u}_{\theta n} \\ \tilde{u}_{zn} \end{bmatrix} = [\mathbf{U}_2] \cdot \mathbf{C}_2 \quad \text{and} \quad \begin{bmatrix} \tilde{\tau}_{rrn} \\ \tilde{\tau}_{r\theta n} \\ \tilde{\tau}_{rzn} \\ \tilde{\tau}_{\theta\theta n} \\ \tilde{\tau}_{\theta zn} \\ \tilde{\tau}_{zzn} \end{bmatrix} = [\mathbf{T}_2] \cdot \mathbf{C}_2 . \tag{C.5}$$

$\mathbf{U}_2$ is a 3×6 matrix, $\mathbf{T}_2$ is a 6×6 matrix and $\mathbf{C}_2$ is a 6×1 coefficients vector. Note that the coefficients in equation C.5 are for the second loading combination, for instance $\tilde{u}_{rn}$ results from the equation $u_r = \tilde{u}_{rn} \sin n\theta \cdot e^{i(\omega t + \xi x)}$ and $\tilde{\tau}_{rrn}$ results from the equation $\tau_{rr} = \tilde{\tau}_{rrn} \sin n\theta \cdot e^{i(\omega t + \xi x)}$. The sign convention for the displacements and stresses is shown in Figure C.2.

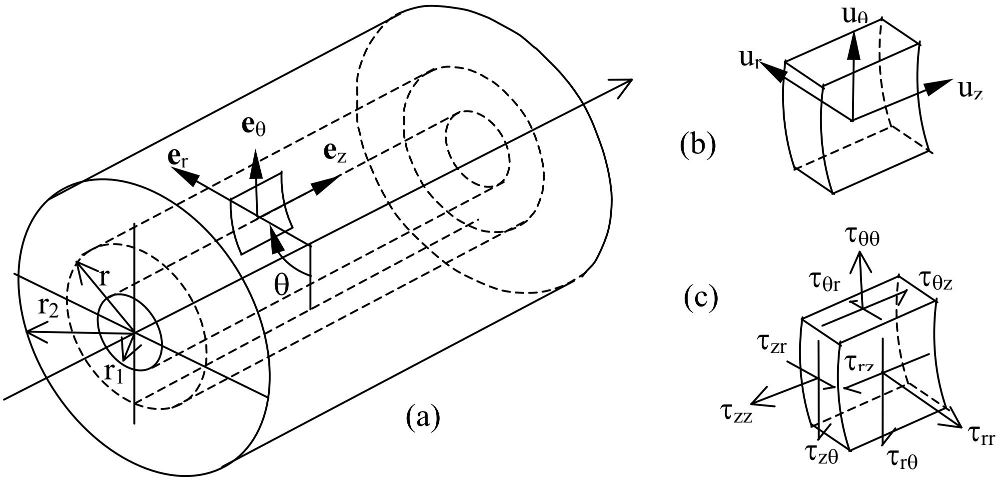

Figure C.2: Coordinate system used for the theory of an elastic continuum with cylindrical geometry, showing (a) the principle directions with their unit vectors for an element of a cylinder at radius *r* and angle θ, (b) the displacement sign convention and (c) the stress sign convention. To model the soil the radius r_1 is set to r_c, *i.e.* the cavity radius and the radius r_2 is set to ∞. (the figure is reproduced from [29]).

To model a free tunnel wall with inner radius r_t and outer radius r_c under anti-symmetrical applied stresses with sinusoidal distribution around the tunnel, equation C.5 is modified to include only surface tractions; *i.e.* $\tilde{\tau}_{rrn}$, $\tilde{\tau}_{r\theta n}$, and $\tilde{\tau}_{rzn}$, so at any radius r

$$\begin{bmatrix} \tilde{u}_{rn} \\ \tilde{u}_{\theta n} \\ \tilde{u}_{zn} \end{bmatrix} = [\mathbf{U}_2]\cdot\mathbf{C}_2 \text{ and } \begin{bmatrix} \tilde{\tau}_{rrn} \\ \tilde{\tau}_{r\theta n} \\ \tilde{\tau}_{rzn} \end{bmatrix} = [\mathbf{T}_{t2}]\cdot\mathbf{C}_2 \tag{C.6}$$

where $\mathbf{T}_{t2}$ comprises of the first three rows of matrix $\mathbf{T}_2$ in C.5. The vector of coefficients $\mathbf{C}_2$ is calculated by solving the two equations which result from calculating the second equation of the pair C.6 at the inner and the outer radius of the tunnel, as follows

$$\left\{ \begin{matrix} \begin{bmatrix} \tilde{\tau}_{rrn} \\ \tilde{\tau}_{r\theta n} \\ \tilde{\tau}_{rzn} \end{bmatrix}_{r=r_t} \\ \begin{bmatrix} \tilde{\tau}_{rrn} \\ \tilde{\tau}_{r\theta n} \\ \tilde{\tau}_{rzn} \end{bmatrix}_{r=r_c} \end{matrix} \right\} = \begin{bmatrix} [\mathbf{T}_{t2}]_{r=r_t} \\ [\mathbf{T}_{t2}]_{r=r_c} \end{bmatrix} \cdot \mathbf{C}_2 = [\mathbf{TT}]\cdot\mathbf{C}_2 . \tag{C.7}$$

The elements of matrix $\mathbf{U}_2$ in equation C.5 are calculated by

$$\mathbf{U}_2(1,1) = \frac{n}{r} I_n(\alpha r) + \alpha I_{n+1}(\alpha r)$$

$$\mathbf{U}_2(1,2) = \frac{n}{r} K_n(\alpha r) - \alpha K_{n+1}(\alpha r)$$

$$\mathbf{U}_2(1,3) = -i\xi I_{n+1}(\beta r)$$

$$\mathbf{U}_2(1,4) = -i\xi K_{n+1}(\beta r)$$

$$\mathbf{U}_2(1,5) = -\frac{n}{r} I_n(\beta r)$$

$$\mathbf{U}_2(1,6) = -\frac{n}{r}K_n(\beta r)$$

$$\mathbf{U}_2(2,1) = \frac{n}{r}I_n(\alpha r)$$

$$\mathbf{U}_2(2,2) = \frac{n}{r}K_n(\alpha r)$$

$$\mathbf{U}_2(2,3) = i\xi I_{n+1}(\beta r)$$

$$\mathbf{U}_2(2,4) = i\xi K_{n+1}(\beta r)$$

$$\mathbf{U}_2(2,5) = -\frac{n}{r}I_n(\beta r) - \beta I_{n+1}(\beta r)$$

$$\mathbf{U}_2(2,6) = -\frac{n}{r}K_n(\beta r) + \beta K_{n+1}(\beta r)$$

$$\mathbf{U}_2(3,1) = i\xi I_n(\alpha r)$$

$$\mathbf{U}_2(3,2) = i\xi K_n(\alpha r)$$

$$\mathbf{U}_2(3,3) = \beta I_n(\beta r)$$

$$\mathbf{U}_2(3,4) = -\beta K_n(\beta r)$$

$$\mathbf{U}_2(3,5) = 0$$

$$\mathbf{U}_2(3,6) = 0$$

where r is the radius of the continuum where the displacements are evaluated. $I_n(\eta)$ and $K_n(\eta)$ are the modified Bessel functions of the first kind and the second kind respectively with order n and argument η. The values of α and β are calculated from the following relationships

$$\alpha^2 = \xi^2 - \omega^2 / c_p^2 \text{ and } \beta^2 = \xi^2 - \omega^2 / c_s^2 \tag{C.8}$$

where $c_p = \sqrt{\frac{\lambda + 2\mu}{\rho}}$ is the speed of compression waves, $c_s = \sqrt{\frac{\mu}{\rho}}$ is the speed of shear waves, λ and μ are Lame's elastic constants, ρ is the density, ν is Poisson's ratio and n is the cross-sectional wavenumber.

The elements of matrix $\mathbf{T}_2$ in equation C.4 are calculated by

$$\mathbf{T}_2(1,1) = [2\mu\frac{(n^2-n)}{r^2} - \lambda\xi^2 + (\lambda+2\mu)\alpha^2]I_n(\alpha r) - 2\mu\frac{\alpha}{r}I_{n+1}(\alpha r)$$

$$\mathbf{T}_2(1,2) = [2\mu\frac{(n^2-n)}{r^2} - \lambda\xi^2 + (\lambda+2\mu)\alpha^2]K_n(\alpha r) + 2\mu\frac{\alpha}{r}K_{n+1}(\alpha r)$$

$$\mathbf{T}_2(1,3) = -2\mu i\xi\beta I_n(\beta r) + 2\mu i\xi\frac{(n+1)}{r}I_{n+1}(\beta r)$$

$$\mathbf{T}_2(1,4) = 2\mu i\xi\beta K_n(\beta r) + 2\mu i\xi\frac{(n+1)}{r}K_{n+1}(\beta r)$$

$$\mathbf{T}_2(1,5) = -2\mu\frac{(n^2-n)}{r^2}I_n(\beta r) - 2\mu\frac{n}{r}\beta I_{n+1}(\beta r)$$

$$\mathbf{T}_2(1,6) = -2\mu\frac{(n^2-n)}{r^2}K_n(\beta r) + 2\mu\frac{n}{r}\beta K_{n+1}(\beta r)$$

$$\mathbf{T}_2(2,1) = 2\mu\frac{(n^2-n)}{r^2}I_n(\alpha r) + 2\mu\frac{n}{r}\alpha I_{n+1}(\alpha r)$$

$$\mathbf{T}_2(2,2) = 2\mu\frac{(n^2-n)}{r^2}k_n(\alpha r) - 2\mu\frac{n}{r}\alpha K_{n+1}(\alpha r)$$

$$\mathbf{T}_2(2,3) = \mu i\xi\beta\, I_n(\beta r) - 2\mu i\xi\frac{(n+1)}{r}I_{n+1}(\beta r)$$

$$\mathbf{T}_2(2,4) = -\mu i\xi\beta\, K_n(\beta r) - 2\mu i\xi\frac{(n+1)}{r}K_{n+1}(\beta r)$$

$$\mathbf{T}_2(2,5) = [-2\mu\frac{(n^2-n)}{r^2} - \mu\beta^2]I_n(\beta r) + 2\mu\frac{\beta}{r}I_{n+1}(\beta r)$$

$$\mathbf{T}_2(2,6) = [-2\mu\frac{(n^2-n)}{r^2} - \mu\beta^2]K_n(\beta r) - 2\mu\frac{\beta}{r}K_{n+1}(\beta r)$$

$$\mathbf{T}_2(3,1) = 2\mu i\xi\frac{n}{r}I_n(\alpha r) + 2\mu i\xi\alpha\, I_{n+1}(\alpha r)$$

$$\mathbf{T}_2(3,2) = 2\mu i\xi\frac{n}{r}K_n(\alpha r) - 2\mu i\xi\alpha\, K_{n+1}(\alpha r)$$

$$\mathbf{T}_2(3,3) = \mu\frac{n}{r}\beta I_n(\beta r) + \mu\left(\xi^2+\beta^2\right)I_{n+1}(\beta r)$$

$$\mathbf{T}_2(3,4) = -\mu\frac{n}{r}\beta K_n(\beta r) + \mu\left(\xi^2+\beta^2\right)K_{n+1}(\beta r)$$

$$\mathbf{T}_2(3,5) = -\mu i \xi \frac{n}{r} I_n(\beta r)$$

$$\mathbf{T}_2(3,6) = -\mu i \xi \frac{n}{r} K_n(\beta r)$$

$$\mathbf{T}_2(4,1) = [-2\mu \frac{(n^2 - n)}{r} + \lambda(\alpha^2 - \xi^2)] I_n(\alpha r) + 2\mu \frac{\alpha}{r} I_{n+1}(\alpha r)$$

$$\mathbf{T}_2(4,2) = [-2\mu \frac{(n^2 - n)}{r^2} + \lambda(\alpha^2 - \xi^2)] K_n(\alpha r) - 2\mu \frac{\alpha}{r} K_{n+1}(\alpha r)$$

$$\mathbf{T}_2(4,3) = -2\mu i \xi \frac{(n+1)}{r} I_{n+1}(\beta r)$$

$$\mathbf{T}_2(4,4) = -2\mu i \xi \frac{(n+1)}{r} K_{n+1}(\beta r)$$

$$\mathbf{T}_2(4,5) = 2\mu \frac{(n^2 - n)}{r} I_n(\beta r) + 2\mu \frac{n}{r} \beta I_{n+1}(\beta r)$$

$$\mathbf{T}_2(4,6) = 2\mu \frac{(n^2 - n)}{r} K_n(\beta r) - 2\mu \frac{n}{r} \beta K_{n+1}(\beta r)$$

$$\mathbf{T}_2(5,1) = 2\mu i \xi \frac{n}{r} I_n(\alpha r)$$

$$\mathbf{T}_2(5,2) = 2\mu i \xi \frac{n}{r} K_n(\alpha r)$$

$$\mathbf{T}_2(5,3) = \mu \frac{n}{r} \beta I_n(\beta r) - \mu \xi^2 I_{n+1}(\beta r)$$

$$\mathbf{T}_2(5,4) = -\mu \frac{n}{r} \beta K_n(\beta r) - \mu \xi^2 K_{n+1}(\beta r)$$

$$\mathbf{T}_2(5,5) = -\mu i \xi \frac{n}{r} I_n(\beta r) - \mu i \xi \beta I_{n+1}(\beta r)$$

$$\mathbf{T}_2(5,6) = -\mu i \xi \frac{n}{r} K_n(\beta r) + \mu i \xi \beta K_{n+1}(\beta r)$$

$$\mathbf{T}_2(6,1) = [\lambda \alpha^2 - (\lambda + 2\mu)\xi^2] I_n(\alpha r)$$

$$\mathbf{T}_2(6,2) = [\lambda \alpha^2 - (\lambda + 2\mu)\xi^2] K_n(\alpha r)$$

$$\mathbf{T}_2(6,3) = 2\mu i \xi \beta I_n(\beta r)$$

$$\mathbf{T}_2(6,4) = -2\mu i \xi \beta K_n(\beta r)$$

$$\mathbf{T}_2(6,5) = 0$$

$$\mathbf{T}_2(6,6) = 0$$

The elements of $\mathbf{U}_1$ and $\mathbf{T}_1$ for the first loading combination can be calculated by

$$\mathbf{T}_1 = \begin{bmatrix} \mathbf{T}_2(1,1) & \mathbf{T}_2(1,2) & -\mathbf{T}_2(1,3) & -\mathbf{T}_2(1,4) & -\mathbf{T}_2(1,5) & -\mathbf{T}_2(1,6) \\ -\mathbf{T}_2(2,1) & -\mathbf{T}_2(2,2) & \mathbf{T}_2(2,3) & \mathbf{T}_2(2,4) & \mathbf{T}_2(2,5) & \mathbf{T}_2(2,6) \\ \mathbf{T}_2(3,1) & \mathbf{T}_2(3,2) & -\mathbf{T}_2(3,3) & -\mathbf{T}_2(3,4) & -\mathbf{T}_2(3,5) & -\mathbf{T}_2(3,6) \\ \mathbf{T}_2(4,1) & \mathbf{T}_2(4,2) & -\mathbf{T}_2(4,3) & -\mathbf{T}_2(4,4) & -\mathbf{T}_2(4,5) & -\mathbf{T}_2(4,6) \\ -\mathbf{T}_2(5,1) & -\mathbf{T}_2(5,2) & \mathbf{T}_2(5,3) & \mathbf{T}_2(5,4) & \mathbf{T}_2(5,5) & \mathbf{T}_2(5,6) \\ \mathbf{T}_2(6,1) & \mathbf{T}_2(6,2) & -\mathbf{T}_2(6,3) & -\mathbf{T}_2(6,4) & -\mathbf{T}_2(6,5) & -\mathbf{T}_2(6,6) \end{bmatrix} \qquad \text{(C.9)}$$

and

$$\mathbf{U}_1 = \begin{bmatrix} \mathbf{U}_2(1,1) & \mathbf{U}_2(1,2) & -\mathbf{U}_2(1,3) & -\mathbf{U}_2(1,4) & -\mathbf{U}_2(1,5) & -\mathbf{U}_2(1,6) \\ -\mathbf{U}_2(2,1) & -\mathbf{U}_2(2,2) & \mathbf{U}_2(2,3) & \mathbf{U}_2(2,4) & \mathbf{U}_2(2,5) & \mathbf{U}_2(2,6) \\ \mathbf{U}_2(3,1) & \mathbf{U}_2(3,2) & -\mathbf{U}_2(3,3) & -\mathbf{U}_2(3,4) & -\mathbf{U}_2(3,5) & -\mathbf{U}_2(3,6) \end{bmatrix}. \qquad \text{(C.10)}$$

C.3 Modelling the soil as a thick cylindrical shell

For the second loading combination, equations C.6 can be modified to model a full soil space with a cylindrical cavity by setting the external radius to infinity. At the external radius, stresses and displacements should decay to zero. To satisfy this requirement all coefficients associated with the modified Bessel function of the first kind in equations C.6 should be set to zero, as the modified Bessel function of the first kind increases with increasing argument. $\mathbf{U}_2$ and $\mathbf{T}_{\mathbf{t}2}$ matrices are arranged in order to give the longitudinal, tangential and radial displacements and stresses in the directions defined for the thin shell (see also Figure C.3). Equations C.6 are rewritten as

$$\tilde{\mathbf{u}}_n = [\mathbf{U}_{\mathbf{m}2}]\cdot\mathbf{B}_2 \text{ and } \tilde{\boldsymbol{\tau}}_n = [\mathbf{T}_{\mathbf{m}2}]\cdot\mathbf{B}_2 \qquad \text{(C.11)}$$

where

$$\tilde{\mathbf{u}}_n = [\tilde{u}_{xn}, \tilde{u}_{\theta n}, \tilde{u}_{rn}]^T,\ \tilde{\boldsymbol{\tau}}_n = [\tilde{\tau}_{xn}, \tilde{\tau}_{\theta n}, \tilde{\tau}_{rn}]^T,\ \mathbf{B}_2 = [\mathbf{C}_2(2,1), \mathbf{C}_2(4,1), \mathbf{C}_2(6,1)]^T,$$

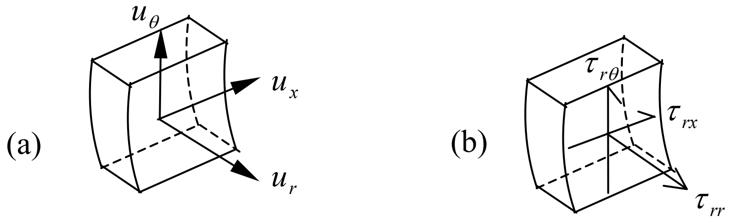

Figure C.3: The displacement and stress sign convention used for modelling the soil. (a) The displacements of infinitesimal cylindrical element. (b) The stresses on the inner surface of a cylindrical element.

$$\mathbf{U}_{\mathbf{m}2} = \begin{bmatrix} \mathbf{U}_2(3,2) & \mathbf{U}_2(3,4) & \mathbf{U}_2(3,6) \\ \mathbf{U}_2(2,2) & \mathbf{U}_2(2,4) & \mathbf{U}_2(2,6) \\ -\mathbf{U}_2(1,2) & -\mathbf{U}_2(1,4) & -\mathbf{U}_2(1,6) \end{bmatrix}, \ \mathbf{T}_{\mathbf{m}2} = \begin{bmatrix} -\mathbf{T}_2(3,2) & -\mathbf{T}_2(3,4) & -\mathbf{T}_2(3,6) \\ -\mathbf{T}_2(2,2) & -\mathbf{T}_2(2,4) & -\mathbf{T}_2(2,6) \\ \mathbf{T}_2(1,2) & \mathbf{T}_2(1,4) & \mathbf{T}_2(1,6) \end{bmatrix}.$$

Knowing the applied forces at the inner surface of the cavity, the second equation of the pair C.11 is used to calculate the vector of coefficients $\mathbf{B}_2$, where the radius of cavity $r = r_c$ is used to calculate $\mathbf{T}_{\mathbf{m}2}$. Hence by substituting any radius *r*, the first pair of equation C.11 is used to find the displacement components in the soil.

C.4 Coupling the tunnel and the soil (the PiP model)

The tunnel is modelled as a thin cylindrical shell and is coupled to the model in the previous section for the soil with a cylindrical cavity.

The input stresses for the tunnel wall are the resultant of applied stresses at the inner surface and the induced stresses at the tunnel soil interface. Using equation C.3 for the tunnel

$$[\mathbf{A}_{\mathbf{E}2}]\cdot\widetilde{\mathbf{u}}_n = -\frac{Eh}{r_a(1-\nu^2)}[\mathbf{A}_2]\cdot\widetilde{\mathbf{u}}_n = (r_t/r_a)\begin{bmatrix}\widetilde{P}_{xn}\\ \widetilde{P}_{yn}\\ \widetilde{P}_{zn}\end{bmatrix} - (r_c/r_a)\begin{bmatrix}\widetilde{\tau}_{xn}\\ \widetilde{\tau}_{yn}\\ \widetilde{\tau}_{zn}\end{bmatrix}$$

or

$$[\mathbf{A}_{\mathbf{E}}]\cdot\widetilde{\mathbf{u}}_n = (r_t/r_a)\widetilde{\mathbf{P}}_n - (r_c/r_a)\widetilde{\boldsymbol{\tau}}_n \qquad \text{(C.12)}$$

where $\widetilde{\mathbf{P}}_n$ is the applied stress at the inner surface of the tunnel and $\widetilde{\boldsymbol{\tau}}_n$ is the induced stress at the tunnel soil interface. The values (r_t/r_a) and (r_c/r_a) in the right hand side of the equation are used to evaluate the equivalent stresses at the middle surface of the shell from the original values at the tunnel wall and at the cavity wall respectively.

For the soil model, using equation C.11 at the interface, *i.e.* $r = r_c$

$$\widetilde{\mathbf{u}}_n = [\mathbf{U}_{\mathbf{m}2}]_{r=r_c}\cdot\mathbf{B}_2$$

and

$$\widetilde{\boldsymbol{\tau}}_n = [\mathbf{T}_{\mathbf{m}2}]_{r=r_c}\cdot\mathbf{B}_2. \qquad \text{(C.13)}$$

Solving C.12 and C.13 to find the vector of coefficients $\mathbf{B}_2$

$$\mathbf{B}_2 = \{\frac{r_a}{r_t}\mathbf{A}_{\mathbf{E}2}[\mathbf{U}_{\mathbf{m}2}]_{r=r_c} + \frac{r_c}{r_t}[\mathbf{T}_{\mathbf{m}2}]_{r=r_c}\}^{-1}\widetilde{\mathbf{P}}_n. \qquad \text{(C.14)}$$

To calculate the soil displacement at radius *r* and angle θ from the tunnel invert for a concentrated tangential load applied at the tunnel invert, equation C.14 is used with $\widetilde{\mathbf{P}}_{\mathbf{n}} = [0,1,0]^T$ and $\mathbf{B}_2$ is evaluated for each *n* (up to enough value for convergence). Then the first pair of equation C.13 at radius *r* is used to calculate the Fourier series components of the displacement. Finally the soil displacement is calculated by

$$\widetilde{\mathbf{u}} = \sum_{n=0}^{n_{\max}} c_{\theta n}\begin{bmatrix}\widetilde{u}_x(n,\xi,\omega)\cdot\sin n\theta\\ \widetilde{u}_\theta(n,\xi,\omega)\cdot\cos n\theta\\ \widetilde{u}_r(n,\xi,\omega)\cdot\sin n\theta\end{bmatrix} \qquad \text{(C.15)}$$

where c_{vn} is defined by equation 4.46 and $n_{\max}$ is maximum value of n included. Note that an alternative way is to substitute $\widetilde{\mathbf{P}}_{\mathbf{n}} = [0, c_{vn}, 0]^T$ and perform the summation in equation C.15 without the coefficients c_{vn}.

A different application of the elastic-continuum theory is presented in Appendix D, where it is used to calculate the full-space Green's functions.

Appendix D

FULL-SPACE GREEN'S FUNCTIONS

The elastic continuum theory in cylindrical coordinates is used in Chapter 4 and Appendix C to model a homogeneous infinite soil with a cylindrical cavity. The calculated expressions for the displacements and stresses are used here to evaluate Green's functions for a full space. The results are then compared with the fundamental solutions for a full space, *i.e.* Green's functions for a full space, which are well known in the Boundary Element method.

For a unit line load applied in a full-space with a wavenumber ξ and an angular frequency ω in the form $1 \cdot e^{i(\xi x+\omega t)}$, the displacement at a line parallel to the line load and at distance r_p with angles (φ_1, φ_2) as shown in Figure D.1 can be written as $\widetilde{G}(\xi, \omega, r_p, \varphi_1, \varphi_2) \cdot e^{i(\xi x+\omega t)}$. The function $\widetilde{G}(\xi, \omega, r_p, \varphi_1, \varphi_2)$ is called Green's function for a full space.

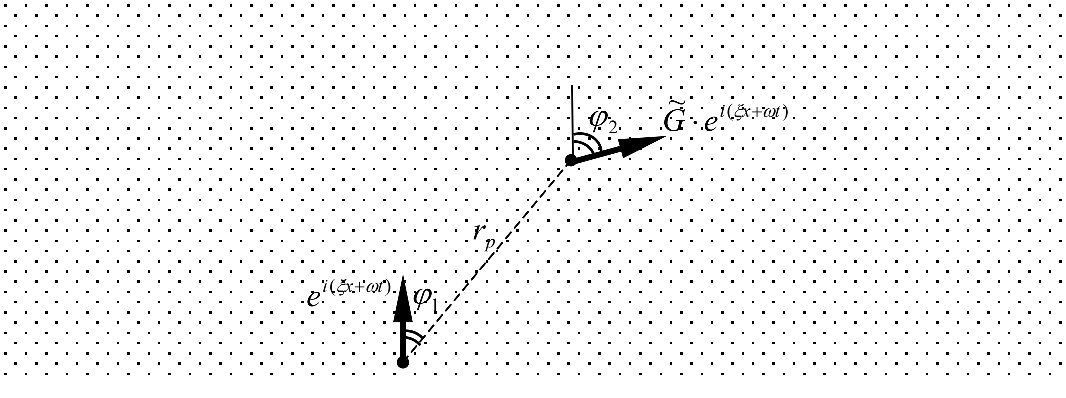

Figure D.1: Green's function for an elastic continuum. The displacement along a line in the space parallel to the applied line load is in the form $\widetilde{G}(\xi, \omega, r_p, \varphi_1, \varphi_2) \cdot e^{i(\xi x+\omega t)}$ where $\widetilde{G}(\xi, \omega, r_p, \varphi_1, \varphi_2)$ is Green's function for a full-space.

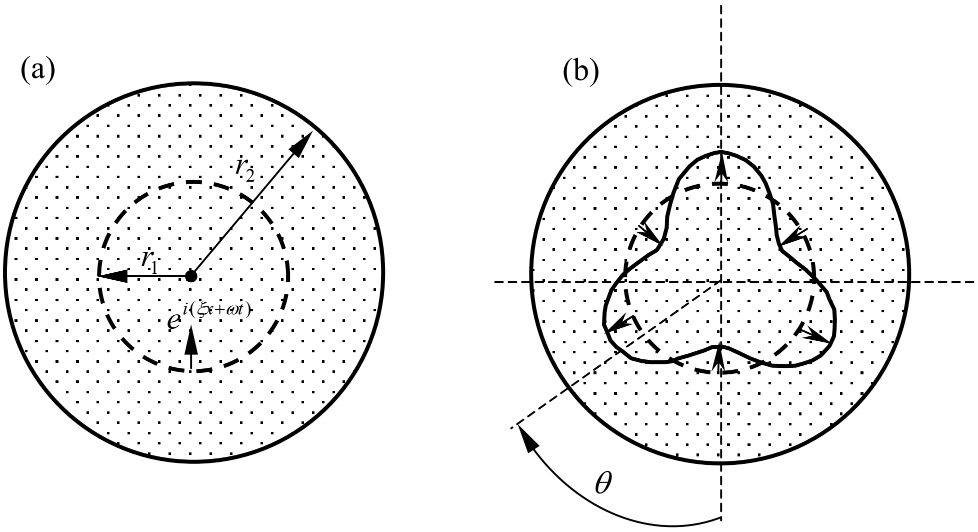

Figure D.2: Decomposition of the line load: (a) into its Fourier components around a cylindrical surface with radius r_1. (b) The load component with $n=3$, *i.e.* with distribution $\cos 3\theta$, according to equation D.1. The other cylindrical boundary r_2 tends to infinity to model a full-space.

The line load in the full space can be written in delta function form and then decomposed into its Fourier series components, see Figure D.2, around some virtual cylinder with radius r_1 as

$$\frac{\delta(\theta)}{r_1}e^{i(\xi x+\omega t)}=\sum_{n=0}^{\infty}a_n\cos(n\theta)\cdot e^{i(\xi x+\omega t)} \tag{D.1}$$

where $a_0=\dfrac{1}{2\pi r_1}$, $a_n=\dfrac{1}{\pi r_1}$ for $n\geq 1$, and θ is measured as shown in Figure D.2.b.

To calculate the full-space displacement at some line parallel to the line load using the elastic continuum theory, the displacement is calculated first for a stress in the form $\cos n\theta\cdot e^{i(\xi x+\omega t)}$ applied radially on the full-space along the virtual cylinder with radius r_1. This displacement is then multiplied by the factor a_n in equation D.1 and the total displacement due to the line load is calculated by summing the displacements for values of n up to some number which is enough for convergence.

To calculate the displacement for a stress in the form $\cos n\theta\cdot e^{i(\xi x+\omega t)}$ applied radially to the virtual cylinder with radius r_1, the full-space is divided into a cylinder with radius r_1 and an infinite domain with a cylindrical cavity as shown in Figure D.3. The applied stress can be written in its longitudinal, tangential and radial components as

$$\boldsymbol{\tau} = \begin{bmatrix} \cos n\theta & 0 & 0 \\ 0 & \sin n\theta & 0 \\ 0 & 0 & \cos n\theta \end{bmatrix} \tilde{\boldsymbol{\tau}}_n \cdot e^{i(\xi x + \omega t)} \text{ with } \tilde{\boldsymbol{\tau}}_n = [0,0,1]^T . \tag{D.2}$$

The applied stress $\boldsymbol{\tau}$ results in internal stresses on the cylinder $\boldsymbol{\tau}_1$ and on the cavity $\boldsymbol{\tau}_2$ with the same sinusoidal distribution. The relationship between the magnitudes of the applied stress and the induced stresses is given by

$$\tilde{\boldsymbol{\tau}}_n = \tilde{\boldsymbol{\tau}}_{n1} + \tilde{\boldsymbol{\tau}}_{n2} . \tag{D.3}$$

The stress-displacement relationships on the cavity can be calculated by

$$\tilde{\boldsymbol{\tau}}_{n2} = [\mathbf{T}_{\mathbf{m}1}]_{r=r_1} \cdot \mathbf{B}_1 \text{ and } \tilde{\mathbf{u}}_{n2} = [\mathbf{U}_{\mathbf{m}1}]_{r=r_1} \cdot \mathbf{B}_1 \tag{D.4}$$

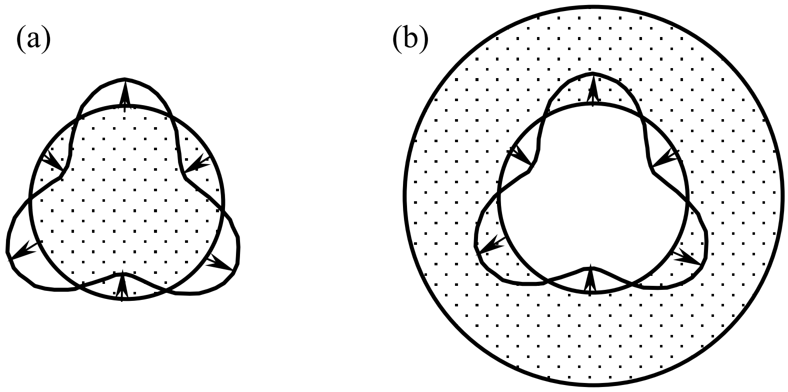

Figure D.3: The full-space model is divided into two models: (a) an infinite cylinder with radius r_1 and (b) an infinite domain with a cylindrical cavity of radius r_1. The applied stress on Figure D.2.b is transferred to the two models above with the same circumferential distribution.

where $\mathbf{T}_{\mathbf{m}1}$, $\mathbf{U}_{\mathbf{m}1}$ are the 3×3 stress and displacement matrices for an infinite domain with a cylindrical cavity under the first loading combination, $\mathbf{B}_1$ is the 3×1 vector of coefficients, see Appendix C.3 and Section 4.4.1 for more details.

The stress-displacement relationships on the surface of the cylinder are calculated by

$$-\tilde{\boldsymbol{\tau}}_{n1} = [\mathbf{T}_{\mathbf{p}1}]_{r=r_1} \cdot \mathbf{E}_1 \text{ and } \tilde{\mathbf{u}}_{n1} = [\mathbf{U}_{\mathbf{p}1}]_{r=r_1} \cdot \mathbf{E}_1 \tag{D.5}$$

where $[\mathbf{T}_{\mathbf{p}1}]$, $[\mathbf{U}_{\mathbf{p}1}]$ are the 3×3 stress and displacement matrices for an infinite cylinder under the first loading combination and $\mathbf{E}_1$ is the 3×1 vector of coefficients.

The elements of $[\mathbf{T}_{\mathbf{p}1}]$ and $[\mathbf{U}_{\mathbf{p}1}]$ are calculated by modifying equations C.5 to model an infinite cylinder under the first loading combination. Note that the modified Bessel function of the second kind tends to infinity for zero argument, *i.e.* at $r = 0$. Hence all coefficients which are associated with this function, should be set to zero. The matrices $[\mathbf{T}_{\mathbf{p}1}]$ and $[\mathbf{U}_{\mathbf{p}1}]$ are arranged to give in order the longitudinal, tangential and radial stresses and displacements in the directions shown in Figure C.3. The elements of $[\mathbf{T}_{\mathbf{p}1}]$ and $[\mathbf{U}_{\mathbf{p}1}]$ are calculated by

$$\mathbf{U}_{\mathbf{p}1} = \begin{bmatrix} \mathbf{U}_1(3,1) & \mathbf{U}_1(3,3) & \mathbf{U}_1(3,5) \\ \mathbf{U}_1(2,1) & \mathbf{U}_1(2,3) & \mathbf{U}_1(2,5) \\ -\mathbf{U}_1(1,1) & -\mathbf{U}_1(1,3) & -\mathbf{U}_1(1,5) \end{bmatrix} \tag{D.6}$$

and

$$\mathbf{T}_{\mathbf{p}1} = \begin{bmatrix} -\mathbf{T}_1(3,1) & -\mathbf{T}_1(3,3) & -\mathbf{T}_1(3,5) \\ -\mathbf{T}_1(2,1) & -\mathbf{T}_1(2,3) & -\mathbf{T}_1(2,5) \\ \mathbf{T}_1(1,1) & \mathbf{T}_1(1,3) & \mathbf{T}_1(1,5) \end{bmatrix}. \tag{D.7}$$

To satisfy the compatibility condition on the cylinder-cavity interface

$$\tilde{\mathbf{u}}_{n2} = \tilde{\mathbf{u}}_{n1}. \tag{D.8}$$

By solving the second pairs of equations D.4 and D.5 and using equation D.8, $\mathbf{B}_1$ can be calculated by

$$\mathbf{B}_1 = [\mathbf{U}_{\mathbf{m}1}]^{-1}[\mathbf{U}_{\mathbf{p}1}] \cdot \mathbf{E}_1 . \tag{D.9}$$

The value of $\mathbf{E}_1$ can be calculated by substituting the values of $\tilde{\boldsymbol{\tau}}_{n1}$ and $\tilde{\boldsymbol{\tau}}_{n2}$ from equations D.5 and D.4 respectively in equation D.3 and using equation D.9 to get

$$\mathbf{E}_1 = \{-[\mathbf{T}_{\mathbf{p}1}] + [\mathbf{T}_{\mathbf{m}1}] \cdot [\mathbf{U}_{\mathbf{m}1}]^{-1}[\mathbf{U}_{\mathbf{p}1}]\}^{-1} \tilde{\boldsymbol{\tau}}_n . \tag{D.10}$$

Knowing the value of $\mathbf{E}_1$, the value of $\mathbf{B}_1$ is calculated from equation D.9. Hence the displacement at any radius r from the centre of the cylinder can be calculated from

$$\tilde{\mathbf{u}}_n = [\mathbf{U}_{\mathbf{p}1}]_r \cdot \mathbf{E}_1 \quad \text{for } r \le r_1 \tag{D.11}$$

and

$$\tilde{\mathbf{u}}_n = [\mathbf{U}_{\mathbf{m}1}]_r \cdot \mathbf{B}_1 \quad \text{for } r \ge r_1 . \tag{D.12}$$

The calculations are performed for values of $n = [0,1,2,..,n_{\max}]$, where $n_{\max}$ is large enough for convergence. The displacement that was calculated from equation D.11 or D.12 is weighted with its Fourier value a_n in equation D.1 and its sinusoidal harmonic, *i.e.* $\cos n\theta$ if radial or longitudinal and $\sin n\theta$ if tangential.

Figure D.4 shows the plane-strain Green's function $\tilde{G}(\xi = 0, \omega, r_p = 7, \varphi_1 = 0^\circ, \varphi_2 = 0^\circ)$, *i.e.* at 7m above the load. The results are calculated by summing the Fourier components up to n=1, 10, 20 and 40. The full-space parameters are those for the soil given in Table 4.1, with hysteric damping factor associated with the shear modulus η_μ =0.06 such that the new soil parameters (with subscript 2) are:

- the shear modulus $\mu_2 = \mu(1 + i\eta_\mu) = 5\times10^6 + 3\times10^5 i\ Pa$;
- the bulk modulus $K_2 = K = E/[3(1-\nu)] = 1.083\times10^7\ Pa$;
- Poisson's ratio $\nu_2 = (3K_2 - 2\mu_2)/[2(3K_2 + \mu_2)] = 0.3 - 0.01i$;

- Lame's constant $\lambda_2 = 2\mu_2 \nu_2 /(1-2\nu_2) = 7.5\times10^6 - 2\times10^5 i\ Pa$;
- the pressure-wave velocity $c_{p2} = \sqrt{(\lambda_2 + 2\mu_2)/\rho} = 94.983 + 1.085i\ m/s$;
- the shear-wave velocity $c_{s2} = \sqrt{\mu_2/\rho} = 50.79 + 1.522i\ m/s$.

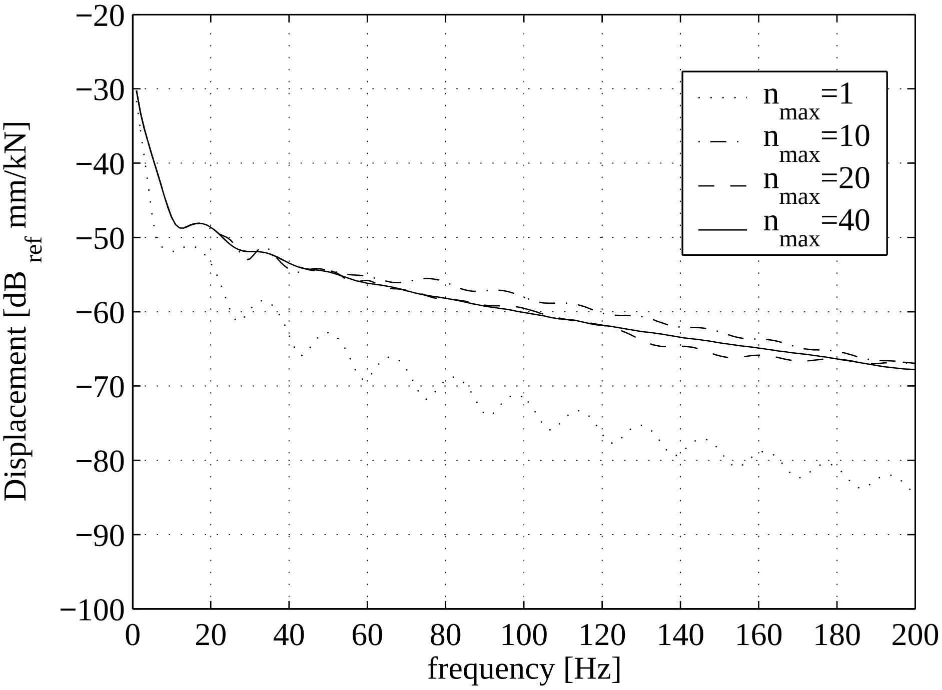

Figure D.4: Green's function for a 2D plane-strain problem, *i.e.* for $\xi = 0$, with $r_p = 7m$, $\varphi_1 = 0^\circ$ and $\varphi_2 = 0^\circ$, calculated by dividing the full-space to a cylinder and a continuum with a cylindrical cavity.

The results in Figure D.4 are recalculated using the direct Green's functions for a harmonic plane-strain problem given by Dominguez [23] as

$$\widetilde{G}(\omega, r_p, \varphi_1, \varphi_2) = \frac{1}{2\pi c_s{}^2 \rho}[-0.5\chi \sin 2\varphi_1 \sin\varphi_2 + \psi\cos\varphi_2 - \chi\cos^2\varphi_1 \cos\varphi_2] \qquad (D.13)$$

where

$$\psi = K_0(\frac{i\omega\cdot r}{c_s}) + (\frac{c_s}{i\omega\cdot r})[K_1(\frac{i\omega\cdot r}{c_s}) - \frac{c_s}{c_p}K_1(\frac{i\omega\cdot r}{c_p})],$$

$$\chi = K_2(\frac{i\omega \cdot r}{c_s}) - (\frac{c_s^2}{c_p^2})K_2(\frac{i\omega \cdot r}{c_p}),$$

$K_n(\kappa)$ is the modified Bessel functions of the second kind with order n and argument κ.

The solution in equation D.13 is also known as the fundamental solution of a plane-strain dynamic problem, which is used in the Boundary Elements method.

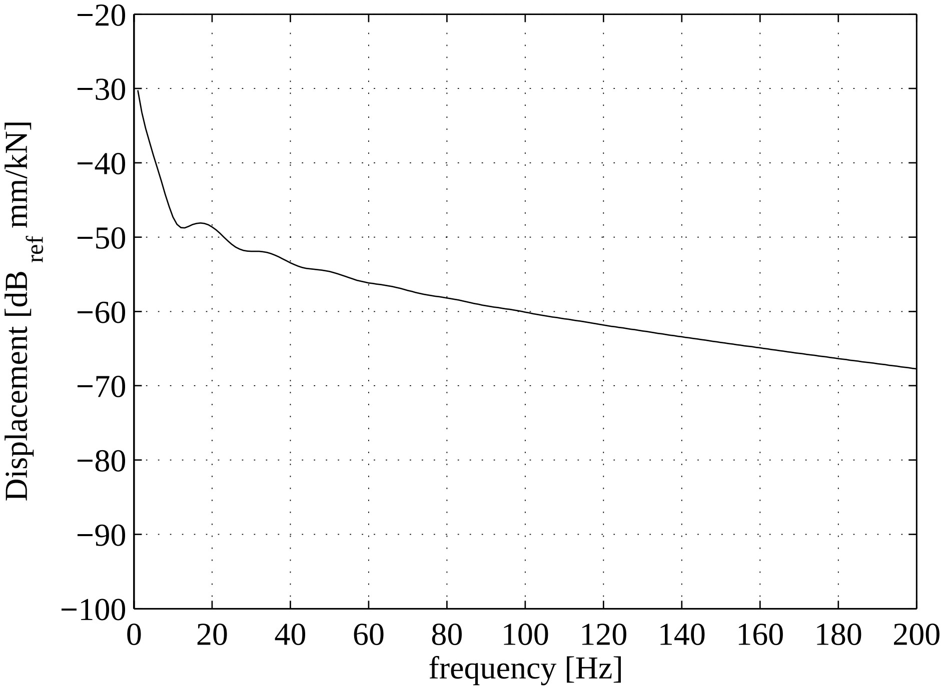

Figure D.5: Green's function for a 2D plane-strain problem, *i.e.* $\xi = 0$, with $r_p = 7m$, $\varphi_1 = 0^\circ$ and $\varphi_2 = 0^\circ$, calculated using the fundamental solution in equation D.13.

Figure D.5 shows the Green's function for $r_p = 7m$, $\varphi_1 = 0^\circ$ and $\varphi_2 = 0^\circ$, calculated using the fundamental solution in equation D.13, which agrees with the results in Figure D.4 for the elastic-continuum theory.